
# BEYOND THE STATIC DESCRIPTION OF THE ELECTRONIC STRUCTURE:EXCITED STATE DYNAMICS IN TRANSITION METAL COMPLEXES AND ORGANIC COMPOUNDS

**Marc Alías Rodríguez**

UNIVERSITAT ROVIRA i VIRGILI

# Beyond the static description of the electronic structure: Excited state dynamics in transition metal complexes and organic compounds.

MARC ALÍAS RODRÍGUEZ

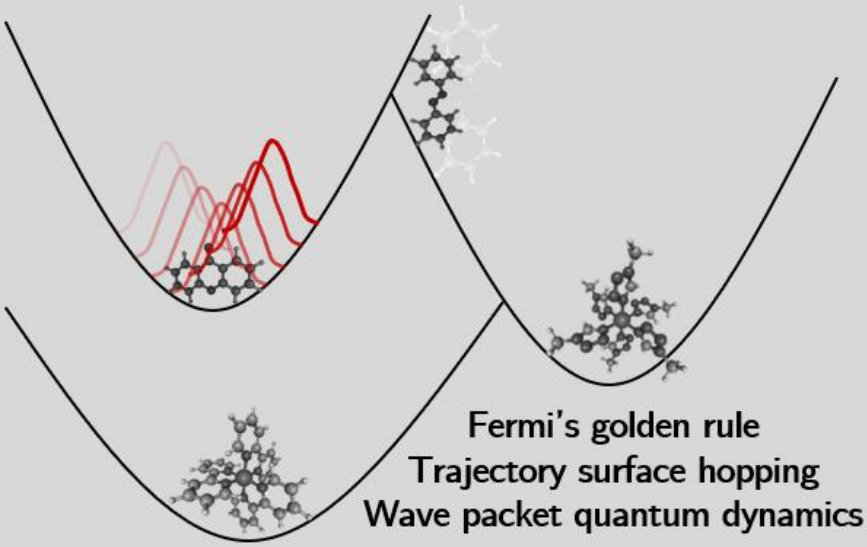


**DOCTORAL THESIS**
**2021**

UNIVERSITAT ROVIRA I VIRGILI
BEYOND THE STATIC DESCRIPTION OF THE ELECTRONIC STRUCTURE:EXCITED STATE DYNAMICS IN TRANSITION METAL COMPLEXES AND ORGANIC COMPOUNDS
Marc Alías Rodríguez

Marc Alías Rodríguez

# Beyond the static description of the electronic structure: Excited state dynamics in transition metal complexes and organic compounds

DOCTORAL THESIS

Supervised by

Prof. Coen de Graaf

Departament de Química Física i Inorgànica

Grup de Química Quàntica

UNIVERSITAT
ROVIRA i VIRGILI

Tarragona 2021

UNIVERSITAT ROVIRA I VIRGILI
BEYOND THE STATIC DESCRIPTION OF THE ELECTRONIC STRUCTURE:EXCITED STATE DYNAMICS IN TRANSITION METAL COMPLEXES AND ORGANIC COMPOUNDS
Marc Alías Rodríguez

UNIVERSITAT ROVIRA i VIRGILI

Departament de Química Física i Inorgànica

Prof. Coen de Graaf, investigador ICREA en el Departament de Química Física i Inorgànica de la Universitat Rovira i Virgili.

FAIG CONSTAR que aquest treball, titulat

**"Beyond the static description of the electronic structure: Excited state dynamics in transition metal complexes and organic compounds"**

que presenta Marc Alías Rodríguez per a l'obtenció del títol de Doctor, ha estat realitzat sota la meva direcció al Departament de Química Física d'aquesta universitat i que acompleix els requeriments per poder optar a la Menció Internacional.

Tarragona , 14 de maig de 2021

Prof. Coen de Graaf

UNIVERSITAT ROVIRA I VIRGILI
BEYOND THE STATIC DESCRIPTION OF THE ELECTRONIC STRUCTURE:EXCITED STATE DYNAMICS IN TRANSITION METAL COMPLEXES AND ORGANIC COMPOUNDS
Marc Alías Rodríguez

# Agraïments/Acknowledgments

El camí que recorrem no és més que el resultat d'un conjunt d'eleccions en una constant de bifurcacions que la vida ens planteja. Moltes persones m'han influit en les decisions que m'han portat fins aquí, vull aprofitar aquest espai per agraïr-los i dedicar-los aquest escrit que aquí presento.

Al poc de començar a la universitat ja em vaig adonar el que els anys més tard acabarien per confirmar-me, que el món de la química experimental no seria el meu. Havia de fer el meu camí en la química teòrica, la química d'ordinador i equacions i ben lluny de reactius i matrassos, per la meva seguretat i la de tots els altres. És per això que voldria començar agraint als membres del grup de Química Quàntica de la URV la bona rebuda que vaig tenir des del començament i tot el temps que hem compartit. Els set anys que he passat aquí fan que senti aquestes parets com una segona casa.

Al meu director de tesis, al professor Coen de Graaf vull agrair-li tot l'esforç i tota la dedicació que ha tingut per ensenyar-me i per totes les discussions científiques que hem tingut al llarg d'aquests anys. Alguns projectes no han sortit bé, tot i això de tots n'he pogut extreure nous coneixements, espero acabar en els propers mesos tot el treball que hem començat i poder seguir col·laborant en el futur perquè és un plaer treballar amb tu. Vull extendre l'agraïment a la resta de membres del *small group meeting* per les fructíferes discussions que s'hi han dut a terme. Mar bajo tu tutela empecé en el mundo de la química teórica y me alegro mucho que así fuera, tienes una gran habilidad para la docencia dada tu gran capacidad para transmitir siempre los conceptos clave con ejemplos altamente ilustrativos. Xavi gràcies perquè les teves preguntes sempre fan replantejar els resultats o raonaments i entendre'ls o aprendre a transmetre'ls millor en futures discussions. Rosa, t'he d'agraïr des de les discussions cíentífiques que hem tingut per mail i en seminaris fins a com ens has cuidat quan hem anat de congrés... Però, també et vull agraïr tota la ajuda en els tràmits burocràtics, sense aquesta ajuda hagués estat tot molt més complicat. Durant aquests anys no només he estat fent recerca

sinó també docència, vull agrair als tres coordinadors d'assignatura amb qui m'ha tocat treballar. Joan, Josep Manel i Maria realment la comunicació ha estat molt facil, moltes gràcies per tots els consells però alhora la llibertat perquè exercis la docència que cregués més adequada en cada moment, ha estat un plaer treballar al vostre costat. Desitjaria extendre aquest agraïment a la resta de professors del grup Toni, Josep Maria, Jordi i Anna perquè heu contribuit en la meva formació tant en la docència que em vau impartir en la meva etapa d'estudiant com en les discussions científiques que directa o indirectament hem tingut durant els seminaris de grup. Per acabar, voldria tenir unes paraules per en Jose, l'Elisenda i en Moisés perquè ells fan possible el bon funcionament del grup. Gràcies per tots els fitxers recuperats després de males decisions i per tenir a punt ordinadors i programes per a que poguem fer la nostra feina.

Vull tenir unes paraules també pels doctorands amb els que he compartit tan bones estones, ha estat un plaer compartir aquests moments amb vosaltres i espero, ben aviat, poder celebrar tot el que la situació actual ens ha fet ajornar. Antonio he echado mucho de menos durante este último año todas las charlas en el despacho y en el trayecto diario hacia Tarragona, guardo un gran recuerdo de todos estos momentos, gracias también por todos los consejos y aclaraciones sobre el depósito, ¡pronto celebramos las dos tesis! Almu, gràcies per no deixar-me tirat a Finlàndia tot i fer-te enfadar tantes vegades jeje. Ho he passat molt bé en els congressos/workshops i moments al despatx que hem compartit, molta sort en aquesta nova etapa que comences! Albert, ja t'ho he dit moltes vegades, però realment és molt estimulant discutir de química amb tu per la il·lusió amb la que transmets i per la curiositat que demostres ja que deixa la porta oberta a noves idees, estic segur que la teva carrera científica serà molt exitosa. Toni, moltes gràcies pel teu bon humor cada dia! Ara recordo amb nostàlgia totes les bromes a l'hora de dinar i tots els sopars i festes que hem compartit. No et preocupis que tot arriba, ets el següent (tic-tac jaja). Khalid, hemos seguido caminos simultáneos en el grado, master y doctorado, además he tenido el placer de compartir docencia donde hemos pasado también magníficos momentos, sigue emprendiendo y luchando por tus proyectos, eres un crack! Yeamin, gracias por presentarnos la cultura y gastronomía de tu país, mucha suerte en tu defensa! Roser, et desitjo el millor en aquesta nova etapa que has començat en l'àmbit de la docència.

Ricardo mucha suerte en el final de tu tesis. Aitor y Yannick us ha tocat arribar en un moment complicat, i hem tingut poques oportunitats de compartir estones, tot i això, aquestes sempre han estat divertides, molta sort! Fei, I wish you all the best, it is nice to see you always positive and smiling! Jianfang, it has been a pleasure share with you some projects. I per tots els nouvinguts que ara comencen, disfruteu molt del camí. També m'agradaria agraïr als que fa més temps que van deixar el grup, perquè les seves experiències i consells m'han ajudat durant la realització d'aquesta tesis. Moltes gràcies Magda, Diego, Gerard, Ximo i Laura!

I would like to thank Prof. Nicolas Ferré for the time I spent on his group in Marseille. It was a great experience from both scientific and personal perspectives. I would like specially to thank Karno, now Dr. Schwinn, for the sites of Marseille that you showed me and the moments that we spent together. També, vull agraïr al Dr. Miquel Huix-Rotllant tot el temps que va invertir en ensenyar-me metodologies completament noves per mi. Va ser molt fàcil treballar amb tu tan a nivell personal com científic per tots els coneixements i idees que tens. Espero seguir aprenent al teu costat.

El meu camí en la química teòrica va començar quan estava al Grau, Marta, Ivan, Arnau, Jowa, Aleix, Joan, Dani, ja vau veure clar que aquest seria el meu camí. Guardo amb gran estima el llibre de química computacional que em vau regalar i tots els moments que hem compartit en sopars, festes, pràctiques de laboratori o tardes estudiant al CRAI. També vull tenir unes paraules pels meus amics del 94, és un plaer seguir fent coses amb vosaltres i disfrutar de la vostra companyia. I Regina, tu has estat la persona que probablement més hagi hagut d'aguantar els meus mals humors aquests últims mesos, gràcies per acompanyar-me en aquest camí!

Per acabar vull enrecordar-me de la meva família, aquest últim any ha estat complicat no poder veure'ns el que estem acostumats, no poder celebrar el Nadal amb tots vosaltres, no poder fer el viatge de cosins, no anar a dinar cada diumenge a casa l'ava... Tot això, et fa adonar de la importància de les petites coses que ja tens interioritzades com a habituals. Vull agrair a les meves àvies que cada dia em segueixin ensenyant, espero seguir aprenent d'elles moltes coses. Pau, moltes gràcies perquè sempre sorprens amb alguna cosa nova, ets una persona que sap de tot. Laura, ets una motivació per esforçar-me cada dia ja que has arribat on ets ara

fruit del teu esforç. Gràcies també per sempre escoltar els meus mals i aguantar la meva hipocondria. Papa, moltes gràcies per cuidar-me i ser una font de coneixements per mi, qualsevol tema es pot discutir amb tu i cada dia aprenc coses noves de tu.

I per qui ja no hi és però em segueix guiant i ajudant cada dia.

# List of contributions

## Publications

**1.** C. Sousa, M. Alías, A. Domingo and C. de Graaf, *Deactivation of Excited States in Transition-Metal Complexes: Insight from Computational Chemistry*, Chem. Eur. J. **25**, 1152-1164 (2019)

**2.** M. Alías, N. D. Alkhaldi, M. Reguero, L. Ma, J. Zhang, C. de Graaf, M. N. Huda and W. Chen, *Theoretical studies on the energy structures and optical properties of copper cysteamine – a novel sensitizer*, Phys. Chem. Chem. Phys. **21**, 21084 (2019)

**3.** J. Wu, M. Alías and C. de Graaf, *Controlling the Lifetime of the Triplet MLCT State in Fe (II) Polypyridyl Complexes through Ligand Modification*, Inorganics **8**, 16-33 (2020)

**4.** M. Alías, C. de Graaf, N. Ferré and M. Huix-Rotllant, *Sub-picosecond intersystem-crossing rate in xanthone studied with wave packet quantum dynamics using a Duschinsky model Hamiltonian*, (in preparation)

**5.** M. Alías and C. de Graaf, *Reversibility of light-induced excited spin state trapping in prototype iron (II) complexes using wave packet quantum dynamics*, (in preparation)

## Research stay

Project: Getting familiar with two methodologies: wave-packet quantum dynamics and quantum mechanics/molecular mechanics.

Supervisor: Nicolás Ferré

Period: 12/02/2019-20/05/2019

UNIVERSITAT ROVIRA I VIRGILI
BEYOND THE STATIC DESCRIPTION OF THE ELECTRONIC STRUCTURE:EXCITED STATE DYNAMICS IN TRANSITION METAL COMPLEXES AND ORGANIC COMPOUNDS
Marc Alías Rodríguez

# Overview of the thesis

**[English version]**
The description of the excited states is important to rationalize processes happening after irradiation of light. The comprehension of them is an important tool to tune materials for different applications. In previous studies in our group, these descriptions were limited to a static calculation of the electronic structure for the involved states. In this thesis, we have gone one step further to describe these processes from a dynamic point of view through three different methodologies.

The first method employed has been the time-dependent Fermi's golden rule in two iron (II) complexes. This method has been proved to accurately determine the intersystem crossing rates and lifetimes in relatively fast processes. However, this gives unphysical rates in the study of an ultra-fast process. This last process is also studied with nuclear quantum dynamics by means of Multi-Configuration time-dependent Hartree (MCTDH). This second methodology needs the creation a priory of a model Hamiltonian and has been used in the reverse-LIESST process of an iron (II) complex and the ultrafast triplet population in xanthone molecule. Finally, the molecular dynamics with trajectory surface hopping (TSH) has been used. This method computes the nuclear displacements from the electronic structure gradients of a particular state on-the-fly and the hop among surfaces from the non-adiabatic couplings. TSH has been employed in the study of the photoisomerization reaction in azobenzene.

**[Spanish version]**
La descripción de los estados excitados es importante para racionalizar procesos que suceden después de irradiar con luz un material. La comprensión de estos estados es una herramienta importante para modificar materiales con diferentes funcionalidades. En estudios previos en nuestro grupo, la descripción se limitó a cálculos estáticos de la estructura electrónica de estos estados. En la presente tesis, hemos ido un paso más

lejos al describir estos procesos desde un punto de vista dinámico a través de tres métodos.

El primero de ellos ha sido la versión dependiente del tiempo de la regla dorada de Fermi para dos complejos de hierro (II). Este método ha demostrado ser preciso para determinar velocidades y tiempos de vida para transiciones de entrecruzamiento entre estados de diferente espín en procesos relativamente rápidos. Sin embargo, los resultados obtenidos con este método para procesos ultrarápidos carecen de significado físico. El mecanismo de este proceso ultrarápidos ha sido estudiado mediante el método multi configuracional dependiente del tiempo a través de productos de Hartree (MCTDH, por sus siglas en inglés). Este segundo método necesita de la creación a priori de un Hamiltoniano modelo y lo hemos usado en el presente trabajo para estudiar el proceso inverso de la captura de estados de espín excitados inducido por luz (reverse-LIESST, por sus siglas en inglés) y la población ultrarápida de los tripletes en una molécula orgánica como la xantona. Finalmente, hemos utilizado las dinámicas moleculares con salto entre superfícies. Este último método calcula los desplazamientos nucleares a partir de los gradientes de la energia electrónica en un estado en particular y los saltos entre superfícies son calculados a través de un algoritmo a partir de los acoblamientos no adiabáticos. Este método ha sido utilizado en el presente texto para el estudio de la reacción de fotoisomerización en azobenzeno.

[**Catalan version**] La descripció dels estats excitats és important per racionalitzar processis que succeeixen després d'irradiar amb llum un material. La comprensió d'aquests estats és una eina fonamental per modificar aquests materials i emprar-los en diferents funcions. En estudis previs en el nostre grup, la descripció d'aquests estats fou limitada a càlculs estàtics d'estructura electrònica. En la tesis actual, hem anat un pas més enllà al descriure aquests processos des d'un punt de vista dinàmic pel que hem utilitzat tres mètodes.

El primer d'ells ha estat la versió depenent del temps de la regla daurada de Fermi per dos complexos de ferro (II). Aquest mètode ha demostrat ser precís per determinar velocitats i temps de vida per transi-

cions d'entrecreuament entre estats d'espín diferent en processos relativament ràpids. Tot i això, els resultats obtinguts amb aquesta metodologia per processos ultraràpids no tenen significat físic. El mecanisme d'aquest procés ultraràpid ha estat estudiat mitjançant el mètode multi configuracional depenent del temps emprant productes de Hartree (MCTDH, per les seves sigles en anglès). Aquest segon mètode necessita de la creació a priori d'un Hamiltonià model i l'hem emprat en el present treball per estudiar el procés invers de la captura d'estats d'espín excitats induït per llum (reverse-LIESST, per les seves sigles en anglès) i la població ultraràpida dels triplets en una molècula orgànica com la xantona. Finalment, hem utilitzat les dinàmiques moleculars amb salts entre superfícies. Aquest últim mètode calcula els desplaçaments nuclears a partir dels gradients de la energia electrònica per un estat en particular i els salts entre superfícies són calculats a través d'un algoritme a partir dels acoblaments no adiabàtics. Aquest mètode ha estat utilitzat en el text actual per l'estudi de la reacció de fotoisomerització de l'azobenzè.

UNIVERSITAT ROVIRA I VIRGILI
BEYOND THE STATIC DESCRIPTION OF THE ELECTRONIC STRUCTURE:EXCITED STATE DYNAMICS IN TRANSITION METAL COMPLEXES AND ORGANIC COMPOUNDS
Marc Alías Rodríguez

# Contents

1. Introduction 1
1.1. General introduction to photoprocesses . . . . . 2
1.2. Experimental techniques . . . . . 3
1.2.1. UV-visible based . . . . . 4
1.2.2. X-ray based . . . . . 6
1.3. Theoretical methodologies . . . . . 9
1.3.1. Static approaches . . . . . 10
1.3.2. Dynamic approaches . . . . . 12
1.4. Systems of interest . . . . . 15
1.4.1. Transition metal complexes . . . . . 15
1.4.2. Organic compounds . . . . . 20
1.5. Objectives . . . . . 22
1.6. References . . . . . 23

2. Theoretical methods 29
2.1. Electronic structure based methods . . . . . 30
2.1.1. Multi-configuration wave function based methods . . 31
2.1.2. Density Functional Theory . . . . . 40
2.1.3. Effective Hamiltonian theory . . . . . 43
2.1.4. Spin-orbit coupling operator . . . . . 45
2.2. Time-related based methods . . . . . 50
2.2.1. Fermi's Golden rule . . . . . 50
2.2.2. Ab Initio Molecular Dynamics . . . . . 53
2.2.3. Multi Configurational Time-Dependent Hartree . . . 59
2.3. References . . . . . 65

3. High-spin state lifetime in $[Fe(bpy)_3]^{2+}$ and $[Fe(mtz)_6]^{2+}$ 71
3.1. Introduction . . . . . 72
3.2. Computational details . . . . . 75
3.3. Results and discussion . . . . . 78
3.3.1. Geometry optimizations and frequencies . . . . . 78
3.3.2. CASPT2 adiabatic energies . . . . . 79

3.3.3. Spin-orbit coupling . . . . . 80
3.3.4. HS state lifetime . . . . . 86
3.4. Conclusions . . . . . 90
3.5. References . . . . . 91

4. Reverse-LIESST in $[Fe(bpy)_3]^{2+}$ and $[Fe(mtz)_6]^{2+}$ 95
4.1. Introduction . . . . . 96
4.2. Computational details . . . . . 100
4.3. Results and discussion . . . . . 102
4.3.1. Fermi's golden rule . . . . . 102
4.3.2. MCTDH . . . . . 112
4.4. Conclusions . . . . . 119
4.5. Future perspectives . . . . . 120
4.6. References . . . . . 123

5. Ultrafast intersystem-crossing rate in xanthone. A Duschinsky rotation model using MCTDH 127
5.1. Introduction . . . . . 128
5.2. Computational details . . . . . 131
5.3. Results and discussion . . . . . 133
5.3.1. Construction of the model vibronic Hamiltonian . . 134
5.3.2. Time-evolution states population . . . . . 146
5.3.3. Vibrationally resolved absorption spectrum . . . . . 150
5.4. Conclusions . . . . . 154
5.5. References . . . . . 156

6. Azobenzene trans-cis isomerization studied with trajectory surface hopping molecular dynamics 159
6.1. Introduction . . . . . 160
6.2. Computational details . . . . . 166
6.3. Results and discussion . . . . . 168
6.3.1. Static calculations . . . . . 168
6.3.2. Dynamic simulations . . . . . 171
6.4. Conclusions . . . . . 185
6.5. References . . . . . 187

7. General conclusions 191

A. Multi-layer trees 199

UNIVERSITAT ROVIRA I VIRGILI
BEYOND THE STATIC DESCRIPTION OF THE ELECTRONIC STRUCTURE:EXCITED STATE DYNAMICS IN TRANSITION METAL COMPLEXES AND ORGANIC COMPOUNDS
Marc Alías Rodríguez

# 1.
# Introduction

## 1.1. General introduction to photoprocesses

Nature has fascinated humans from their first days. Having the knowledge to understand its functioning is essential to control and eventually take advantage of it. Among the different Earth surroundings, light is particularly interesting because life would not be possible without it. Photosynthesis is needed to understand the plants growth, and therefore, essential for the others members of the food chain that are nourished of them.

Photosynthesis is the process used by plants to convert inorganic matter to organic matter upon light absorption. The process has been extensively studied during decades and the main steps involved in it are well-established nowadays.[1] However, some details such as oxidation states of the species or the excited states playing a role in deactivation processes are a common topic in photochemistry and some of them still remain unclear[2,3] and need to be clarified by both theory and experiments.

Despite photosynthesis is probably the most widely studied photoprocess because of its importance, there are hundreds of other processes occurring after the interaction with light that are interesting for their applications in synthesis, technology or energy storage among others. These processes can be classified into photochemical or photophysical processes depending on the change suffered by the irradiated molecule. In photophysics the process ends in the initial molecule and in photochemistry the process finishes with a new molecule.

The process starts by the absorption of a photon that changes the electronic distribution from the ground state to an excited state configuration. The states whose interaction integrals with the ground state via the dipole operator are not vanishing are easily populated and have high oscillator strengths, these are the so-called bright states. Those states without (or very low) probability to be populated from the ground state are called dark states.

Several transitions may happen in a photoprocess and they are commonly represented in the well-known Jablonski diagram (Fig. 1.1). The process starts with an absorption from the ground state to a bright excited state. Thereafter, a vibrational relaxation within the excited state or a relaxation to another electronic state can happen. Two different non-radiative

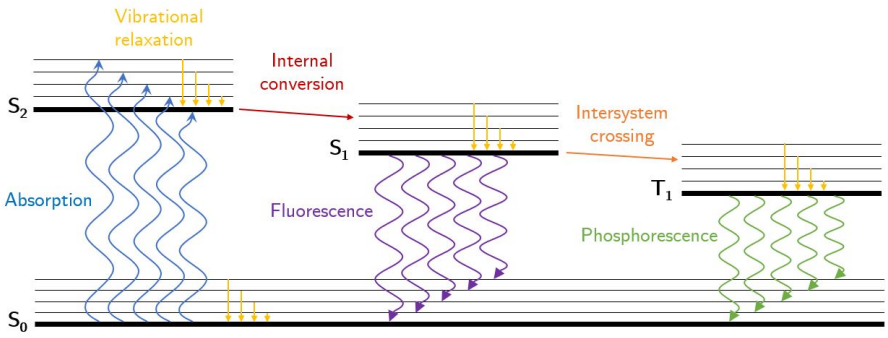


**Figure 1.1.** Jablonski diagram. Schematic representation of the possible transitions in a photoprocess.

transitions are distinguished depending whether there is a change in the spin multiplicity (intersystem-crossing) or not (internal conversion). Following Kasha's rule, radiative transitions are mainly produced from the lowest state of a given multiplicity.[4] The fluorescence is produced from the lowest excited state with the same spin multiplicity as the ground state and the phosphorescence process is produced from excited states with different spin multiplicities than the ground state. The latter transitions are typically slower processes because they are, in a non-relativistic frame, spin forbidden.

## 1.2. Experimental techniques

There are in nature several processes happening at very different timescales (Fig. 1.2). In the current work, we are mainly interested in sub picosecond processes which are known within the scientific community as ultrafast chemistry. The even faster processes such as electron dynamics that occur in the attosecond time-scale[5] are beyond the scope of this chapter.

The ultrafast chemistry was pioneered by A. H. Zewail, who was awarded with the Nobel Prize in 1999 for his contributions to the field. The so-called pump-probe experiments opened the door to follow the time evo-

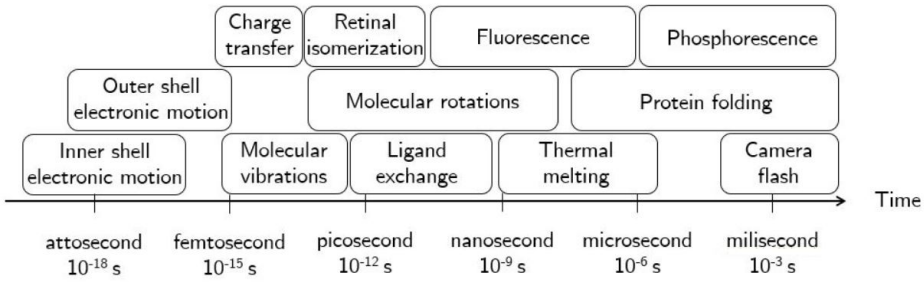


**Figure 1.2.** Time-scales of several processes in nature.

lution of chemical processes like bond breaking in great detail. The basic pump-probe experiment fires two light pulses at the sample with a controlled time delay between the first and second pulse. The first one, known as the pump pulse, brings the target molecule to an electronically excited state. The second pulse probes the electronic state based on the understanding that the response of the system varies in time depending on the evolution of the electronic state induced by the pump pulse.

Most time-resolved studies are based on radiative processes, although electrons can also be used as probe.[6] In this aspect the development of ultrafast electron diffraction and ultrafast electron microscopy, also carried out in Zewail's group,[7] allowed the study of the photophysics of acetophenone and its photochemical cleavage to benzaldehyde.[8] The first time-resolved spectroscopy studies were mostly performed using sub ps pulses produced with UV-Vis lasers. However, it was readily recognized that shorter pulses can be generated when higher energy radiation is used. This gave rise to X-ray based experiments. The following sections will shortly summarize the most commonly used variants of the UV-Vis and X-ray based techniques.

### 1.2.1. UV-visible based

The UV-visible covers the wavelengths from the visible to the ultraviolet, approximately in the 200-800 nm range. This was probably the first spectroscopic technique used because this is the excitation range for most of

the low-lying excited states in molecules, as confirms a great number of coloured compounds. It has the great advantage that both the pump and the probe pulses are generated from a single laser and do not have to deal with synchronization problems.

### Transient absorption in the UV-Vis

In transient absorption, after the promotion of the system from the ground to the excited state by the absorption of a photon from the pump probe, a second pulse promotes the system once more from the excited state to a high-lying excited state in a process called excited state absorption (ESA). The information extracted by the technique is a variation in the optical density as function of time. It is very common to represent the information in a two-dimensional plot which shows the time delay on one axis and the probe wave lengths used on the other, while the response of the system, the change in the optical density (absorption intensity), is represented with a colour code. This two-dimensional plot is often converted in a one-dimensional plot where one of the variables is kept constant (Fig.1.3). The absorption wave length is characteristic for each excited state, therefore, the variation of the optical density, i.e absorption in time after subtracting the absorption at zero time, allows to rationalize the excited states population transfer along the process.

### Femtosecond resolved fluorescence

In the fluorescence process, after the first photon from the pump pulse is absorbed to promote the electron distribution from the ground to an excited state, a second photon from the probe pulse causes an excited state absorption as in transient absorption. The difference here is that instead of recording the absorption, one measures the fluorescence from the excited states. The fluorescence signal is collected after mixing it with a gate pulse. This technique also delivers two-dimensional and one-dimensional plots but the difference is that instead of measuring the variation in the optical density, the intensity is directly measured (Fig. 1.3).

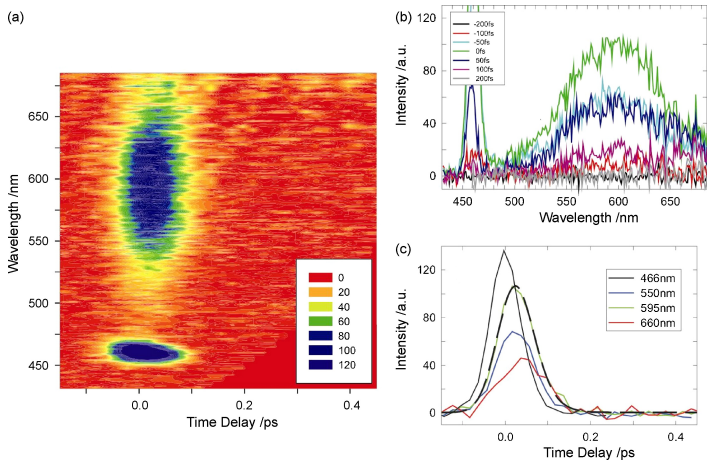


**Figure 1.3.** Time-resolved fluorescence spectra of $Fe(bpy)_3$. a) Two-dimensional plot upon excitation at 400 nm. b) Spectra at different time delays. c) Time traces at different wavelengths. Figure extracted from Ref. 9.

### 1.2.2. X-ray based

The main advantage of using an X-ray source instead of UV-visible laser light is that the former produces wave packets of higher energy. Following the Heisenberg uncertainty principle, higher energies correspond to shorter times, therefore, it is possible to achieve shorter laser pulses and better time resolutions from the X-ray sources. This makes X-ray based techniques specific to easily recognize oxidation and spin states along time. The disadvantage in X-ray experiments is that two different lasers are needed and the synchronisation between the pulses is not an easy task. Experimentalists are still working hard to further improve the obtained signals.

Picosecond to femtosecond time resolutions require ultra-short X-ray pulses. Some of the most common sources that can generate ultra-short X-ray pulses are briefly described in the next lines. First, the plasma-based sources generate isotropic pulses in the order of hundreds femtoseconds. There are also large-scale facilities such as synchrotrons that produce X-ray pulses of picosecond order of magnitude that can also be reduced to femtosecond scale after using a slicing scheme. Within the large scale fa-

cilities X-ray Free Electron Lasers (XFEL) have emerged as an important tool in the recent years because they can produce coherent and very intense pulses of the tens of femtosecond order of magnitude. There are very small number of XFEL installations in the world such as European XFEL in Germany, SwissFEL in Swizertland, LINAC in United States or SACLA in Japan to name a few of them. [6]

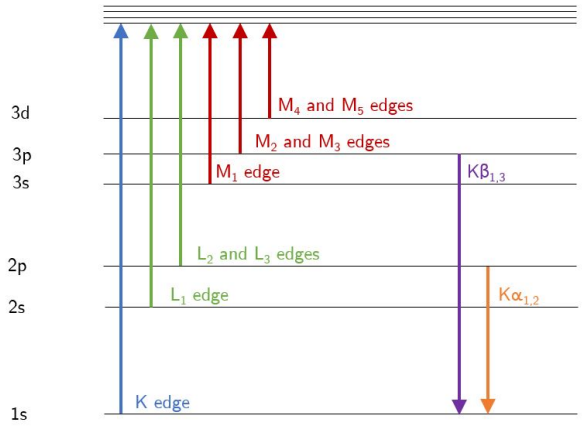


**Figure 1.4.** Schematic diagram for the main transitions in core-level spectroscopy. Absorption process in the left side and emission in the right.

The X-ray based spectroscopy, as mentioned above, is more energetic than the UV-visible one. Then, instead of dealing with excitations involving frontier orbitals, the transitions occur between core and unoccupied valence orbitals. It is, therefore, also known as core-level spectroscopy. Figure 1.4 illustrates Siegbahn's notation for labeling the main transitions. The most intense transitions are the electric-dipole allowed, with $\Delta l = \pm 1$. The main features of K edge in first row transition metal complexes correspond to the 1s $\rightarrow$ p-like transitions and the $L_3$ edge to a 2p $\rightarrow$ d-like ones.

### X-ray absorption spectroscopy

Two variants can be distinguished depending on the energy range in the response signal that is focused on (see Fig. 1.5). In the first place, X-ray

Absorption Near Edge Spectroscopy (XANES) extracts information from the rising edge and pre-edge absorption. The rising edge is associated to the allowed transition from the core-level to an unoccupied valence orbital (e.g. TM-1s $\rightarrow$ 4p-like in the case of a first row transition metal), while the pre-edge absorption is typically caused by transitions in which electrons are transferred to the partially filled TM-3d shell. XANES provide detailed information about the valence electronic structure around the absorbing center, especially when combined with electronic structure calculations.[10] On the other hand, there is the Extended X-ray Absorption Fine Structure (EXAFS) spectroscopy, focusing on the scattering states. These basically unbound electrons provide information about the geometry near the optically active center, and hence, time resolved EXAFS signals can be used to follow structural changes on an ultrashort timescale.[11]

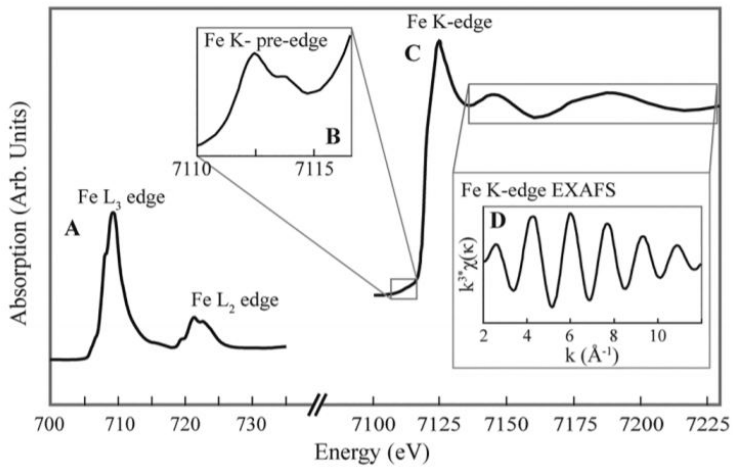


**Figure 1.5.** Different regions in X-ray absorption spectroscopy for $FeCl_4^{2-}$. A region shows the L edges, B (pre-edge) and C (K-edge) regions form the XANES and D is the Fourier transform of the EXAFS. Figure extracted from Ref. 12.

### X-ray emission spectroscopy

The creation of a core hole creates an extremely unstable electronic structure, which decays very fast under the emission of a photon. This relax-

ation does not necessarily involve the electron that was previously excited, but the core-hole can also be filled by electrons occupying other valence levels. Hence, the detection of this emission (X-ray emission spectroscopy, XES) also provides information about the valence electronic structure of the system. Contrary to emission processes in the absence of core holes, relaxing the core-hole is an extremely fast process (sub fs) and hence useful as probe signal for the study of ultrafast processes. XES is element and site-specific, this makes it a very powerful technique to identify spin and oxidation state changes as function of time. (Fig.1.6).

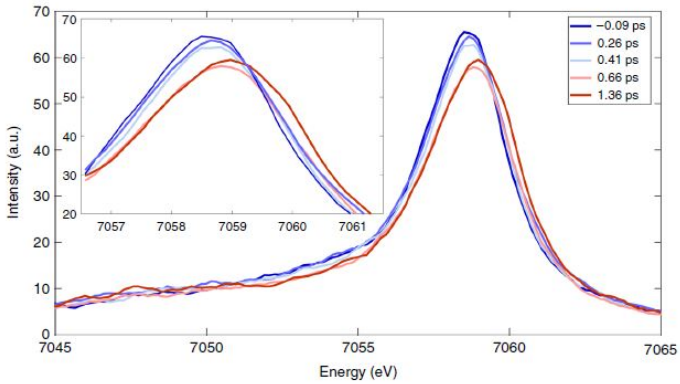


**Figure 1.6.** X-ray emission spectroscopy. XES intensity at different energies along time. Figure taken from Ref. 13.

## 1.3. Theoretical methodologies

Herein, a general discussion is presented about some key aspects of the theoretical description of excited state dynamics. A more detailed discussion about the mathematical procedures employed to solve the physical problems is given in the next chapter and an extended discussion on the most common methods to study excited state deactivation in transition metal complexes was published in a recent mini review by our group [14] which is found among other important reviews on similar topics about theoretical methods on excited states. [15–17] There are mainly two different strategies to provide information about excited state deactivation from a theoretical point of view: the static and dynamic approaches.

### 1.3.1. Static approaches

The first and probably the easiest way to approach the problem is to consider that the rate of a process depends exclusively on the size of the coupling and the energy difference between the involved states. With this premise, two different physical phenomena can be distinguished and qualitatively described in a non-radiative deactivation process: intersystem crossings involving states of different multiplicities and internal conversions between states of the same multiplicity.

Both phenomena can not be treated in a standard non-relativistic quantum chemical setting. The Born-Oppenheimer approximation leads to orthogonal electronic states and vanishing coupling. This causes that non-adiabatic coupling is not easily calculated and consequently the internal conversion rate. To obtain information about the intersystem crossings, the spin-orbit coupling operator has to be added to the Hamiltonian.

#### Intersystem crossing

The first theoretical speculations about the intersystem crossing rates were mainly based on the permitted/forbidden character of the spin orbit coupling among the states involved in the crossing, typically singlet-triplet transitions. Based on the non-symmetric character of the spin-orbit Hamiltonian, El-Sayed proposed that the SO coupling between states does not vanish for transitions involving electron replacements among molecular orbitals of different symmetry.[18] Transitions that do not involve states with changes in the symmetry of the occupied molecular orbitals do not couple unless considering vibronic spin-orbit interactions. In organic compounds, this indicates that the $^1\mathrm{n}\pi^* \rightarrow {}^3\pi\pi^*$ and $^1\pi\pi^* \rightarrow {}^3\mathrm{n}\pi^*$ transitions are allowed while the $^1\mathrm{n}\pi^* \rightarrow {}^3\mathrm{n}\pi^*$ and $^1\pi\pi^* \rightarrow {}^3\pi\pi^*$ are forbidden.

Although these observations allowed to rationalize which transitions were allowed and forbidden, they did not provide enough information to discern between fast and slow intersystem crossings in different systems. This only became possible with the implementation of spin-orbit interactions in several quantum packages facilitating the explicit computation of couplings in real molecules. Then, it was immediately recognized that ISC

rates are much larger in molecules containing second- or third-row main group elements (sulphur, phosphorus, selenium, etc.) or transition metals compared with classic organic molecules because of the more pronounced relativistic effects in the former.

### Internal conversion

The picture is completely different between states that belong to the same spin multiplicity. The states that share the same spin and spatial symmetry interact through non-adiabatic couplings, which are strictly zero within the Born-Oppenheimer approximation because the states are mutually orthogonal by definition. Then, the discussion on the efficiency of the internal conversions is based on the topology and accessibility of the different conical intersections of the potential energy surfaces of the states under consideration.

Conical intersections are 3N-8 dimensional hypersurfaces that fulfill two conditions. The first is that the adiabatic energy of state i and j must coincide ($V_i = V_j$) and the second is that the interaction between the two states i.e. the non-adiabatic coupling has to be 0 ($\langle \Psi_i | \hat{H} | \Psi_j \rangle = H_{ij} = 0$). The population transfer between states increases proportionally with the coupling and inversely with the energy difference between them. Conical intersections are singularities in the potential energy surface where the energy difference and the coupling are zero which makes it impossible to rationalize the population transfer precisely at this point but it is clear that close to the conical intersection the population transfer is very effective. Releasing one of the restrictions that define the hypersurface of conical intersection, an hypersurface with one more degree of freedom can be defined where the energies of the diabatic states coincide but the non-adiabatic couplings between them do not vanish. These points are called avoided crossings and the population transfer is in general very rapid in these points.

The use of adiabatic representations of the electronic states limits the study of internal conversion to the conical intersections and their immediate surroundings. Because, the algorithms to search conical intersections

in fact are looking for minimum energy points within these surfaces (minimum energy conical intersections or MECI), only a small region of the conformational space is explored. The possible existence of regions with large couplings and quasi degenerate diabatic states, and hence, efficient populations transfer cannot be accounted for only looking for conical intersections.

### 1.3.2. Dynamic approaches

Static approaches has provided many useful insights into the understanding of ultrafast chemistry, but there are some questions that cannot be resolved without explicitly taking into account the dynamical aspects of the problem. It is virtually impossible to give quantitative estimates of the crossing rates or evaluate the relative efficiency of different relaxation paths within a static approach.

Researchers have applied several theoretical approaches to study the dynamics from a theoretical point of view, but only the two methods employed in this work are briefly commented here. In this section, only a qualitative description of their main characteristics, advantages and disadvantages is given, as stated before, a more detailed mathematical account can be found in the next chapter.

#### Trajectory surface hopping, TSH

This method combines the classical time-evolution of the nuclei based on Newton's equations of motion with a quantum description of the electronic structure. The forces exerted by the electrons on the nuclei are computed using the gradients for the electron density of the excited state populated at each moment of the simulation. The population transfer between electronic states is accounted through different mathematical approaches but the most widely used is Tully's algorithm. This approach has mostly been applied for the study of systems where internal conversions play a major role but has been recently extended to the study of intersystem crossings adding spin-orbit coupling terms in the algorithm.[19]

The main advantage of this method is the explicit calculation of the gradients on-the-fly used to determine the motion of the system along time, avoiding tedious fitting procedures or introduction of pre-established force-fields. The method stays conceptually very close to standard molecular dynamics simulations and makes use of standard electronic structure methods. Hence, it is relatively easy to apply, when enough computer power is available. The problem of this method lies in the classical treatment of the nuclei which induces coherence/decoherence problems in the electronic wave function, the introduction of empirical parameters in the algorithms such as the fewest switching and the need of a large number independent trajectories to obtain accurate population statistics.

### Multi-configuration time-dependent Hartree, MCTDH

In this method both the nuclei and electrons are treated from a quantum perspective. The potential energy surfaces are computed previously and the information is translated into a model Hamiltonian. Thereafter, the nuclear wave functions are propagated using the Dirac-Frenkel principle.

The main advantage of MCTDH is that both the nuclei and electrons are studied at quantum level. The use of quantum probabilities to describe the excited state populations samples all different relaxation paths with one single trajectory. Moreover, being an ab initio method, the model Hamiltonian can be set-up at any desired level of quantum chemical accuracy. It also allows to activate/deactivate some parameters in the Hamiltonian to clarify very specific details of the relaxation mechanism. One of the main problems of the method is the intrinsic complexity of the creation of the Hamiltonian, which in its simplest form only consists of terms that involve one nuclear vibrational mode,

$$\lambda_{k,ij} = \frac{\partial}{\partial Q_k} H_{ij} \tag{1.1}$$

where i, j label electronic states and k a vibrational mode. It is not only a laborious procedure, but it is also far from trivial to account for the

vibronic coupling involving several vibrational modes at the same time,

$$\lambda_{kl,ij} = \frac{\partial^2}{\partial Q_k \partial Q_l} H_{ij} \tag{1.2}$$

herein i, j label again electronic states and k, l vibrational modes. These terms were included in the early days of MCTDH when only very small molecules were studied and symmetry restrictions limited the pairs of modes effectively interacting.[20] As the systems grew bigger that could be treated with MCTDH, symmetry is lost in most cases and more pairs of vibrations start to interact, which makes the construction of the Hamiltonian more laborious. In addition, it is extremely complicated to express the model Hamiltonian in coordinates other than the normal modes because the nuclear kinetic operators are no longer diagonal and need to be transformed through complex mathematical equations. However, it is almost mandatory to use these coordinates to represent motions far away from an equilibrium situation because the interaction among these modes becomes extremely important when using normal mode coordinates. For example, a model dihedral angle that needs to be described with a linear combination of five normal modes and where the potential energy surfaces are fitted using 11 points along each normal modes, would need $11^5$=161051 geometries where the Schrödinger equation must be solved to determine the energies and being able to introduce the interactions among the modes in the Taylor expansions of the model Hamiltonian:

$$\lambda_{ij}^{(k,l,m,n,o)} = \frac{\partial H_{ij}}{\partial Q_k} \frac{\partial H_{ij}}{\partial Q_l} \frac{\partial H_{ij}}{\partial Q_m} \frac{\partial H_{ij}}{\partial Q_n} \frac{\partial H_{ij}}{\partial Q_o} \tag{1.3}$$

Herein i and j represent the electronic states, when i=j $H_{ij}$ is the energy of the state and when i≠j $H_{ij}$ is the coupling among them and k, l, m, n and o are the vibrational normal modes.

The number of $\lambda_{ij}$ parameters would be $5^5$=3125 parameters for each term on the Hamiltonian which in a small model Hamiltonian formed by 4 states would require 4!×3125=75000 parameters. This is a large amount of parameters, that together with the important amount of single point calculations to perform the fitting, for describing only one of the motions on the system. These facts make the use of curvilinear coordinates, despite

complicated nuclear kinetic energy operators, necessary to describe these situations in a model Hamiltonian.

## 1.4. Systems of interest

All the above explained methodologies are quite general and can in principle be applied to any molecular system, but in the current work we mainly focus on two different type of systems. On the one hand, the transition metal complexes with spin states that are close in energy, and on the other hand, some organic molecules with relatively fast photochemical/photophysical properties.

### 1.4.1. Transition metal complexes

The first theory to rationalize the basic characteristics of transition metal complexes was put forward by Bethe and van Vleck in the 1930s, and is now known as the crystal field theory. This theory treats the ligands as point charges that destabilize the d orbitals of the central metal atom. The orbitals directly pointing at these point charges are more destabilized than those oriented in other directions. Hence, the d orbitals splitting depends on the geometry of the complex (Fig. 1.7). The strength of the ligand field determines the electron distribution over the orbitals and consequently, also the number of unpaired electrons, which are responsible for the magnetic properties of the complex.

The molecular orbital theory appeared at the same time and helped to understand, among others, the stability of molecules and the mechanism of chemical bond formation. This theory studies the bonds between atoms from a quantum mechanical perspective and states that the molecular orbitals are linear combination of atomic orbitals, which are classified into bonding, non-bonding or anti-bonding type depending on the phase of the atomic orbitals in the molecular orbital.

The combination of both theories produced the ligand field theory. This states that the transition metal ion has nine valence orbitals (five nd orbitals, three (n+1)p and one (n+1)s) that can combine with ligand orbitals of the same symmetry and in the same energy range.[21] There are

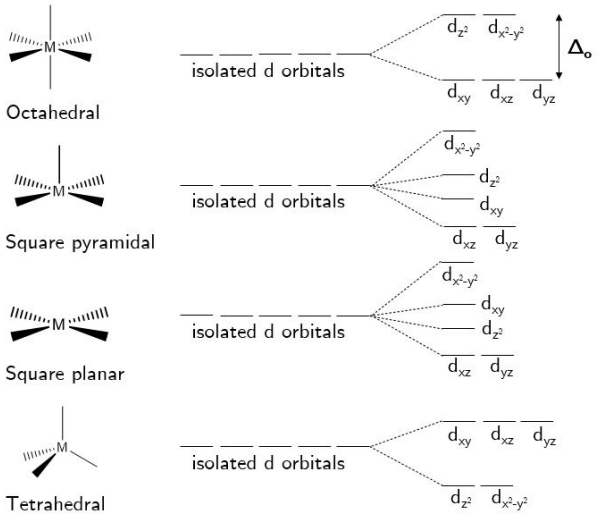


**Figure 1.7.** Splitting of d orbitals depending on the geometry of the complex within crystal field theory.

mainly two types of interactions between ligands and metal atoms. The strong $\sigma$ interaction between metal and ligand orbitals oriented in the same direction causing a strong overlap between them. The $\pi$ interaction is weaker because the overlap is produced laterally. Both interactions can have bonding and anti-bonding character.

The schematic molecular orbitals diagram that emerges from ligand field theory gives information about the orbitals of the metal and ligands that interact. The resulting MOs are linear combination of the metal and ligand orbitals with the same irreducible representation of the symmetry group.

Figure 1.8 shows how frontier metal and ligand orbitals interact in a transition metal complex with (quasi-) octahedral symmetry. The main orbitals in this diagram for analysing physico-chemical properties of these complexes such as magnetism or spectroscopy are the ones labeled with $e_g$, $t2_g$ and $e_g^*$. The former correspond to a bonding interaction of sigma type between the ligand orbitals and the $d_{x^2-y^2}$, $d_{z^2}$ of the metal with larger

contributions from the ligand ones. The second group of orbitals correspond to the $d_{xy}$, $d_{xz}$, $d_{yz}$ orbitals of the metal and can be considered as mostly non-bonding orbitals assuming a weak $\pi$ interaction. The last two correspond to the antibonding $\sigma$ orbitals which are the interaction between the $d_{x^2-y^2}$, $d_{z^2}$ of the metal and the ligand orbitals with higher contribution of the metal ones.

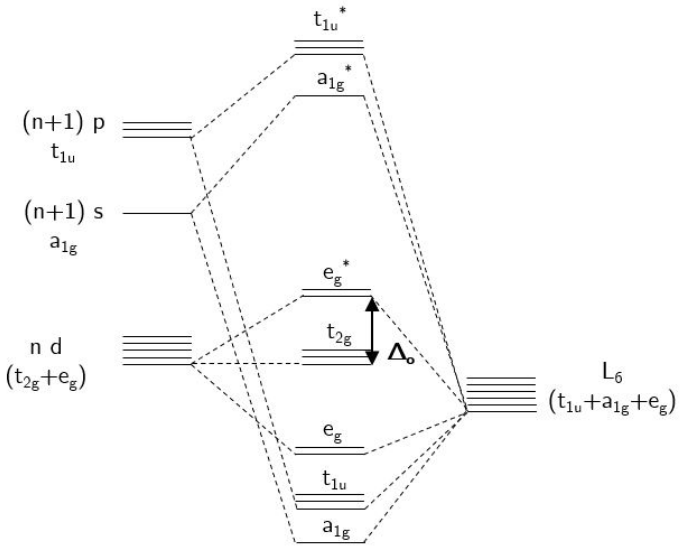


**Figure 1.8.** Molecular orbitals diagram of a (quasi-)octahedral TM complex considering only $\sigma$ interaction.

The energy difference between these two last groups of orbitals defines the ligand field strength, $\Delta_o$ which is the key to rationalize the paramagnetic or diamagnetic character of the complex. Although the $\sigma$-interactions are definitely the strongest ones, neglecting the $\pi$-interactions is not always justified. Changes in the relative energy of the $t_{2g}$ orbitals can substantially modify the strength of the ligand field (see Fig. 1.9). The $t_{2g}$ orbitals of the metal can increase its energy interacting with doubly occupied $\pi$ or p orbitals from $\pi$-donor ligands such as $I^-$ usually forming low-spin complexes. But they can also interact with empty orbitals from $\pi$-acceptor ligands such as CO which tend to form high-spin complexes.

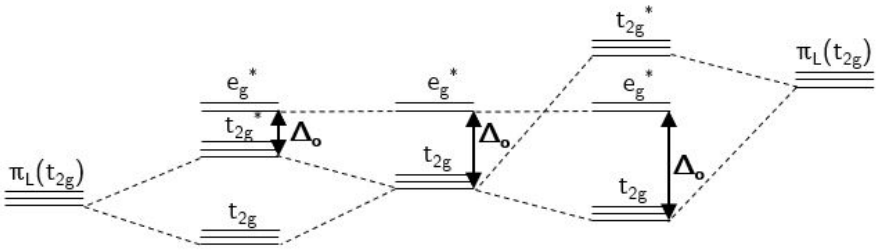


**Figure 1.9.** Schematic representation of the influence of the $\pi$ interaction in a MO diagram. On the left, the diagram with a $\pi$-donor ligand. In the middle, the diagram without considering $\pi$ interaction, and on the right, the resulting diagram with $\pi$-acceptor ligands.

This thesis mostly focuses on the prototype iron (II) complexes of quasi-octahedral symmetry. Therefore, we will use the labels of the $O_h$ symmetry point group throughout the remainder of the text. These complexes show a $d^6$ electronic configuration that can form low-spin diamagnetic compounds with $t_{2g}^6$ or high-spin paramagnetic complexes with $t_{2g}^4 e_g^2$ electronic configurations. Our group is particularly interested in the study of the role played by the excited states in these complexes. They are important for the understanding of the photoprocesses that are the basis of spin-crossover phenomena and photocatalysis.

The spin-crossover induced by light is known as light induced excited spin state trapping (LIESST). The process is usually studied in high-symmetric $FeN_6$ core complexes with $[Fe(bpy)_3]^{2+}$used as the prototype complex in the field. The absorption of light populates the bright $^1$MLCT states, the details of the subsequent deactivation mechanism and the quantum yield for the SCO process have been matter of study from both theoretical[22,23] and experimental[24,25] perspectives (see Sec. 4.1 for further information). Recent publications in the field, suggested the use of less symmetric $FeN_4O_2$ core complexes to compare the deactivation mechanism from the $^1$T states (d-d excitation), which are forbidden in high-symmetrical complexes, with the usual $^1$MLCT excitation allowed in the two type of complexes.[26,27]

Another promising application of iron(II) complexes is their use as photocatalysts. Redox properties are more favoured in MLCT states following the Rehm-Weller equation because of their higher facility to be reduced or oxidised. Then, complexes with longer-living MLCT states such as $[Ru(bpy)_3]^{2+}$ are highly appreciated in photocatalysis.[28] This catalyst is actively used in the area of energy storage and $H_2$ production from water[29] but also in asymmetric catalysis for the production of enantio-enriched $\alpha$-alkylated aldehide from and aldehyde and racemic $\alpha$-bromocarbonyl acting together with an organo-catalyst.[30] Despite the larger natural abundance of iron compared to ruthenium, the iron equivalent can unfortunately not be used in photocatalysis, because the MLCT state of $[Fe(bpy)_3]^{2+}$is too short-living for effective oxidation or reduction reactions. Ligand modifications that increase the $\sigma$ donating character or increase the $\pi$ conjugation on the ligands are studied both theoretically[31] and experimentally[32] to stabilize the MLCT state and increase its lifetime to mimic the behaviour observed for the $[Ru(bpy)_3]^{2+}$ complex. This would allow the substitution of Ru complexes for Fe ones in photocatalysis.

Although the attention in this thesis is focused in monometallic molecular complexes, a few lines are dedicated to ultrafast processes in metalloproteins and bimetallic complexes because of their importance in biological systems and potential magnetic applications, respectively. The cofactors in metalloproteins are cations that have a first coordination sphere similar to molecular transition metal complexes and no larger differences should be expected in the basic features of the electronic structure. The main difference comes from the higher rigidity of the protein which can result in completely different deactivation paths than in small model complexes. Recently, some experimental studies on the excited state dynamics in heme proteins have been published.[13] From a theoretical perspective Falahati et al. performed the first excited state dynamics calculations on these proteins[33] but they did not include protein effects. The inclusion of the environment will become a reality in the near future by the combination of QM/MM calculations and wave packet quantum dynamic methodologies through the implementation of the QM/MM Hessians.[34] The bimetallic complexes have more complex electronic structure than the monometallic ones because apart from local spin crossover, they can also have metal-to-

metal charge transfer states (MMCT) inducing profound changes in the magnetic properties of the complex. Furthermore, for bimetallic complexes with two paramagnetic centers, (anti-)ferromagnetic exchange couplings are also at play. An illustrative example of such behaviour can be found in the CoFe Prussian blue analogue, whose initial $Co^{III}$(S=0)$Fe^{II}$(S=0) diamagnetic state gives rise to the magnetic $Co^{II}$(S=3/2)$Fe^{III}$(S=1/2) electronic configuration when irradiated with light. Cammarata et al. experimentally studied this ultrafast process to establish whether this change is triggered by a metal-to-metal charge transfer or induced by a local spin transition preceding the charge transfer.[35] Theoretical calculations on these complexes are complicated because of the difficulty of accurately treating the MMCT states,[36] but the potential of these complexes will continue attracting scientists and new perspectives from theoretical chemists are expected in the next years.

### 1.4.2. Organic compounds

Organic compounds with interesting photophysical properties mostly absorb in the UV-visible region of the spectra. These compounds have typically conjugated $\pi$ bonds that reduce the $\pi$-$\pi^*$ gap compared to molecules with isolated double bonds. The main states that participate in the process arise from electron replacements among three type of orbitals. These are the n orbitals which are non-bonding or lone-pair of usually N, O or S atoms, the $\pi$ and the $\sigma$ orbitals, either with bonding or antibonding character.

Molecular orbitals theory is also very illustrative to characterize the states involved in the photoprocess of an organic compound (Fig. 1.10). The ground state, $S_0$ is usually a closed-shell system and the excited states are open-shell singlets or triplets. These low-lying excited states have usually $n\pi^*$ or $\pi\pi^*$ character and triplets are slightly lower in energy than the singlets of the same character because of the increased exchange interaction in the former as expressed by Hund's rule.[37]. The $n\pi*$ states are expected to be significantly more stable than $\pi\pi^*$ states but there are two effects that decrease the energy gap between these two families of states. In the first place, *pure* n orbitals (2p from O) strongly mix with $\sigma$-orbital increasing the bonding energy but destabilizing the n orbital. Secondly,

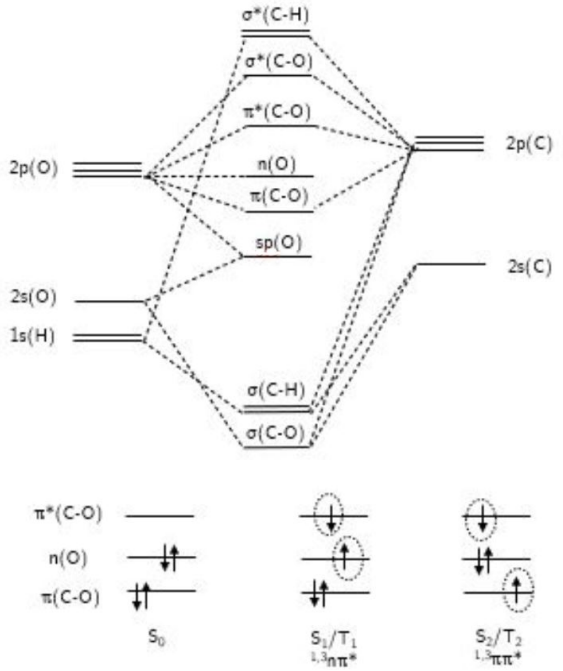


**Figure 1.10.** Schematic molecular orbitals diagram for formaldehyde in the top. The main steps involved in its photochemistry at the bottom. The encircled electrons are either low-spin or high-spin coupled depending on the total spin of the electronic state.

the extended double bond conjugation decreases the $\pi$ bonding energy i.e. the $\pi$-$\pi^*$ gap. These two effects can lead to almost degenerate n$\pi^*$ and $\pi\pi^*$ states in a large number of highly-conjugated aromatic compounds containing heteroatoms.[38]

Among the huge amount of organic compounds with photophysical properties, nucleobases are especially interesting organic molecules as they play an important role in the storage of genetic information,being part of the nucleic acids. For obvious reasons, they have ultrafast excited state deactivation channels. These compounds are extensively exposed to UV light from the sun and without such effective deactivations these nucleobases could suffer changes in their chemical structures, causing mutations dam-

aging the genetic information. The deactivation mechanisms have been studied by many research groups and can be produced through a non-radiative mechanism via an internal conversion or a radiative process by means of fluorescence. The later is produced with a low quantum yield and in the sub-picosecond time scale, therefore, femtosecond pump-probe experiments were needed to observe it.[39] This review also presented the main theoretical results. Most studies were limited at that time to the calculation of $^1\pi\pi^*$ state vertical energy, but the interpretation of the results and the comparison to experiment is complicated due to the existence of a large amount of tautomers. Later, the studies were mainly focused in the search of critical points in the potential energy surfaces from a static perspective, Merchan et al. rationalised the ultrafast deactivation and the low fluorescence quantum yield of pyrimidine basis by means of mapping the PES at CASPT2 level.[40] After that, Thiel and coworkers performed one of the firsts dynamic simulations using trajectory surface hopping at OM2/MRCI level in pyrimidine bases.[41] Their results suggested a fast $S_2 \rightarrow S_1$ deexcitation within 50 fs and the subsequent internal conversion to the ground state in less than 1 ps. A few articles have been published studying the deactivation of each nucleobase carrying different electronic structure methods from then. The general trend indicates a faster and less complex process in purine basis than in pyrimidine. However, the enhancement of quantum packages is still expected to perform these simulations at higher electronic structure level.[42] Recent publications, despite not directly study the non-adiabatic dynamics, study the redox properties of a native and a damaged DNA fragment. The use of QM/MM methodology allow to sample the conformations in a small DNA fragment formed by 39 nucleobases pairs and conclude that the substitution of guanine nucleobase by its oxidate derivative 8-oxoguanine protects of oxidation the rest of DNA chain.[43]

## 1.5. Objectives

The group has ample experience in the study of excited states in both transition metal complexes and organic compounds using the quasi-dynamic Fermi's golden rule approach and the determination of minima, transition states, conical intersections on potential energy surfaces. The nuclear dy-

namic effects, i.e the thermal disorder, has been studied with CPMD for the electronic ground state. The main objective of this thesis is to go one step further introducing a dynamic picture of the processes that happen when a system is brought to an electronically excited state and obtain time-resolved information. There are different types of methodologies to deal with the excited state dynamics problem, and this thesis aims at a critical exploration of these methods to decide which one is to be used in each particular problem.

This will be achieved in the following way.

- Determine the validity of Fermi's golden rule for relaxation processes taking place at different time scales by determining the high-spin lifetime in two iron (II) complexes.
- Design a general applicable strategy to build a model Hamiltonian for spin-crossover complexes and illustrate it for the reverse-LIESST process in two protoype iron (II) complexes.
- Provide a fully quantum mechanical description of the decay process through wave packet quantum dynamics methodology and compare the results with those obtained using Fermi's golden rule.
- Replace the standard fitting procedure by a in principle simpler method based on Duschinsky rotation to build a model Hamiltonian and determine the deactivation mechanism for the ultrafast ISC in xanthone.
- Explore the possibilities of molecular dynamics with trajectory surface hopping in the study of the excited state dynamics of the azobenzene photoisomerization.

## 1.6. References

[1] R. Leegood, *Encyclopedia of Biological Chemistry (Second Edition) by William J. Lennarz and M. Daniel Lane (eds.)* (Academic Press, Waltham), chapter Photosynthesis, pp. 492–496 (2013).

[2] J. Yano, and V. Yachandra, *$Mn_4Ca$ Cluster in Photosynthesis: Where and How Water is Oxidized to Dioxygen*, Chem. Rev. **114**, 4175–4205 (2014).

[3] J. R. Reimers, M. Biczysko, D. Bruce, D. F. Coker, T. J. Frankcombe, H. Hashimoto, J. Hauer, R. Jankowiak, T. Kramer, J. Linnanto, F. Mamedov, F. Müh, M. Rätsep, T. Renger, S. Styring, J. Wan, Z. Wang, Z.-Y. Wang-Otomo, Y.-X. Weng, C. Yang, J.-P. Zhang, A. Freiberg, and E. Krausz, *Challenges facing an understanding of the nature of low-energy excited states in photosynthesis*, Biochimica et Biophysica Acta (BBA) - Bioenergetics **1857**, 1627–1640 (2016).

[4] M. Kasha, *Characterization of electronic transitions in complex molecules*, Discuss. Faraday Soc. **9**, 14–19 (1950).

[5] A. Palacios, and F. Martin, *The quantum chemistry of attosecond molecular science*, WIRES Comput. Mol. Sci. **10**, e1430 (2020).

[6] M. Chergui, and E. Collet, *Photoinduced Structural Dynamics of Molecular Systems Mapped by Time-Resolved X-ray Methods*, Chem. Rev. **117**, 11 025–11 065 (2017).

[7] M. Chergui, and A. H. Zewail, *Electron and X-Ray Methods of Ultrafast Structural Dynamics: Advances and Applications*, Chem. Phys. Chem. **10**, 28–43 (2009).

[8] S. T. Park, J. S. Feenstra, and A. H. Zewail, *Ultrafast electron diffraction: Excited state structures and chemistries of aromatic carbonyls*, J. Chem. Phys. **124**, 174 707 (2006).

[9] A. Cannizo, C. Milne, C. Consani, W. Gawelda, C. Bressler, F. van Mourik, and M. Chergui, *Light-induced spin crossover in Fe(II)-based complexes: The full photocycle unraveled by ultrafast optical and X-ray spectroscopies*, Coord. Chem. Rev. **254**, 2677–2686 (2010).

[10] F. M. F. de Groot, J. C. Fuggle, B. T. Thole, and G. A. Sawatzky, *2p x-ray absorption of 3d transition- metal compounds: An atomic multiplet description including the crystal field*, Phys. Rev. B **42**, 5459–5468 (1990).

[11] J. A. van Bokhoven, and C. Lamberti, *X-ray absorption and X-ray emission spectroscopy : theory and applications* (John Wiley & Sons, United States of America) (2016).

[12] B. P. von der Heyden, *Shedding light on ore deposits: A review of synchrotron X-ray radiation use in ore geology research*, Ore Geol. Rev. **117**, 103 328 (2020).

[13] D. Kinschel, C. Bacellar, O. Canelli, B. Sorokin, T. Katayama, G. F. Mancini, J. R. Rouxel, Y. Obara, J. Nishitani, H. Ito, T. Ito, N. Kurahashi, C. Higashimura, S. Kudo, T. Keane, F. A. Lima, W. Gawelda, P. Zalden, S. Schulz, J. M. BUrdarz, D. Khakhulin, A. Galler, C. Bressler, C. J. Milne, T. Penfold, M. Yabashi, T. Suzuki, K. Misawa, and M. Chergui, *Femtosecond X-ray emission study of the spin cross-over dynamics in haem proteins*, Nat. Comm. **11**, 4145 (2020).

[14] C. Sousa, M. Alías, A. Domingo, and C. de Graaf, *Deactivation of Excited States in Transition-Metal Complexes: Insight from Computational Chemistry*, Chem. Eur. J. **25**, 1152–1164 (2019).

[15] C. Daniel, *Photochemistry and photophysics of transition metal complexes: Quantum chemistry*, Coord. Chem. Rev. **282-283**, 19–32 (2015).

[16] S. Mai, F. Plasser, J. Dorn, M. Fumanal, C. Daniel, and L. González, *Quantitative wave function analysis for excited states of transition metal complexes*, Coord. Chem. Rev. **361**, 74–97 (2018).

[17] E. Tapavicza, I. Tavernelli, and U. Rothlisberger, *Trajectory Surface Hopping within Linear Response Time-Dependent Density-Functional Theory*, Phys. Rev. Lett. **98**, 023 001 (2007).

[18] M. A. El-Sayed, *The triple state: its radiative and non-radiative properties*, Acc. Chem. Res. **1**, 8–16 (1968).

[19] M. Richter, P. Marquetand, J. González-Vazquez, I. Sola, and L. González, *SHARC: ab Initio Molecular Dynamics with Surface Hopping in the Adiabatic Representation Including Arbitrary Couplings*, J. Chem. Theory Comput. **7**, 1253–1258 (2011).

[20] A. Raab, G. Worth, H.-D. Meyer, and L. S. Ceberdaum, *Molecular dynamics of pyrazine after excitation to the $S_2$ electronic state using a realistic 24-mode model Hamiltonian*, J. Chem. Phys. **110**, 936 (1999).

[21] C. J. Ballhausen, *Introduction to ligand field theory* (McGrawHill Book Company, United States of America) (1962).

[22] C. Sousa, C. de Graaf, A. Rudavskyi, R. Broer, J. Tatchen, M. Etinski, and C. M. Marian, *Ultrafast Deactivation Mechanism of the Excited Singlet in the Light-Induced Spin Crossover of [Fe(2,2'-bipyridine)$_3$]$^{2+}$*, Chem. Eur. J. **19**, 17 541 –17 551 (2013).

[23] C. Sousa, M. Llunell, A. Domingo, and C. de Graaf, *Theoretical evidence for the direct $^3$MLCT-HS deactivation in the light-induced spin crossover of Fe(II)–polypyridyl complexes*, Phys. Chem. Chem. Phys. **20**, 2351–2355 (2018).

[24] W. Zhang, R. Alonso-Mori, U. Bergmann, C. Bressler, M. Chollet, A. Galler, W. Gawelda, R. G. Hadt, R. W. Hartsock, T. Kroll, K. S. Kjaer, K. Kubiček, H. T. Lemke, H. W. Liang, D. A. Meyer, M. M. Nielsen, C. Purser, J. S. Robinson, E. I. Solomon, Z. Sun, D. Sokaras, T. B. van Driel, G. Vankó, T.-C. Weng, D. Zhu, and K. J. Gaffney, *Tracking excited-state charge and spin dynamics in iron coordination complexes*, Nature **509**, 345–348 (2014).

[25] G. Auböck, and M. Chergui, *Sub-50-fs photoinduced spin crossover in [Fe(bpy)$_3$]$^{2+}$*, Nat. Chem. **7**, 629–633 (2015).

[26] S. Zerdane, L. Wilbraham, M. Cammarata, O. Iasco, E. Riviére, M.-L. Boillot, I. Ciofini, and E. Collet, *Comparison of structural dynamics and coherence of d–d and MLCT light-induced spin state trapping*, Chem. Sci. **8**, 4978 (2017).

[27] S. Zerdane, M. Cammarata, O. Iasco, M.-L. Boillot, and E. Collet, *Photoselective MLCT to d-d pathways for light-induced excited spin state trapping*, J. Chem. Phys. **151**, 171 101 (2019).

[28] C. B. Larsen, and O. S. Wenger, *Photoredox Catalysis with Metal Complexes Made from Earth-Abundant Elements*, Chem. Eur. J. **23**, 1–21 (2017).

[29] K.Kalyanasundaram, *Photophysics, photochemistry and solar energy conversion with tris(bipyridyl)ruthenium(II) and its analogues*, Coord. Chem. Rev. **46**, 159–244 (1982).

[30] D. A. Nicewicz, and D. W. C. MacMillan, *Merging Photoredox Catalysis with Organocatalysis: The Direct Asymmetric Alkylation of Aldehides*, Science **322**, 77–80 (2008).

[31] J. Wu, M. Alías, and C. de Graaf, *Controlling the Lifetime of the Triplet MLCT State in Fe(II) Polypyridyl Complexes through Ligand Modification*, Inorganics **8**, 16–33 (2020).

[32] W. Zhang, K. S. Kjaer, R. Alonso-Mori, U. Bergmann, M. Chollet, L. A. Fredin, R. G. Hadt, R. W. Hartsock, T. Harlang, T. Kroll, K. Kubiček, H. T. Lemke, H. W. Liang, Y. Liu, M. M. Nielsen, P. Persson, J. S. Robinson, E. I. Solomon, Z. Sun, D. Sokaras, T. B. van Driel, T.-C. Weng, D. Zhu, K. Wärnmark, V. Sundströmb, and K. J. Gaffney, *Manipulating charge transfer excited state relaxation and spin crossover in iron coordination complexes with ligand substitution*, Chem. Sci. **8**, 515 (2017).

[33] K. Falahati, H. Tamura, I. Burghardt, and M. Huix-Rotllant, *Ultrafast carbon monoxide photolysis and heme spin-crossover in myoglobin via nonadiabatic quantum dynamics*, Nat. Commun. **9**, 4502–4509 (2018).

[34] K. Schwinn, N. Ferré, and M. Huix-Rotllant, *Efficient Analytic Second Derivative of Electrostatic Embedding QM/MM Energy: Normal Mode Analysis of Plant Cryptochrome*, J. Chem. Theory Comput. **16**, 3816–3824 (2020).

[35] M. Cammarata, S. Zerdane, L. Balducci, G. Azzolina, S. Mazerat, C. Exertier, M. Trabuco, M. Levantino, R. Alonso-Mori, J. M. Glownia, S. Song, L. Catala, T. Mallah, S. F. Matar, and E. Collet, *Charge transfer driven by ultrafast spin transition in a CoFe Prussian blue analog*, Nat. Chem. **13**, 10–14 (2021).

[36] A. Domingo, M. A. Carvajal, C. de Graaf, K. Sivalingam, F. Neese, and C. Angeli, *Metal-to-metal charge-transfer transitions: reliable ex-*

*citation energies from ab initio calculations*, Theor. Chem. Acc. **131**, 1264 (2012).

[37] B. Wardle, *Principles and Applications of Photochemistry* (John Wiley & Sons, United Kingdom) (2009).

[38] Y. Ohshima, and M. Baba, *$S_1$ $^1A_2(n\pi^*)$ and $S_2$ $^1A_1(\pi\pi^*)$ states of jet-cooled xanthone*, J. Phys. Chem. A **107**, 8851–8855 (2003).

[39] C. Crespo-Hernández, B. Cohen, P. M. Hare, and B. Kohler, *Ultrafast Excited-State Dynamics in Nucleic Acids*, Chem. Rev. **104**, 1977–2019 (2004).

[40] M. Merchán, R. González-Luque, T. Climent, L. Serrano-Andrés, E. Rodríguez, M. Reguero, and D. Peláez, *Unified Model for the Ultrafast Decay of Pyrimidine Nucleobases*, J. Phys. Chem. B **110**, 26 471–26 476 (2006).

[41] Z. Lan, E. Fabino, and W. Thiel, *Photoinduced Nonadiabatic Dynamics of Pyrimidine Nucleobases: On-the-Fly Surface-Hopping Study with Semiempirical Methods*, J. Phys. Chem. B **113**, 3548–3555 (2009).

[42] S. Mai, M. Richter, P. Marquetand, and L. González, *Topics is Current Chemistry. Photoinduced Phenomena in Nucleic Acids I by Mario Barbatti, Antonio Carlos Borin and Susanne Ullrich (eds.)* (Springer Berlin, Heidelberg, Germany), chapter Excitation of Nucleobases from a Computational Perspective II: Dynamics, pp. 99–154 (2015).

[43] P. Diamantis, I. Tavernelli, and U. Rothlisberger, *Redox Properties of Native and Damaged DNA from Mixed Quantum Mechanical/Molecular Mechanics Molecular Dynamics Simulations*, J. Chem. Theory Comput. **16**, 6690–6701 (2020).

# 2.
# Theoretical methods

Theoretical chemistry tries to explain chemical tendencies or physical properties using equations and mathematical approaches to solve these. The equations can be built up from different levels of theory and using different levels of approximations. In this section, we will put in a wider context the equations used during the development of the current thesis. The most commonly used methods will be only shortly described while the more novel information will be treated in detail. This chapter has been split in two parts, each focusing on a different property computed through the equations. On the one hand, the electronic structure methods where the electronic energy and wave function are computed solving the time-independent Schrödinger equation. In spite of not computing directly the energy, effective Hamiltonian theory and the description of the spin-orbit coupling Hamiltonian are also discussed there. On the other hand, there are the methods used to analyse the time evolution of a quantum system which can treat time either explicitly or obtain information about the dynamics in a more indirect manner through mathematical approximations.

## 2.1. Electronic structure based methods

This first part discusses the quantum methods that have been used to evaluate the electronic energy. All these methods are based on solving the time-independent Schrödinger equation within the Born-Oppenheimer approximation.

$$\hat{H}\Psi = E\Psi \tag{2.1}$$

The electronic methods used during this thesis can be divided in wave function based or post-Hartree Fock methods and methods based on density functional theory (DFT). The first ones possess a clear hierarchy of increasing accuracy and are able to deal with the multi-configurational character of the system in a straightforward manner. The second ones are the most used in quantum chemistry because of their extraordinary balance between velocity and accuracy.

### 2.1.1. Multi-configuration wave function based methods

The large majority of the chemical problems can be handled using only a single Slater Determinant. However, in some particular systems such as biradical molecules, bond dissociations, magnetic couplings or excited states, a multi-configuration treatment is usually a must. Post Hartree-Fock methods recover part of the electron correlation absent in Hartree-Fock where the many-electron wave function is represented by just one anti-symmetrized product whereas the post Hartree-Fock methods expand the many-electron wave function in terms of a (long) series of Slater determinants. The exact energy within a non-relativistic, Born-Oppenheimer and time-independent perspective is obtained using Full CI with an infinite one-electron basis set. Full CI includes in the many-electron wave function all the Slater Determinants generated for a particular basis set. Unfortunately, it is not a viable alternative because the size of the CI-matrix increases factorially with the number of basis functions and the method becomes rapidly prohibitive, even for very small systems with reasonable basis sets. For this reason, several approaches have been developed to treat only a smaller, yet representative subset of all the configurations.

Among the methods that use linear wave function expansion, separating them from the exponential expansion in the coupled cluster methods, two different classes can be distinguished. The first one orders the determinants by increasing excitation level with respect to the reference, usually the HF determinant, and truncates the expansion at a certain excitation level. Brillouin's theorem states that the interaction of a determinant, expressed in its optimised molecular orbitals, with the determinant that differ by one orbital occupation is strictly zero, therefore the inclusion of the double excitation determinants, at least, is a must [1]. Alternatively, the subset of determinants can also be constructed based on chemical knowledge. The most common example of this type of multi-configurational wave function is the Complete Active Space Self-Consistent Field (CASSCF).

### Complete Active Space Self-Consistent Field (CASSCF)

This method can be considered an intermediate approach between HF and Full CI. It relies on a complete expansion of the wave function, like Full CI albeit in a smaller subspace called active space. In the HF method only a single determinant is used, therefore its corresponding coefficient is fixed to one to fulfill the wave function normality, then the optimisation procedure only acts in the set of molecular orbitals i.e. the SCF coefficients. The paradigm in Full CI is completely antagonistic, the set of Slater determinants form a complete basis, therefore only the CI-coefficients are optimised and the shape of molecular orbitals does not have any influence in the final energy. CI-coefficients will adapt to the set of molecular orbitals used. In the CASSCF approach, the CI-coefficients and the orbital expansion coefficients have to be optimised at the same time because the Full CI space is not totally represented and the shape of molecular orbitals plays a key role. The active space depends at the same time of the SCF and CI sets of coefficients, therefore is not unique and they have a reciprocal dependency. Probably the most informative representation of molecular orbitals is in natural orbitals, which are obtained by the diagonalisation density matrix.

$$\Psi_{CAS} = c_0\Phi_0 + \sum_{i,p\in CAS} c_i^p\Phi_i^p + \sum_{ij,pq\in CAS} c_{ij}^{pq}\Phi_{ij}^{pq} + \sum_{ijk,pqr\in CAS} c_{ijk}^{pqr}\Phi_{ijk}^{pqr} + ... \tag{2.2}$$

where i,j and k are active orbitals occupied in $\Phi_0$ and p,q and r represent active orbitals that are empty in $\Phi_0$. $\Phi_i^p$ is a singly excited determinant with respect to $\Phi_0$, replacing an electron in orbital i by an electron in p, and analogous for the doubly, triply and higher excited determinants, until exhausting all possible replacements within the CAS.

In CASSCF calculations, the molecular orbitals are split in three different classes. The first group contains the so-called inactive orbitals, they are doubly occupied in all the determinants of the wave function. The second group is formed by active orbitals, they are empty, partially or doubly occupied depending on the determinant. Finally, there are the virtual orbitals which are empty in all the determinants. To build the wave function,

the Slater determinants or anti-symmetrized Hartree products are linearly combined to form configuration state functions. CSFs are constructed to become eigenfunctions of the $\hat{S}^2$ operator and the eigenvalue characteristic of the imposed spin multiplicity. The quality of the CASSCF wave function depends critically on how the selection of active space is made. There is unfortunately no universal recipe to make the division of orbitals, although important steps are being made in that direction lately,[2] and hence, some chemical knowledge is required to construct the CASSCF wave function for each particular problem.

CASSCF calculations recover part of the electron correlation and the leading configurations of the hypothetical exact many-electron wave function. The electron correlation gained in CASSCF calculations is only the so-called static correlation. The lack of dynamic correlation makes CASSCF energies not practical for quantitative proposal many times. However, the CASSCF wave function is very useful to describe multi configurational systems from a qualitative view and it is also widely used as reference wave function for methods that aim for a more quantitative description such as CASPT2, NEVPT2 or DDCI.

To deal with excited states, the CI matrix is diagonalised using an optimised set of molecular orbitals. The Davidson procedure is performed for the selected roots, it means that instead of a full diagonalization procedure, only those rows and columns corresponding to the selected states are diagonalised. The eigenvectors generated are the CI-coefficients for each configuration in the state and the eigenvalue is the energy of the root at CASSCF level. The CI-coefficients are generated for the set of molecular orbitals used, but these MO are optimised and therefore change at each step.

Because the expansion of the active space is only complete in a small subset of the MO space, the outcomes of the calculations depend on the space described by these molecular orbitals Depending on the way these MO are optimised, it is possible to distinguish between two different situations, commonly known as the state-average and state-specific approaches.

**State-average (SA-CASSCF)** is the most common way to proceed when a CASSCF calculation is done. In this kind of calculations, the MOs are optimised to obtain the minimum average energy solution for

the selected states. It means that the orbitals are quite satisfactory for all the states but they do not match perfectly with the optimal orbitals for any of them. In this approach, all the states are orthogonal among each other by definition.

**State-specific (SS-CASSCF)** is used when an average description does not suffice; either very high precision is required or the optimal orbitals for the states of interest are very different. The latter is very common when metal-to-metal charge transfer processes are studied.[3] The state-specific approach result in optimal orbitals for each individual state, and hence, provides the lowest energy for that state under the restrictions of the active space. This approach is particularly complicated for high-lying states because they can suffer root flipping. Moreover, the states are not necessarily orthogonal among each other in this approach.

### Complete Active Space Second Order Perturbation Theory (CASPT2)

This multi-configurational reference perturbative method uses an optimised CASSCF state as zeroth order wave function. As explained, CASSCF is only able to account for the static electron correlation and in the perturbative part the dynamic electron correlation is added by the treatment of determinants not generated within the active space.

The exact Hamiltonian, within non-relativistic Born-Oppenheimer framework, is split in perturbation theory into a zeroth order Hamiltonian that can be solved exactly and a supposedly small perturbative part.

$$\hat{H} = \hat{H}^{(0)} + \hat{V} \tag{2.3}$$

The perturbative part is usually expressed as a Taylor expansion. Theoretically, perturbation theory converges to the Full CI solution in the limit of infinite order. However, an infinite order perturbation is an utopia. In the case of CASPT2 the Taylor expansion is cut to the second order, it includes first and second order perturbative corrections to the zeroth order energy. Because of the Taylor expansion is only expanded up to the second order, one must include as much physics as possible in the zeroth order

Hamiltonian, making the perturbative correction as small as possible to converge in better results.

The sum of the zeroth and first order corrections to the energy exactly coincide with the CASSCF energy.

$$E_{CASSCF} = \left\langle \Psi^{(0)} \right| \hat{H} \left| \Psi^{(0)} \right\rangle = \\ = \left\langle \Psi^{(0)} \right| \hat{H}^{(0)} \left| \Psi^{(0)} \right\rangle + \left\langle \Psi^{(0)} \right| \hat{V} \left| \Psi^{(0)} \right\rangle = E^{(0)} + E^{(1)} \quad (2.4)$$

Therefore, in CASPT2 and all other variants of multi-configurational reference second-order perturbation theory, the correction to the energy comes from the second order correction term. From Rayleigh-Schrödinger perturbation theory, the second order correction is the interaction between the zeroth order wave function and the first order wave function through the perturbative operator.

$$E^{(2)} = \left\langle \Psi_0^{(0)} \right| \hat{V} \left| \Psi_0^{(1)} \right\rangle = \sum_{i \neq 0} \frac{\left\langle \Psi_i^{(0)} \right| \hat{V} \left| \Psi_0^{(0)} \right\rangle \left\langle \Psi_0^{(0)} \right| \hat{V} \left| \Psi_i^{(0)} \right\rangle}{E_i^{(0)} - E_0^{(0)}} \quad (2.5)$$

Note that this perturbation operator is usually not explicitly defined, it is written down as the difference between the exact and the zeroth order Hamiltonian. The zeroth order Hamiltonian in CASPT2 is a generalization of the Fock operator to the multi-configurational reference, keeping its effective one-electron operator nature. It converges to the standard zeroth order Hamiltonian of Møller-Plesset perturbation theory in the limit of zero active orbitals.

The first order wave function is spanned along those determinants that directly interact with the reference CASSCF wave function in the so-called First Order Interacting Space (FOIS). Recalling that the Slater-Condon rules state that only single and double excitations can directly interact with the zeroth order wave function,[1] the first order wave function is

formed by external CAS determinants generated by single or double excitations to the determinants of the CASSCF reference wave function. These determinants can be grouped in eight different classes depending on the distribution of holes (annihilation operators in the inactive orbitals) and particles (creation operators in the virtual orbitals). Following this notation, the configurations are: a) 1 hole (1h) excitation from the inactive orbitals to the active space, b) 1 particle (1p) excitation from the active orbitals to the virtuals, c) 1 hole-1 particle (1h-1p) excitation from inactive to virtuals, d) 2 holes (2h) double excitation from inactive to active orbitals, e) 2 particles (2p) double excitation from active to virtual orbitals, f) 2 holes-2 particles (2h-2p) double excitation from inactive to virtual orbitals, g) 1 hole-2 particles (1h-2p) one excitation from inactive to virtuals and another from active to virtuals and h) 2 holes-1 particle (2h-1p) one excitation from inactive to active and another from inactive to virtual orbitals. The relative weight of each configuration, $\Psi_i^{(0)}$, in the final wave function is given by:

$$c_i^{(1)} = \frac{\left\langle \Psi_i^{(0)} \middle| \hat{V} \middle| \Psi_0^{(0)} \right\rangle}{E_i^{(0)} - E_0^{(0)}} \tag{2.6}$$

From this equation it is clear that external configurations for which the expectation value $\hat{H}^{(0)}$ is much higher than $E^{(0)}$ are prone to have a smaller weight in the final wave function than those with expectation values closer to the reference energy. The weight of the zeroth order wave function, $\omega$, is called reference weight

$$\Psi = \omega\Psi^{(0)} + \Psi^{(1)} = \omega\Psi^{(0)} + \sum_{i\neq 0} \frac{\left\langle \Psi_i^{(0)} \middle| \hat{V} \middle| \Psi_0^{(0)} \right\rangle}{E_i^{(0)} - E_0^{(0)}} \Psi_i^{(0)} \tag{2.7}$$

This parameter plays an important role assessing the quality of a calculation. Only when the reference weight is similar, one can safely compare the energy (or any other property) of two different electronic states.

The presence of an energy difference in the denominator of the second order correction energy and first order wave function is a potential problem

in CASPT2. If this energy difference tends to zero, an unrealistic second order energy correction is obtained, marking the presence of a weak intruder state. In order to repair this problem, a correction to the denominator is applied, the so-called level shift technique. [4]

$$\tilde{E}^{(2)} = \sum_{j \neq 0} \frac{\left\langle \Psi_0^{(0)} \middle| \hat{V} \left| \Phi_j \right\rangle \left\langle \Phi_j \right| \hat{V} \middle| \Psi_0^{(0)} \right\rangle}{E_j - E_0^{(0)} + \mu} \tag{2.8}$$

A new expression for the second order correction energy is used to ensure the non-zero value of the original denominator, where $\mu$ is the applied level-shift and $\omega$ is the reference weight of the zeroth order wave function.

$$E^2 = \tilde{E}^{(2)} + \mu \left( 1 - \frac{1}{\omega} \right) \tag{2.9}$$

Other perturbative methods such as NEVPT2 [5] do not show the presence of intruder states, because they introduce more 'physics' in the zeroth order Hamiltonian including explicitely two electron interactions for the active space orbitals by the use of Dyall Hamiltonian. However, in some particular problems such as in the spin-state energetics of transition metal complexes, CASPT2 has shown a better agreement with experimental results. [6]

Another problem that appeared in the early days of CASPT2 was an unbalanced description for closed shell electronic structures compared with those having unpaired electrons. The correlation energy was systematically overestimated for open-shell systems, which generated errors in computed dissociation energies, excitation energies, bond formations, among other properties. A careful analysis of the problem showed that the origin lied in the definition of the diagonal elements of the Fock-like matrix of the zeroth order Hamiltonian. The diagonal elements of this Fock-like operator have a clear meaning for inactive and virtual orbitals, corresponding to the Koopman's estimate of the ionization potential and electron affinity, respectively. However, such clear-cut definition does not exist for the diagonal elements corresponding to the active orbitals with fractional occupation. In these cases the diagonal element corresponds to a weighted average of the two properties:

$$F_{pp} = -\frac{1}{2}(D_{pp}(IP)_p + (2 - D_{pp})(EA)_p) \tag{2.10}$$

where $D_{pp}$ is the $p^{th}$ element of the one-particle density matrix. This property generates too small denominators in the second-order energy correction and is the origin of the systematic overestimation of the correlation energy of the electronic states with marked open-shell character. To repair this overestimation an extra term was added to Eq. 2.10; $1/2D_{pp}\epsilon$ when an active orbital receives an electron (acts as a 'virtual' orbital) and $-1/2(2 - D_{pp})\epsilon$ when an electron is removed from it (acts as an 'inactive' orbital). The average shift parameter $\epsilon$ was fixed at 0.25 a.u. and improves the unshifted results in many cases, although its value has been matter of continuous discussion since its publication. [7,8]

Following the first implementation of CASPT2 in the early 1990's several small variations were published in the literature. Three of them are briefly explained below.

**Single-state (SS-CASPT2)** was the first implementation of CASPT2. [9] It uses as zeroth order wave function a CASSCF optimsed wave function. This is a diagonalize then perturb approach. The zeroth order Hamiltonian allows to introduce part of the dynamic electron correlation to the CASSCF energy, where only the static electron correlation is included, but it does not open the possibility to revise the relative importance of the configurations in the CAS under the influence of dynamic correlation.

$$\hat{H}_0^{\alpha} = |\alpha\rangle \langle\alpha| \hat{F} |\alpha\rangle \langle\alpha| + \sum_k |k\rangle \langle k| \hat{F} |k\rangle \langle k| + Q_{sd}^{\alpha} \hat{F}^{\alpha} Q_{sd}^{\alpha} \tag{2.11}$$

where $\hat{F}$ is a generalized Fock operator, the sum over k includes all states within the CAS orthogonal to the reference state $\alpha$ and $Q_{sd}^{\alpha}$ is the FOIS corresponding to the $\alpha$ state.

**Multi-state (MS-CASPT2)** is an extension of the original formalism developed by Roos and coworkers and needs at least two different reference states. [10] It mixes the states obtained at CASSCF level under the influence of the dynamic correlation captured by CASPT2. This is specially important for geometries close to avoided crossings where the

CASSCF wave function is often not a good zeroth order description. It is found within the "diagonalize then perturb then diagonalize" type of perturbation methods. The diagonal terms of the effective Hamiltonian constructed to include the dynamic correlation effects in CASSCF wave functions are the SS-CASPT2 energies for each root and the off-diagonal terms are obtained by calculating the interaction among CASSCF states through the perturbative correction to their CASSCF wave functions.

$$\hat{H}_0^\alpha = \sum_\beta |\beta\rangle \langle\beta| \hat{F} |\beta\rangle \langle\beta| + \sum_k |k\rangle \langle k| \hat{F} |k\rangle \langle k| + Q_{sd}^\alpha \hat{F}^\alpha Q_{sd}^\alpha \qquad (2.12)$$

where $\beta$ includes all reference states, including $\alpha$.

MS-CASPT2 energies are obtained by diagonalization of this effective Hamiltonian obtained from the zeroth order Hamiltonian. One of the problems of this method is that the interaction between $\beta$ and $\alpha$ through the zeroth order Hamiltonian is different to the one obtained between $\alpha$ and $\beta$. In order to keep the Hermitian character of the Hamiltonian the off-diagonal matrix element is taken as the average of both interactions.

**Extended Multi-state (XMS-CASPT2)** is a slight variation of the original multi-state approach, in which not only the diagonal matrix elements of the Fock matrix are considered but also the off-diagonal ones.

$$\hat{H}_0^\alpha = \sum_\beta \sum_\gamma |\beta\rangle \langle\beta| \hat{F} |\gamma\rangle \langle\gamma| + \sum_k |k\rangle \langle k| \hat{F} |k\rangle \langle k| + Q_{sd}^\alpha \hat{F}^\alpha Q_{sd}^\alpha \qquad (2.13)$$

where $\beta$ and $\gamma$ includes all reference states, including $\alpha$.

The interaction of the reference states $\alpha$ and $\beta$ is of course zero when the full Hamiltonian is considered but becomes non-zero for the approximate zeroth order Hamiltonian. This extension solved the appearance of discontinuities in the energy surface near conical intersections and avoided crossings shown by MS-CASPT2, while CASSCF energies smoothly changed in these areas.[11] XMS-CASPT2 still shows the same problems with the

Hermitian character of the Hamiltonian and the same recipe as in MS-CASPT2 is used to deal with it.

### 2.1.2. Density Functional Theory

Density functional theory (DFT) is without any doubt the most widely used method in quantum chemistry, only a brief summary and some words about time-dependent (TD-DFT) are pretended in this text. Modern DFT was put on a firm basis by Hohenberg, Kohn and Sham in the mid-1960s. The theory is based on the fact that the energy of a system depends in a one-to-one fashion on their particular electron distribution or electron density, therefore the energy is a functional (a function that depends on another function) of electron density. The exact energy needs to know the exact functional and this is unfortunately not the case. However, the great advantage of the theory is that it introduces a description with electron correlation at the price of a Hartree-Fock calculation. The density functional to calculate the energy of the system can be expressed as a sum of different terms: the independent electronic kinetic energy ($T_S$) functional, the nuclei-electron interaction ($E_{Ne}$) functional, the nuclei-nuclei interaction ($V_{NN}$) functional, the functionals for the Coulombic (J) and exchange interactions among electrons and the electron correlation energy.

$$E[\rho] = T_S[\rho] + E_{Ne}[\rho] + J[\rho] + V_{NN} + E_{xc}[\rho] \tag{2.14}$$

Unfortunately, the exact expression for the exchange and correlation functionals are unknown and the effort to obtain accurate expressions for these has became as a fundamental field within theoretical chemistry.

One of the problems of DFT compared with post HF methods is that it is a single determinant method and therefore not able to deal with multi-configurational systems. However, DFT produces very accurate geometries, energies or frequencies with little computational effort in closed-shell or monoconfigurational systems. The enhancement in DFT functionals appears through more complex expressions for the exchange-correlation functional and is usually illustrated through the well-known Jacob's ladder. In this graphical representation, local density approximation (LDA)

functionals using only the electronic density are found at the bottom of the ladder. The inclusion of the density gradient ($\nabla\rho$) and the Laplacian of the density ($\nabla^2\rho$) are the two next steps giving rise to the generalized gradient approximation (GGA) and meta generalized gradient approximation (meta-GGA) functionals, respectively. Further improvement comes about by the inclusion of a certain amount of exact or HF exchange, they are the so-called hybrid functionals. Finally, the functionals that are found near the top in this ladder are the double-hybrid functionals mixing some MP2 correlation energy in addition to using HF exchange.

### Time-dependent Density Functional Theory (TD-DFT)

This method was developed to deal with excited states as an extension of standard DFT theory which is limited to the ground state. However, in photochemical and photophysical problems excited states play a central role, and therefore their inclusion and treatment is a must. The time dependency is introduced in the density, then an observable A is a functional of the initial wave function and the time-dependent density as states the Runge-Gross theorem.[12] Moreover, there exists a correspondence between the density and the Kohn-Sham molecular orbitals. It leads to write the time-dependent Kohn-Sham equation as:

$$\left(-\frac{1}{2}\nabla^2 + V_{\mathit{eff}}(r,t)\right)\Psi_i(r,t) = i\frac{\partial}{\partial t}\Psi_i(r,t) \tag{2.15}$$

$$V_{\mathit{eff}}(r,t) = V_H(r,t) + V_{xc}(r,t) + V_{ext}(r,t) \tag{2.16}$$

The time-dependent exchange-correlation functional is unknown as in the standard Hohenberg-Kohn-Sham DFT formalism. The adiabatic approximation is the simplest and most successful approximation to deal with the time-dependency. It states that the exchange-correlation potential reacts instantaneously and without memory to any temporal change in the time-dependent density, therefore all retardation and memory effects are neglected and the same functionals can be used as in standard DFT.[13]

$$V_{xc} = \frac{\delta A_{xc}[\rho]}{\delta \rho(r,t)} \approx \frac{\delta E_{xc}[\rho]}{\delta \rho(r)} \tag{2.17}$$

Apart from the explicit time evolution of the density, the formalism can also be used to study the response to external perturbations. The current implementations of TD-DFT only consider the linear response of the density, it means that here higher order terms are neglected.

$$\rho(r,t) = \rho_0(r) + \delta\rho(r,t) \tag{2.18}$$

It has the great advantage that the perturbation can be expressed in the basis of unperturbed Kohn-Sham molecular orbitals.

To study excited states in molecular spectroscopy, the dynamic dipole moment, $\alpha$, is calculated. This is the response function over the dipole moment ($\mu$) when an electric field ($\epsilon$) is applied.

$$\mu_x(t) = \mu_x + \int_{-\infty}^{\infty} dt' \alpha_{xz}(t-t')\epsilon_z(t') \tag{2.19}$$

Fourier transformation changes the response from a time-domain to a frequency domain to obtain information about the energetics of the system.

$$\delta\mu_x(\omega) = \alpha_{xz}(\omega)\epsilon_z(\omega) \tag{2.20}$$

In the frequency domain, the dipole polarizability can be expressed as a sum-over-states. The poles in polarizability indicate the energies of infinite response of the density to the external perturbation, that is where the system changes to an excited state.

$$\bar{\alpha}(\omega) = \sum_I \frac{f_I}{\omega_I^2 - \omega^2} \tag{2.21}$$

where $f_I$ is the oscillator strength $\frac{2}{3}\omega_I |\langle \Psi_0 | \hat{r} | \Psi_i \rangle|^2$ and $\omega_I = E_I - E_0$.

It is also possible and more convenient to express the dynamic polarizability in the basis of unperturbed KS molecular orbitals. This gives rise

to the well-known Casida equations which within the adiabatic approximation have the form written down in Eq. 2.22. Diagonalization of all the matrices in Casida's equations allows to obtain the energies of excited states and the character of them expressed in terms of single orbital replacements, that is, a list of the coefficients indicating the importance of each single transition.

$$\begin{pmatrix} A & B \\ B^* & A^* \end{pmatrix} \begin{pmatrix} X \\ Y \end{pmatrix} = \Omega \begin{pmatrix} -I & 0 \\ 0 & I \end{pmatrix} \begin{pmatrix} X \\ Y \end{pmatrix} \tag{2.22}$$

where A is a matrix with elements $A_{ia,jb} = \delta_{ia}\delta jb\epsilon_{a,i} + (ia|f_{Hxc}|jb)$ and the matrix elements of B are $B_{ia,bj} = (ia|f_{Hxc}|bj)$. X and Y are vectors that contain information about the transition dipole moments, $\Omega$ about the excited state energies and I is the identity matrix. The indexes i and j refers to occupied orbitals while a and b to virtual orbitals.

The Tamm-Dancoff approximation (TDA) neglects the B matrix from the Casida equation. Despite dealing with much simpler equations, it gives accurate excitation energies, and solves in most cases the problems of triplet instabilities that sometimes appear in the first Casida implementation. As disadvantage one must keep in mind that TDA tends to give less accurate oscillator strengths. TD-DFT has been proving to be a fast method to obtain excited state energies for lower-lying excited states. However, the main inconveniences of standard TD-DFT are its incapacity to deal with double excitations and it can only treat single excitations, its problem to describe charge transfer states and the lack of consensus about the most convenient functional to calculate excitation energies, especially for transition metal complexes. There is only little benchmarking for these latter compounds in the literature, contrary to systems with only main-group elements.

### 2.1.3. Effective Hamiltonian theory

Effective Hamiltonian is widely used in quantum mechanics to extend the direct interaction between two electronic states A and B with the effect of other intermediate states that interact with both A and B. This turns the bare, direct interaction into an effective or 'dressed' interaction between

the two states, which in principle describes more accurately the interaction without increasing the complexity of the description. In the current project, the effective Hamiltonian has been used uniquely to improve the description of spin-orbit couplings, therefore the theoretical explanation will be mainly addressed to this property. However, effective Hamiltonians are much more general and can be applied to study many other properties such as the energy. The basic idea of effective Hamiltonian theory is to project all the information contained in a complete Hamiltonian of space S into a smaller subspace $S_0$.

First, one has to write down the Hamiltonian of the full Hilbert space (S) of dimension N×N.[14] The diagonal terms coincide with the energy of the spin-free states and the off-diagonal terms are direct SO couplings between states. The diagonalization of the Hamiltonian produces the SO wave functions ($\Psi_p$, $\Psi_q$,..) expressed as linear combinations of the spin free states ($\phi_a$, $\phi_b$,...) as appreciated in Equation 2.23 and their corresponding eigenvalues ($E_p$, $E_q$, ...).

$$\begin{aligned} \Psi_p &= c_{p,a}\phi_a + c_{p,b}\phi_b + ... + c_{p,N}\phi_N \\ \Psi_q &= c_{q,a}\phi_a + c_{q,b}\phi_b + ... + c_{q,N}\phi_N \end{aligned} \tag{2.23}$$

It should be stressed here that the term 'spin-free states' is somewhat ambiguous as it makes reference to those states which are eigenfunctions of the $S^2$ operator, and hence, obviously, have spin coordinates. The reason for calling these states 'spin-free states' is the fact that they are determined in a non-relativistic frame, in which spin-operator is not included in the Hamiltonian, but instead, the spin is added ad-hoc in the wave function by imposing the restrictions of the eigenfunctions of the $S^2$ operator. Then, the usual singlet, doublet, triplet, etc. wave functions are considered spin-free states.

Secondly, a smaller space $S_0$ of dimension m must be selected spanned by those spin-free states for which the effective spin-orbit coupling is calculated. All the SO wave function are projected onto $S_0$ and those m projections with largest norms $\sum_{k \in S_0} |c_{p,k}|^2$ are selected.

$$\tilde{\Psi}_p = \sum_{k \in S_0} c_{p,k} \phi_k \tag{2.24}$$

The norms give a direct check on the validity of the model space. Small norms indicate that the selected subspace is too small and some spin-free states strongly mixed with the ones in the subspace are not included in $S_0$, therefore the chosen subspace does not correctly describe the physics of the system.

Next, the projections of the SO wave functions are orthonormalized. Several orthogonalization schemes exist, among them we have selected the orthogonalization of des Cloizeaux (also known as Löwdin orthogonalization) which involves the overlap matrix $S^{-\frac{1}{2}}$.

$$\tilde{\Psi}_k^{\perp} = S^{-\frac{1}{2}} \tilde{\Psi}_k \tag{2.25}$$

The effective Hamiltonian is constructed using the orthonormalised projections of SO wave functions $\tilde{\Psi}_k^{\perp}$ and their respective eigenvalues $E_k$ using Bloch's formula.

$$H_{ij}^{SO,eff} = \langle \phi_i | \hat{H}^{SO,eff} | \phi_j \rangle = \langle \phi_i | \left[ \sum_{k \in S_0} \left| \tilde{\Psi}_k^{\perp} \right\rangle E_k \left\langle \tilde{\Psi}_k^{\perp} \right| \right] | \phi_j \rangle \tag{2.26}$$

Eigenvectors and eigenvalues of this smaller Hamiltonian coincide with the projected orthonormalised SO wave function and their energies, respectively. It means that effective SO coupling contains not only the direct SO but also the higher order couplings.

### 2.1.4. Spin-orbit coupling operator

In non-relativistic quantum chemistry transition dipole moments and coupling matrix elements among states with different spin moments are strictly zero. Spin-orbit coupling (SOC) arises naturally in Dirac's relativistic

theory and hence states of different spin can only couple through the appearance of relativistic effects. For instance, in one-electron atoms, spin $s$ and orbital $l$ angular momentum are strictly speaking not good quantum numbers because they couple through the SOC operator and it is actually only possible to have knowledge about the total angular momentum $j$ which is the sum of $l$ and $s$.

Building a relativistic theory is however not an easy task and some problems already arise when writing down the Hamiltonian. In the first place, there is the fact that strictly speaking many-body interaction terms should be included in the expression. Luckily, three-body potentials can be neglected because they were proven to cause only very small variations on the final result and dealing with two-body potentials was concluded to be accurate enough. The second matter of concern is the fact that the instantaneous electron-electron attraction is described in quantum chemistry through the Coulomb potential and due to the movement of charged particles a magnetic term appears, which is of no importance in non-relativistic theory as there are no spin-operators in the Hamiltonian, but cannot be neglected in relativistic description. Furthermore, relativistic theory does not allow to work with instantaneous interactions due to the finite speed of light. The two terms derived to take into account these two effects are known as Breit correction. It has to be noticed that Coulomb-Breit terms are not Lorentz invariant, but dealing with it is almost impossible in the molecular scenario due to the exponential scaling of this transformation.[15]

In molecular applications, one has to abandon the idea of Lorentz invariance and has to work with approximate two-body Hamiltonians. The Hamiltonian that results after applying the Dirac equation with the Coulomb-Breit terms is the so-called Dirac-Coulomb-Breit Hamiltonian. Moreover, it can be split into a spin-free part also called scalar-relativistic Hamiltonian and a spin-dependent part. This separation has the advantage that scalar relativistic effects can be easily included in the variational optimization of molecular orbitals. Therefore, this Hamiltonian is used as starting point for deriving simpler Hamiltonians more appropriate for chemical applications but a simplification is needed because the use of a spinor basis as in four-component's Dirac wave function is computationally much more demanding than the usual one-electron orbital basis.

## One- and two-electron spin-orbit operators

There are several Hamiltonians in quantum chemistry to treat the one-electron and two-electron spin-orbit coupling terms. Among them the most widely used are the Breit-Pauli Hamiltonian and the Douglas-Kroll transformed Hamiltonian.

The Breit-Pauli Spin-Orbit Hamiltonian was derived by Pauli in 1927, one year before Dirac's four component theory. It is probably the most renowned one- and two-electron spin-orbit Hamiltonian. This Hamiltonian is obtained assuming a purely Coulombic potential and that the magnetic field comes from the intrinsic spin moment of the electron as in the Dirac-Coulomb-Breit Hamiltonian but reducing it from a four-component to a two-component Hamiltonian. It deals with the spin-free, magnetic and relativistic terms at the same time. To study the spin-orbit coupling, it is only necessary to retain those two electron terms that involve direct coupling between spin and orbital angular moments. Then, orbit-orbit, spin-spin and Fermi contact terms can be neglected and scalar relativistic effects are accounted for in the spin-free Hamiltonian.[16] The two remaining terms form the Breit-Pauli spin-orbit Hamiltonian:

$$\hat{H}_{SO}^{BP} = \frac{1}{2m_e^2c^2}\sum_i\sum_I \frac{Z_I}{\hat{r}_{iI}^3}(\hat{r}_{Ii}\times\hat{p}_i)\cdot\hat{s}_i - \frac{1}{2m_e^2c^2}\sum_i\sum_{j\neq i}\frac{1}{\hat{r}_{ij}^3}(\hat{r}_{ij}\times\hat{p}_i)\cdot(\hat{s}_i+2\hat{s}_j) \tag{2.27}$$

It describes the interaction of the spin magnetic moment of electron $i$ with nuclei $I$ and the interaction among two electrons $i$ and $j$. The main limitation of this operator is that it is not bounded from below and it can collapse within the variational principle.

The Douglas-Kroll Hamiltonian can be obtained from the Dirac-Coulomb-Breit Hamiltonian by transforming the latter with properly chosen unitary operators.

$$\begin{aligned}\hat{H}^{+}_{SO} = 2c^2 \sum_i \sum_I \frac{\hat{A}_i}{\hat{E}_i + m_e c^2} \frac{Z_I}{r^3_{iI}} \times (\hat{r}_{iI} \times \hat{p}_i)\hat{s}_i \frac{\hat{A}_i}{\hat{E}_i + m_e c^2} \\ -2c^2 \sum_i \sum_{i \neq j} \frac{\hat{A}_i \hat{A} j}{\hat{E}_i + m_e c^2} \left[ \frac{1}{\hat{r}^3_{ij}} (\hat{r}_{ij} \times \hat{p}_i)(\hat{s}_i + 2\hat{s}_j) \right] \frac{\hat{A}_i \hat{A}_j}{\hat{E}_i + 2m_e c^2}\end{aligned} \tag{2.28}$$

where $\hat{E}_i$ is the relativistic kinetic energy operator $\sqrt{\hat{p}_i^2 c^2 + m_e^2 c^4}$ and $A_i$ the kinematic factor $\sqrt{\frac{\hat{E}_i + m_e c^2}{2\hat{E}_i}}$

It excludes the electron-positron pair creation and has the advantage that it is bounded from below, therefore it keeps the variational principle. In the limit $p_i \to 0$, the Douglas-Kroll and Breit-Pauli Hamiltonians coincide.

### Effective one-electron spin-orbit coupling operators

These operators only treat explicitly the one-electron Spin-Orbit Hamiltonian. In heavy atoms, the one-electron term of the spin-orbit Hamiltonian largely dominates over the two-electron part. Therefore, it is not surprising trying to avoid the explicit treatment of the computationally demanding two-electron term. Several approaches have been developed, among them, two are presented here.

The introduction of effective nuclear charges in the operator was one of the first ideas and leads to a simple and not very demanding approach to treat spin-orbit coupling. The operator is represented by a one-electron one-center operator and has almost the same form as the usual Breit-Pauli one-electron term. The difference is that instead of dealing with the nuclear charge it uses the effective nuclear charge as the 'real' nuclear charge seen by an electron because of the shielding done by all other electrons.

$$\hat{H}_{SO}^{eff} = \frac{1}{2m^2c^2} \sum_i \sum_I \frac{Z_I^{eff}}{\hat{r}_{iI}^3} \hat{l}_{I_{i_I}} \hat{s}_{i_I} \tag{2.29}$$

One of the limitations is that it only accounts for the effect of electrons belonging to orbitals centred in the same nucleus $I$. But, probably the main problem comes from the definition of the effective nuclear charge because this is not a physical observable and has to be parametrised. This approach is generally considered too simple for obtaining accurate results.

Spin-Orbit Mean-Field (SOMF) developed by Hess et al. is one of the most rigorous approaches within the effective one-electron spin-orbit operators.[17] It can use any full microscopic SOC Hamiltonian such as $\hat{H}_{SO}^{BP}$ or $\hat{H}_{SO}^{+}$ mentioned above. It treats explicitly the one-electron interaction between electron $i$ and $j$ and reduces factorially the treatment of the two-electron interaction, it only accounts for the interaction of i-k and j-k where k run overs all other orbitals and $n_k$ is the occupation number of the corresponding k orbital. The ij matrix element of this Hamiltonian is described:

$$\begin{aligned}\langle i(1)|\, \hat{H}_{SO}^{mf}\, |j(1)\rangle &= \langle i(1)|\, \hat{h}_{SO}(1)\, |j(1)\rangle \\ &+ \frac{1}{2} \sum_k n_k \Big[ \langle i(1)k(2)|\, \hat{H}_{SO}(1,2)\, |j(1)k(2)\rangle \\ &- \langle k(1)i(2)|\, \hat{H}_{SO}(1,2)\, |j(1)k(2)\rangle - \langle i(1)k(2)|\, \hat{H}_{SO}(1,2)\, |k(1)j(2)\rangle \Big]\end{aligned} \tag{2.30}$$

This method has been proven to be successful even in light elements where two-electron terms are as important as the one-electron terms, therefore it is implemented in the majority of quantum packages.

## 2.2. Time-related based methods

In this second part of the chapter, the methods employed to study time-evolution of systems are explained. Several methods have been used and are here presented in order of complexity. We have divided them in three different types. Firstly, Fermi's Golden rule, which does not treat explicitly the time, but can best be seen as the time-independent mathematical expression derived from the perturbation theory to compute intersystem-crossing or internal conversion rates. Secondly, ab initio molecular dynamics where the motion of molecules is followed in real time. At this level of theory, the electronic wave function is studied at quantum level and nuclear movement is treated classically following Newton's equations of motion. Finally, Multi-Configuration Time-Dependent Hartree (MCTDH), which treats both the nuclear and electronic motions from a quantum point of view.

### 2.2.1. Fermi's Golden rule

Understanding photophysical or photochemical processes is not possible without detailed knowledge about the electronic states involved. However this is not an easy task to deal with. In spite of its apparent simplicity, Fermi's Golden rule has been surprisingly accurate for computing ISC in several organic systems and transition metal complexes. It is derived from the second order Rayleigh-Schrödinger perturbation theory with the pure-spin Born-Oppenheimer states as zeroth order basis functions and the perturbative Hamiltonian is given by the sum of the spin-orbit coupling and nuclear kinetic operators. Neglecting the spin-vibronic terms, the decay rate from an initially to a final vibronic states is given by:

$$k_{ISC} = \frac{2\pi}{\Omega_a} \sum_{\alpha} \sum_{\beta} \sum_{k} \left| \langle \Psi_a^{\alpha}, \{\nu_{aj}\} | \hat{H}_{SO} | \Psi_b^{\beta}, \{\nu_{bk}\} \rangle \right|^2 \delta(E_{aj} - E_{bk}) \quad (2.31)$$

where a, b label electronic states, j, k vibronic levels, $\alpha$ and $\beta$ are the MS-components of the initial and final states, respectively and $\Omega_a$ is the degeneration of the initial state.

The spin-orbit coupling term can be expanded in a Taylor expansion around a reference geometry:

$$\begin{aligned}\langle \Psi_a^\alpha, \{\nu_{aj}\}|\hat{H}_{SO}|\Psi_b^\beta, \{\nu_{bk}\}\rangle &= \langle\{\nu_{aj}\}|\langle\Psi_a^\alpha|\hat{H}_{SO}|\Psi_b^\beta\rangle\{\nu_{bk}\}\rangle \\ &+ \langle\{\nu_{aj}\}|\sum_m \left.\frac{\partial\langle\Psi_a^\alpha|\hat{H}_{SO}|\Psi_b^\beta\rangle}{\partial Q_m}\right|_{q_0} Q_m\,|\{\nu_{bk}\}\rangle \\ &+ \langle\{\nu_{aj}\}|\sum_m\sum_n \left.\frac{\partial^2\langle\Psi_a^\alpha|\hat{H}_{SO}|\Psi_b^\beta\rangle}{\partial Q_m\partial Q_n}\right|_{q_0} Q_m Q_n\,|\{\nu_{bk}\}\rangle + ... \quad (2.32)\end{aligned}$$

Because only the direct spin-orbit coupling is used the single remaining term in the Taylor expansion is the first one. Within the Condon approximation, which neglects all vibronic spin-orbit interaction, the ISC rate is given by a direct product of the electronic and the vibrational part.

$$k_{ISC} = \frac{2\pi}{\Omega_a}\sum_\alpha\sum_\beta \left|\langle\Psi_a^\alpha|\hat{H}_{SO}|\Psi_b^\beta\rangle\right|^2 \times \sum_k |\langle\{\nu_{aj}\}|\{\nu_{bk}\}\rangle\,|^2\delta(E_{aj}-E_{bk}) \quad (2.33)$$

This makes that the spin-orbit and the vibrational contributions can be calculated separately. The way in which the spin-orbit term is computed has been extensively discussed in previous sections (see Sec. 2.1.3 and Sec. 2.1.4). The calculation of the vibrational overlap between initial and final states requires a mathematical description of the vibrational density of states (VDOS) at the energy of the initial state. However, instead of explicitly determining the VDOS, it is more convenient to replace the delta distribution by an appropriate expression in the energy or time regime.

In the time-independent approach, the delta function is replaced by a step function of finite width.

$$k_{ISC} = \frac{2\pi}{\eta\ \Omega_a}\sum_\alpha\sum_\beta \left|\langle\Psi_a^\alpha|\hat{H}_{SO}|\Psi_b^\beta\rangle\right|^2 \times \sum_{k|\eta|(E_{aj}-E_{bk})|} |\langle\nu_{aj}|\nu_{bk}\rangle\,|^2 \quad (2.34)$$

The vibrational part is explicitly obtained summing over Franck-Condon

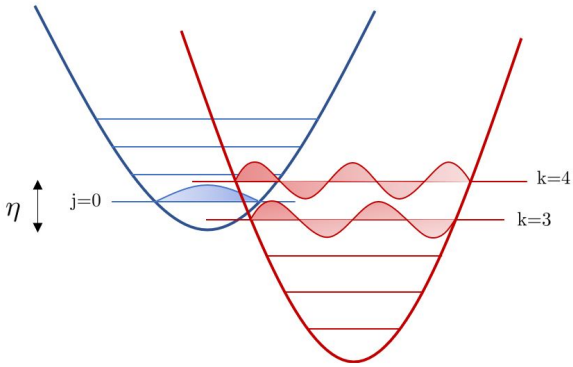


**Figure 2.1.** Schematic representation of vibrational overlap among cold vibrational initial state and vibrational states within $\eta$ in the final state.

factors of all states in the interval $\eta$ (Fig. 2.1) . The approach is simple but computationally demanding for large molecules and large energy gaps. This approach can be extended beyond the Condon approximation through the inclusion of linear spin-vibronic coupling.[18]

The time-dependent approach is based on a Fourier transformation of the delta function. Applying the Condon approximation and assuming a harmonic model for the potential energy surfaces of both states, the ISC rate can be determined by numerical integration.[19]

$$k_{ISC}^{corr} = \frac{1}{\Omega_a} \sum_{\alpha} \sum_{\beta} \left| \langle \Psi_a^{\alpha} | \hat{H}_{SO} | \Psi_b^{\beta} \rangle \right|^2 \int_{-\infty}^{\infty} dt G(t) e^{it\Delta E_{ab}^0 + (1/2)T_r\Omega_a} \quad (2.35)$$

where G(t) is a function that depends on J, D, $\Omega_a$, $\Omega_b$, S and B. Herein, J and D comes from the Duschinsky rotation and represent the normal modes of both states in the same basis and the displacement of the minimum along each normal mode, respectively (further details in Sec. 5.3.1). $\Omega_a$, $\Omega_b$, S and B are diagonal matrices with elements $(\Omega_a)_{ii} = \omega_{a_i}$, $(\Omega_b)_{ii} = \omega_{b_i}$, $S_{ii} = sinh(i\omega_{b_i}t)$ and $B_{ii} = sinh(i\omega_{b_i}t/2)$ where $\omega$ are the vibrational frequencies of each state in each normal mode.

It is much faster than the time-independent method and shows almost

the same results. Cumulant expansion and short-time approximation are two more approximate time-dependent approaches that usually converge faster to their final value.

All the approaches explained above assume vibrationally cold ($\nu$=0) initial states. It is however relatively simple to introduce the temperature in time domain. The initial electronic state has its population distributed over the accessible vibrational levels. Thermal population of higher vibrational levels is carried out assuming a Boltzmann population of vibrational states. [20]

$$k_{ISC} = \frac{2\pi}{Z\ \Omega_a} \sum_{\alpha} \sum_{\beta} \sum_{j,k} e^{-\beta E_j} \left| \langle \Psi_a \alpha, \{\nu_{aj}\} | \hat{H}_{SO} | \Psi_b^{\beta}, \{\nu_{bk}\} \rangle \right|^2 \delta(E_{aj} - E_{bk}) \tag{2.36}$$

where $Z = \sum_j e^{-\beta E_j}$ is the canonical partition function for vibrational term in the initial state and $\beta$ is the inverse temperature.

### 2.2.2. Ab Initio Molecular Dynamics

To study fast (photo-)chemical processes in more details one needs to go beyond the static or 'quasi-dynamic' description by Fermi's golden rule. Molecular dynamics methods propagate the molecular motions in real time. Obviating the purely classical techniques, where atoms are the smallest particles (i.e no explicit electrons), we shortly discuss here the Ab Initio Molecular Dynamics (AIMD) methods, which treat the electrons from a quantum perspective and the nuclei classically. We have grouped them in two different types. On the one hand, Car-Parrinello Molecular Dynamics (CPMD) computes the electron density at the beginning of the simulation and then propagates it without needing to explicitly calculate it again. On the other hand, Born-Oppenheimer Molecular Dynamics (BOMD) solves the time-independent Schrödinger equation at each time step and calculates the gradients of the energy of the electronic state under study with respect to nuclear displacements to determine the forces exerted on the nuclei by the electrons. A section for excited state dynamics

has been included in BOMD. Within CPMD, we have added Metadynamics section because we used it in CPMD formalism but Metadynamics in Born-Oppenheimer formalism is also possible.

### Car-Parrinello Molecular Dynamics (CPMD)

This method was developed in 1985 by Car and Parrinello,[21] having in mind the idea of obtaining large dynamic simulations at an accurate electronic level. As many other quantum methods CPMD uses a Lagrangian which searches minimal energy conformations.[22]

$$L_{CP} = \frac{1}{2}\sum_I M_I \dot{R}_I^2 + \frac{\mu}{2}\sum_i \left\langle \dot{\phi}_i \middle| \dot{\phi}_i \right\rangle - E(R,\{\phi\}) + \sum_{i,j}\lambda_{ij}(\langle\phi_i|\phi_j\rangle - \delta_{ij}) \tag{2.37}$$

The first and second term accounts for the kinetic energy of nuclei and electrons, respectively. The third term accounts for the Hamiltonian energy, usually the Kohn-Sham energy but in fact any electronic structure method can be used to evaluate this term. The fourth term is the constraint of orthonormality among orbitals and is introduced in the dynamics through the Lagrangian multipliers method. The electronic mass is substituted by a fictitious mass, $\mu$. It allows to enlarge the time-step in the integration (it has to be shorter than the fastest movement in the process). Moreover, it ensures the decoupling between electronic and nuclear movement. Periodic boundary conditions (PBC) are customarily used to avoid problems with boundary effects caused by finite size of the system.

From the Lagrangian and assuming a completely decoupled system among nuclei and electrons, the so-called adiabatic picture, it is simple to obtain the equations of motion for both nuclei (Eq. 2.38) and electrons (Eq. 2.39) using a classical description through the Newton's motion equations.

$$M_I \ddot{R}_I = -\frac{\partial E(R,\{\phi\})}{\partial R_I} + \sum_{i,j}\lambda_{ij}\frac{\partial}{\partial R_I}\langle\phi_i|\phi_j\rangle \tag{2.38}$$

$$\mu\ddot{\phi}_i = H(R,\{\phi\})\phi_i + \sum_j \lambda_{ij}\phi_j \tag{2.39}$$

where H(R, $\{\phi\}$) is the one-particle Hamiltonian.

Because of the decoupling among nuclei and electrons is easier to deal with plane wave basis sets rather than atom-centered basis sets.

The total energy of the system has to be kept constant during the simulation.

$$E_{tot} = \frac{1}{2}\sum_I M_I \dot{R}_I^2 - E(R,\{\phi\}) + \frac{\mu}{2}\sum_i \left\langle \dot{\phi}_i \middle| \dot{\phi}_i \right\rangle = E_{phys} + T_e \quad (2.40)$$

During the dynamics the electron cloud is considered to be "cold" and the temperature is solely determined by the kinetic energy of the nuclei. For a meaningful simulation, $T_e$ has to smoothly oscillate around a value close to zero and hence, the conservation of energy must be ensured through the first two terms. With the condition that the temperature oscillates around a predetermined value, several approaches such as rescaling of velocities, simulated annealing/heating or the use of thermostats have been tested. Among them, the last one turned out to be the most successful approach as it stays closest to physical reality and changes less aggressively the simulation parameters. The system absorbs or dissipates energy from/into the bath. Most commonly, Nosé-Hoover thermostat are used in CPMD simulations.

**Metadynamics** are able to simulate processes that take place on a larger time scale. The introduction of the CPMD algorithm largely extended the simulation time scale but, there are still a lot of processes that take place on a much longer timescale than the simulations affordable nowadays. In standard CPMD, it is almost impossible to escape from the (meta-)stable minima because they usually correspond to deep potential energy wells, which severely limits the sampling to the immediate (meta-)stable minimum surroundings. To overcome this sampling bottleneck the metadynamics technique was introduced. In this method, the sampling is facilitated by the addition of a bias potential into the Hamiltonian (Fig. 2.2). It acts on a selected number of degrees of freedom, the so-called collective variables (CV).

The bias potential can be written as a sum of Gaussians deposited in the

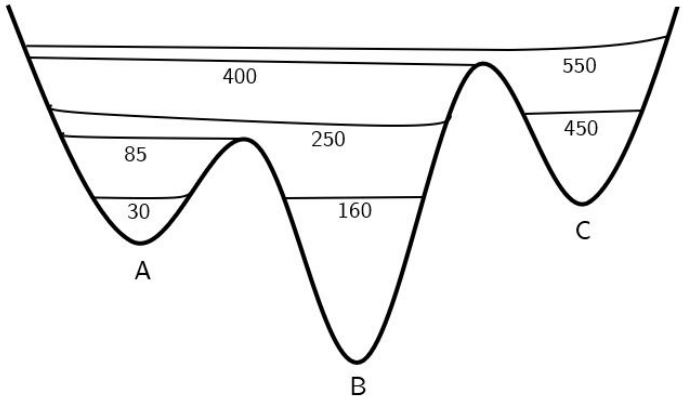


**Figure 2.2.** Schematic representation of PES along a CV and the number of Gaussians to fill the wells.

CV space during the simulation time.[23]

$$V_G(S,t) = \int_0^t dt' \omega \exp\left(-\sum_{i=1}^{d} \frac{(S_i(R) - S_i(R(t')))^2}{2\sigma_i^2}\right) \tag{2.41}$$

Herein, $\omega$ is an energy rate proportional to the height of the Gaussian, $\sigma_i$ is the width of the Gaussian for the $i^{th}$ CV, S is the geometry projection onto the collective variable space and runs over the total number of CV, d. Metadynamics not only allows to sample a larger part of the conformational space, but also provides information on the Free Energy Surface (FES) along the different CV after the subtraction of the added bias potential from the total energy.

The most critical part of the method is the way in which CV are defined. CV must contain sufficient information about the most relevant degrees of freedom of the system and the process under study. Inconsistent choices of CV can easily lead to either extremely long simulation times or (even worse) erroneous conclusions on the physics of the system. There are many ways to define the set of CVs, but typical once involve bond stretchings, bending angles, torsion dihedrals or the coordination number of an atom.

This differs from CPMD because it does not propagate the electronic wave function in time, but rather explicitly calculates it at each time step by solving the time-independent Schrödinger equation at each nuclear frame. Although it is computationally more demanding than propagating the electronic wave function in time, BOMD is a must in those regions of the conformational space where two electronic states are close in energy. Such situations are very likely to happen in photochemical processes where one deals with excited states whose populations evolve in time from one to the others.

Among the different methods to describe the dynamics of an electronically excited state molecule, trajectory surface hopping is probably the most popular one within the mixed quantum/classical family. Other methods frequently used for this purpose have an explicit quantum treatment for both nuclei and electrons such as Multi-Configuration Time-Dependent Hartree (MCTDH) which is extensively explained below or Full Multiple Spawning (FMS) where Gaussian functions evolve classically on adiabatic Potential Energy Surfaces (PESs).[24]

Trajectory Surface Hopping (TSH) is a computational technique developed to study excited state dynamics. Although TSH is grouped within BOMD because it explicitly computes the electronic wave function and gradients at each step, it is intrinsically non Born-Oppenheimer because it explores non-adiabatic regions in which switching among different electronic states is more probable. The basic idea in this technique is to start a dynamics in an excited state and evolve it in time allowing changes in the electronic state for which the forces on the nuclei are calculated, also known as surface hopping. It permits to distinguish the most probable pathways for excited state deactivation and the most populated states after averaging a sufficiently large amount of independent trajectories.

The motion of the nuclei is described as in standard classical MD dynamics by Newton's equation of motion. The gradients depends on the state dominating the simulation at that time. When a surface hop among states occurs, the gradients are computed from the new state. The time step $\Delta$t

must be shorter than the fastest process in the molecule, typically a bond stretching which occur on the femtosecond scale.

Because TSH pretends to describe sudden changes in the electronic structure upon small changes in the nuclear arrangement, it needs to go beyond the Born-Oppenheimer approximation (BOA). However, the enormous cost of solving the time-dependent Schrödinger equation without applying the BOA inspired a more pragmatic solution. The time-dependent wave function $\Phi$ is expressed as a linear combination of adiabatic time-independent Born-Oppenheimer wave functions $\Psi_n$ over all the selected states N, weighted by time-dependent complex expansion coefficients.

$$\Phi(R, r, t) = \sum_{i}^{N} c_i(t)\Psi_i(R, r) \tag{2.42}$$

$\Psi_i$(R,r) are the eigenvectors of the time-independent Schrödinger equation within the selected electronic structure method.

The expansion coefficients are set to 0 at the beginning of the simulation for all the electronic states except the initially populated state whose coefficient is set to 1. The expansion coefficients evolve in time through:

$$i\hbar\dot{c}_k = \sum_{j} c_j(V_{kj} - i\hbar \cdot \dot{R}d_{kj}) \tag{2.43}$$

The expression is derived by inserting the wave function of Eq. 2.42 in the time-dependent Schrödinger equation. $V_{kj}$ is the interaction between state k and j $\langle\Psi_k|\,\hat{H}\,|\Psi_j\rangle$, it coincides with the adiabatic energy of state j when j=k and is strictly 0 when j≠k because of the orthonormality among states; $d_{kj}$ is the non-adiabatic coupling vector $\langle\Psi_k|\nabla_R\Psi_j\rangle$ between states k and j.

There exist several algorithms to determine the hopping probability from one state to another.[25] However, the most widely used is Tully's algorithm. The original proposal, published in the early 1970s[26] was slightly modified approximately twenty years later to avoid that the system gets trapped in an ever ongoing back-and-forth hopping between two electronic

states.[27,28] This 'fewest-switches' algorithm calculates the hopping probability $g_{kj}$ between states as follows:

$$g_{kj}(t+\delta t) = max\left[0, \frac{(2\hbar^{-1}Im(c_k c_j^* V_{kj}) - 2Re(c_k c_j^* \dot{R}\cdot d_{jk}))\delta t}{c_k c_k^*}\right] \quad (2.44)$$

Tully's algorithm states that the hop is produced between state k and j when Eq. 2.45 is satisfied, where $\xi$ is a random number between 0 and 1.

$$\sum_{i}^{j-1} g_{ki} \leq \xi \leq \sum_{i}^{j} g_{ki} \quad (2.45)$$

Because the electrons move much faster than the nuclei, calculating the hopping probabilities at each time step $\Delta t$ is not sufficient. Instead a second, smaller time step $\delta t$ is introduced that interpolates the time-dependent wave function $\Phi(R, r, t)$ between $t$ and $t+\Delta t$ through the evolution of the expansion coefficients $c_n$ of the adiabatic states. The algorithm does not explicit calculate $d_{kj}$ at each time $\delta t$ (which would require solving the time-independent Schrödinger equation every smaller time step), but approximates it through a linear interpolation that connects the couplings at $t$ and $t+\Delta t$. Now, $\delta t$ can be of the order of attoseconds without significantly increasing the computational cost. Provided $\Delta t$ is not too large, this approximate time evolution of the wave function gives an optimal ratio of accuracy versus computational cost.

### 2.2.3. Multi Configurational Time-Dependent Hartree

Multi configurational time-dependent Hartree or MCTDH, as it is commonly known, is a method to study the time evolution of the nuclei as quantum particles. This time evolution is studied solving the time-dependent Schrödinger equation:

$$i\hbar\frac{\partial}{\partial t}\Psi = \hat{H}\Psi \quad (2.46)$$

where $\Psi$ is the wave function of the nuclei evolution.

MCTDH provides a description of the system taking into account the quantum nature of both electrons and nuclei. The equations of motion are derived by applying the Dirac-Frenkel variational principle, then the norm and energy are conserved, if the Hamiltonian is Hermitian and time-independent and the wave function is contained in the space of allowed variations. [29]

### Wave function

The central *ansatz* of MCTDH is to write the wave function that describes the quantum evolution of the nuclei as a Hartree product of one-particle functions. The standard method treats all the nuclei as distinguishable particles, it neglects particle exchange symmetry which removes the necessity of antisymmetrizing the Hartree product as in the N-electron wave function. Derivations for identical particles leads to MCTDHB for bosons dealing with permanents instead of Hartree products and MCTDHF for fermions using Slater determinants to represent the wave function. [30]

For a chemist more accustomed to quantum mechanics for electrons, probably the easiest way to understand the MCTDH wave function is comparing it with a many-electron wave function. The main novelty with respect to the electronic wave function is that this wave function includes a dependency with time. In an increasing level of accuracy and complexity in the electronic wave function paradigm one starts from Hartree-Fock with one determinant, then moves to Configuration Interaction (e.g. CASSCF) using a wave function with the most relevant determinants, and finally, there is the Full CI wave function, including all determinants. The corresponding ladder of nuclear wave functions of increasing complexity and accuracy, starts with time-dependent Hartree using just one Hartree product. This Hartree product can be thought of in its simplest form as a direct product of the lowest energy solution for the harmonic oscillator along each normal mode, although many other analytical functions can be used as basis function in this Hartree product. Next comes the multi-configuration time-dependent Hartree with the most relevant Hartree products and finally, the standard propagation method that includes all Hartree products.

Therefore, the nuclear MCTDH wave function paradigm may be compared with CASSCF in the electronic world.

The CASSCF wave function (Eq. 2.2) is expressed as a linear combination of Slater determinants (SD). The larger the coefficient of a particular SD, the more important its electron distribution in the electronic state of interest. A similar reasoning holds for the MCTDH wave function.

$$\Psi_{MCTDH} = \sum_{J} A_J(t)\phi_J(Q,t) \tag{2.47}$$

The coefficients $A_J(t)$ of the different Hartree products $\phi_J(Q,t)$ indicate the importance of the different vibrational levels for each mode $Q$ in the nuclear wave function. Since both the Hartree products and the coefficients are time-dependent, the wave function is not unique. To obtain singular equations of motion, additional constraints have to be imposed on the basis functions.

Following with the analogy with electronic structure calculations where each SD is formed by a set of molecular orbitals, each Hartree product in the nuclear wave function depends on a set of single-particle functions (SPFs).

$$\phi_J = \prod_{k=1}^{f} \varphi_{jk}(Q_k,t) \tag{2.48}$$

These SPFs depend linearly on a primitive basis, typically using discrete variable representations (DVRs) playing the same role as the atom-centered basis functions in the molecular orbitals but here used to represent the nuclear movement along a vibrational mode.

$$\varphi_j^{(k)}(Q_k,t) = \sum_{k=1}^{n_k} a_{kj}^{(k)}(t)\chi_j^{(k)}(Q_k) \tag{2.49}$$

Atomic orbitals are usually split in a radial and an angular part. The radial part can be represented by a Gaussian or a Slater function. Concurrently,

DVRs can be expressed using different functions, but the most popular ones are the solution to the harmonic oscillator.

$$\chi_j^{(k)} = N \cdot e^{-kQ_k^2} \cdot H_j(Q_k) \tag{2.50}$$

Herein, $H_j$ is a Hermite polynomial of degree j that corresponds to the vibrational level k of mode Q.

MCTDH shares another aspect with CASSCF. It was previously explained that the molecular orbitals in CASSCF can be optimised for one particular state in a state-specific calculation or optimised for a number of states at the same time in a state average calculation. Similar procedures exist in MCTDH when more than one electronic state is treated. Two different approaches are used to include the electronic states.

**The single-set** scheme adds one extra degree of freedom to the wave function representing the electronic state. Therefore, it uses the same average wave function for all the states and it does not need to deal with the orthogonality problem when multiple electronic states are treated independently.

$$\Psi(Q_1, Q_2, ..., \alpha, t) = \sum_{j_1=1}^{n_1} ... \sum_{j_p=1}^{n_p} \sum_{\alpha=1}^{\sigma} A_{j_1...j_p,\alpha}(t) \varphi_{j_1}^{(1)} ... \varphi_{j_p}^{(p)} |\alpha> \tag{2.51}$$

**The multi-set** approach was introduced by Fang and Guo[31] and writes one wave function for each electronic state. Despite the increased dimensionality and the orthogonality problem, the multi-set approach has been proven to be more efficient because SPFs adapt better to the different electronic states and less configurations are required to obtain similar accuracy as in a single-set approach.

$$\Psi(q_1, q_2, ..., \alpha, t) = \sum_{\alpha=1}^{\sigma} \Psi^{(\alpha)} |\alpha> \tag{2.52}$$

MCTDH can treat larger systems than the standard propagation method. However, it still scales exponentially over the number of degrees of freedom (DOF), since only the base of exponential has been reduced with respect to the standard propagation method. Combining several vibrational modes into one increases the computational efficiency, the SPFs do not only depend anymore on one single DOF but on a collection of them. However, it still has an exponential increase of the particle grid and to overcome this scaling, standard MCTDH is used to propagate SPFs in the so-called multilayer MCTDH (ML-MCTDH).

**The multilayer** version of MCTDH is a very efficient implementation for treating systems with large numbers of DOFs.[32] SPFs depend on a set of other SPFs recursively and in the first layer they depend on a set of vibrational modes.

$$\varphi_m^{1;k}(Q_k^1,t)=\sum_{j_{1k}}^{N_{1k}}...\sum_{j_{dk}}^{N_{dk}}A^{2;k}_{m;j_{1k},..,j_{dk}}(t)\cdot\chi_{j_{1k}}^{(k,1_k)}(Q_{1_k}^{2;k})\cdot....\cdot\chi_{j_{dk}}^{(k,d_k)}Q_{d_k}^{2;k}) \quad (2.53)$$

In principle, as many layers as desired can be added, only limited to the implementation on the code. Increasing the number of layers makes more expensive the top layer of SPFs, but reduces the number of SPFs to propagate, or in other words, the dimension of A-vector. ML-MCTDH does not provide improved computational efficiency in small systems, but it is really useful for systems with a large number of DOFs. A graphical tree

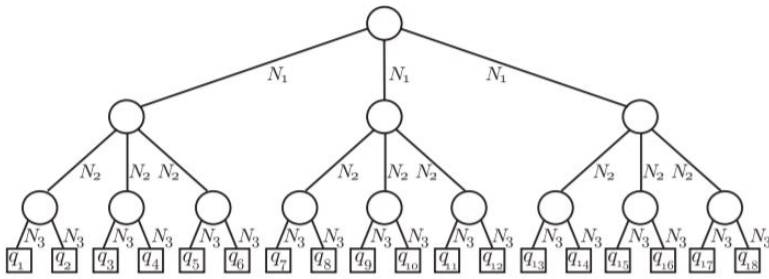


**Figure 2.3.** Graphical tree representation in ML-MCTDH. Extracted from Ref. 32.

representation (Fig. 2.3) is often used to clarify the multilayer concept, where a circle represents a set of coefficients and a square a set of time-independent primitive basis functions. Only the single-set formalism has been developed in ML-MCTDH, otherwise a tree for each electronic state would be needed which would complicate both the algorithm and the tree specification.

### The model Hamiltonian

The Hamiltonian in MCTDH is used to propagate the nuclear wave function in time using the TDSE (see Eq. 2.46). It takes a square matrix form of dimension N, where N is the number of electronic states included in the process. The Hamiltonian must be Hermitian and time-independent to fulfill the Dirac-Frenkel variational principle as mentioned above. The vibronic coupling model is frequently used in MCTDH,[33] which adopts diabatic electronic states instead of adiabatic electronic states that are eigenfunctions of the electronic Hamiltonian. Diabatic states do not show singularities in their PESs such as adiabatic ones at the conical intersections. The switching from adiabatic to a diabatic basis can be made by orthogonal transformation. In the diabatic basis, non-adiabatic couplings appear in the off-diagonal terms of the Hamiltonian.

The multi-mode Hamiltonian may be expanded in the diabatic basis in a low-order Taylor expansion.

$$\hat{H} = \left( -\sum_i \frac{\omega_i}{2} \frac{\partial^2}{\partial Q_i^2} + \sum_i \frac{\omega_i}{2} Q_i^2 \right) I + W \tag{2.54}$$

The first term corresponds to the nuclear kinetic energy operator, the second term is the harmonic potential and I is the identity matrix. W describes the changes in potential energy both in the on-diagonal and

off-diagonal terms.

$$\begin{aligned} W_{nn}(Q) &= E_n + \sum_i \kappa_i^{(n)} Q_i + \sum_{i,j} \gamma_{ij}^{(n)} Q_i Q_j + ... \\ W_{nn'}(Q) &= \sum_i \lambda_i^{(nn')} Q_i + \sum_{i,j} \mu_{ij}^{(nn')} Q_i Q_j + ...(n \neq n') \end{aligned} \tag{2.55}$$

Herein, E(n) is the electronic energy in the established center of coordinates, usually the Franck-Condon geometry, $\kappa_i^{(n)}$ is the on-diagonal linear term for state n in mode i, $\gamma_{ij}^{(n)}$ is the on-diagonal quadratic term for state n coupling modes i and j, $\lambda_i^{(nn')}$ is the off-diagonal term coupling states n and n' along mode i and $\mu_{ij}^{(nn')}$ is the off-diagonal quadratic coupling for states n and n' along modes i and j.

The expansion can be extended to higher orders either for one particular mode or for the coupling between different modes. The potentials may also take other shapes such as Morse potentials, exponentials or any other analytical function desired. In the off-diagonal terms, one frequently uses non-adiabatic couplings for states of the same multiplicity and spin-orbit coupling for states belonging to different multiplicities. A fitting is frequently used to obtain diabatic potentials and non-adiabatic couplings. In these cases the diagonalisation of the Hamiltonian within diabatic basis must end up in the previously calculated adiabatic potentials.

## 2.3. References

[1] F. Jensen, *Introduction to Computational Chemistry* (John Wiley & Sons, Inc., Hoboken, NJ, USA) (2006).

[2] C. J. Stein, and M. Reiher, *autoCAS: A Program for Fully Automated Multiconfigurational Calculations*, J. Comput. Chem. **40**, 2216–2226 (2019).

[3] A. Domingo, M. A. Carvajal, C. de Graaf, K. Sivalingam, F. Neese, and C. Angeli, *Metal-to-metal charge-transfer transitions: reliable excitation energies from ab initio calculations*, Theor. Chem. Acc. **131**, 1264 (2012).

[4] B. O. Roos, and K. Andersson, *Multiconfigurational perturbation theory with level shift — the $Cr_2$ potential revisited*, Chem. Phys. Lett. **245**, 215 – 223 (1995).

[5] C. Angeli, R. Cimiraglia, S. Evangelisti, T. Leininger, and J.-P. Malrieu, *Introduction of n-electron valence states for multireference perturbation theory*, J. Chem.Phys. **114**, 10 252–10 264 (2001).

[6] K. Pierloot, Q. M. Phung, and A. Domingo, *Spin State Energetics in First-Row Transition Metal Complexes: Contribution of (3s3p) Correlation and Its Description by Second-Order Perturbation Theory*, J. Chem. Theory Comput. **13**, 537–553 (2017).

[7] S. Vela, M. Fumanal, J. Ribas-Ariño, and V. Robert, *On the zeroth-order hamiltonian for CASPT2 calculations of spin crossover compounds*, J. Comput. Chem. **37**, 947–953 (2016).

[8] M. Kepenekian, V. Robert, and B. Le Guennic, *What zeroth-order Hamiltonian for CASPT2 adiabatic energetics of Fe(II)$N_6$ architectures?*, J. Chem. Phys. **131**, 114 702 (2009).

[9] K. Andersson, P. A. Malmqvist, B. O. Roos, A. J. Sadlej, and K. Wolinski, *Second-order perturbation theory with a CASSCF reference function*, J. Phys. Chem. **94**, 5483–5488 (1990).

[10] J. Finley, P. Åke Malmqvist, B. O. Roos, and L. Serrano-Andrés, *The multi-state CASPT2 method*, Chem. Phys. Lett. **288**, 299 – 306 (1998).

[11] T. Shiozaki, W. Győrffy, P. Celani, and H.-J. Werner, *Communication: Extended multi-state complete active space second-order perturbation theory: Energy and nuclear gradients*, J. Chem. Phys. **135**, 081 106 (2011).

[12] M. E. Casida, and M. Huix-Rotllant, *Density-Functional Methods for Excited States by Nicolas Ferré, Michael Filatov and Miquel Huix-Rotllant* (Springer International Publishing, Cham), chapter Many-Body Perturbation Theory (MBPT) and Time-Dependent Density-Functional Theory (TD-DFT): MBPT Insights About What Is Miss-

ing In, and Corrections To, the TD-DFT Adiabatic Approximation, pp. 1–60 (2016).

[13] I. Tavernelli, and B. Curchod, *TDDFT for excitation energies*, Workshop Benasque (2012), Benasque, Spain.

[14] C. Sousa, M. Llunell, A. Domingo, and C. de Graaf, *Theoretical evidence for the direct* $^3$*MLCT-HS deactivation in the light-induced spin crossover of Fe(II)-polypyridyl complexes*, Phys. Chem. Chem. Phys. **20**, 2351–2355 (2018).

[15] C. M. Marian, *Spin–orbit coupling and intersystem crossing in molecules*, Comput. Mol. Sci. **2**, 187–203 (2012).

[16] K. G. Dyall, and K. Faegri Jr, *Introduction to Relativistic Quantum Chemistry* (Oxford University Press, United States of America) (2007).

[17] B. A. Heß, C. M. Marian, U. Wahlgren, and O. Gropen, *A mean-field spin-orbit method applicable to correlated wavefunctions*, Chem. Phys. Lett. **251**, 365 – 371 (1996).

[18] J. Tatchen, N. Gilka, and C. M. Marian, *Intersystem crossing driven by vibronic spin–orbit coupling: a case study on psoralen*, Phys. Chem. Chem. Phys. **9**, 5209–5221 (2007).

[19] M. Etinski, J. Tatchen, and C. M. Marian, *Time-dependent approaches for the calculation of intersystem crossing rates*, J. Chem. Phys. **134**, 154 105 (2011).

[20] M. Etinski, V. Rai-Constapel, and C. M. Marian, *Time-dependent approach to spin-vibronic coupling: Implementation and assessment*, J. Chem. Phys. **140**, 114 104 (2014).

[21] R. Car, and M. Parrinello, *Unified Approach for Molecular Dynamics and Density-Functional Theory*, Phys. Rev. Lett. **55**, 2471–2474 (1985).

[22] J. Hutter, *Car–Parrinello molecular dynamics*, Comput. Mol. Sci. **2**, 604–612 (2012).

[23] A. Barducci, M. Bonomi, and M. Parrinello, *Metadynamics*, Comput. Mol. Sci. **1**, 826–843 (2011).

[24] L. M. Ibele, A. Nicolson, and B. F. E. Curchod, *Excited-state dynamics of molecules with classically driven trajectories and Gaussians*, Mol. Phys. **118**, e1665 199 (2020).

[25] E. Fabiano, G. Groenhof, and W. Thiel, *Approximate switching algorithms for trajectory surface hopping.*, Chem. Phys. **351**, 111–116 (2008).

[26] J. C. Tully, and R. K. Preston, *Trajectory Surface Hopping Approach to Nonadiabatic Molecular Collisions: The Reaction of $H^+$ with $D_2$*, J. Chem. Phys. **55**, 562–572 (1971).

[27] J. C. Tully, *Molecular dynamics with electronic transitions*, J. Chem. Phys. **93**, 1061–1071 (1990).

[28] S. Hammes-Schiffer, and J. C. Tully, *Proton transfer in solution: Molecular dynamics with quantum transitions*, J. Chem. Phys. **101**, 4657–4667 (1994).

[29] H.-D. Meyer, U. Manthe, and L. S. Cederbaum, *The multi-configurational time-dependent Hartree approach*, Chem. Phys. Lett. **165**, 73–78 (1990).

[30] H.-D. Meyer, *Studying molecular quantum dynamics with the multiconfiguration time-dependent Hartree method*, Comput. Mol. Sci. **2**, 351–374 (2012).

[31] J. Fang, and H. Guo, *Multiconfiguration time-dependent Hartree studies of the $CH_3I/MgO$ photodissociation dynamics*, J. Chem. Phys. **101**, 5831–5840 (1994).

[32] O. Vendrell, and H.-D. Meyer, *Multilayer multiconfiguration time-dependent Hartree method: Implementation and applications to a Henon–Heiles Hamiltonian and to pyrazine*, J. Chem. Phys. **134**, 044 135 (2011).

[33] G. A. Worth, H.-D. Meyer, H. Köppel, L. S. Cederbaum, and I. Burghardt, *Using the MCTDH wavepacket propagation method to describe multimode non-adiabatic dynamics*, Int. Rev. Phy. Chem. **27**, 569–606 (2008).

UNIVERSITAT ROVIRA I VIRGILI
BEYOND THE STATIC DESCRIPTION OF THE ELECTRONIC STRUCTURE:EXCITED STATE DYNAMICS IN TRANSITION METAL COMPLEXES AND ORGANIC COMPOUNDS
Marc Alías Rodríguez

# 3.
# High-spin state lifetime in $[Fe(bpy)_3]^{2+}$ and $[Fe(mtz)_6]^{2+}$

## 3.1. Introduction

Spin-crossover (SCO) is a molecular phenomena wherein the spin state of the system changes because of an external stimulus. The external perturbation can be of different nature such as pressure, temperature, light irradiation or the influence of a magnetic field. The magnetic state changes from a typically diamagnetic low spin state to a paramagnetic high spin state. Although the phenomena is typically appreciated in first row transition metal complexes showing $d^4$ to $d^7$ electron configurations,[1] it is also observed in some organic diradicals.[2]

Among the different transition metal complexes showing spin-crossover, Fe(II) complexes have probably been the most widely studied ones. Fe(II) shows a $d^6$ electron configuration and is usually presenting a (quasi-) octahedral coordination. In these complexes, the magnetic state varies from a diamagnetic low spin-state (S=0) to a paramagnetic high spin-state (S=2).

The magnetic bistability gives to these complexes a wide range of possibilities in different applications such as thermochromic paints, molecular switches or nanophotonic devices to name a few of them.[3] To this aim low and high spin states must show a reasonable lifetime in the working temperatures. This lifetime can vary from a few picoseconds to several hours or even days and one of the key parameters that controls the lifetime of the meta-stable states is the LS-HS adiabatic energy difference which is mainly determined by the strength of the ligand field.

Despite these singlet and quintet spin states do not couple through the effective one-electron spin-orbit operator, their coupling can be described by using explicit two-electron spin-orbit operators or through higher order interactions by means of effective Hamiltonian theory. Hence, taking into account this (effective) singlet-quintet spin-orbit coupling converts the diabatic purely singlet and quintet potential energy surfaces shown in upper part of Fig. 3.1 into a single ground state adiabatic surface where the character of the wave function changes from virtually pure singlet in point A to pure quintet in point C, and strongly mixed around point B (all the points are referred to the lower panel of Fig. 3.2) . The high-spin to

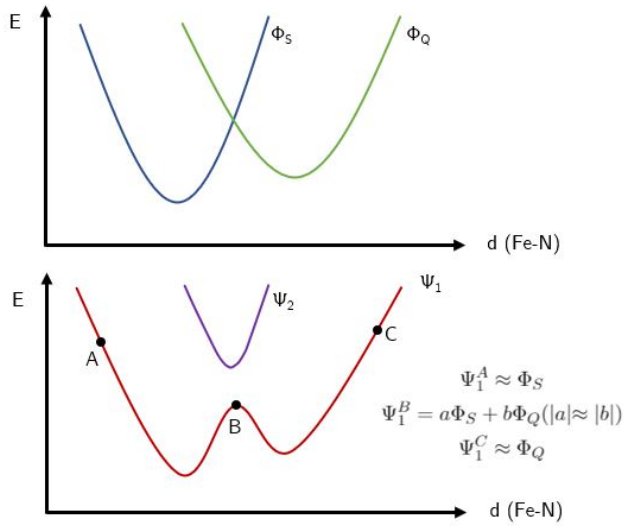


**Figure 3.1.** Schematic representation of the singlet-quintet PES along the Fe-N symmetric stretching. Energies of the spin-free states on the top and energies after the inclusion of the spin-orbit coupling on the bottom.

low-spin relaxation mechanism in these compounds with meta-stable high-spin states was ascribed mainly to tunneling processes by Hauser et al. [4] because the transition may be produced from the overlap of vibrational wave functions and does not necessarily need to reach the intersystem crossing geometry as in classical mechanics. From a quantum mechanical point of view, the rate constant for a tunneling process depends on the coupling between states and the Franck-Condon factor (i.e vibrational overlap between states).

The transition metal complexes of interest have a $FeN_6$ core structure. We consider $[Fe(bpy)_3]^{2+}$ (bpy = 2,2'bipyridine) (Fig.3.2 left) as an example of a bidentate complex with short-living high-spin state and $[Fe(mtz)_6]^{2+}$(mtz = 1-methyl-1*H*-tetrazole) (Fig.3.2 right) as a monodentate complex with extremely large high-spin state lifetimes.

Iron(II) trisbipyridine complex is considered a prototype complex in fast spin-crossover processes and has been extensively studied from experimental and theoretical perspectives. The spin-crossover is completed in less

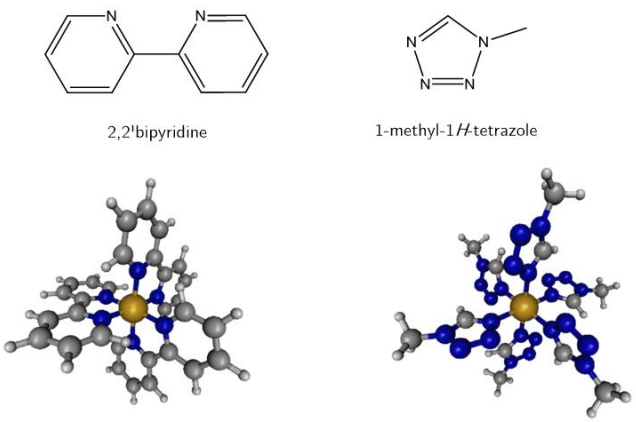


**Figure 3.2.** Two-dimensional representation of the ligands on top and three-dimensional representation of the transition metal complexes on bottom.

than 200 fs but the short lifetime of the 650 ps for the generated quintet state in aqueous solution [5] exclude this complex of applications requiring switchable magnetic properties.

Iron(II) hexamethyltetrazole presents two different Fe environments on its crystallographic structure, called site A and B. [6] Site A shows thermal spin-crossover at 78K and is found in its low-spin state below this temperature. Site B is still found in the high-spin state at 10K, the lowest temperature reached in the experiment. The main geometrical difference between both sites was determined to be the rotational angles of ligands and its influence on the spin-state energies was extensively studied by Rudavskyi et al. [7] We do not pretend to discriminate between them in this study, only study the process in nearly degenerate quintet-singlet states as happens in both sites of $[Fe(mtz)_6]^{2+}$.

The main goal of the current chapter is the study of the lifetime of the $^5T_2$ state in two different Fe(II) complexes. In order to estimate it computationally we make use of Fermi's golden rule to take into account the tunneling effect. The comparison between the two complexes will provide information about the ability of the approach based on Fermi's golden rule to give reliable estimates of the relaxation rates in relatively fast

($[Fe(bpy)_3]^{2+}$) and extremely slow ($[Fe(mtz)_6]^{2+}$) deactivations.

## 3.2. Computational details

The intersystem crossing rates have been calculated using the VIBES program[8] based on the time-dependent approach of Fermi's golden rule (as detailed in Sec. 2.2.1). The number of grid points and the spacing between them were selected upon convergence of the correlation and cumulant functions. Only in one case, we have used the time-independent approach and $\eta$ was chosen as 1000 $cm^{-1}$ after some testing of its influence. The basic ingredients for the calculations are: 1) the vibrational normal modes and frequencies of the states to account the full vibrational overlap; 2) the adiabatic electronic energy difference between the states, and 3) the module of spin-orbit among the different components of each state.

The vibrational modes and frequencies are computed after a geometry optimization for the lowest singlet (LS) and quintet (HS) states using TurboMole 6.4 package.[9] The Perdew-Becke-Ernzerhof (PBE0) hybrid functional is used in combination with the triple-$\zeta$ valence polarized Gaussian-type basis set, def2-TZVP. Two-electron integrals are approximated by the resolution of identity (RI). The hessian matrix is calculated through analytical second derivatives within the harmonic approximation. No symmetry restrictions are imposed during the optimization procedure.

Adiabatic energies of both systems are calculated at CASPT2 level from the minimum energies obtained in a relaxed scan along the Fe-N symmetric expansion mode. The geometries at each point are optimised through a restricted optimization fixing the Fe-N distances using TurboMole 6.6 package. The optimisations are carried out for the ground state at B3LYP/def2-SVP level. $C_2$ symmetry is imposed in the case of $[Fe(bpy)_3]^{2+}$ and no symmetry restrictions are applied in $[Fe(mtz)_6]^{2+}$.

CASPT2 calculations are performed using MOLCAS 8.2 and OpenMolcas 18.09, the latter is the almost identical copy of the former created after the decision of the developers to change to an open source strategy for future releases, both version will from now on be referred to as

*Molcas* for simplicity.[10] The reference wave function is a CASSCF state-averaged (SA) wave function. The active space is formed by 10 electrons distributed over 12 orbitals, three more orbitals are added to those calculations that include MLCT states. The molecular orbitals for these systems are well-established[11,12] and include two $\sigma$ orbitals mainly corresponding to a small bonding interaction between ligands and Fe, the three 3d ($t_{2g}$) orbitals of Fe, the two 3d ($e_g$) orbitals of Fe with a small anti-bonding contribution respect to the ligands, an additional set of five 4d orbitals on Fe to introduce radial electron correlation and three $\pi^*$ orbitals corresponding to the aromatic system of the ligands. Despite its apparently insignificant natural occupation numbers (<0.02), the Fe 4d orbitals are essential to describe properly the energy of states with different electron configuration.[13] The average natural orbitals for the quintet state wave function in $[Fe(bpy)_3]^{2+}$ are drawn in Fig.3.3, but the same shape is qualitatively obtained in $[Fe(mtz)_6]^{2+}$and wave functions of other states.

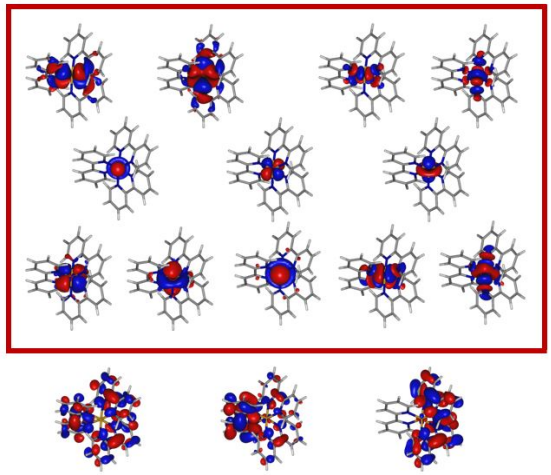

**Figure 3.3.** Active space natural orbitals in $[Fe(bpy)_3]^{2+}$ for a CAS(10,15). Two $\sigma$ orbitals in top-left, $e_g$ orbitals in the top-right, $t_{2g}$ orbitals in the second-row, Fe 4d orbitals in the third row and $\pi^*$ at the bottom. In red the MOs that are also found in a CAS(10,12).

The basis sets used were ano-rcc type with the following contractions: (7s6p5d4f3g2h) for the Fe, (4s3p1d) for N bonded with Fe, (3s2p) for C

and the other N and (2s) for H atoms. The computational cost of the two-electron integrals is reduced through the Cholesky decompostition using the default threshold of $10^{-4}$. The Douglas-Kroll-Hess Hamiltonian is used to account for the scalar relativistic effects. The perturbation theory was applied to estimate the effect of dynamic electron correlation for all electrons except the deep core ones (Fe [$1s^2...2p^6$]; C,N [$1s^2$]). The standard IPEA shift of 0.25 $E_h$ and the level shift technique with a 0.15 $E_h$ level shift are applied in the zeroth order Hamiltonian in all the calculations.

The spin-orbit coupling is calculated in the singlet-quintet intersystem-crossing geometry using Molcas.[10] The interactions are treated within the atomic mean field integrals (AMFI) approximation. The settings for CASPT2 calculations are the same as for the adiabatic energy differences. The off-diagonal spin-orbit matrix elements are calculated using the CASSCF wave functions and the CASPT2 energies are used on the diagonal. The effective spin-orbit coupling is computed using the obtained spin-orbit energies and wave functions in a home-made program.

The geometrical distortion is taken into account from different snapshots of a metadynamics simulation. We performed one simulation on the singlet and another on the quintet surface. They are carried out through the CPMD 3.15 package[14] using periodic-boundary-conditions (PBC). The system cell is a cubic box of 6859 $Å^3$. The molecule, $[Fe(bpy)_3]^{2+}$, is placed in the centre of the box together with 298 water molecules and two $Cl^-$ to preserve the charge neutrality. The core electrons are described using Troullier-Martins non-conserving pseudopotentials and valence electrons are treated using a plane waves basis set using a cut-off of 80 Ry. The coordination number defined in (Eq.3.1) has been taken as collective variable.

$$CN_i = \sum_{i \neq j}^{n_{list}} \frac{1 - (\frac{d_{ij}}{d^0})^p}{1 - (\frac{d_{ij}}{d^0})^{p+q}} \tag{3.1}$$

where $d^0$ is fixed at 2.1 Å and p and q parameters at 21. Geometries with a coordination number around 3 are taken to sample the intersystem-crossing region. Unfortunately, the description of $[Fe(mtz)_6]^{2+}$CPMD

wave function is not accurately obtained and the subsequent metadynamics could not be carried out.

## 3.3. Results and discussion

The results have been divided in four different sections. In the first part, information is given about the optimised geometry of the different electronic states. In the second, the adiabatic energies at the CASPT2 level are described. Thereafter, the (effective) spin-orbit couplings are determined, and finally, the rates from the high-spin to the low-spin state are computed and discussed using different approaches. Moreover, each section includes a subsection for each of the complexes studied.

### 3.3.1. Geometry optimizations and frequencies

The geometries are optimised using the PBE0 functional for both singlet and quintet states. Minima are confirmed through the positive second derivatives, normal modes and frequencies are also used to compute the vibration overlap. The main geometrical differences in these states are briefly commented below. No significant differences are expected in the internal ligand geometries, instead they are mainly concentrated in the $FeN_6$ core structure.

#### $[Fe(bpy)_3]^{2+}$ geometries

In the low-spin optimised geometry, the six Fe-N distances fall all in the 1.996-1.997 Å interval, showing a high symmetry. The three N-Fe-N bidentate angles are almost invariant at 80.9°. The nine interligand N-Fe-N angles slightly varies between 88.7-95.3° interval. Finally, the three N-Fe-N opposed angles are practically identical with a value of 174.6°.

In the high-spin optimised geometry, the six Fe-N distances are larger and have a small deviation, they vary from 2.190 to 2.207 Å. This can be easily rationalised because of the small Jahn-Teller effect in $t_{2g}^4 e_g^2$ electronic configuration of the Fe(II) ion. The larger distances allow to decrease the

N-Fe-N to 75.1° without increasing the electronic repulsion. The interligands N-Fe-N angle is increased to the range 91.2-98.3°, the smaller space occupied by each ligand allows a larger separation among them. Finally, the N-Fe-N opposed angles slightly change to the range 166.9-168.9°.

#### $[Fe(mtz)_6]^{2+}$ geometries

The Fe-N distances in this system are slightly larger than in the previous one because of the weaker ligand field. Moreover, the monodentate character of the ligands makes all N-Fe-N angles (virtually) equal.

In the low-spin state, the six Fe-N distances are 2.008 Å. The ligands' disposition is almost orthogonal, the N-Fe-N angles insignificantly change between 89.1-90.9° and the opposite N-Fe-N angle is 180.0. In the high-spin state geometry, the six Fe-N distances are within the range 2.214-2.219 Å and the N-Fe-N angles do not change with respect to the ones observed in the LS optimal geometry. The geometry optimization on the isolated molecular complex ends up in an unrealistic interligand dihedral angle of 45° to minimize the steric repulsion, on the contrary to the smaller experimental value observed caused by crystal packing effects. [15]

### 3.3.2. CASPT2 adiabatic energies

The adiabatic energy differences are computed from the minimum for each spin state. Calculations with smaller basis set for the Fe center and neglecting the dynamic electron correlation contribution arising for the 3s and 3p Fe orbitals were also performed. However, these computational settings did not produce accurate spin-state energy differences, as also observed by Pierloot and coworkers. [16] The geometries are obtained performing a relaxed scan for the low-spin state keeping the six Fe-N distances fixed. They are generated in the distances range from 1.9 to 2.3 Å, in steps of 0.02 Å. In the case of $[Fe(mtz)_6]^{2+}$, an additional restriction is introduced, the C-N-Fe-N interligand dihedral angle is fixed to 10° to avoid the unrealistic angle that the isolated molecular complex tends to adopt to minimize the steric repulsion, as observed above for the optimised geometries.

### $[Fe(bpy)_3]^{2+}$ energies

CASPT2 predicts an Fe-N distance of 1.92 Å for the low-spin and 2.14 Å for the high-spin state. They are about 0.05 Å shorter than the experimental ones,[17] which appears to be a general shortcoming of CASPT2 for the prediction of Fe-N distances in SCO complexes. However, this has no consequence for the energetics because the shifts are equal for both spin-states. The adiabatic energy difference is found to be 0.675 eV, in line with the experimental estimates that determined the LS-HS energy difference to be larger than 5000 $cm^{-1}$ ($\approx$ 0.620 eV).[18]

### $[Fe(mtz)_6]^{2+}$energies

The equilibrium Fe-N distance for the low-spin state of this complex is found at 1.95 Å and for the high-spin state at 2.16 Å. The slightly longer Fe-N distances in comparison to the previous complex are caused by the weaker ligand field produced by tetrazole. This is also reflected in a much smaller adiabatic energy difference found at -0.035 eV, indicating a quasi-electronic degeneracy between singlet and quintet states in the complex. Here, we recall that the experimental results for the complex suggest two different sites, one with a preference for the low-spin, the other for the high-spin state but both with very small spin-state energy differences.

## 3.3.3. Spin-orbit coupling

The Hamiltonian used to describe the spin-orbit coupling is the Douglas-Kroll-Hess Hamiltonian. This is an effective one-electron operator which is only able to account for couplings between states that differ by at most one in their respective total spin quantum number. Therefore, the lack of explicit two-electron terms makes the direct singlet-quintet coupling strictly zero. The equations for the two-electron terms are known[19] (see Sec. 2.1.4 for further details) and can in principle be implemented in standard (non-relativistic) quantum chemistry codes. However, the huge computational cost and their smallness in comparison to the one-electron terms made that none of the packages that we have checked accounts for

the explicit two-electron spin-orbit operators. Hence, we rely on the alternative procedure described in Sec. 2.1.3 and estimate the indirect coupling between the singlet and the quintet states with effective Hamiltonian theory.

The perturbation theory is not the best choice for the calculation of higher order in properties such as spin-orbit coupling because of the presence of an energy difference in the denominator and the non-Hermitian character of the Hamiltonian. However, quasi-degenerate perturbation theory is very intuitive to rationalize and decompose most of the obtained results. Herein, we use the expression at second order (QDPT2):

$$H_{ij}^{SO} = \langle \phi_i | \hat{H}^{SO} | \phi_j \rangle + \sum_{\mu \neq i,j} \frac{\langle \phi_i | \hat{H}^{SO} | \phi_\mu \rangle \langle \phi_\mu | \hat{H}^{SO} | \phi_j \rangle}{E_\mu - E_j} \tag{3.2}$$

### SOC in $[Fe(bpy)_3]^{2+}$

The effective spin-orbit coupling has first been computed at the CASPT2 intersystem-crossing geometry (Conformation ISC in Table 3.3). The $^1A_1$ and $^5T_2$ states are the spin-free selected states to be projected into the subspace and the norms of all the corresponding SOC states were higher than 0.96. Moreover, the influence of MLCT states in the effective coupling has been studied through their introduction in a larger calculation based on the CAS(10,15) wave function. To complete the picture, the effect of geometrical distortions has been examined in several snapshots taken from the metadynamics calculation around the intersystem-crossing region.

Although there are small variations, the overall results are similar in all the conformations, then for simplicity we present here the results in a small number of representative conformations (taking a few of each metadynamics simulation) and in the symmetric $D_3$ geometry.

QDPT2 allows to decompose the spin-orbit coupling as a sum over the different intermediate states. The results are summarized in Table 3.1 and clearly indicate that the most relevant intermediate state is the $^3T_{1g}$ which can be easily rationalised because it is the intermediate state closest

in energy to the singlet and quintet and has a strong direct coupling with both states.

The influence of MLCT states in the symmetric structure is also studied. The results are almost identical with and without the inclusion of MLCT states in the indirect coupling. It can be easily explained by the small $^3$MLCT-$^5T_{2g}$ spin-orbit coupling in the symmetric structure and the high relative energy of the $^3$MLCT states. This coupling increases in some distorted conformations,[20] therefore we tried to study the influence of MLCT states also in some distorted geometries. Unfortunately, we have not been able to obtain the CASSCF wave function for the MLCT states in any of these conformations (RASSCF and GASSCF methods were also tried without success). However, the MLCT states are around 20000 cm$^{-1}$ higher in energy than the $^5T_{2g}$ and $^1A_{1g}$ states in these geometries and even with relatively large $^3$MLCT-$^5T_{2g}$ couplings the influence of MLCT states on the resulting $^1A_{1g}$-$^5T_{2g}$ spin-orbit coupling is expected to be very small, contrary to the previously studied $^3$MLCT-$^5T_{2g}$ spin-orbit couplings near the LS equilibrium distance, where these two states are very close in energy.

The Table 3.1 also show that discrepancies exist between the effective Hamiltonian theory and the quasi-degenerate perturbation theory. These differences are mainly associated to two intrinsic characteristics of the perturbative method used. The first is that QDPT loses accuracy when the initial and final states have larger energy differences. Eq. 3.2 shows that the larger the difference between $E_i$ and $E_j$, the larger the difference becomes between $H_{ij}$ and $H_{ji}$. The relative similarity of the couplings with both methods in the ISC geometry where singlet and quintet are quasi degenerate in comparison with the disagreement in most of the conformations where the energy difference is larger helps to corroborate this hypothesis. The shortcoming is that in QDPT2 the interactions are expanded up to second order and only the interactions through one state are accounted here while all higher order terms are taken into account in the effective Hamiltonian.

We plot the value of the coupling against the energy difference with the intermediate spin (IS) states (Fig. 3.4). For each conformation, the graph

**Table 3.1.** Influence of the intermediate states in the singlet-quintet spin-orbit coupling. All the couplings and energies are expressed in $cm^{-1}$.

| Conf. | $\phi_\mu$ | $H_{S\mu}^{SO}$ | $H_{\mu Q}^{SO}$ | $\gamma_{S\mu Q}$ | $H_{QDPT}^{SO}$ | $H_{eff}^{SO}$ | $\Delta E$ |
|---|---|---|---|---|---|---|---|
| ISC | $^3T_{1g}$ | 528.6 | 284.2 | 20.8 | 21.8 | 32.7 | -186 |
| | $^3T_{2g}$ | 55.0 | 232.3 | 1.0 | | | |
| ISC(10,15) | $^3T_{1g}$ | 548.1 | 448.5 | 27.9 | 29.0 | 29.9 | -317 |
| | $^3T_{2g}$ | 55.8 | 247.7 | 1.0 | | | |
| | $^3MLCT$ | 24.6 | 58.1 | 0.03 | | | |
| 1a | $^3T_{1g}$ | 525.6 | 252.2 | 40.3 | 42.3 | 30.1 | 2615 |
| | $^3T_{2g}$ | 92.3 | 291.1 | 1.9 | | | |
| 2a | $^3T_{1g}$ | 516.1 | 464.0 | 32.2 | 34.4 | 28.2 | 696 |
| | $^3T_{2g}$ | 122.7 | 275.2 | 2.2 | | | |
| 1b | $^3T_{1g}$ | 523.7 | 464.5 | 19.4 | 20.6 | 43.0 | -5623 |
| | $^3T_{2g}$ | 69.7 | 294.3 | 1.1 | | | |
| 2b | $^3T_{1g}$ | 519.4 | 452.2 | 23.8 | 25.4 | 37.0 | -3168 |
| | $^3T_{2g}$ | 99.3 | 272.5 | 1.6 | | | |

$\Delta E$=$\Delta E$(HS-LS)
$\gamma_{S\mu Q}$ is the $2^{nd}$ order perturbative correction from state $\mu$.
$H_{S\mu}^{SO}$ and $H_{\mu Q}^{SO}$ are the average matrix elements $\langle\phi_S|\,\hat{H}^{SO}\,|\phi_\mu\rangle$ and $\langle\phi_\mu|\,\hat{H}^{SO}\,|\phi_Q\rangle$, respectively.
The labels a and b refers to conformations from the singlet and quintet simulations, respectively.

displays the smallest of the singlet-triplet or quintet-triplet energy difference. Both plots show that the spin-orbit coupling tends to become larger in those conformations with smaller energy difference as expected from a perturbative reasoning based on Eq. 3.2.

The results also show that all the conformations taken from the high-spin metadynamics have the quintet lower in energy than the singlet state. This can be explained from the 2.1 Å value chosen as $d^0$ parameter in the metadynamic simulations (Eq. 3.1). This value is the experimental value for the intermediate spin state minimum and most probably also very close to the real intersystem-crossing geometry, but this 2.1 Å is slightly longer than the value obtained at CASPT2 level for the Fe-N distance at which the ISC takes place. Furthermore, we have observed a slightly

larger effective-spin orbit coupling for the conformations taken from the high-spin metadynamics. This is probably for two reasons: a) the energy differences with the IS state are in general smaller, and b) the LS state is always closer to the IS than the HS state (the direct spin-orbit coupling is larger between $^1A_{1g}$-$^3T_{1g}$ than $^3T_{1g}$-$^5T_{2g}$) again using a perturbative reasoning smaller differences between IS and LS are favoured to obtain higher singlet-quintet couplings. However, the observed differences are not dramatic and the effective couplings in the different conformations do not differ by more than a factor of two.

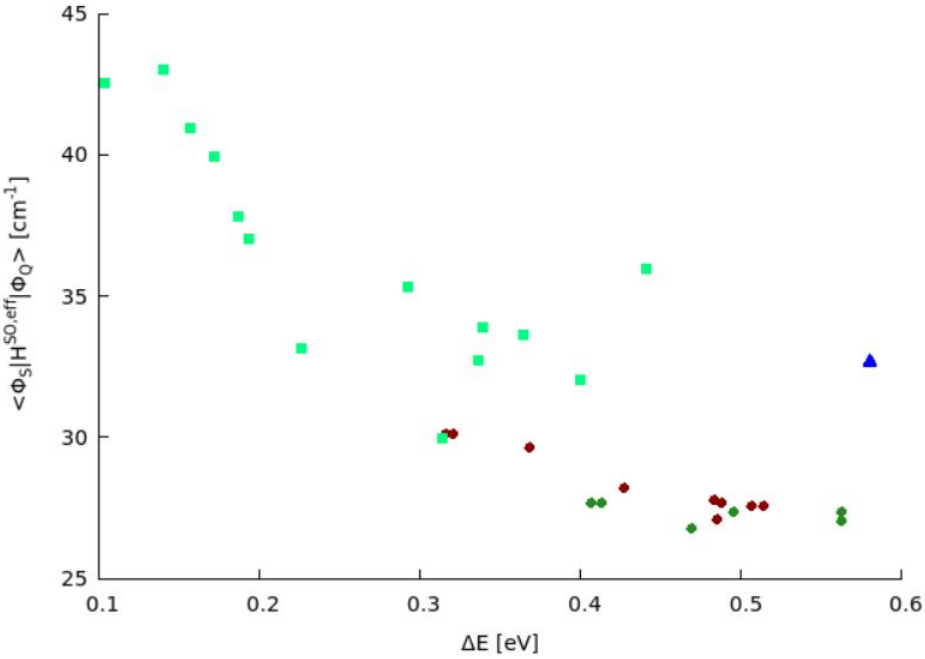


**Figure 3.4.** Effective spin-orbit coupling as function of the energy difference $E_T - E_{(S,Q)}$ between the lowest triplet state and the quintet or singlet state. $E_Q$ or $E_S$ is selected to minimize the difference. Light colors with squared marks are used for those conformations obtained from high-spin metadynamics and dark colors with circle marks for the conformations from the low-spin metadynamics. The green squares correspond to $E_T - E_S$ (singlet is higher in energy than quintet) and the red points to $E_T - E_Q$ (quintet is higher in energy). The symmetric structure is plotted as blue triangle.

The geometrical distortions modify the value of spin-orbit coupling by a factor smaller than 2 comparing the most dissimilar conformations. This indicates that the strong influence of thermal disorder in the spin-orbit observed in previous studies in the group for the (effective) spin-orbit coupling in the Franck-Condon region,[20] is mainly caused by changes affecting the MLCT states which are not playing a role here because of their very high relative energy.

### SOC in $[Fe(mtz)_6]^{2+}$

The spin-orbit coupling has been computed at the singlet-quintet ISC geometry obtained at CASPT2 level using the relaxed scan along the symmetric Fe-N expansion mode. The same set-up as in $[Fe(bpy)_3]^{2+}$ is used to obtain the effective spin-orbit coupling. The perturbative analysis (Table 3.2) also shows that the $^3T_{1g}$ state is the most relevant state because of its larger coupling and smaller energy gap in comparison to the next closest state, the $^3T_{2g}$. The difference between the perturbative theory and the effective Hamiltonian is considerably larger than expected as the singlet and quintet states are (nearly) degenerate in this geometry and seems an ideal situation for applying QDPT2. Apparently, the coupling between external states is sufficiently important to make perturbation theory not accurate enough.

**Table 3.2.** Influence of the intermediate states in the singlet-quintet spin-orbit coupling. All the couplings and energies are expressed in $cm^{-1}$.

| Conformation | $\phi_\mu$ | $H^{SO}_{S\mu}$ | $H^{SO}_{\mu Q}$ | $\gamma_{S\mu Q}$ | $H^{SO}_{QDPT}$ | $H^{SO}_{eff}$ | $\Delta E$ |
|---|---|---|---|---|---|---|---|
| ISC | $^3T_{1g}$ | 537.2 | 465.1 | 40.4 | 41.3 | 31.4 | 15 |
| | $^3T_{2g}$ | 41.0 | 259.0 | 0.9 | | | |

$\Delta E$=$\Delta E$(HS-LS)
$\gamma_{S\mu Q}$ is the $2^{nd}$ order perturbative correction from state $\mu$.
$H^{SO}_{S\mu}$ and $H^{SO}_{\mu Q}$ are the average matrix elements $\langle\phi_S|\,\hat{H}^{SO}\,|\phi_\mu\rangle$ and $\langle\phi_\mu|\,\hat{H}^{SO}\,|\phi_Q\rangle$, respectively.

Unfortunately, it has not been possible to perform metadynamics simulations for the $[Fe(mtz)_6]^{2+}$crystal. Hence, the effect of the geometrical distortions could not be studied in the system, but it is expected to be

small as in the other complex under discussion. All calculations performed so far showed that geometry distortions mostly affect the couplings that involve MLCT states and have much less effect on metal-centered states.

### 3.3.4. HS state lifetime

The intersystem-crossing rates, and therefore, the lifetimes are computed using the Condon approximation. Within this approximation, the ISC rates are computed as a direct product between the spin-orbit and the vibrational terms. The (effective) spin-orbit coupling is computed using the effective Hamiltonian theory and the vibrational overlap is computed using time-dependent and time-independent approaches. Moreover, the effect of variations in the temperature on the lifetime of the HS states is studied for $[Fe(bpy)_3]^{2+}$. This is done by using a collection of vibrational states for the initial electronic state instead of only considering the $\nu = 0$ level. The population of these initial states is determined by the Boltzmann distribution.

#### HS lifetime in $[Fe(bpy)_3]^{2+}$

The lifetime has been computed as the inverse of the direct product between the effective spin-orbit couplings in different conformations and the vibrational overlaps using time-dependent approaches at vibrationally cold states and at 300 K (Table 3.3). As vibrational states are only well-defined with respect to a minimum structure, the vibrational overlap is necessarily extracted from the optimized structures, while the spin-orbit couplings are not only for the CASPT2 intersystem-crossing geometry, but also for the distorted structures extracted from the metadynamics. The use of the Heisenberg picture transforms the calculation of the golden rule rate from a frequency domain to a time domain reaching an exact (within the model) time correlation expression. This expression is in some cases difficult to converge and an alternative expression using cumulants to approximate probability distributions was also derived for vibrationally cold states.[8] Then, the correlation and cumulant expressions are obtained for the vibrationally cold states while only the correlation expression is available for the intersystem-crossing at 300K.

**Table 3.3.** Singlet quintet effective spin-orbit coupling in $cm^{-1}$ at different conformations and its corresponding lifetime using different approaches in $[Fe(bpy)_3]^{2+}$.

| | | T = 0K | | T=300K |
|---|---|---|---|---|
| Conformation | $\langle {}^1A \vert \hat{H}^{SO,eff} \vert {}^5T_2 \rangle$ | $\tau_{corr}$ /ns | $\tau_{cum}$/ns | $\tau_{corr}$/ns |
| ISC | 32.7 | 77.9 | 14.5 | 2.14 |
| ISC (10,15) | 29.9 | 92.8 | 17.3 | 2.54 |
| 1a | 30.1 | 91.7 | 17.1 | 2.51 |
| 2a | 28.2 | 104.7 | 19.5 | 2.87 |
| 3a | 27.1 | 113.6 | 21.1 | 3.11 |
| 4a | 27.7 | 108.5 | 20.2 | 2.97 |
| 5a | 27.7 | 108.6 | 20.2 | 2.98 |
| 6a | 26.8 | 116.1 | 21.6 | 3.18 |
| 7a | 27.8 | 107.6 | 20.0 | 2.94 |
| 8a | 30.1 | 91.7 | 17.1 | 2.51 |
| 9a | 27.7 | 108.6 | 20.2 | 2.98 |
| 10a | 27.6 | 109.4 | 20.4 | 3.00 |
| Avg.[(a)] | 28.1 | 106.1 | 19.7 | 2.9 |
| 1b | 43.0 | 45.0 | 8.4 | 1.24 |
| 2b | 37.0 | 60.7 | 11.3 | 1.66 |
| 3b | 33.6 | 73.6 | 13.7 | 2.02 |
| 4b | 40.9 | 49.6 | 9.2 | 1.36 |
| 5b | 40.0 | 52.1 | 9.7 | 1.43 |
| 6b | 32.7 | 77.8 | 14.5 | 2.13 |
| 7b | 32.0 | 81.1 | 15.1 | 2.22 |
| 8b | 42.5 | 46.0 | 8.6 | 1.26 |
| 9b | 37.8 | 58.1 | 10.8 | 1.59 |
| 10b | 35.3 | 66.7 | 12.4 | 1.83 |
| Avg.[(b)] | 37.5 | 61.1 | 11.4 | 1.67 |

[(a)] Average of the ten structures extracted from the singlet metadynamics.
[(b)] Average of the ten structures extracted from the quintet metadynamics.
The labels a and b refers to conformations from the singlet and quintet simulations, respectively.

The results (Table 3.3) show sizeable differences between time correlation and cumulant functions, although both approaches give lifetimes of the same order of magnitude. They also show that the intersystem crossing at 300K is around one order of magnitude faster than in the vibrationally cold case. The average lifetimes for the distorted structures are slightly shorter in the conformations taken from the quintet metadynamics and slightly larger in those extracted from the singlet metadynamics than the calculated for the ideal structure. However, the variation is much smaller than was observed for the $^3$MLCT-$^5T_{2g}$ intersystem crossing in the Franck-Condon region. There the $^3$MLCT lifetime was found to vary by several orders of magnitude depending on the local distortions. The calculated lifetime is slightly larger than the observed experimentally ($\sim$ 600ps). One of the possible reasons for this discrepancy is the fact that the explicit two-electron spin-orbit coupling terms are not included in our calculations.

### HS lifetime in $[Fe(mtz)_6]^{2+}$

The lifetime for this complex is computed using the effective spin-orbit coupling obtained at the LS-HS intersystem crossing geometry and the vibrational overlap from different approaches. In spite of the apparent convergence of correlation and cumulant functions, the vibrational overlap using the different functions changes dramatically. The value obtained from the time correlation expression change by several orders of magnitude upon choosing a different number of grid points and time integration interval. Table 3.4 shows some of the values for the vibrational overlap, all the time intervals were larger than the time to reach convergence for the correlation function ($\sim$ 5fs).

In principle, the application of the correlation function should lead to the most exact answer, since no additional approximation are introduced to speed-up the calculation of the lifetime as is done in the cumulant approach. In all previous applications of the time-dependent Fermi's golden rule in SCO complexes,[21] we have found that both approaches predict intersystem crossing rates of the same order of magnitude, illustrating that the approximations in the cumulant approach are (in general) not severe. However, because the two lifetime estimates for the HS-LS conversion in

**Table 3.4.** ISC rates calculated with the time correlation function ($\kappa_corr$) and cumulant expression ($\kappa_cum$) as function of the time integration interval, the number of grid points and the damping factor $\eta$.

| Total interval (fs) | N. of points | $\kappa_{corr}$ ($s^{-1}$) | $\kappa_{cum}$ ($s^{-1}$) | $\eta$ ($cm^{-1}$) |
|---|---|---|---|---|
| 20 | 1024 | -0.00503 | $6.93\times10^{9}$ | 0.0 |
| 20 | 73536 | 29.1 | $8.00\times10^{9}$ | 0.0 |
| 20 | 262144 | 0.191 | $8.00\times10^{9}$ | 0.0 |
| 20 | 262144 | 0.191 | $8.00\times10^{9}$ | 10.0 |
| 20 | 1310720 | 0.731 | $8.00\times10^{9}$ | 0.0 |
| 80 | 512 | $6.93\times10^{9}$ | $6.37\times10^{9}$ | 0.0 |
| 80 | 18384 | 0.0277 | $8.00\times10^{9}$ | 0.0 |
| 80 | 73536 | -0.0239 | $8.00\times10^{9}$ | 0.0 |

$[Fe(mtz)_6]^{2+}$turn out to differ by several orders of magnitudes, we also used the Franck-Condon time-independent approach to determine which of the two is the most reliable one (Table 3.5).

**Table 3.5.** Singlet quintet effective spin-orbit coupling in $cm^{-1}$ and its lifetime using different approaches in $[Fe(mtz)_6]^{2+}$.

| Conformation | $\langle {}^1A \vert \hat{H}^{SO,eff} \vert {}^5T_2 \rangle$ | $\tau_{corr}$ | $\tau_{cum}$ | $\tau_{FC}$ |
|---|---|---|---|---|
| HS-LS cross | 31.4 | 8.9 s | 2.0 ns | $\sim$ 10 years |

As expected, the time-independent approach predicts a very long lifetime, in line with the experimental observations that the HS lives for days in this material. Therefore, we conclude that in this case the time-dependent estimate based on the correlation function is the most reliable, although for these extremely long lifetimes we cannot pretend to be correct within an order of magnitude. It is more realistic to lower the pretensions and only be able to mark this process as an extremely slow one. It seems clear that the large discrepancies between the time-independent and time-dependent (correlation) approaches come from a very small vibrational overlap and can be probably associated with numerical noise in the integration.

## 3.4. Conclusions

Fermi's golden rule is shown to be an appropriate tool to determine rates of intersystem crossing processes. This technique is able to predict the time scale of the high-spin state lifetime in the right order of magnitude for the two iron(II) complexes studied. In the Condon approximation, the vibrational and the spin-orbit terms do not interact which reduces to three the ingredients that are needed to apply the methodology: i) the adiabatic energy difference, ii) the vibrational overlap and iii) the (effective) spin-orbit coupling.

The SS-CASPT2 methodology using as reference a CASSCF wave function with 10 electrons over 12 molecular orbitals produces accurate spin-state energetics. However, the inclusion of the Fe-3s and 3p orbitals in the perturbative treatment is a must and the basis sets for iron must contain not only f, but also g and h functions to accurately describe the cusp in the wave function when two electrons approach each other. i.e. the dynamic correlation effect, which is significantly larger in the more compact LS state with six electrons in the Fe-3d($t_{2g}$) orbitals than in the HS state, where the 6 d-electrons are distributed over all five 3d orbitals.

A good description for the vibrational overlap is obtained using the Hessians, i.e frequencies and normal modes, from DFT methodology. For the fast ISC processes (in the sub-ns time scale), both time-dependent approaches (time correlation and cumulant) compute the same order of magnitude for the rate, and the inclusion of the temperature decreased by almost one order of magnitude the high-spin state lifetime showing a better agreement with the experimental value. It seems that time-dependent approaches for the study of high-spin to low-spin relaxation rates work well in relatively fast processes, even better including the temperature in the analysis by means of Boltzmann distribution. However, time-independent approaches give more accurate results in slow processes and only the correlation time-dependent expression is also producing an acceptable result.

The spin-orbit coupling between singlet and quintet states is strictly zero using the effective one-electron operators implemented in the standard (non-relativistic) quantum chemistry packages. The effective Hamiltonian theory is an elegant and efficient way to determine accurate effective SO

couplings involving other states (not only second order couplings). However, QDPT2 is more convenient to analyze the effect of the other states in the coupling. This analysis allowed us to determine that the main intermediate state coupling the singlet and the quintet is the $^3T_{1g}$ with smaller contributions of the other states. A careful inspection of the coupling in the different conformations also confirmed that there is a tendency towards larger effective spin-orbit coupling between singlet and quintet for those conformations with lower-lying triplet states. However, the direct couplings in the distorted geometries do not drastically change compared to the symmetric conformation contrary to what was observed for the $^3$MLCT-$^5T_{2g}$ coupling in the Franck-Condon geometry. The small differences between the symmetric and the distorted conformations in this case can be explained by the localized character of the $d^6$ states which do not change very much when the geometry is slightly distorted.

In the comparison between both systems, it is observed that the effective spin-orbit coupling between singlet and quintet states in $[Fe(bpy)_3]^{2+}$ and $[Fe(mtz)_6]^{2+}$ is almost identical. The difference comes from the vibrational overlap of the states because of the low- to high-spin relative energies. This is the key factor to produce these large differences in the high-spin state lifetime.

## 3.5. References

[1] J. A. Real, A. B. Gaspar, and M. C. Muñoz, *Thermal, pressure and light switchable spin-crossover materials*, Dalton Trans. **12**, 2062–2079 (2005).

[2] M. R. Geraskina, A. T. Buck, and A. H. Winter, *An Organic Spin Crossover Material in Water from a Covalently Linked Radical Dyad*, J. Org. Chem. **79**, 7723–7727 (2014).

[3] G. Molnár, L. Salmon, W. Nicolazzi, F. Terki, and A. Bousseksou, *Emerging properties and applications of spin crossover nanomaterials*, J. Mater. Chem. C **2**, 1360 (2014).

[4] A. Hauser, C. Enachescu, M. L. Daku, A. Vargas, and N. Amstutz, *Low-temperature lifetimes of metastable high-spin states in*

*spin-crossover and in low-spin iron(II) compounds: The rule and exceptions to the rule*, Coord. Chem. Rev. **250**, 1642 – 1652 (2006), 16th International Symposium on the Photochemistry and Photophysics of Coordination Compounds.

[5] A. Cannizzo, C. Milne, C. Consani, W. Gawelda, C. Bressler, F. van Mourik, and M. Chergui, *Light-induced spin crossover in Fe(II)-based complexes: The full photocycle unraveled by ultrafast optical and X-ray spectroscopies*, Coord. Chem. Rev. **254**, 2677 – 2686 (2010), 18th International Symposium on the Photochemistry and Photophysics of Coordination Compounds Sapporo, 2009.

[6] J. Kusz, H. Spiering, and P. G *X-ray structure stydy of the light-induced metastable states of the spin-crossover compound $[Fe(mtz)_6(BF_4)_2]$*, J. Appl. Cryst. **34**, 229 – 238 (2001).

[7] A. Rudavskyi, R. W. A. Havenith, R. Broer, C. de Graaf, and C. Sousa, *Explanation of the site-specific spin crossover in $[Fe(mtz)_6(BF_4)_2]$*, Dalton Trans. **42**, 14 702 (2013).

[8] M. Etinski, J. Tatchen, and C. M. Marian, *Time-dependent approaches for the calculation of intersystem crossing rates*, J. Chem. Phys. **134**, 154 105 (2011).

[9] *TURBOMOLE V6.4.2 2012, a development of University of Karlsruhe and Forschungszentrum Karlsruhe GmbH, 1989-2007, TURBOMOLE GmbH, since 2007; available from* `http://www.turbomole.com`.

[10] I. Fdez. Galván, M. Vacher, A. Alavi, C. Angeli, F. Aquilante, J. Autschbach, J. J. Bao, S. I. Bokarev, N. A. Bogdanov, R. K. Carlson, L. F. Chibotaru, J. Creutzberg, N. Dattani, M. G. Delcey, S. S. Dong, A. Dreuw, L. Freitag, L. M. Frutos, L. Gagliardi, F. Gendron, A. Giussani, L. González, G. Grell, M. Guo, C. E. Hoyer, M. Johansson, S. Keller, S. Knecht, G. Kovačević, E. Källman, G. Li Manni, M. Lundberg, Y. Ma, S. Mai, J. P. Malhado, P. A. Malmqvist, P. Marquetand, S. A. Mewes, J. Norell, M. Olivucci, M. Oppel, Q. M. Phung, K. Pierloot, F. Plasser, M. Reiher, A. M.

Sand, I. Schapiro, P. Sharma, C. J. Stein, L. K. Sørensen, D. G. Truhlar, M. Ugandi, L. Ungur, A. Valentini, S. Vancoillie, V. Veryazov, O. Weser, T. A. Wesołowski, P.-O. Widmark, S. Wouters, A. Zech, J. P. Zobel, and R. Lindh, *OpenMolcas: From Source Code to Insight*, J. Chem. Theory Comput. **15**, 5925–5964 (2019).

[11] K. Pierloot, and S. Vancoillie, *Relative energy of the high-($^5T_{2g}$) and low-($^1A_{1g}$) spin states of $[Fe(H_2O)]^{2+}$, $[Fe(NH_3)]^{2+}$ and $[Fe(bpy)_3]^{2+}$: CASPT2 versus density functional theory*, J. Chem. Phys. p. 124303.

[12] B. Ordejón, C. de Graaf, and C. Sousa, *Light-Induced Excited Spin-State Trapping in Tetrazole-Based Spin Crossover Systems*, J. Am. Chem. Soc. pp. 13 961–13 968.

[13] K. Andersson, and B. O. Roos, *Excitation energies in the nickel atom studied with the complete active space SCF method and second-order perturbation theory*, Chem. Phys. Lett. **191**, 507 – 514 (1992).

[14] *CPMD V3.15 2012, CPMD, http://www.cpmd.org/*
*Copyright IBM Corp 1990-2008, Copyright MPI für Festkörperforschung Stuttgart 1997-2001.*

[15] C. Sousa, C. de Graaf, A. Rudavskyi, and R. Broer, *Theoretical Study of the Light-Induced Spin Crossover Mechanism in $[Fe(mtz)_6]^{2+}$ and $[Fe(phen)_3]^{2+}$*, J. Phys. Chem. A **121**, 9720–9727 (2017).

[16] K. Pierloot, Q. M. Phung, and A. Domingo, *Spin State Energetics in First-Row Transition Metal Complexes: Contribution of (3s3p) Correlation and Its Description by Second-Order Perturbation Theory*, J. Chem. Theory Comput. **13**, 537–553 (2017).

[17] S. Dick, *Crystal structure of tris(2,20-bipyridine)iron(II) bis(hexafluorophosphate), $(C_{10}H_8N_2)_3Fe(PF_6)_2$*, Z. Kristallogr. New. Cryst. Struct. p. 356.

[18] A. Hauser, *Spin Crossover in Transition Metal Compounds II. Topics in Current Chemistry by P. Gütlich and H. A. Goodwin* (Springer Berlin, Heidelberg, Germany), chapter Light-Induced Spin Crossover and the High-Spin→Low-Spin Relaxation, pp. 155–198 (2004).

[19] K. G. Dyall, and K. Faegri Jr, *Introduction to Relativistic Quantum Chemistry* (Oxford University Press, United States of America) (2007).

[20] C. Sousa, M. Llunell, A. Domingo, and C. de Graaf, *Theoretical evidence for the direct $^3$MLCT-HS deactivation in the light-induced spin crossover of Fe(II)–polypyridyl complexes*, Phys. Chem. Chem. Phys. **20**, 2351–2355 (2018).

[21] C. Sousa, C. de Graaf, A. Rudavskyi, R. Broer, J. Tatchen, M. Etinski, and C. M. Marian, *Ultrafast Deactivation Mechanism of the Excited Singlet in the Light-Induced Spin Crossover of [Fe(2,2'-bipyridine)$_3$]$^{2+}$*, Chem. Eur. J. **19**, 17 541 –17 551 (2013).

# 4.
# Reverse-LIESST in $[Fe(bpy)_3]^{2+}$ and $[Fe(mtz)_6]^{2+}$

## 4.1. Introduction

Spin-crossover can be produced by external perturbations such as temperature, pressure or light irradiation. When light is the external stimulus, the process is known as light induced excited spin-state trapping or LIESST. The detailed description of this process requires the study of the role of the different excited states, their character, their critical points or the transition rates among them, and has attracted the attention from both experimental and theoretical sites.

LIESST is the photophysical process that converts a material from its low-spin state to the high-spin after light irradiation. Reverse-LIESST is the contrary process, the photoconversion is produced from the high-spin to the low-spin state. This last has been less studied but it could also be potentially interesting to enhance the magnetic bistabilty in high-spin materials.

The direct process has been largely studied in $[Fe(bpy)_3]^{2+}$ which has acquired the status of prototype complex on the field. In this compound, the process starts with the absorption of a photon that populates the $^1$MLCT states. After two intersystem crossings, a vibrationally hot high-spin state is reached in approximately 100 fs. Finally, the excited high-spin state relaxes through a vibrational cooling in the next 10 ps. Theoretical and experimental studies have been carried out to determine the first steps of the process.

Several experiments have been performed to clarify the states involved in the deactivation mechanism. The improvements in the lasts years on the time-resolved spectroscopy allowed to propose a path from their results. However, the interpretation of the results seems contradictory and the answer is still unclear.

Zhang et al. performed experiments in this prototype complex with time-resolved X-ray spectroscopy.[1] Their experiments were based on iron X-ray fluorescence after the photoionization of an Fe-1s electron. The iron 3p-1s (K$\beta$) time-resolved fluorescence was employed because happens in the sub-femtosecond time-scale and is sensitive to the iron spin multiplicity. The results suggested that the intermediate $^3$MC states were populated during the deactivation process.

Auböck et al. proposed two pump-probe transient absorption experiments.[2] One of them used a probe in the ultraviolet range and the other in the visible range. Their results suggested that the $^5T_{2g}$ state was reached after two consecutive intersystem crossing transitions in less than 50 fs. The first one occurred within the MLCT manifold and the second from the triplet MLCT to the high-spin metal-centred state, and therefore the $^3$MC states did not play a role. They also proposed that non-totally-symmetric vibrational modes, possibly high-frequency ones belonging to the bipyridine ligands, mediate the process.

The first theoretical studies, mostly based on the relative energies of the different excited states, suggested an intersystem crossing from the singlet to the triplet within the MLCT band and a subsequent intersystem crossing from the $^3$MLCT to the metal-centred high spin state.[3] The role of $^5$MLCT states was also discarded using the same energetic argument.[4] Later studies based on the Fermi's golden rule indicated that intermediate triplet metal-centred states were needed to transfer the population to the quintet states because the coupling between $^3$MLCT and $^5T_{2g}$ states was almost negligible.[5] However, the last publications, reopened the possibility of a direct deactivation from $^3$MLCT when taking into account geometrical distortions due to thermal disorder.[6]

A different theoretical perspective has been given by the Iuchi group. They developed a model Hamiltonian to describe the energy of the d-d (or MC) states generated by the diagonalization of the 210 Slater determinants arising from the Fe $3d^6$ configurations introduced on the model. They performed molecular dynamics in water at very low computational cost using their model and suggested a fast internal conversion within the triplet metal-centred manifold ($^3T_{2g} \rightarrow {}^3T_{1g}$).[7] Recently, they extended the model Hamiltonian to describe the MLCT states at the same time as the MC states with accurate potential energy surfaces and couplings at very low computational cost.[8]

The next logical theoretical step on the ultrafast deactivation for this complex is an explicit quantum dynamic study of the process. These studies have been performed in other transition metal complexes using MCTDH and TSH. Some key studies are briefly exposed in the following lines.

The intersystem-crossing to the long-lived luminiscent triplets in a protoypical Cu(I) phenantroline complex, $[Cu(dpm)_2]^+$ (dmp=2,9-dymethyl-1,10-phenantroline), was studied by Capano et al.[9] They used a fitted linear vibronic Hamiltonian from DFT/TD-DFT data in MCTDH which suggested a first rapid internal conversion from the bright $S_3$, $^1$MLCT to $S_2$ and $S_1$ states followed by a second step where the relaxation within the singlet manifold along a pseudo Jahn-Teller mode and the intersystem crossing to the triplets in the Franck-Condon region were competitive processes. In the PJT distorted geometries, singlet and triplets become nearly degenerate, therefore an efficient coupling was produced there. Thereafter, internal conversion within the triplets to reach the lowest energy state of this multiplicity takes place and the system is trapped in the $T_1$ state in a pseudo Jahn-Teller distorted geometry. Later, they used on-the-fly TSH methodology with a non-hybrid functional and the results again indicated the first internal conversion in 100 fs,[10] as in their previous studies using MCTDH.

The rhenium (I) carbonyl complexes, $[Re(X)(CO)_3(bpy)]$ (X=Cl, Br, I and bpy=2,2'-bipyridine) have been extensively studied by Daniel's group. They created a linear vibronic model Hamiltonian using the gradients and Hessians of excited states at the Franck-Condon geometry along the six main normal modes.[11] The main structural deformation in $S_1$ compared to FC geometry was the Re-X stretching because of the MLCT/XLCT mixing character of this state. This explained the increasing lifetime of the excited singlet states from the lighter (Cl) to the heavier (I) contrary to what is expected from the magnitude of the spin-orbit coupling. They performed a study including more normal modes in the model Hamiltonian from the minimum energy seam of crossing, minimum energy conical intersection and the minima for the involved states by the seam model function (SMF)/single-component artificial force induced reaction (SC-AFIR) approach and carried out a careful vibrational analysis at each critical geometry.[12] They have also studied another complex of the same family, $[Re(im)(CO)_3(phen)]$ (im=imidazole and phen=1,10-phenantroline) proving the influence of spin vibronic-coupling by switching on/off these parametres in the model Hamiltonian. Their study suggested that the intersystem crossing involved the bright state $S_2$ ($^1$MLCT) and the $T_3$ corresponding to the triplet interligand state ($^3$IL) followed by an internal

conversion to the $T_1$ with $^3$MLCT character.[13]

Falahati et al. studied the carbon monoxide photolysis and heme spin-crossover in myoglobin using wave packet quantum dynamics. They generated a fitted model Hamiltonian from CASPT2 potential energy surfaces of the 20 lowest singlet, triplet and quintet states along the main normal modes, which were selected following the largest reorganization energy criterion.[14] The results suggested a fast internal conversion from the bright $^1$Q to the $^1$MLCT state when the Fe-C(O) photolysis was also produced. The first intersystem crossing to the $^3$MLCT states happened in 76 fs and the quintet states were reached in the $^5$MLCT state in 429 fs.

Despite the important amount of studies about the light induced excited spin state trapping process, only a limited amount of studies about the reverse has been published to our knowledge. Hauser observed that both the LIESST and the reverse processes happened in an iron (II) complex with only high-energy MLCT states, $Fe(ptz)_6(BF_4)_2$ (ptz=1-propyltetrazole) and he also studied the influence of a solid dilution using the system $Zn_{1-x}Fe_x(ptz)_6(BF_4)_2$.[15] Few decades later, Marino et al. studied the LIESST and the reverse processes for this complex using time-resolved optical pump/probe spectroscopy.[16] They suggested that the reverse process happened in two sequential steps. The first one from the absorbing $^5E_g$ to a $^3T_{1g}$ state in 1.7ps and a second step from this triplet to the singlet ground state in 39 ps. The study also showed that the quantum efficiency for the reverse process was 0.1 at 10K clearly lower than the 0.8 efficiency observed for the direct process at the same temperature.

The aim of this chapter is to elucidate the deactivation path for the reverse-LIESST process in two prototype iron (II) complexes, $[Fe(bpy)_3]^{2+}$ and $[Fe(mtz)_6]^{2+}$ (Fig. 3.2). The latter has high-energy MLCT states because of its weak ligand field strength and low $\pi$ conjugation on the ligands but this is not the case for the bipyridine complex. This excludes the MLCT states as absorbing states in the reverse LIESST. In fact, in experimental studies of this compound the $^5E_g$ was populated. The stronger ligand field and the larger $\pi$ conjugation of $[Fe(bpy)_3]^{2+}$ significantly lowers its $^5$MLCT states and can in principle be reached by light in the UV-Vis part of the spectrum. However, to simplify the comparison of the two compounds, we also assume an initial population transfer to the $^5E_g$ states to

activate the reverse-LIESST. Two different methodologies have been performed to elucidate the mechanism. The first is the Fermi's golden rule approach which has been used in the group to clarify the LIESST mechanism for different Fe(III) and Ru(II) complexes,[17,18] besides the Fe(II) complexes studied in this chapter and $[Fe(phen)_3]^{2+}$.[5,6,19] The methodology was also employed to determine the $^3$MLCT states lifetime in a set of iron(II) complexes with ligand modifications such as $[Fe(bpy)(CN)_4]^{2-}$.[20] The second methodology is the wave packet quantum dynamics using MCTDH through a model Hamiltonian obtained by the fitting of the CASPT2 potential energy surfaces along the main normal modes.

## 4.2. Computational details

In this section, we will mention the set up for the calculations in each of the two different methodologies used. First, we will comment the details for the Fermi's golden rule method in a brief manner because the general approach has been already explained in the previous chapter. In the second part, the procedure for performing the wave packet quantum dynamics calculations is explained.

In the first approach, we compute the rates for the possible intersystem-crossing transitions in the overall mechanism by means of the time-dependent Fermi's golden rule through the VIBES program.[21] Herein, the three basic requirements for this methodology are the adiabatic energy differences, the vibrational overlaps and the (effective) spin-orbit couplings.

The adiabatic energy differences are determined at CASPT2 level through a bidimensional scan. The restricted optimizations are performed using TurboMole 6.4 package[22] with the set up explained in Sec. 3.2, but without the symmetry restrictions. In the scan, instead of keeping equal the six Fe-N distances at each geometry, we distinguish two types of Fe-N bonds: four in the equatorial plane and two perpendicular to this plane in axial position. This allows to reduce the $FeN_6$ core symmetry from $O_h$ to $D_{4h}$ which is important because most of the states playing a role in this process have an unpaired number of electrons in the $e_g$ orbitals and gain stability breaking the octahedral symmetry, as consequence of the Jahn-Teller effect. The CASPT2 calculations are carried out with

OpenMolcas[23] using the basis set, the 10 electrons distributed over 12 molecular orbitals active space and the rest of set up detailed in Sec. 3.2.

The vibrational overlap is determined by the Hessians, frequencies and normal modes of the states obtained at DFT level with TurboMole 6.4. The spin-orbit coupling is determined with OpenMolcas by means of the effective Hamiltonian theory using the CASSCF direct spin-orbit couplings in the off-diagonal and the CASPT2 energies in the on-diagonal terms. Further details about both calculations are found in Sec. 3.2.

The thermal disorder is taken into account by (randomly) selecting several snapshots of a high-spin state dynamics. This is performed through the CPMD 3.15 package[24] using periodic-boundary-conditions (PBC). The system cell and the basis set are the same as those used in the previous chapter.

The wave packet quantum dynamic simulations are performed using the Multi-Layer Multi-Configuration Time Dependent Hartree (ML-MCTDH) method implemented in the 8.5.11 version of the Heidelberg package updated in 2019.[25] The simulation was performed for 1.5 ps and included 15 electronic states (4 singlets, 6 triplets and 5 quintets) and 33 vibrational normal modes. A four-layer representation of the wave function was employed, where the vibrations were grouped by type and pseudo-symmetry (Table 4.7) for defining the branches and mode combination. In the first layer, four main groups of vibrations were used (low-frequency ligand modes, Fe-N core modes, mid-frequency ligand modes and high-frequency ligand modes). We included 3 single particle functions (SPFs) for each of the branches and each mode was represented by 61 primitive basis functions or discrete variable representations (DVRs), which are the eigenfunctions of the harmonic oscillator, and the same number of grid points (see Fig. A.2 in Appendix A for further details). The initial conditions were established to represent the conformational space in the vicinity of the $^5T_{2g}$ CASPT2 minimum.

The on-diagonal terms of the model Hamiltonian are obtained through a fitting procedure from the CASPT2 adiabatic energies along the main normal modes. These energies are calculated using *Molcas* with the same active space, basis sets and general set-up detailed in Sec. 3.2. The direct

spin-orbit couplings at Franck-Condon geometry were introduced in the off-diagonal terms of the model Hamiltonian.

## 4.3. Results and discussion

Herein, we present the obtained results in two sections, one for each methodology employed. In the first section we briefly comment the main details for obtaining the rates of Fermi's golden rule and will discuss them trying to distinguish a dominant path. The construction of the model Hamiltonian and the results obtained with it using wave packet quantum dynamics by means of MCTDH are detailed next.

### 4.3.1. Fermi's golden rule

The intersystem crossing rates computed using the Fermi's golden rule, as previously mentioned, need three main ingredients: the adiabatic energy differences, the vibrational overlap between states and the (effective) spin-orbit coupling. The results for the lasts two are rapidly mentioned in the next lines while the adiabatic energy results are more accurately detailed because of the relative novelty of the procedure employed. The last section shows the rates for each pair of states and the discussion of the overall mechanism.

The vibrational overlap between the different electronic states is obtained from the normal modes, frequencies and Hessian at the optimised geometry of each excited state. The optimizations have been performed at DFT level and show the expected pronounced Jahn-Teller effect for those states dominated by electronic configurations with unpaired electrons in the $e_g$ orbitals (for its most representative Slater determinant). The optimization of $^3T_{2g}$ state is (almost) impossible because of root-flipping with the high-lying components of $^3T_{1g}$, but the parallel character of the curves for these states along the Fe-N symmetric stretching brings us to think that the $^3T_{2g}$ minimum has to be similar than the $^3T_{1g}$ one. Therefore, we consider for the first the optimised geometry and vibrational normal modes obtained for the latter. We also use the geometries and normal modes for the quintet and singlet states described in the previous chapter.

The optimised geometry for the $^3T_{1g}$ state in $[Fe(bpy)_3]^{2+}$ shows a marked asymmetry. There are two Fe-N distances between 2.001-2.008 Å, two in the range 2.151-2.154 Å and the others two fall in the interval 2.215-2.221 Å. The N-Fe-N angles vary in the range 74.5-79.1° significantly smaller than in the singlet ground state because of the enlargement of the Fe-N distances. The nine N-Fe-N interligand angles are in the interval 87.5-97.6° and the three opposed N-Fe-N angles slightly change in the range 170.5-173.5°. The minimum for the $^5E_g$ state is found in a geometry where two Fe-N distances are 2.138 Å, two fall in the interval 2.287-2.290 Å and the other two are in the range 2.413-2.418 Å. The three bidentate N-Fe-N angles vary from 68.1 to 75.0°, exhibiting shorter values than in the optimised triplet geometry because of the larger average Fe-N distances. The nine interligand N-Fe-N angles fall in the interval 92.1-97.1° and the opposite angles in the range 160.5-167.0°. The analysis of these geometrical parameters indicates that both states show a pronounced Jahn-Teller effect.

In $[Fe(mtz)_6]^{2+}$, the optimised geometry for the $^3T_{1g}$ state also shows that there are three pairs of Fe-N distances. The two shortest distances are in the range 1.991-1.992 Å, the two intermediate fall in the interval 2.149-1.150 Å and the two largest 2.225-2.226 Å. Being a complex with monodentate ligands, it does not comes as a surprise that all 15 N-Fe-N angles are almost equivalent and only show small variations in the range 88.9-91.3°. The three N-Fe-N opposite angles have the same value of 179.9°. The $^5E_g$ optimised geometry displays the two shortest Fe-N distances in the range 2.143-2.144 Å, the two intermediate in the interval 2.332-2.334 Å and the two largest at 2.415-2.456 Å. This state, as the others of the complex, shows a small variation on the different N-Fe-N angles which fall in the range 89.3-92.2° and the opposite N-Fe-N angles that are found in the interval 178.2-179.5°. The pronounced Jahn-Teller effect is also observed for these states in this prototype complex.

The spin-orbit coupling needed for the calculation of the intersystem-crossing rates is again determined by means of the effective Hamiltonian theory after the calculation of the direct couplings using the DKH effective one-electron Hamiltonian. It is computed at the CASPT2 quasi-equilibrium geometry for the high-spin state and in the case of $[Fe(bpy)_3]^{2+}$ also in several conformations taken from the high-spin dynamic simula-

**Table 4.1.** Effective spin-orbit coupling in $cm^{-1}$ between the main pair of states involved in the first ISC, the symmetric geometry and some thermal distorted geometries taken from the HS dynamics are used for $[Fe(bpy)_3]^{2+}$ and the symmetric one for $[Fe(mtz)_6]^{2+}$.

| System | Conformation | $^5E_g$-$^3T_{1g}$ | $^5E_g$-$^3T_{2g}$ | $^5E_g$-$^1A_{1g}$ |
|---|---|---|---|---|
| $[Fe(bpy)_3]^{2+}$ | $D_3$ (HS min.) | 17.4 | 109.7 | 2.9 |
| | 1 | 16.3 | 118.8 | 0.8 |
| | 2 | 13.4 | 111.9 | 1.2 |
| | 3 | 25.1 | 118.7 | 0.7 |
| | 4 | 17.2 | 109.8 | 1.5 |
| | 5 | 24.4 | 114.9 | 1.0 |
| $[Fe(mtz)_6]^{2+}$ | $D_3$ (HS min.) | 9.2 | 116.4 | 1.2 |

tion. Unfortunately, it has not been possible to run the dynamics for the $[Fe(mtz)_6]^{2+}$ as detailed in the previous chapter, but the same tendencies about thermal disorder as in the other complex are expected.

Tables 4.1 and 4.2 show the effective spin-orbit coupling in the high-spin CASPT2 quasi-equilibrium geometry and, in the case of $[Fe(bpy)_3]^{2+}$, also in some of the CPMD conformations. Table 4.1 shows the couplings between the states that can play a role in the first intersystem-crossing. The couplings in the symmetric geometries for the different systems are almost identical only with a very small variations, the effective spin-orbit coupling between $^5E_g$ and $^3T_{2g}$ is slightly larger in $[Fe(mtz)_6]^{2+}$ while the other two couplings are slightly larger for $[Fe(bpy)_3]^{2+}$. These couplings seem to indicate a preference for the $^5E_g$-$^3T_{2g}$ transition over the other possibilities. The role of the thermal distortions is almost negligible and the differences, despite being small, are mainly associated to the number of states included in the subspace of the effective Hamiltonian.

In $[Fe(bpy)_3]^{2+}$, the Fe-N distances in the conformations from the HS dynamics are slightly larger than in the CASPT2 quasi-equilibrium geometry. This causes the quasi degeneration of, not only $^1A_{1g}$ and $^3T_{1g}$, but also with the $^3T_{2g}$ states in some of these conformations. Then, to achieve acceptable norms (>0.96) for the wave functions using the effective Hamiltonian theory, the inclusion of $^3T_{2g}$ states in the small subspace

**Table 4.2.** Effective spin-orbit coupling in $cm^{-1}$ between the main pair of states involved in the second ISC, the symmetrical geometry and some thermal distorted geometries taken from the HS dynamics are used for $[Fe(bpy)_3]^{2+}$ and the symmetric one for $[Fe(mtz)_6]^{2+}$.

| System | Conf. | $^3T_{1g}$-$^1A_{1g}$ | $^3T_{1g}$-$^5T_{2g}$ | $^3T_{2g}$-$^1A_{1g}$ | $^3T_{2g}$-$^5T_{2g}$ |
|---|---|---|---|---|---|
| $[Fe(bpy)_3]^{2+}$ | $D_3$ | 512.6 | 475.3 | 112.8 | 301.1 |
| | 1 | 502.4 | 470.1 | 113.0 | 287.0 |
| | 2 | 519.1 | 476.0 | 51.9 | 287.5 |
| | 3 | 509.7 | 463.1 | 96.0 | 292.0 |
| | 4 | 512.4 | 475.1 | 107.3 | 295.9 |
| | 5 | 512.8 | 472.9 | 73.0 | 446.4 |
| $[Fe(mtz)_6]^{2+}$ | $D_3$ | 528.5 | 482.4 | 12.1 | 285.1 |

at these conformations is needed. This ends up in a slightly smaller couplings, specially for the $^5E_g$-$^1A_{1g}$ coupling because the direct coupling is strictly zero and the coupling via other states will be reduced because of the lower number of states outside the subspace. These small details do not cause an important variation in the effective spin-orbit coupling which are similar in the symmetric geometry and the distorted conformations. Then, in the next sections the rates will be discussed only considering the effective spin-orbit coupling found at the CASPT2 quasi-equilibrium geometry for simplicity.

Table 4.2 shows the couplings between the pairs of states in the second intersystem-crossing of the process. The effective spin-orbit coupling for both systems in the symmetric structure is almost identical except for the $^3T_{2g}$-$^1A_{1g}$ coupling, which differ by an order of magnitude in the two complexes. Table 4.2 also shows very small discrepancies between the couplings at the symmetric structure and at different conformations, being the largest discrepancies about a factor of two but never changing the order of magnitude of the coupling. However, the $^3T_{2g}$ state is not necessarily the only intermediate, relaxation can also occur through the $^3T_{1g}$ state. The couplings to the singlet and the quintet state are very similar from this state.

### Adiabatic energy differences

The energy differences are computed through a scan at CASPT2 level using the DFT (B3LYP/def2-SVP) partially optimised structures. We have used the bidimensional approach to take into account the Jahn-Teller effect at CASPT2 level of accuracy for the involved states. The bidimensional calculations are performed distinguishing two different types of Fe-N distances: the axial and the equatorial. Both distances vary in the range 1.90-2.42 Å generating geometries each 0.04 Å. The diagonal of the matrix contains the energies along the symmetric stretching mode which are used in Fig. 4.1 to rationalize the possible deactivation paths for this process.

**$[Fe(bpy)_3]^{2+}$.** Figure 4.1 shows the adiabatic energies of the electronic states along the Fe-N symmetric stretching mode. It is possible observing this picture account for the possible deactivation paths involving states accessible from an energetic point of view. The excitation to the $^5E_g$ state happens from the HS state minimum region, then four different deactivation paths are available which are:

a) $^5E \rightarrow {}^3T_2 \rightarrow {}^3T_1 \rightarrow {}^1A_1$ ($^5T_2$)

b) $^5E \rightarrow {}^3T_2 \rightarrow {}^1A_1$ ($^5T_2$)

c) $^5E \rightarrow {}^3T_1 \rightarrow {}^1A_1$ ($^5T_2$)

d) $^5E \rightarrow {}^1A_1$

The overall mechanism is proposed from the data obtained for the rates of these transitions, where we consider both the possibility to relax to the singlet ground state or come back to the quintet state. The calculations of the adiabatic energy difference do not only consider the symmetric expansion, but also accounts for the axial-equatorial (ax-eq) symmetry breaking. Table 4.3 shows the adiabatic energy difference obtained using the stretching symmetric expansion and introducing the ax-eq asymmetry. The results clearly indicate that the asymmetry effect is pronounced in those states with unpaired electrons in the $e_g$ orbitals ($^5E_g$, $^3T_{1g}$, $^3T_{2g}$) because of the strong Jahn-Teller effect. The stabilization in these states

**Table 4.3.** Relative energies [eV] and distances of the CASPT2 quasi-equilibrium geometries [Å] in $[Fe(bpy)_3]^{2+}$ for each state along the Fe-N symmetric expansion mode and the asymmetric expansion distinguishing between the axial and the equatorial Fe-N distances.

| State | Symmetric | | Asymmetric | | |
|---|---|---|---|---|---|
| | d(Fe-N) | E | $d(Fe-N)_{eq}$ | $d(Fe-N)_{ax}$ | E |
| $^1A_{1g}$ | 1.94 | 0.000 | 1.94 | 1.94 | 0.000 |
| $^3T_{1g}$ | 2.04 | 1.248 | 1.98 | 2.14 | 1.108 |
| $^3T_{2g}$ | 2.04 | 1.761 | 1.98 | 2.18 | 1.593 |
| $^5T_{2g}$ | 2.14 | 0.675 | 2.14 | 2.14 | 0.675 |
| $^5E_g$ | 2.22 | 2.173 | 2.30 | 2.10 | 1.952 |

ranges from 0.15 to 0.22 eV and significant differences between the axial and equatorial Fe-N distances, of around 0.2 Å, are also observed.

**$[Fe(mtz)_6]^{2+}$.** The accessible states from the $^5E_g$ state, when initially populated at the HS state minimum energy are the same as in the previous complex. The $^5E_g$ and the $^3T_{2g}$ states are nearly degenerate at this region and one is above the other with small geometrical distortions, then in principle, we still keep the possibility of the $^3T_{2g}$ population. The ligand field strength in this complex is lower than in $[Fe(bpy)_3]^{2+}$ and this causes a smaller relative energy for the high and intermediate spin states as shown in Figure 4.2. The differences in relative energies are, as expected, causing larger differences for the $^5E_g$, $^3T_{1g}$ and $^3T_{2g}$ states when the axial-equatorial asymmetry is included (Table 4.4). Energy relaxation and geometrical distortions caused by the Jahn-Teller effect are of the same order of magnitude as found in the previous one.

### Intersystem-crossing rates

The rates for the conversion between states are computed using the time-dependent approach of Fermi's golden rule. Table 4.5 shows the intersystem-crossing rates for the different transitions using both the time-correlation and cumulant approaches and the adiabatic energies computed at CASPT2

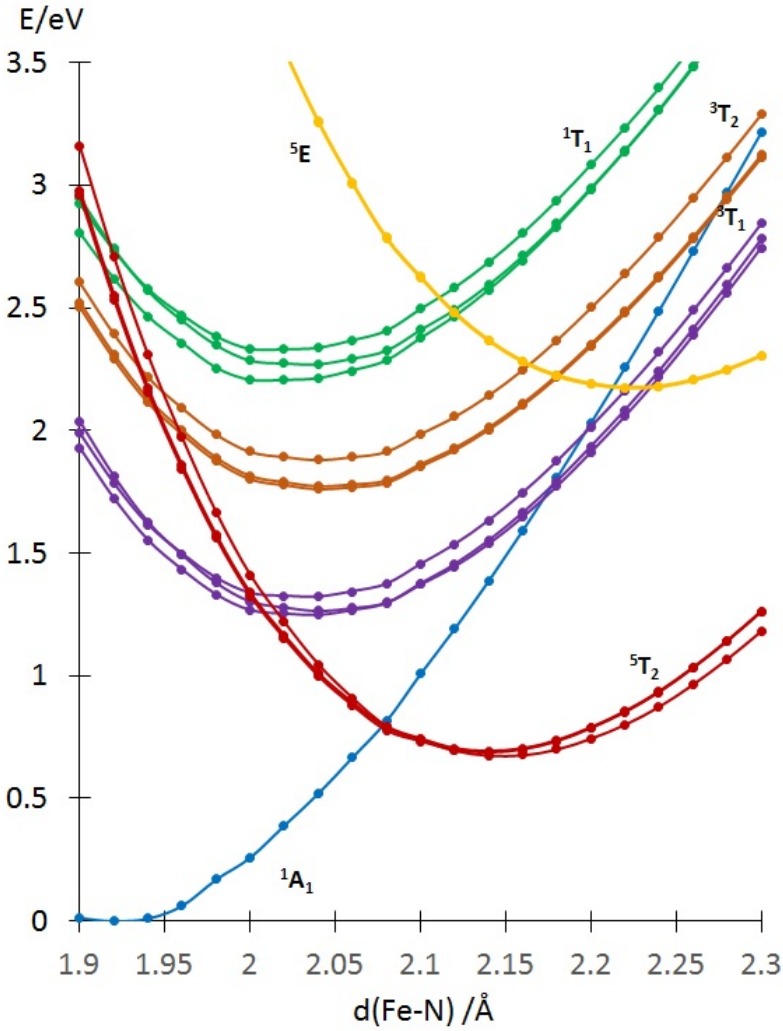


**Figure 4.1.** CAS(10,12)/PT2 potential energy surface along the Fe-N symmetric stretching mode for the lowest states in $[Fe(bpy)_3]^{2+}$. The closed-shell singlet, $^1A_{1g}$ is represented in blue, the intermediate $^3T_{1g}$ states in purple, $^3T_{2g}$ in brown, $^1T_{1g}$ in green and $^5E_g$ in yellow.

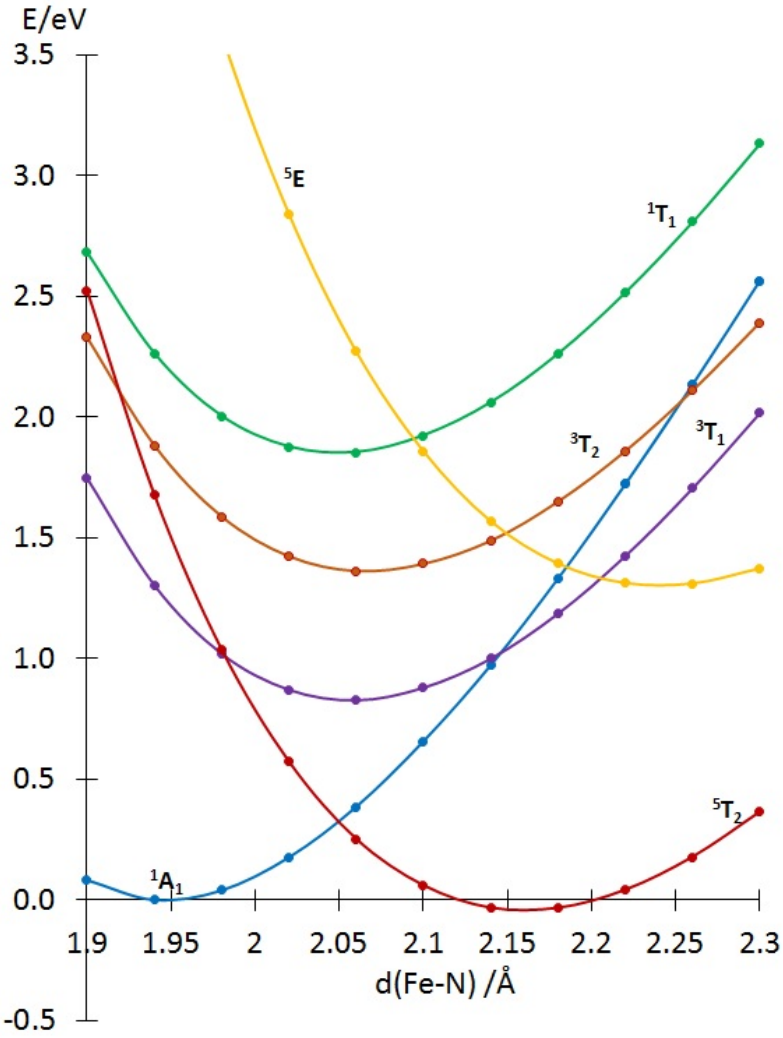


**Figure 4.2.** CAS(10,12)/PT2 potential energy surface along the Fe-N symmetric stretching mode for the lowest states in $[Fe(mtz)_6]^{2+}$. The closed-shell singlet, $^1A_{1g}$ is represented in blue, the intermediate $^3T_{1g}$ states in purple, $^3T_{2g}$ in brown, $^1T_{1g}$ in green and $^5E_g$ in yellow. Only the lowest state of each type is shown in the figure.

**Table 4.4.** Relative energies [eV] and distances of the CASPT2 quasi-equilibrium geometries [Å] in $[Fe(mtz)_6]^{2+}$ for each state along the Fe-N symmetric expansion mode and the asymmetric expansion distinguishing between the axial and the equatorial Fe-N distances.

| State | Symmetric | | Asymmetric | | |
|---|---|---|---|---|---|
| | d(Fe-N) | E | $d(Fe-N)_{eq}$ | $d(Fe-N)_{ax}$ | E |
| $^1A_{1g}$ | 1.94 | 0.000 | 1.94 | 1.94 | 0.000 |
| $^3T_{1g}$ | 2.06 | 0.808 | 2.10 | 1.94 | 0.747 |
| $^3T_{2g}$ | 2.06 | 1.363 | 2.02 | 2.18 | 1.236 |
| $^5T_{2g}$ | 2.18 | -0.035 | 2.18 | 2.14 | -0.048 |
| $^5E_g$ | 2.26 | 1.311 | 2.14 | 2.46 | 1.102 |

level using the bidimensional scan taking into account the ax-eq symmetry breaking and the symmetric Fe-N expansion mode. The differences between the results using the adiabatic energy differences from the mono and bidimensional scans are small, being typically within one order of magnitude of difference. However, Table 4.5 shows again the enormous dissimilitudes between the cumulant and correlation expressions, being more dramatic the differences that are found in the case of $[Fe(mtz)_6]^{2+}$.

As we have discussed in the previous chapter, the correlation expression is in principle more accurate than the cumulant. Taking as valid the rates obtained with the correlation expression, the process takes two intersystem-crossings for $[Fe(bpy)_3]^{2+}$. The first involves a transition from the $^5E_g$ state to the intermediate $^3T_{1g}$ in 268 ns (Table 4.5). Then, a second ISC from the intermediate spin state to the singlet ground state or back to the quintet state is produced at femtosecond time scale. The rates seem to indicate that the conversion to the quintet is preferred, in accordance with the low quantum yield experimentally observed in this process for other iron(II) complexes.[16] However, they differ by five orders of magnitude with the ones observed experimentally for $[Fe(ptz)_6]^{2+}$ and indicates that the relaxation time from the excited quintet state, $^5E_g$, is slower than thermal relaxation of the quintet ground state $^5T_2$ which seems in principle counterintuitive.

The results for the rates in $[Fe(mtz)_6]^{2+}$ (Table 4.5) show a first intersys-

**Table 4.5.** Rates (lifetimes) of the possible intersystem crossings in the reverse-LIESST process. The values in parenthesis are the values computed using the symmetric expansion approach to compute the CASPT2 adiabatic energies.

| $\phi_i$ | $\phi_f$ | $[Fe(bpy)_3]^{2+}$ | | $[Fe(mtz)_6]^{2+}$ | |
|---|---|---|---|---|---|
| | | $\tau_{corr}$ | $\tau_{cum}$ | $\tau_{corr}$ | $\tau_{cum}$ |
| $^5E_g$ | $^3T_{1g}$ | 283(63) ns | 17(8) ns | 4(1008) ms | 3.1(2.9) ns |
| $^5E_g$ | $^3T_{2g}$ | 8(6) ms | 148(70) ns | -[a] | -[a] |
| $^5E_g$ | $^1A_{1g}$ | 45(3.3) $\mu$s | 5.4(1.0) $\mu$s | 53(931) ms | 4.1(2.4) $\mu$s |
| $^3T_{1g}$ | $^1A_{1g}$ | 257(752) fs | 264(859) fs | 328(350) fs | 1.16(1.15) ps |
| $^3T_{1g}$ | $^5T_{2g}$ | 30(18) fs | 32(19) fs | 1.85(1.97) ps | 6.55(6.48) ps |
| $^3T_{2g}$ | $^1A_{1g}$ | 26.3(1.2) ns | 33.2(1.7) ns | -[b] | -[b] |
| $^3T_{2g}$ | $^5T_{2g}$ | 228(770) fs | 227(851) fs | -[b] | -[b] |

[a] The rate can not be computed because the final state is more stable than the initial state.
[b] The rates are not computed because the initial state can not be populated within this approach.

tem crossing from the $^5E_g$ to the $^3T_1$ state in 4 ms followed by a faster second intersystem crossing from the latter to the $^5T_{2g}$ or the $^1A_{1g}$. These rates show even more differences with the experimental results[16] than in the previous complex and the differences in the ISC rates between the two expressions are completely meaningless.

This seems to indicate that Fermi's golden rule, which assumes that the processes happens after reaching the equilibrium, is not the most appropriate method to study the photodeactivation of ultrafast non-equilibrium processes. These lasts relax following the gradients of the excited states and typically transfer population when crossing with other surfaces without the necessity to reach a minimum. Moreover, this method is not able to distinguish between different quantum yields from the LIESST and the reverse processes, because it computes the rates from the equilibrium geometries.

These reasons bring us to explore new methodologies treating the problem with a more accurate approach, including time explicitly. For this, we have carried out wave packet quantum dynamic simulations using the Multi-

Configuration Time-Dependent Hartree (MCTDH) methodology.

### 4.3.2. MCTDH

This method needs the creation of a model Hamiltonian to propagate the nuclear wave function. The model Hamiltonian is generated through a fitting procedure using the energies along the normal modes obtained at CASPT2 level. This process only considers metal centered states, therefore the active space used is formed by 10 electrons distributed over 12 molecular orbitals. The first problem to be solved in this procedure is the definition and selection of the main normal modes. We make use of the normal modes obtained in the optimization of the ground state at PBE0 level and we have followed two strategies to select which are the main normal modes involved in the process.

The first criterion to select the normal modes has been the geometry difference between the states involved in the process. After aligning the optimized geometry of state A and B (being A and B electronic states involved in the process) the geometry difference is projected onto the ground state normal modes basis following the expression:

$$G_A = G_B + L_0\lambda \tag{4.1a}$$

$$L_0^{-1}(G_A - G_B) = \lambda \tag{4.1b}$$

$$\lambda_k = \sum_l L_{kl}^0(G_{Al} - G_{Bl}) \tag{4.1c}$$

Herein, $\lambda$ is the vector that contains all the geometrical differences between states A and B in the basis of ground state normal modes. $G_A$ and $G_B$ are the Cartesian geometries for states A and B, respectively and $L_0$ is the L matrix of the ground state which contains the 3N-6 vibrational normal modes.

A home made Python program creates geometries along the vibrational normal modes following the Eq. 4.1a. The coordinates are expressed in mass-frequency-weighted Cartesian (MWFC) coordinates. This program is also able to project the difference between two Cartesian geometries into the basis of a given state normal modes as expressed in Eq. 4.1c. The

**Table 4.6.** Ground state normal modes with largest geometrical differences between the states involved in the process. The low-frequency modes are represented in green, the mid-frequency in blue, the high-frequency in violet and the modes localized in the Fe-N core in red.

| | $^1A_{1g}$ | $^3T_{1g}$ | $^5T_{2g}$ | $^5E_g$ |
|---|---|---|---|---|
| $^1A_{1g}$ | - | 19, 20, 21, 11, 27, 24 | 19, 18, 27, 34, 60, 99 | 19, 18, 21, 27, 10, 34 |
| $^3T_{1g}$ | | - | 19, 20, 18, 11, 27, 21 | 19, 21, 18, 10, 20, 23 |
| $^5T_{2g}$ | | | - | 21, 10, 19, 18, 23, 9 |
| $^5E_g$ | | | | - |

largest components of $\lambda$ vector, in absolute value, correspond to those modes containing the largest geometrical differences between both states and consequently the largest gradients are expected to be found along these normal modes. Table 4.6 shows the normal modes with largest differences for $[Fe(bpy)_3]^{2+}$.

This criterion is very useful to recognize the modes that are expected to be rapidly activated because of their large gradients. However, this selection does not always include the modes responsible for the (pseudo-)Jahn-Teller effect for the high-symmetry states. The modes may not contribute much to the overall geometry distortion but still be very important in the initial stages of the deactivation to open otherwise closed channels. An important example is the double cone potential of the electronic states of E symmetry along the vibrational e modes ($E \bigotimes e$), popularly known as the *Mexican hat* distortion. To include these fundamentally important normal modes in the model Hamiltonian, we performed calculations at a lower computational cost (PBE0/def2-svp) to detect them by ocular inspection. Table 4.7 shows all the normal modes included in the model Hamiltonian and also assigns the type of vibrations and their symmetry. The assignment of the type and symmetry of normal modes has been performed by combination of a careful observation of our computed modes and frequencies

**Table 4.7.** Irreducible representation of the $D_3$ symmetry group and character of the vibrational modes included in the wave packet dynamics simulation.

| Normal mode | Type of mode | Symmetry of the mode |
|---|---|---|
| 7, 8 | ligands wagging bending | e |
| 9 | ligands wagging bending | $a_1$ |
| 10, 11 | ligands twisting bending | e |
| 18 | ligands rocking bending | $a_1$ |
| 19 | Fe-N symmetric stretching | $a_1$ |
| 20, 21 | Fe-N asymmetric stretching | e |
| 23, 24 | C-H ligands out-of-plane | e |
| 25, 26 | N-Fe-N bidentate bending | e |
| 27 | N-Fe-N bidentate bending | $a_1$ |
| 30 | ligands rocking bending | $a_1$ |
| 32, 33 | Fe-N asymmetric stretching | e |
| 34 | Fe-N asymmetric stretching | $a_2$ |
| 44, 45 | ligands rocking bending | e |
| 46, 47 | ligands scissoring bending | e |
| 48 | ligands scissoring bending | $a_1$ |
| 53, 54 | ligands in-plane stretching | e |
| 58, 59 | ligands in plane-stretching | e |
| 60 | ligands in plane-stretching | $a_1$ |
| 95, 96 | ligands in plane-stretching | e |
| 97, 98 | ligands in plane-stretching | e |
| 99 | ligands in plane-stretching | $a_1$ |

together with the study performed by Alexander et al. where an explicit $D_3$ symmetry restriction was imposed to label the modes.[26] The irreducible representations within the $D_3$ point group of symmetry are $a_1$, $a_2$ and e which have been the labels used to assign the modes.

The fitting of these states has been performed through a Python program[27]. Because the outcome of the fitting procedures depend on the initial guess, one first has to generate proper quasi-diabatic curves. The quasi-diabatization in some cases can be done by maximum overlap of the CI coefficients, but in our case of nearly degenerate 3d orbitals ($d_{xy}$,

$d_{xz}$ and $d_{yz}$ are strictly degenerate within the $O_h$ point group symmetry) makes it unavoidable that not only the CI coefficients have to be followed but also the orbital expansion coefficients in order to keep track of the different (at some point of the potential energy surface nearly degenerate) electronic states. To follow the diabatic character of the states in two geometries the (approximate) overlap was calculated between two states following the expressions:

$$\left\langle \Psi^A \middle| \Psi^B \right\rangle = \sum_i \sum_j c_i^A c_j^B \left\langle \Phi_i^A \middle| \Phi_j^B \right\rangle \tag{4.2a}$$

$$\Phi^A = |\phi_1 \phi_2 \dots \phi_N| \qquad \Phi^B = |\psi_1 \psi_2 \dots \psi_N| \tag{4.2b}$$

$$\langle \Phi^A | \Phi^B \rangle = \sum_{i,j}^{N} \langle \phi_i | \psi_j \rangle = \mathcal{S} \tag{4.2c}$$

$$\mathcal{S} = \mathcal{U} \lambda \mathcal{V} \tag{4.2d}$$

$$\widetilde{\phi}_i = \sum_j \phi_j U_{ji} \qquad \widetilde{\psi}_i = \sum_j \psi_j V_{ji} \tag{4.2e}$$

$$\langle \Phi^A | \Phi^B \rangle = \prod_i^N \lambda_i \tag{4.2f}$$

Herein $\Psi$ represents the electronic wave function for the states A and B. $\Phi^A$ and $\Phi^B$ are Slater determinants of the corresponding states. The molecular orbitals of the active space for each pair of determinants are transformed to corresponding orbitals. The corresponding orbital transformation searches for two sets of orbitals such that each orbital in $\Phi^A$ has one and only one corresponding orbital in $\Phi^B$. In other words, each orbital in A has a partner in B that is as similar as possible and orthogonal to all the others. Then, the overlap between pairs of Slater determinants is expressed as a direct product between pairs instead of a matrix. This procedure is performed for the active orbitals and the inactive set of orbitals is assumed equal for both states and then their overlap as one.

Following the different electronic states based on the calculation of the overlap at two subsequent points on the potential energy surface has been

successful for the quintet states, but did not give the desired results along some of the vibrational modes for the triplets and singlets in regions of the potential energy surface showing nearly degenerate states. Although we have not been able to univocally clarify the origin of this failure, the most obvious explanation is that otherwise non-interacting components of the $^{1,3}T_{1g,2g}$ states become mixed due to small (numeric) symmetry breaking. Because this mixing occurs in an uncontrollable manner, it becomes impossible to follow the different components of such a state by overlap with the states on the preceding geometry. In these cases, the quasi-diabatic surfaces were constructed manually through comparison with the quintet surfaces.

Once the calculated energies were assigned to the different quasi-diabatic states, the surfaces of each multiplicity were fitted employing a first and second order Taylor expansion in $Q_i$. Third and fourth order expansion were also included when the quadratic fitting was not accurate enough. The fitting procedure was performed self-consistently until reaching an error $<$0.01 eV for each mode. This defines the diagonal terms of the Hamiltonian which take the form of Taylor polynomia with the coefficients obtained from the fitting extended with the nuclear kinetic operator. Next, the non-adiabatic couplings were not introduced in the model Hamiltonian. In the off-diagonal terms, the spin-orbit coupling at the Franck-Condon geometry was introduced. The variations in the spin-orbit coupling along the normal modes (i.e vibronic spin-orbit couplings) were not described in this approximate model Hamiltonian, because these vibronic couplings are proved to be almost negligible among MC states in similar iron(II) complexes.[28]

Then, the overall model Hamiltonian is formed approximately for 2200 parameters and can be expressed as follows.

$$H = \begin{pmatrix} E_S^{(j)} & H_{ST}^{(j,k)} & 0 \\ H_{ST}^{(j,k)} & E_T^{(k)} & H_{TQ}^{(k,l)} \\ 0 & H_{TQ}^{(k,l)} & E_Q^{(l)} \end{pmatrix} + \sum_i^{N_{vib,list}} \left( -\frac{\omega_{i,0}}{2} \frac{\partial^2}{\partial Q_i^2} \right) \begin{pmatrix} 1 & 0 & 0 \\ 0 & 1 & 0 \\ 0 & 0 & 1 \end{pmatrix} + \begin{pmatrix} \lambda_i^{(j)} & 0 & 0 \\ 0 & \lambda_i^{(k)} & 0 \\ 0 & 0 & \lambda_i^{(l)} \end{pmatrix} Q_i + \begin{pmatrix} \kappa_i^{(j)} & 0 & 0 \\ 0 & \kappa_i^{(k)} & 0 \\ 0 & 0 & \kappa_i^{(l)} \end{pmatrix} Q_i^2 + \begin{pmatrix} \gamma_i^{(j)} & 0 & 0 \\ 0 & \gamma_i^{(k)} & 0 \\ 0 & 0 & \gamma_i^{(l)} \end{pmatrix} Q_i^3 + \begin{pmatrix} \delta_i^{(j)} & 0 & 0 \\ 0 & \delta_i^{(k)} & 0 \\ 0 & 0 & \delta_i^{(l)} \end{pmatrix} Q_i^4 \quad (4.3)$$

Herein, the 3 by 3 matrices are in fact a 15 by 15 matrices formed by the singlet, triplet and quintet matrices with dimensions 4 by 4, 6 by 6 and 5 by 5, respectively where j runs over all the singlets, k over the triples and l the quintets. $\lambda_i^{(j,k,l)}$ is the linear expansion coefficient for state j, k or l along mode i, $\kappa_i^{(j,k,l)}$ is the quadratic expansion coefficient, $\gamma_i^{(j,k,l)}$ is the cubic expansion coefficient and $\delta_i^{(j,k,l)}$ is the quartic coefficient.

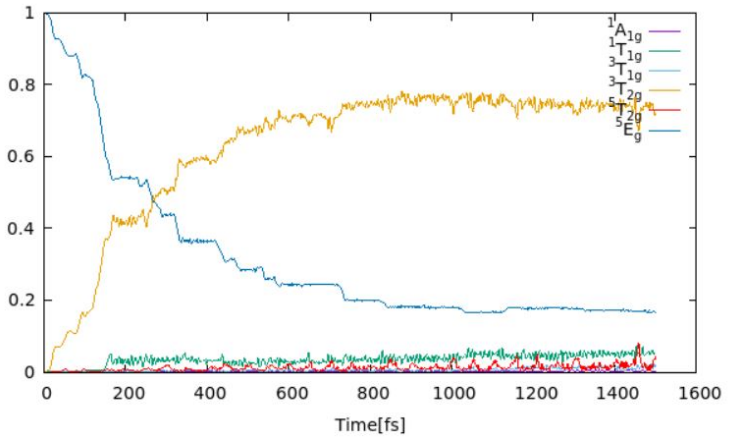


**Figure 4.3.** Time evolution of the diabatic states population during 1.5 ps simulation started in the $^5E_g$ state.

The results of the simulation (Fig. 4.3) show a first intersystem crossing from $^5E_g$ to $^3T_{2g}$ largely taking place in the first 400 fs. From there on, the population of the $^5E_g$ state continues its decay at a slower rate and the population of the $^3T_{2g}$ remains almost constant in time. Figure 4.3 also shows small oscillations in the population of other diabatic states, but it is complicated to identify a tendency for them. We have performed simulations starting from the two different components of the $^5E_g$ but the results are nearly identical and only one of them is presented here for simplicity.

We have also performed the dynamics using a larger nuclear wave function with the inclusion of more SPFs for each of the nodes (see Fig. A.3 in Appendix A). The results are displayed in Figure 4.4 and shows the same tendencies observed previously (Fig. 4.3) although small, but significant differences were detected. Figure 4.4 shows that the population of the intermediate state $^3T_{2g}$ reaches a maximum at 685 fs and then starts to decrease slowly with an almost 2% of population loss between 700 to 1500 fs which in an exponential fitting gives a lifetime of 24 ps to this intermediate state. Moreover, the population remaining in the initial state is lower when the larger nuclear wave function is employed. In addition, a considerable population of the $^5T_{2g}$ is found ($\approx$ 10% at 1.5 ps) compared with the 2% found in the $^1A_{1g}$ which is in good agreement with the low quantum yield for the reverse-LIESST process experimentally observed.

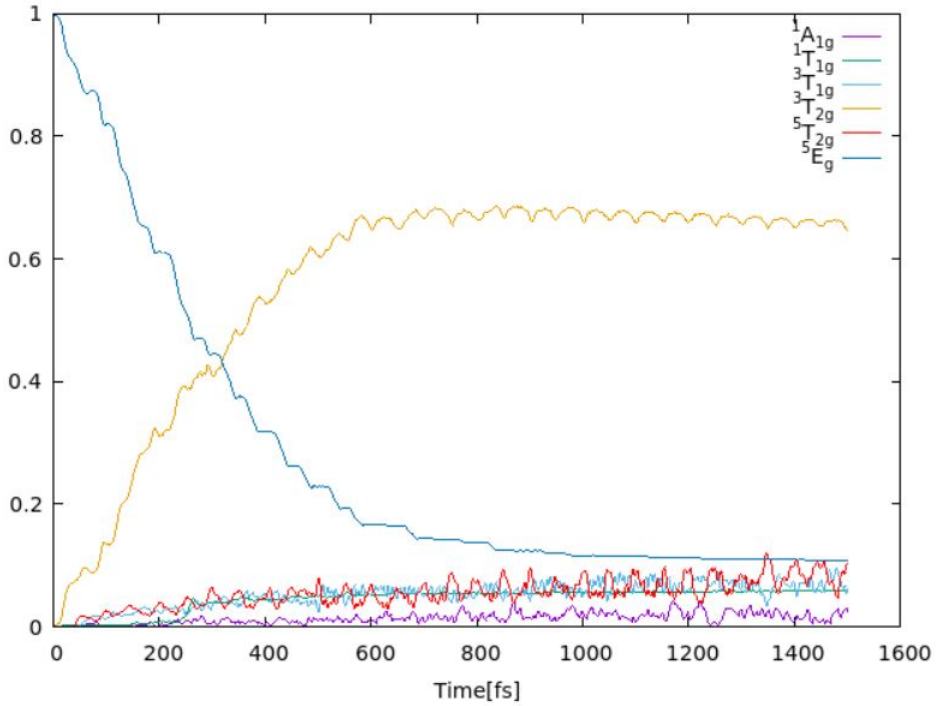


**Figure 4.4.** Time evolution of the diabatic states population during 1.5 ps simulation started in the $^5E_g$ state using the large nuclear wave function.

## 4.4. Conclusions

Fermi's golden rule has been proved to be not the most adequate method to describe ultrafast processes such as the reverse-LIESST in two iron (II) complexes. The correlation and cumulant expressions of the time-dependent Fermi's golden rule differ by not less than a few orders of magnitude. The first major conclusion of this chapter is the evidence provided that this method is not sufficiently accurate to be generally applicable for all ultrafast deactivation processes. It is, however, very practical for slower processes where the equilibrium geometry of the intermediate states is reached or for ultrafast decays when the equilibrium geometries of the excited state populated by the absorption process is located in the Franck-Condon region. The latter scenario happens to be the case for the first

intersystem crossing in the LIESST process of $[Fe(bpy)_3]^{2+}$, explaining the accurate estimates obtained with Fermi's golden rule in previous studies of this molecule. Alternatively, MCTDH is a more appropriate method for describing ultrafast decays and has given accurate results for the study of the reverse-LIESST process in $[Fe(bpy)_3]^{2+}$.

The first transition in the reverse-LIESST process of $[Fe(bpy)_3]^{2+}$ involves the $^5E_g$ and the $^3T_{2g}$ states and the lifetime of the former is about 350 fs. The second step in the process is an intersystem crossing from these intermediate states to the low-spin state or a re-population of the lowest high-spin state. Our calculations suggest that the dominant transition is the re-population of the $^5T_{2g}$ state from the intermediate state in approximately 24 ps. The MCTDH results for this complex point in the same direction as those experimentally found for the propyl-tetrazole iron (II) complex, therefore no significant differences are expected for the MCTDH results for the two iron (II) complexes studied in this project, although we have, unfortunately, not been able to setup the MCTDH calculations for the $[Fe(mtz)_6]^{2+}$ complex due to a lack of time.

## 4.5. Future perspectives

The plans in the near future are to generate a similar model Hamiltonian for the other complex, $[Fe(mtz)_6]^{2+}$. This complex is similar to the propyl-tetrazole complex whose reverse-LIESST process has been studied from an experimental perspective. The results for the metyhyltetrazole complex would allow to univocally rationalize the effect of the gap among states in the deactivation process when compared with the results of the bipyridine complex. Moreover, the effect of the vibronic spin-orbit coupling, despite expected to be small from the results of thermal disorder, needs to be explicitly studied by its introduction in the model Hamiltonian.

Despite reverse-LIESST being quite interesting, the LIESST has been more extensively studied from both experimental and theoretical perspectives. The lack of time has not allowed us to create a model Hamiltonian for the LIESST process which is expected to be more complex than the one for the reverse-LIESST for the importance of the non-adiabatic couplings defining the $^1$MLCT-$^1T_{1g}$ or the $^3$MLCT-$^3T_{1g}$ transitions. However, we

have done some steps in the process of constructing a model Hamiltonian that deserve to be mentioned.

First, we have dedicated a huge amount of effort to compute the CASPT2 potential energy surfaces along the main modes for the MC and MLCT states. The active space used in Ref. 5 adding three ligand $\pi^*$ orbitals to the CAS(10,12) was shown in Ref. 6 to be impossible to maintain for geometries that are not strictly symmetric. The minimal active space to accurately represent the relevant MC and the lowest MLCT states is formed by 10 electrons distributed over 13 orbitals, which is only adding one ligand-$\pi^*$ orbital. This was the active space used to generate the reference wave function for the SS-CASPT2 calculations to be used to generate the potential energy surfaces, but several problems associated with the methodology appeared:

1) It turns out to be difficult (if not impossible) to keep the selected active space orbitals in some of the geometries visited during the scan of the potential energy surfaces. Distortions of the geometry, specially the Fe-N distance enlargement, often cause the loss of the $\pi^*$ orbital being replaced with orbitals that account for the dynamic correlation on the metal instead.

2) A huge amount of singlets and triplets have to be included in the state average CASSCF wave function to guarantee the presence of the low-lying singlet and triplet MLCT states among the solutions of the self-consistent field procedure. This is mainly for two reasons: i. The normal modes are taken from a PBE0 ground state optimization whose equilibrium Fe-N distance is almost 0.1 Å larger than the quasi-equilibrium geometry at CASPT2 level (1.99 to 1.92 Å). The DFT Franck-Condon geometry is much closer to the CASPT2 $^{1,3}$MC minima than to the CASPT2 ground state and MLCT quasi-equilibrium geometries. Larger distances lead to lower ligand field, and hence, favour states with higher occupations of the $e_g$ orbitals because of their Fe-N antibonding character. This has the immediate consequence that the MC states are strongly stabilized while the MLCT states (with no electrons in the $e_g$ orbitals) are pushed up in energy, mostly because of the weaker hole-particle Coulomb interaction and for the triplet MLCT states one can also point at the reduced interatomic exchange interaction, which decays rapidly with increasing distance. Thus,

taking the PBE0 optimized geometry as reference point, there are many singlet and triplet MC states with lower CASPT2 energy than the MLCT states, not only the well-known $^1T_{1g}$ and $^3T_{1g,2g}$ states, but also the $^1T_{2}g$ state and even many singlets and triplets arising from double excitations compared with the singlet closed-shell determinant. ii. The CASPT2 energy correction is much larger for the MLCT states than for the MC states. Although a somewhat larger dynamic correlation cannot be excluded, the largest part of the larger stabilization of the MLCT must be ascribed to orbital relaxation effects. The need to perform state average CASSCF calculations with a large number of roots, most of them of MC character, lead unavoidably to a bias in the orbital optimization towards the Fe-$3d^6$ configuration, and a poorer description of the Fe-$3d^5L^1$ MLCT states, which only represent a small fraction of the state average. CASPT2 will partially repair this bias towards the MC states when determining the second-order energy correction of the MLCT states through the perturbative estimate of the singles with respect to the CAS wave function and lower the MLCT more than MC states for which the orbitals are much closer to optimal.

3) The typical problem with the SS-CASPT2 method.[29] The crossings among states at CASSCF and CASPT2 level occure at different geometries. This not only generates unphysical singularities in the potential energy surfaces, but also largely complicates the fitting of the PESs because two different crossings are observed. This problem can in principle be solved using a perturbatively corrected wave function, such as (X)MS-CASPT2 which was created to repair this failure of the SS-CASPT2 approach. However, this multi-state methods are computationally still hardly affordable with the huge amount of states that are necessary in the state average description of the CASSCF wave function.

As alternative, we propose the use of DFT calculation with the TPSSh functional which has been used in previous studies for this and other transition metal complexes of the same family and showed results similar to those obtained with CASPT2. For consistency, we re-started the procedure of the construction of the model Hamiltonian using the normal modes at TPSSh level. We applied the same procedure to select the main normal modes (Eq. 4.1c) and observed that the most important mode connecting the MC states is the Fe-N symmetric stretching, as previously expected

and found in the PBE0 modes. The next step, the fitting of the potential energy surfaces is being performed at present.

The analysis of the vibrational modes shows that many terms play a negligible role in the deactivation because the minima obtained using the multidimensional potential energy surface computed as a sum of one-dimensional modes is exactly equal as the fully-optimized minimum. Moreover, the geometry difference between the $^1$MLCT and the $^1A_{1g}$ projected in the basis of the ground state normal modes not only shows that the Fe-N symmetric stretching does not contribute to connect the optimal geometries of the two states but also that the displacements along the main modes are actually small, indicating very similar minima for both states. This is probably the reason why the LIESST process has been accurately described in previous calculations by means of Fermi's golden rule. This assumes that the excited state reaches its minimum geometry and account the rates from there. The $^1$MLCT, which is the bright state, is directly irradiated close to its minimum, then the rates computed with this method are expected to be accurate enough. This is our hypothesis but obviously the explicit wave packet quantum dynamic simulation is necessary to confirm that those rates and overall mechanism are still valid.

## 4.6. References

[1] W. Zhang, R. Alonso-Mori, U. Bergmann, C. Bressler, M. Chollet, A. Galler, W. Gawelda, R. G. Hadt, R. W. Hartsock, T. Kroll, K. S. Kjaer, K. Kubiček, H. T. Lemke, H. W. Liang, D. A. Meyer, M. M. Nielsen, C. Purser, J. S. Robinson, E. I. Solomon, Z. Sun, D. Sokaras, T. B. van Driel, G. Vankó, T.-C. Weng, D. Zhu, and K. J. Gaffney, *Tracking excited-state charge and spin dynamics in iron coordination complexes*, Nature **509**, 345–348 (2014).

[2] G. Auböck, and M. Chergui, *Sub-50-fs photoinduced spin crossover in [Fe(bpy)$_3$]$^{2+}$*, Nat. Chem. **7**, 629–633 (2015).

[3] C. de Graaf, and C. Sousa, *Study of the Light-Induced Spin Crossover Process of the [Fe$^{II}$(bpy)$_3$]$^{2+}$ Complex*, Chem. Eur. J. **16**, 4550–4556 (2010).

[4] C. de Graaf, and C. Sousa, *On the role of the Metal-to-Ligand Charge Transfer States in the Light-Induced Spin Crossover in $Fe^{II}(bpy)_3$*, Int. J. Quantum Chem. **111**, 3385–3393 (2013).

[5] C. Sousa, C. de Graaf, A. Rudavskyi, R. Broer, J. Tatchen, M. Etinski, and C. M. Marian, *Ultrafast Deactivation Mechanism of the Excited Singlet in the Light-Induced Spin Crossover of [Fe(2,2'-bipyridine)$_3$]$^{2+}$*, Chem. Eur. J. **19**, 17 541 –17 551 (2013).

[6] C. Sousa, M. Llunell, A. Domingo, and C. de Graaf, *Theoretical evidence for the direct $^3$MLCT-HS deactivation in the light-induced spin crossover of Fe(II)–polypyridyl complexes*, Phys. Chem. Chem. Phys. **20**, 2351–2355 (2018).

[7] S. Iuchi, and N. Koga, *Insight into the light-induced spin crossover of $[Fe(bpy)_3]^{2+}$ in aqueous solution from molecular dynamics simulation of d-d excited states*, Phys. Chem. Chem. Phys. **18**, 4789–4799 (2016).

[8] S. Iuchi, and N. Koga, *A model electronic Hamiltonian to describe low-lying d-d and metal-to-ligand-charge-transfer states excited states of $[Fe(bpy)_3]^{2+}$*, J. Comput. Chem. **42**, 166–179 (2021).

[9] G. Capano, M. Chergui, U. Rothlisberger, I. Tavernelli, and T. J. Penfold, *A Quantum Dynamics Study of the Ultrafast Relaxation in a Protoypical Cu (I)-Phenantroline*, J. Phys. Chem. A **118**, 9861–9869 (2014).

[10] G. Capano, T. J. Penfold, M. Chergui, and I. Tavernelli, *Photophysics of a copper phenantroline and wavepacket-based quantum dynamics: a synergetic approach*, Phys. chem. Chem. Phys. **19**, 19 590–19 600 (2017).

[11] J. Eng, C. Gourlaouen, E. Gindensperger, and C. Daniel, *Spin-Vibronic Quantum Dynamics for Ultrafast Excited-State Processes*, Acc. Chem. Res. **48**, 809–817 (2015).

[12] Y. Harabuchi, J. Eng, E. Gindensperger, T. Taketsugu, S. Maeda, and C. Daniel, *Exploring the Mechanism of Ultrafast Intersystem Crossing*

*in Rhenium (I) Carbonyl Bipyridine Halide Complexes: Key Vibrational Modes and Spin-Orbit Quantum Dynamics*, J. Chem. Theory Comput. **12**, 2335–2345 (2016).

[13] M. Fumanal, E. Gindensperger, and C. Daniel, *Ultrafast Excited-State Decays in $[Re(CO)_3(N,N)(L)]^{n+}$: Nonadiabatic Quantum Dynamics*, J. Chem. Theory Comput. **13**, 1293–1306 (2017).

[14] K. Falahati, H. Tamura, I. Burghardt, and M. Huix-Rotllant, *Ultrafast carbon monoxide photolysis and heme spin-crossover in myoglobin via nonadiabatic quantum dynamics*, Nat. Commun. **9**, 4502–4509 (2018).

[15] A. Hauser, *Reversibility of light-induced excited spin state trapping in the $Fe(ptz)_6(BF_4)_2$, and the $Zn_{1-x}Fe_x(ptz)_6(BF_4)_2$ spin-crossover systems*, Chem. Phys. Lett **124**, 543–548 (1986).

[16] A. Marino, P. Chakraborty, M. Servol, M. Lorenc, E. Collet, and A. Hauser, *The role of ligand-field states in the ultrafast photophysical cycle of the prototypical iron(II) spin-crossover compound $[Fe(ptz)_6](BF_4)_2$*, Angew. Chem. Int. Ed. **53**, 3863–3867 (2014).

[17] S. Saureu, and C. de Graaf, *TD-DFT study of the light-induced spin crossover of Fe(III) complexes*, Phys. Chem. Chem. Phys. **18**, 1233 (2016).

[18] G. Alcover-Fortuny, J. Wu, R. Caballol, and C. de Graaf, *Quantum Chemical Study of the Interligand Electron Transfer in Ru Polypyridyl Complexes*, J. Phys. Chem. A **122**, 1114–1123 (2018).

[19] C. Sousa, C. de Graaf, A. Rudavskyi, and R. Broer, *Theoretical Study of the Light-Induced Spin Crossover Mechanism in $[Fe(mtz)_6]^{2+}$ and $[Fe(phen)_3]^{2+}$*, J. Phys. Chem. A **121**, 9720–9727 (2017).

[20] J. Wu, M. Alías, and C. de Graaf, *Controlling the Lifetime of the Triplet MLCT State in Fe(II) Polypyridyl Complexes through Ligand Modification*, Inorganics **8**, 16–33 (2020).

[21] M. Etinski, J. Tatchen, and C. M. Marian, *Time-dependent approaches for the calculation of intersystem crossing rates*, J. Chem. Phys. **134**, 154 105 (2011).

[22] *TURBOMOLE V6.4.2 2012, a development of University of Karlsruhe and Forschungszentrum Karlsruhe GmbH, 1989-2007, TURBOMOLE GmbH, since 2007; available from* `http://www.turbomole.com`.

[23] I. Fdez. Galván, M. Vacher, A. Alavi, C. Angeli, F. Aquilante, J. Autschbach, J. J. Bao, S. I. Bokarev, N. A. Bogdanov, R. K. Carlson, L. F. Chibotaru, J. Creutzberg, N. Dattani, M. G. Delcey, S. S. Dong, A. Dreuw, L. Freitag, L. M. Frutos, L. Gagliardi, F. Gendron, A. Giussani, L. González, G. Grell, M. Guo, C. E. Hoyer, M. Johansson, S. Keller, S. Knecht, G. Kovačević, E. Källman, G. Li Manni, M. Lundberg, Y. Ma, S. Mai, J. P. Malhado, P. A. Malmqvist, P. Marquetand, S. A. Mewes, J. Norell, M. Olivucci, M. Oppel, Q. M. Phung, K. Pierloot, F. Plasser, M. Reiher, A. M. Sand, I. Schapiro, P. Sharma, C. J. Stein, L. K. Sørensen, D. G. Truhlar, M. Ugandi, L. Ungur, A. Valentini, S. Vancoillie, V. Veryazov, O. Weser, T. A. Wesołowski, P.-O. Widmark, S. Wouters, A. Zech, J. P. Zobel, and R. Lindh, *OpenMolcas: From Source Code to Insight*, J. Chem. Theory Comput. **15**, 5925–5964 (2019).

[24] *CPMD V3.15 2012, CPMD, http://www.cpmd.org/ Copyright IBM Corp 1990-2008, Copyright MPI für Festkörperforschung Stuttgart 1997-2001.*

[25] H. D. Meyer, and O. Vendrell, *The MCTDH package*, http://mctdh.uni-hd.de/ (2013).

[26] B. D. Alexander, T. J. Dines, and R. W. Longhurst, *DFT calculations of the structures and vibrational spectra of the $[Fe(bpy)_3]^{2+}$ and $[Ru(bpy)_3]^{2+}$ complexes*, Chem. Phys. **352**, 19–27 (2008).

[27] *Huix-Rotllant, private communication.*

[28] A. Rudavskyi, *Spin crossover mechanisms unraveled by theory towards the design of new materials* (University of Groningen, Netherlands) (2014).

[29] J. Finley, P. Åke Malmqvist, B. O. Roos, and L. Serrano-Andrés, *The multi-state CASPT2 method*, Chem. Phys. Lett. **288**, 299 – 306 (1998).

# 5.

# Ultrafast intersystem-crossing rate in xanthone. A Duschinsky rotation model using MCTDH

## 5.1. Introduction

Intersystem-crossing (ISC) is the non-radiative transition between states of different multiplicities. It depends on the magnitude of spin-orbit coupling which is an intrinsic relativistic interaction, and therefore, the coupling will be larger in those molecules containing heavy elements. The process usually happens at a time scale faster than a picosecond in transition metal complexes or organic compounds containing heavy elements such as sulphur but not in organic compounds only formed by second row elements.

Despite not presenting any of the aforementioned properties, xanthone shows a surprising ultrafast ISC rate from the excited singlets to the triplet states. This makes it a good triplet sensitizer with applications as initiator in photopolymerization [1] or pharmaceutical properties as anticarcenogenic and antibacterial among others. [2,3]

Xanthone (Fig. 5.1) is an organic molecule within the family of aromatic ketones that shows $C_{2v}$ symmetry at the ground state optimised geometry. Within this point group symmetry, the irreducible representation for the involved singlet states is $A_1$ for the ground state and $S_2$ ($\pi\pi^*$ character) whereas $S_1$ which is an $n\pi^*$ state belongs to $A_2$, this makes $S_1$ dark and $S_2$ a bright state in the symmetric conformation. In the low-lying triplet states, $T_1$ ($n\pi^*$) belongs to the $A_2$ irreducible representation, $T_2$ ($\pi\pi^*$) and $T_3$ ($\pi\pi^*$) to $A_1$ and $T_4$ ($\pi\pi^*$) to $B_1$. In this molecule, the $n\pi^*$ and $\pi\pi^*$ triplet states are nearly degenerate. The mechanism from the bright singlet state to the low-lying triplet state has been studied experimentally and theoretically but still remains unclear.

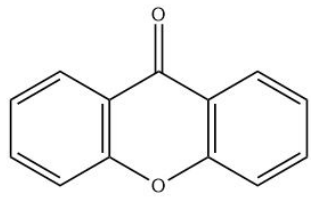


**Figure 5.1.** Schematic representation of xanthone molecule

From an experimental perspective, Ohshima et al. measured the excitation spectrum of xanthone in a supersonic jet.[4] They determined the vibrationally resolved spectrum for both $S_2$ and $S_1$. The study suggested that the zero point energy difference between these excited states was around 0.45 eV. The transition from the ground state to $S_1$ ($^1A_2$) is electronically forbidden within $C_{2v}$ symmetry. For this reason, the intensities are low and they increase when couple with $a_2$ vibrational modes. The vibrations that couple the electronic transition from the ground state to the bright state $S_2$ ($^1A_1$) are necessarily of $a_1$ symmetry to keep the symmetry of the vibronic state equal as the one of the electronic state. Moreover, they observed a slight increase in the sequential peaks separation of the absorption spectrum because of small positive anharmonicity. They associated it to the strong vibronic coupling between excited states and they suggested a very fast intersystem crossing rate of 100 fs.

Later, the study of Itoh on the emission and excitation spectra of xanthone vapour confirmed the same energies for the $S_1$ and $T_1$ zero point transitions as in the previous study.[5] The analysis of emission spectra, both fluorescence and phosphorescence, showed that C=O stretching mode is the most important mode along which these radiative phenomena occur.

From a theoretical point of view Marian and coworkers studied the deactivation pathway using Fermi's golden rule.[6] They studied several intersystem crossing rates between pairs of states of different multiplicity to propose the most probable deactivation path. The study went beyond the Condon approximation and suggested that the El-Sayed forbidden deactivation channel in gas-phase, between $^1\pi\pi^*$ and $^3\pi\pi^*$ was two orders of magnitude faster than the El-Sayed allowed channel between $^1\pi\pi^*$ and $^3n\pi^*$ states. However, this El-Sayed forbidden channel was one order of magnitude slower than the channel between the $^1n\pi^*$ and $^3\pi\pi^*$ states. The lack of internal conversion rates, because of the limitation of the methodology, did not close the door about the overall deactivation mechanism on this molecule. They also determined that increasing the polarity of the solvent, the relative energy of $\pi\pi^*$ states decrease and the energy of $n\pi^*$ states increase. These differences in relative energies is a key factor in the determination of intersystem-crossing rates which decrease in the El-Sayed allowed channels when the polarity of the solvent increase.

The theoretical studies of this family of compounds were extended to the wave packet dynamic calculations by Huix-Rotllant et al.[7] They propagated the nuclear wave function using a model Hamiltonian in MCTDH for the most relevant singlet and triplet states of acetophenone along all the vibrational normal modes, except the eight with highest frequencies which correspond to C-H stretchings and were discarded. In the study, the dynamics are initially accelerated by an impulse along all the included vibrational normal modes to observe the population of triplet states in 1.3 ps whereas was experimentally measured at 42 ps by Zewail and coworkers.[8] The initial impulse removes all physical relevance from the calculated lifetimes but allowed them to propose a general deactivation path. Performing MCTDH simulations for about 50 ps is still a rather costly process and has no sense a priory without the inclusion of bath modes able to dissipate energy from the system. The proposed path is a sequential mechanism $S_1(^1n\pi^*) \rightarrow T_2\ (^3\pi\pi^*) \rightarrow T_1(^3n\pi^*)$, the $^3\pi\pi^*$ state acts as an intermediate state that needs to accumulate population before transferring it to the most stable triplet state.

We present in this chapter a new model Hamiltonian based on Duschinsky rotation.[9] The model Hamiltonian writes the multivariant diabatic PES using the harmonic approximation and transforming the normal modes of each state to a common basis through Duschinsky rotation matrix and the couplings among states are introduced in the off-diagonal terms of the Hamiltonian. The advantage of this model Hamiltonian is that with an appropriate analytical expression for the couplings, the idea of a tedious fitting procedure to determine the diabatic potential and the non-adiabatic coupling expressions, commonly used in MCTDH, can be abandoned. In addition, the use of the Duschinsky rotation in the model Hamiltonian allow to study the influence of the mode mixing between states by including the J rotation matrix or an identity matrix. The model is used in MCTDH to calculate the ultrafast triplet population and the vibrationally resolved absorption spectrum in xanthone.

## 5.2. Computational details

We have carried out geometry optimizations at (TD-)DFT level for the states involved in the process using the Gaussian16-A03 version.[10] The functional used was BV5LYP which is formed by the Becke 88 exchange functional and V5LYP correlation functional, which is found as the standard B3LYP functional in other quantum chemistry packages. The selected basis set was a valence triple-$\zeta$ with two sets of polarized functions within the Kalsruhe family, def2-TZVPP. The minima were confirmed by frequency calculations, both the Hessian eigenvalues and eigenvectors were used in the construction of the model Hamiltonian.

The shape of the diabatic potential energy surfaces is well-described at (TD-)DFT level. However, this is not always the most accurate method to determine the vertical energies, for this reason, we planned the calculation of vertical energies with, in principle, more accurate electronic structure based methods. Then, the diabatic potential surfaces are rigidly shift with the obtained vertical energies at the higher computational level (Fig. 5.2).

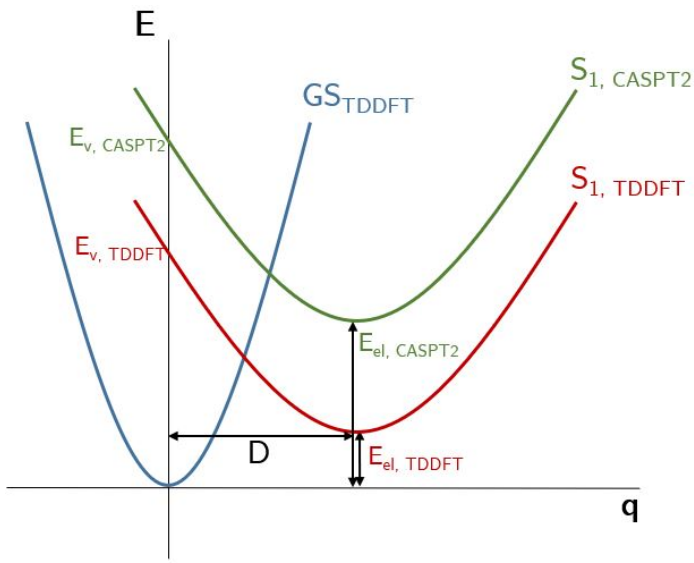


**Figure 5.2.** Schematic rigid shift applied to the excited states.

At the ground state optimized geometry, i.e. the Franck-Condon geometry, we have computed the energy of states at different levels, but the method used to rigidly shift the electronic energies in the model Hamiltonian has been CASPT2. In our calculations, we include 12 electrons in 11 molecular orbitals (Fig. 5.3). The basis set selected is an ano-rcc type with 4s3p2d1f for C and O and 3s2p1d for H and the computational cost of the two-electron integrals is reduced by means of Cholesky decomposition using the $10^{-4}$ threshold. The reference wave function is a state-specific CASSCF function and the perturvative part is applied to the CASSCF obtained roots through a SS-CASPT2 calculation. This part is carried out using *Molcas*.[11]

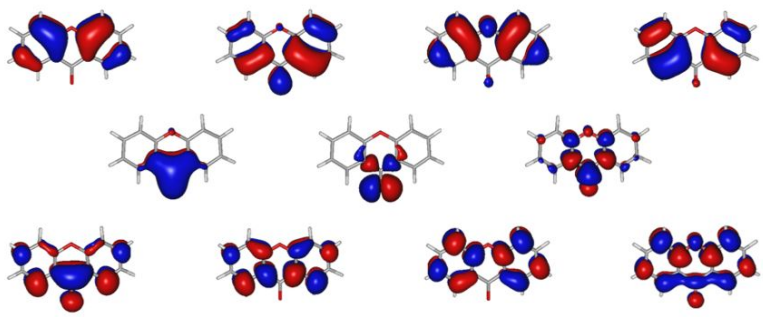

**Figure 5.3.** Active space natural orbitals in xanthone for a CAS(12,11). The four included $\pi$ orbitals mainly centred on phenyl rings in the top row, $\pi$ C-O, O non-bonding and $\pi^*$ C-O from left to right in the middle and the four $\pi^*$ orbitals on phenyl rings at the bottom row.

The spin-orbit coupling and the explicit calculation of non-adiabatic couplings is performed using *Molcas*. We have used the state interaction method for both cases.

$$H_{ij} = \langle \Psi_i | \hat{H} | \Psi_j \rangle \tag{5.1}$$

For the spin-orbit calculations, we employed the Douglas-Kroll-Hess effective one electron operator as Hamiltonian and the state-average CASSCF states as $\Psi_i$ and $\Psi_j$, whereas for the non-adiabatic coupling we used the regular electronic Hamiltonian with the non-orthogonal state-specific states ($\Psi_i$ and $\Psi_j$).

The wave packet quantum dynamics are carried out using the 8.5.10 version of the Heidelberg package MCTDH.[12] The multi-layer (ML-MCTDH) method is employed to speed up the calculations which are carried out along all the 63 vibrational normal modes. The simulation was extended for 1.5 ps and included 6 electronic states (14 in the simulations considering one state for each azimuthal component of the triplet) which coincide with the number of electronic degrees of freedom. A six-layer representation of the wave function is used (see Fig. A.1 in Appendix A) where the vibrations are grouped by type and frequency value. In the first layer, they are divided in three main branches depending on the nature of the vibrations: in-plane, out-of-plane and high-frequency corresponding to the C-H stretchings. We included 2 single-particle functions (SPFs) for each of the branches and each vibrational normal mode was initially represented by 31 primitive basis functions or discrete variable representations that coincide with the lowest energy solutions of an harmonic oscillator along the corresponding mode and the number of grid points along the mode.

The model Hamiltonian used in the simulation has been defined from the Duschinsky rotation for the on-diagonal terms (potential and nuclear kinetic operators). The off-diagonal terms are composed by non-adiabatic couplings for states within the same azimuthal $M_S$ values and direct spin-orbit couplings for states with different $M_S$ value. More detailed information about the construction of the Hamiltonian is given in the next section.

## 5.3. Results and discussion

The chapter is divided in three different parts. In the first part, the Duschinsky model to represent the diabatic states and few approximations to treat the couplings among states are presented. In the second part, the results for the intersystem crossing in xanthone with the model are shown and discussed. Finally, the model is used to determine the vibrationally resolved spectrum and compare it with experiments.

### 5.3.1. Construction of the model vibronic Hamiltonian

The model Hamiltonian can be separated in two different classes of terms. The on-diagonal terms represent the energy of a particular state whereas the off-diagonal terms accounts for the coupling among states which are spin-orbit couplings for states with different multiplicity, or more precisely between states with different $M_S$ projections and non-adiabatic couplings for states with the same $M_S$ projection.

The most commonly used coordinates in the construction of vibronic model Hamiltonians are the normal modes because of the simple expression in the nuclear kinetic energy expressed in these coordinates compared with the complicated one obtained in other coordinates such as curvilinear or polyspherical ones.[13]

The normal modes are linear combinations of the mass-weighted cartesian (MWC) displacements $d_{ij}$.

$$d_{ij} = M_i^{1/2} \cdot \delta_{ij} \tag{5.2}$$

To avoid the coupling of translations and rotations with vibrational modes, it is necessary to create a D matrix which contains 3N-6 vectors orthogonal to the six translation and rotation vectors, in other words, D is a rectangular matrix of dimension 3N-6×3N that transforms from Cartesian to internal coordinates.[14] The transformation of the full 3N×3N Hessian matrix (H), which contains the second derivatives of the energy along all the mass-weighted displacements, to the 3N-6×3N-6 reduced Hessian matrix (H') where the translation and rotational normal modes have been excluded is defined as follows:

$$H' = D^{\dagger} H D \tag{5.3}$$

Next we define the L matrix, which is the matrix that diagonalizes the reduced Hessian matrix (H').

$$L^{\dagger} H' L = W \tag{5.4}$$

The obtained eigenvalues are the frequencies (W) and the eigenvectors are the normal modes in MWC coordinates (q). The MWC can be transformed to mass-frequency-weighted Cartesian coordinates (MFWC) which are the direct product between the square-root of the frequency and the mass-weighted Cartesian coordinates.

$$Q_i = \omega_i^{1/2} \cdot q_i \tag{5.5}$$

These coordinates are often very useful to express the terms of the model Hamiltonian.

### Diabatic functions

The energy of each diabatic state is a multi-variant function that depends on the vibrational or potential energy $\hat{V}$ and the kinetic nuclear energy $\hat{T}$. Using the harmonic approximation, the mathematical function for the vibrational energy is expressed as a quadratic polynomial where the amplitude depends on the frequency of each state along all the vibrational normal modes.

$$\hat{V} = \sum_{i}^{3N-6} \frac{\omega_i^2}{2} q_i^2 = \sum_{i}^{3N-6} \frac{\omega_i}{2} Q_i^2 \tag{5.6}$$

The kinetic energy depends on the second derivative along the normal modes.

$$\hat{T} = \sum_{i=1}^{3N-6} -\frac{1}{2}\frac{\partial^2}{\partial q_i^2} = \sum_{i=1}^{3N-6} -\frac{w_i}{2}\frac{\partial^2}{\partial Q_i^2} \tag{5.7}$$

For simplicity, these summations can also be expressed in matrix form.

$$\hat{T} = -\frac{1}{2}\nabla q^T \nabla q = -\frac{1}{2}\nabla Q^T W \nabla Q \tag{5.8a}$$

$$\hat{V} = \frac{1}{2} q^T W^2 q = \frac{1}{2} Q^T W Q \tag{5.8b}$$

Herein, W is a 3N-6 diagonal cubic matrix which contains the frequency values. Q is the 3N-6 vector that contains the displacements normal modes, $\nabla$Q is the 3N-6 vector containing the first derivative respect to each normal mode while $Q^T$ and $\nabla Q^T$ are the transposed of the Q and $\nabla Q$ vectors, respectively.

The normal modes for the different states represent the same dimensional Hilbert space (assuming that there is no rotational-vibrational coupling). However, the normal modes are specific for each state and a change of basis is required to express the information of the different states in a common basis. The Duschinsky rotation connects the normal modes of the different states and allows to express the modes of excited state i ($q_i$) in the basis of state 0 ($q_0$).

$$q_i = Jq_0 + D \tag{5.9}$$

The rotation matrix J is defined from the L matrices of both the final and the initial state and gives information about the normal modes mixing between both electronic states (Fig. 5.4, with a more accurate description in the next lines).

$$J = L_i^{-1} L_0 \tag{5.10}$$

The displacement vector D computes the mass-weighted Cartesian difference between the minima of the states i and 0. The $k^{th}$ value of the D vector coincides with the displacement between both states along the normal mode k. Figure 5.2 graphically shows that the displacement of the ground state and excited state minima along a normal mode mode is represented by the D vector. This displacement in Cartesian coordinates is expressed in the basis of state 0 through the L matrix.

$$D = L_i^{-1} M^{1/2} (R_0 - R_i) \tag{5.11}$$

The Duschinsky rotation allows to represent the excited state normal modes in the basis of the ground state modes. It affects the Hamiltonian

operators which have to be transformed from the excited state normal modes to the ground state normal modes.

The mathematical expression and the derivation of the harmonic potential of excited states expressed in the basis of the ground state normal modes using MWC and MFWC coordinates is as follows:

$$\hat{V}(q) = \frac{1}{2}(Jq_0 + D)^T W_i^2((Jq_0 + D) \tag{5.12a}$$

$$\hat{V}(q) = \frac{1}{2}q_0^T(J^T W_i^2 J)q_0 + D^T W_i^2 Jq_0 + \frac{1}{2}D^T W_i^2 D \tag{5.12b}$$

$$\hat{V}(Q) = \frac{1}{2}W_i^{1/2}(JW_0^{-1/2}Q_0 + D)^T W_i(W_i^{1/2}(JW_0^{-1/2}Q_0 + D) \tag{5.12c}$$

$$\hat{V}(Q) = \frac{1}{2}Q_0^T(J^T W_i^2 W_0^{-1} J)Q_0 + D^T W_i^2 W_0^{-1/2} JQ_0 + \frac{1}{2}D^T W_i^2 D \tag{5.12d}$$

The obtained expressions appear as rather awkward multi-variable functions, but the different terms appearing in the equation can be easily interpreted with their equivalents in a single-variable second degree polynomial. The first term, $J^T W_i^2 J$ in MWC coordinates, is the 'effective frequency' of the excited electronic state projected in the basis of ground state normal modes or from a mathematical point of view indicates the amplitude of the polynomial in each mode. The second term, $D^T W_i^2 J$ in MWC coordinates, gives information about the displacement between the excited state minimum geometry and the ground state minimum, i.e. the Franck-Condon geometry, along each normal mode. The third term, $D^T W_i^2 D$, accounts for the energy difference between the excited and the ground states at the Franck-Condon geometry or the y-intercept of the excited state polynomia.

The application of the Duschinsky in the kinetic operator demonstrates that there is no change in MWC coordinates and a term relating J and the frequency of ground state normal modes when expressed in MFWC

coordinates.

$$\hat{T}(q) = -\frac{1}{2}\left(\frac{\partial}{\partial q_i}\frac{\partial q_0}{\partial q_0}\right)^T\left(\frac{\partial}{\partial q_i}\frac{\partial q_0}{\partial q_0}\right) \tag{5.13a}$$

$$\hat{T}(q) = -\frac{1}{2}\left(J^T\frac{\partial}{\partial q_0}\right)^T\left(J^T\frac{\partial}{\partial q_0}\right) \tag{5.13b}$$

$$\hat{T}(q) = -\frac{1}{2}\left(\frac{\partial}{\partial q_0}\right)^T\left(\frac{\partial}{\partial q_0}\right) \tag{5.13c}$$

$$\hat{T}(Q) = -\frac{1}{2}\left(\frac{\partial}{\partial Q_i}\frac{\partial Q_0}{\partial Q_0}\right)^T W_i\left(\frac{\partial Q_0}{\partial Q_0}\frac{\partial}{\partial Q_i}\right) \tag{5.13d}$$

$$\hat{T}(Q) = -\frac{1}{2}\left((JW_i^{1/2}W_0^{-1/2})^{-1}\frac{\partial}{\partial Q_0}\right)^T W_i\left((JW_i^{1/2}W_0^{-1/2})^{-1}\frac{\partial}{\partial Q_0}\right) \tag{5.13e}$$

$$\hat{T}(Q) = -\frac{1}{2}\left(\frac{\partial}{\partial Q_0}\right)^T JW_0J^T\left(\frac{\partial}{\partial Q_0}\right) \tag{5.13f}$$

Duschinsky rotation is a very simple and efficient way of transforming the normal modes of excited states in the basis of the ground state. Its only limitation is the complete elimination of the rotational and translation normal modes in both states. If this cannot be done exactly, such as in systems with strong rovibrational coupling, part of the information contained in the excited state is lost expressing them in the ground state normal modes basis. For this reason, Duschinsky rotation is only accurate between states that do not differ too much geometrically.

Figure 5.4 shows the influence of the normal modes mixing between different states of xanthone by means of a graphical representation of the J matrix. A color for each term in the matrix is assigned, those terms with an absolute value close to 1 have dark red colors and those with values close to 0 receive light red colors. Dark red dots on the diagonal indicate a nearly one-to-one correspondence between the normal mode in the ground and excited state, while the presence of dark off-diagonal dots indicate that more than one ground state mode is required to properly

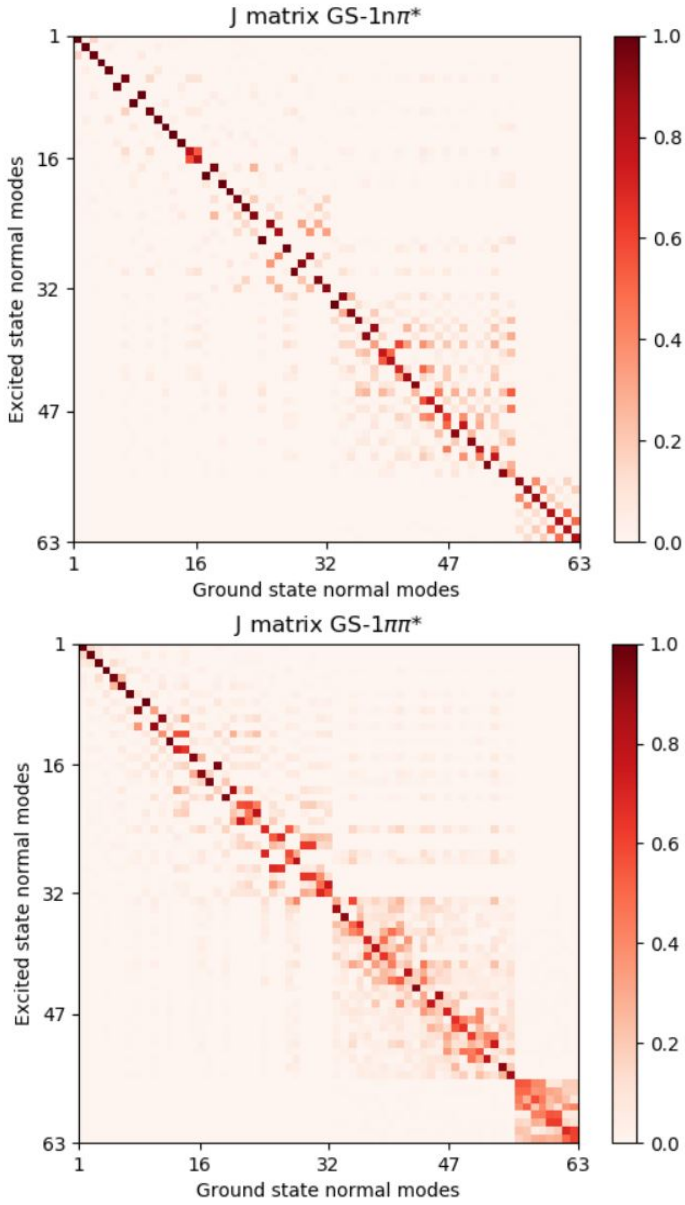


**Figure 5.4.** J matrix in xanthone between the $^1$n$\pi^*$ and the ground state at the top and between the $^1\pi\pi^*$ and ground state at the bottom.

express the excited vibrational mode. Figure 5.4 makes clear that the vibrational modes in xanthone are significantly different for each electronic state. Instead of being almost identical to a simple unit matrix, J is better understood as having significant block-diagonal character, which indicates that the mixing of modes is mainly performed by types of vibrations. The figure also allow to compare the mixture of the normal modes for the different states and this clearly indicates that the effect is more pronounced in $^1\pi\pi$ state than in $^1$n$\pi$. However, the influence of J in any of the cases does not seem to be as dramatic as in the mixing of the lowest singlet and triplet states in uracil.[15]

Photophysical properties are strongly dependent of the involved states' relative energy. The geometry optimizations are carried out at the TD-DFT level but at the Franck-Condon geometry, other electronic structure based methods are explored (Tab. 5.1). To incorporate the different vertical excitation energies obtained with these, in principle, more accurate computational schemes, we assumed that the shape of potential electronic surfaces is well represented at TD-DFT level and only a rigid shift is applied to the multidimensional surfaces (Fig. 5.2).

The results are dramatically dependent on the electronic structure based method used. Table 5.1 shows the vertical energy for the main electronic states with several methods (TD-DFT, CASPT2, CASSCF and DMRG-CASSCF), other results such as those obtained with ADC(2) methodology were not included because they do not improve the agreement with the available experimental data. The CASPT2 results based on a state-average orbital optimization are affected by a lack of flexibility in the wave function description, therefore the best results are apparently those obtained with a state-specific description or quasi state-specific in a state average description including the minimum number of states in the optimization procedure. The results with a quasi state-specific description are marked in bold in the Table 5.1 and are the ones used to rigidly shift the potential energy surfaces.

The relatively large CASPT2 energy differences using equal active spaces and basis sets apparently find their origin in small details such as the state-specific or state-average optimization of the wave function, the single- or multi-state treatment in the perturbative part, and the number of states

included in the average description (this last results has not been included in Table 5.1 for simplicity). All these facts point in the same direction, namely that this is a strongly correlated system and that the inclusion of more orbitals in the active space is necessary to obtain a stable reference wave function for including the dynamic electron correlation. With this aim, we have performed DMRG-CASSCF calculations for the singlets including 22 electrons distributed over 19 orbitals. The results seem to recover a larger part of the static electron correlation when compared with the CASSCF calculation in the smaller (12,11) active space, specially for the $^1\pi\pi^*$ state. Supposedly, this better reference wave function should produce more accurate energies in a perturbative treatment of the remaining dynamic correlation. Unfortunately, these DMRG+PT2 calculations are very CPU-intensive and no definite results have been obtained so far. We

**Table 5.1.** Electronic vertical energies [eV] of the main triplet and singlet states at the ground state optimised geometry.

| | DFT[(a)] | CASPT2[(b)] | | | CASSCF[(c)] | DMRG[(d)] | Expt.[(e)] |
|---|---|---|---|---|---|---|---|
| | | A | B | C | | | |
| $S_1$ | 3.00 | **3.93** | 3.68 | 3.83 | 3.96 | 3.91 | 3.34 |
| $S_2$ | 3.38 | **4.33** | 4.58 | 4.40 | 5.57 | 5.00 | 3.81 |
| $T_1$ | 2.69 | **3.76** | 3.50 | 3.65 | - | - | |
| $T_2$ | 2.80 | **3.79** | 3.76 | 3.68 | - | - | |
| $T_3$ | 3.36 | **3.99** | 3.90 | 4.03 | - | - | |
| $T_4$ | 3.46 | **4.05** | 3.92 | 4.03 | - | - | |
| $T_5$ | 3.76 | **4.58** | 4.41 | 4.46 | - | - | |

[(a)] DFT: (TD)-BV5LYP/def2-TZVPP.
[(b)] CASPT2. The three CASPT2 values correspond to SS-CASPT2 (A,B) or MS-CASPT2 (C). Calculations B and C use a SA(3,5)-CAS(12,11) as reference wave function, where SA(3,5) stands for state-average with 3 singlets and 5 triplets in the optimization of the wave function. A optimizes the molecular orbitals within each irreducible representation. In bold the result using A set-up which is the one used in the model Hamiltonian.
[(c)] CASSCF: SA(3)-CASSCF(12,11)/ ano-type basis set.
[(d)] DMRG: SA(3)-DMRG-CASSCF(22,19)/ ano-rcc-VDZP.
[(e)] Expt.: Experimental zero point energy differences, values extracted from Ref. 4.
In almost all the electronic structure based methods, $T_5$ is higher in energy than the bright $S_2$ state and therefore not included in the dynamics.

expect to use the DMRG+PT2 vertical energies in our model Hamiltonian to compare with the below-described wave packet dynamics.

### Coupling among states

The off-diagonal elements of the Hamiltonian matrix represent the coupling among the different electronic states. The couplings are classified in two types depending on their nature. Spin-orbit coupling (SOC) measures the interaction of states belonging to different spin multiplicities and also accounts for the coupling among states of the same multiplicity but with different $M_S$ values. Non-adiabatic coupling (NAC) affects states of the same multiplicity and the same $M_S$ value.

The SOC is computed using the effective one-electron Hamiltonian (see Sec. 2.1.4 and Sec. 5.2 for further details). The couplings at Franck-Condon, in a quasi $C_{2v}$ symmetrical geometry reveal that the non-vanishing couplings are those that follow the El-Sayed rule (Table 5.2). The expansion along out-of-plane normal modes generate sizeable couplings among $n\pi^*$-$n\pi^*$ and $\pi\pi^*$-$\pi\pi^*$ states.

To accurately represent the different components of a triplet state, one needs to align the molecule along the magnetic axis which are the eigenvectors of the magnetic anisotropy matrix D. However, as long no external magnetic fields are applied, the different $M_S$ components are degenerate and the spin anisotropy does not really play a role. Therefore, no action was taken to discern among different populations in the components within a triplet state neither to study the influence of a magnetic field during the process, only to generate an overall pathway of the process in the gas phase.

The calculation of NAC is not an easy task within ab initio quantum chemical methods because the application of the Born-Oppenheimer approximation produces orthogonal states and a diagonal Hamiltonian, with the adiabatic energy on the diagonal and zero values for the off-diagonal terms. However, there are several approximations to estimate the NACs and those used in this chapter are briefly commented here. The first two

**Table 5.2.** Absolute spin-orbit in $cm^{-1}$ coupling between singlets and triplets at Franck-Condon geometry.

| $\Psi_i$ | $\Psi_j$ | $\langle\Psi_i\vert\,\hat{H}^{SO}\,\vert\Psi_j\rangle$ |
|---|---|---|
| $S_1$ ($^1n\pi^*/^1A_2$) | $T_1$ ($^3n\pi^*/^3A_2$) | 0.045 |
| $S_1$ ($^1n\pi^*/^1A_2$) | $T_2$ ($^3\pi\pi^*/^3A_1$) | 45.139 |
| $S_1$ ($^1n\pi^*/^1A_2$) | $T_3$ ($^3\pi\pi^*/^3A_1$) | 10.311 |
| $S_1$ ($^1n\pi^*/^1A_2$) | $T_4$ ($^3\pi\pi^*/^3B_2$) | 24.178 |
| $S_2$ ($^1\pi\pi^*/^1A_1$) | $T_1$ ($^3n\pi^*/^3A_2$) | 4.964 |
| $S_2$ ($^1\pi\pi^*/^1A_1$) | $T_2$ ($^3\pi\pi^*/^3A_1$) | 0.000 |
| $S_2$ ($^1\pi\pi^*/^1A_1$) | $T_3$ ($^3\pi\pi^*/^3A_1$) | 0.000 |
| $S_2$ ($^1\pi\pi^*/^1A_1$) | $T_4$ ($^3\pi\pi^*/^3B_2$) | 0.000 |

were explored as a short-cut to avoid the usual, rather laborious fitting-based procedure.

The first approach used to calculate the non-adiabatic couplings is based on the expression derived from a two-state problem adopting a parabolic-plus-hyperbolic shape. In principle, the linear vibronic coupling term ($\lambda_i$) can be extracted from this simple model, following the expression published in the MCTDH review by Burghardt and coworkers.[16]

$$\lambda_i = \sqrt{\frac{1}{8}\left.\frac{\partial^2(V_1 - V_2)^2}{\partial Q_i^2}\right|_{Q=0}} \tag{5.14}$$

After applying it to our case, we obtained imaginary linear expansion coefficients for the non-adiabatic couplings along some of the normal modes. To find the origin of these unphysical coefficients, we derived the expression from the beginning for a two-state model where the coupling between

states depends linearly on the geometrical distortion.

$$\hat{H} = \begin{pmatrix} E_1 & \lambda Q \\ \lambda Q & E_2 \end{pmatrix} = \begin{pmatrix} V_1 & 0 \\ 0 & V_2 \end{pmatrix} \tag{5.15a}$$

$$\begin{vmatrix} E_1 - V & \lambda Q \\ \lambda Q & E_2 - V \end{vmatrix} = 0 \tag{5.15b}$$

$$V_{1,2} = \frac{E_1 + E_2}{2} \pm \sqrt{(E_1 - E_2)^2/4 + \lambda^2 Q^2} \tag{5.15c}$$

$$\frac{1}{4}\left[(V_1 - V_2)^2 - (E_1 - E_2)^2\right] = \lambda^2 Q^2 \tag{5.15d}$$

$$\lambda = \sqrt{\frac{1}{8}\left(\frac{\partial^2 (V_1 - V_2)^2}{\partial Q^2} - \frac{\partial^2 (E_1 - E_2)^2}{\partial Q^2}\right)} \tag{5.15e}$$

Herein, $V_1$ and $V_2$ are the adiabatic potentials and $E_1$, $E_2$ the diabatic potentials for the corresponding states while $\lambda$ is the linear expansion coefficient of the non-adiabatic couplings.

Then, we observed that the Equation 5.14 can not be applied to our case mainly for two reasons. The first is that the potentials obtained using the Duschinsky rotation are the diabatic ($E_1$, $E_2$) and not the adiabatic ones ($V_1$, $V_2$). The second is that this method assumes that the second derivative for the diabatic potentials vanish, this is, within the harmonic approximation, only valid when the effective frequencies of both states are equal which is not the case in our model.

The second methodology employed to compute the non-adiabatic coupling was accounting for the direct interaction between states. The problem is that the standard SA-CASSCF approach delivers states that are mutually orthogonal, and therefore do not interact. For this reason, the state-specific description for each state was employed which removes the strict orthogonality between the states and allows us to calculate the interaction by:

$$\gamma_{ij} = \frac{\langle \Psi_i | \hat{H} | \Psi_j \rangle - H^{av} \langle \Psi_i | \Psi_j \rangle}{1 - (\langle \Psi_i | \Psi_j \rangle)^2} \tag{5.16}$$

with

$$H^{av} = \frac{\langle \Psi_i | \hat{H} | \Psi_i \rangle + \langle \Psi_j | \hat{H} | \Psi_j \rangle}{2} \tag{5.17}$$

This expression for $\gamma$ arises from the diagonalization of the two by two Hamiltonian after a Löwdin orthogonalization of states $i$ and $j$.[17]

The coupling between state $S_1$ and $S_2$ at Franck-Condon geometry is strictly 0 for the $C_{2v}$ symmetry because they transform following different irreducible representations. For this reason, we performed the calculation at Q=$\pm$1 along all the normal modes to obtain the linear expansion coefficient for the coupling. Small displacement along out-of-plane normal modes are expected to generate large couplings between $S_1$ and $S_2$. Unfortunately, the near degeneracy of the triplet states causes root flipping and strong mixing between diabatic triplet states in the state-specific optimization of the wave function of the states. Therefore, it was not possible to get reliable estimates for the couplings among triplets using this approach.

The third, and most common, method to obtain the couplings is by means of a fitting procedure. This consists in computing the adiabatic curves along the normal modes and determine self-consistently the diabatic surfaces and the non-adiabatic couplings assigning analytical expressions for both in the Hamiltonian which after diagonalisation ends up again in the previous adiabatic energies. This was the method employed to obtain the couplings among triplet states introduced in our model Hamiltonian.

There is still another way to obtain the non-adiabatic couplings which is based on the search of the conical intersections between pairs of states. On each point of the 3N-8 dimensional hypersurface of conical intersections an orthogonal two-dimensional plane can be defined, the so-called branching plane. This surface is defined by two vectors: the g-vector or the difference of energy vector and the h-vector or the non-adiabatic coupling vector. The projection of this last vector onto the basis of the ground state normal modes gives the linear expansion coefficients for the non-adiabatic couplings for the pair of states. Despite the apparent simplicity and rigorous definition of the coupling, this methodology was discarded because

of the difficulty of finding all the conical intersections between the states involved in the process at a sufficiently accurate level of theory.

### 5.3.2. Time-evolution states population

The model Hamiltonian is formed by approximately 4600 parameters. This is used to study the evolution of states in time can be expressed as follows.

$$\begin{aligned}
\hat{H} = &\sum_i \sum_j E_{S_i} |S_i\rangle \langle S_i| + E_{T_j} |T_j\rangle \langle T_j| + \lambda_{SO}^{ij} |S_i\rangle \langle T_j| \\
&+ \sum_k^{N_{vib}} \frac{\omega_k}{2} \frac{\partial^2}{\partial Q_k^2} + \sum_i \lambda_{S_i}^k Q_k |S_i\rangle \langle S_i| + \delta_{S_i}^k Q_k^2 |S_i\rangle \langle S_i| \\
&+ \sum_j \lambda_{T_j}^k Q_k |T_j\rangle \langle T_j| + \delta_{T_j}^k Q_k^2 |T_j\rangle \langle T_j| \\
&+ \sum_{k_1}^{N_{oop}} \sum_i \sum_j \lambda_{SO}^{ij,k_1} Q_{k_1}^2 |S_i\rangle \langle T_j| + \gamma_{S_1,S_2}^{k_1} Q_{k_1} |S_1\rangle \langle S_2| \\
&+ \sum_{j_1} \sum_{j_2} \kappa_{j_1,j_2}^{k_1} Q_{k_1} |T_{j_1}\rangle \langle T_{j_2}| + \mu_{j_1,j_2}^{k,1} Q_{k_1}^2 |T_{j_1}\rangle \langle T_{j_2}| \\
&+ \sum_{k_2}^{N_{ip}} \sum_i \sum_j \lambda_{SO}^{ij,k_2} Q_{k_2} |S_i\rangle \langle T_j| + \gamma_{S_1,S_2}^{k_2} Q_{k_2} |S_1\rangle \langle S_2| \\
&+ \sum_{j_1} \sum_{j_2} \kappa_{j_1,j_2}^{k_2} Q_{k_2} |T_{j_1}\rangle \langle T_{j_2}| + \mu_{j_1,j_2}^{k,2} Q_{k_2}^2 |T_{j_1}\rangle \langle T_{j_2}| + h.c.
\end{aligned} \tag{5.18}$$

Herein i runs over the singlet electronic states and j, $j_1$ and $j_2$ over all the triplets. The k index runs over all the vibrational modes, $k_1$ only considers the out-of-plane normal modes and $k_2$ the in-plane modes. The terms $\lambda_{S_i(T_j)}^k$ and $\delta_{S_i(T_j)}^k$ are the Duschinsky terms $D^T W_i^2 W_0^{-1/2} J$ and $J^T W_i^2 W_0^{-1} J$ along the mode k, respectively. The spin-orbit coupling at Franck-Condon geometry is $\lambda_{SO}^{ij}$ and the vibronic terms are $\lambda_{SO}^{ij,k_1(K_2)}$. The term $\gamma_{S_1S_2}^{k_1(k_2)}$ represents the non-adiabatic vibronic coupling between the singlets along mode $k_1(k_2)$ determined through the state-interaction.

The out-of-plane modes are symmetric and the expansion coefficients are represented by quadratic terms when the value of the coupling at Franck-Condon are not zero. The terms $\kappa_{j_1,j_2}^{k_1(k_2)}$ and $\mu_{j_1,j_2}^{k_1(k_2)}$ are the linear and quadratic off-diagonal non-adiabatic couplings among triplets computed by means of fitting procedure. The term +h.c. is an abbreviation of plus the Hermitian conjugate and is added to indicate that all terms to fulfill the hermitian character of the Hamiltonian are not explicitly indicated.

The bright state in xanthone is $S_2$, the dynamics are started from this state at Franck-Condon geometry. The results with this model indicate the following deactivation path: $S_2 \rightarrow S_1 \rightarrow T_2 \rightarrow T_1$ (Fig. 5.5). The initial internal conversion between singlets is followed by an El-Sayed allowed path to transfer population to the triplets. Finally, the lower-lying triplet state is populated through another internal conversion, the $T_2$ only acts as an intermediate state.

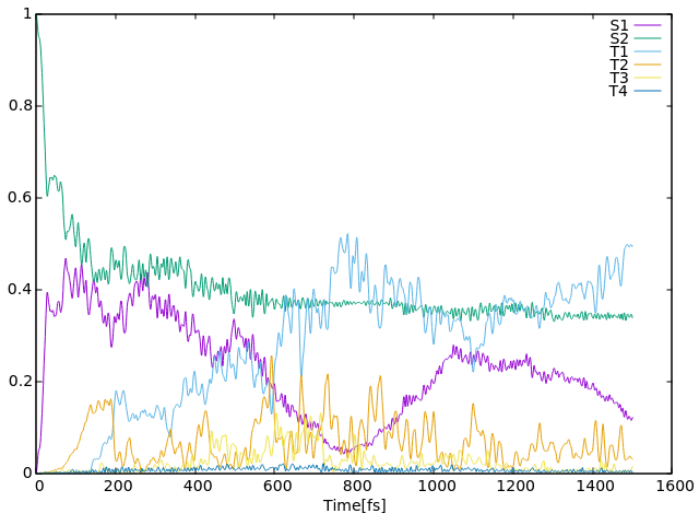


**Figure 5.5.** Time-evolution population for the wave packet dynamics starting in $S_2$ at Franck-Condon geometry.

The first step is an internal conversion which happens very rapidly. Despite the small deviations to 0 from the expected value of the wave function along the out-of-plane normal modes, the quantum treatment of the nuclei

motion produces non vanishing couplings and this is enough to efficiently transfer population between singlet states. The second step is an initial population of the $T_2$ state which rapidly unloads to the $T_1$ state. $T_2$ acts as an intermediate state that accumulates population before transferring it to the low-lying $T_1$ state. The states $T_3$ and $T_4$ remain almost unpopulated during the whole simulation. The simulation indicates that the deactivation process happens within the first 800 fs and then the population starts to oscillate among the involved states, because the modes that can dissipate the excess energy through a bath representing the neighbouring molecules are not included in the model Hamiltonian.

To study the influence of the starting geometry in the deactivation process, we started the simulations in ten random conformations of xanthone obtained by ground state CPMD dynamics. The results do not show significant differences with the ones starting in the Franck-Condon geometry presented in Figure 5.5.

We have also considered the effect of the initial state in the process. The simulation starting from $S_1$ instead of $S_2$ shows the same general deacti-

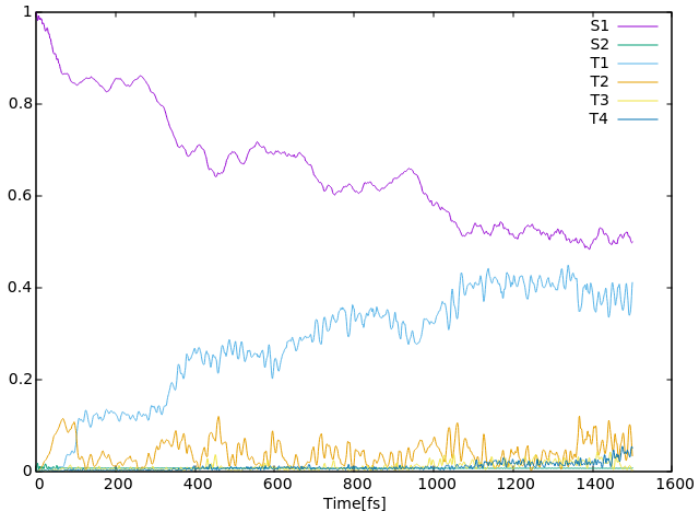


**Figure 5.6.** Time-evolution population for the wave packet dynamics starting in $S_1$ at Franck-Condon geometry.

vation path (Fig. 5.6). However, the population of the triplet states is significantly slower in this case. This suggests that the internal conversion from $S_2$ to $S_1$ acts as an impulse for a more efficient transfer population to the triplets in the xanthone molecule.

Finally, we studied the ratio of population transferred to the triplet states through a vibronic spin-orbit mechanism and the population transferred via an El-Sayed allowed channel. Methodologies using model Hamiltonians are very useful to study these effects because the parameters in the Hamiltonian can be easily included and removed. The $S_1$-$T_2$ spin-orbit coupling was put to zero in a simulation starting from $S_1$ at Franck-Condon geometry. Since, the direct $S_1$-$T_1$ spin-orbit coupling at Franck-Condon geometry is strictly 0, the only possibility to transfer population to the triplets is through the non-vanishing vibronic spin-orbit coupling between $S_1$-$T_1$ along the out-of-plane normal modes. The results show that no population is transferred to the triplets by this path (Fig. 5.7). This can be surprisingly because the non-adiabatic coupling between $S_1$ and $S_2$ is also zero at the Franck-Condon zero and are the non-vanishing vibronic

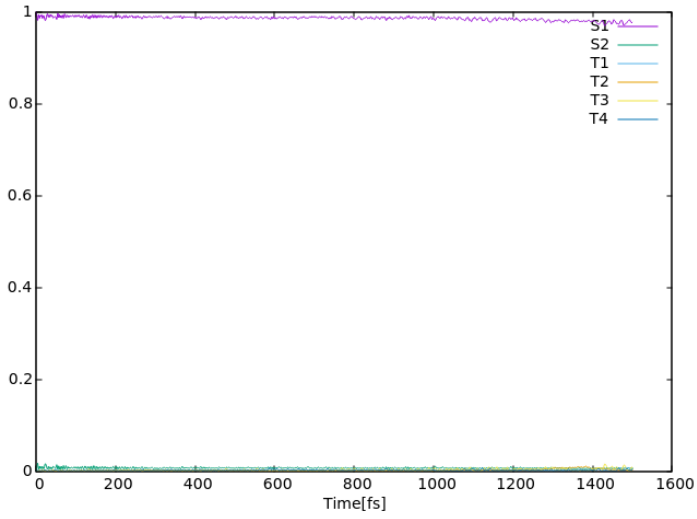


**Figure 5.7.** Time-evolution population for the wave packet dynamics starting in $S_1$ at Franck-Condon geometry without the inclusion of $S_1$-$T_2$ spin-orbit coupling.

couplings along out-of-plane vibrational modes which allow to transfer population between these states. However, the vibronic non-adiabatic couplings between $S_1$ and $S_2$ along these modes are one order of magnitude larger than the vibronic spin-orbit coupling between $S_1$ and $T_1$. Then, this could be the reason why the vibronic spin-orbit couplings between these latter states do not play an important role.

### 5.3.3. Vibrationally resolved absorption spectrum

Quantum wave packet dynamics calculations also allow to calculate other spectroscopic properties such as the absorption. Raab et al. determined the photo-absorption spectrum for pyrazine molecule using a model Hamiltonian including 24 modes with the two lowest singlet states and applying $D_{2h}$ symmetry[18]. Manthe et al. studied the photo-dissociation of the $NO_2$ molecule including the three modes[19]. The spectrum can be calculated from the Fourier transform of the autocorrelation function.[16]

$$\sigma(\omega) \propto \omega \int_{-\infty}^{+\infty} dt C(t) e^{i\omega t} \tag{5.19}$$

Herein, the autocorrelation function takes the expression:

$$C(t) = \langle \Psi(0) | \Psi(t) \rangle \tag{5.20}$$

The autocorrelation function for calculating the absorption spectrum is obtained by placing the initial wave function on the excited state surface of interest at the Franck-Condon geometry. Thereafter, the wave function is propagated in time and the autocorrelation function calculated as the inner product with the wave function at time t=0. The spectrum is obtained by Fourier transform of the autocorrelation function (Eq. 5.19). This approach to compute the vibrational spectrum assumes that the transition dipole moment is constant with respect to the nuclear coordinates as states the Condon approximation.

The Fourier transform in Eq. 5.19 goes to infinity, but the simulation time is necessarily finite. This is particularly problematic in processes where the autocorrelation function does not vanish at infinite time such as occurs

for the photoabsorption to bound states. To solve this shortcoming, the autocorrelation function is multiplied by a damping factor that forces the function to be 0 at time T.

$$g(t) = \cos\left(\frac{\pi t}{2T}\right)\Theta\left(1 - \frac{|t|}{T}\right) \tag{5.21}$$

$\Theta$ is the Heaviside step function that switches from 1 to 0 at time T. This smoothly forces the autocorrelation function to 0, but causes a broadening in the spectral lines.

The photoabsorption spectrum for the bright $S_2$ state is computed. This spectrum is computationally obtained from the Fourier transform using the autocorrelation function obtained from two simulations: a) including couplings among states in the model Hamiltonian and b) without taking into account couplings among states. The spectrum can also be determined from the vibrational overlaps between the $S_2$ and the ground state as implemented in the Gaussian code using a static perspective.[20] The results are also compared with the experimental photoabsorption spectrum. The great advantage of obtaining the spectra from wave packet quantum dynamics is the opportunity to study the effect of other states on it, but it is difficult to obtain information about the vibrations involved in the different transitions. To label each peak with a vibration, one would need to deactivate vibrations one by one of the model Hamiltonian and compare the effect on the spectrum with the one obtained using the complete Hamiltonian. However, from a static picture, it is much simpler to relate each peak with the transitions from the modes causing them. The shapes of the spectra obtained from the static description as a sum of the Franck-Condon factors and the one without considering couplings with other excited states are identical (very small differences caused by the precision of the numerical integration).

Figure 5.8 shows the $S_2$ vibrationally resolved spectra in xanthone. The figure shows the spectrum determined in four different ways. The experimental spectrum was determined by Ohshima et al.[4] and is used as reference to rigidly shift the other spectra with respect to the here established $0_0^0$ peak. From a computational perspective, the spectrum is determined from a static perspective as a sum of the Franck-Condon factors using the

Gaussian code.[20] The spectrum is also computed using the wave packet quantum dynamics explained previously, using a damping factor of 100 fs. Two different spectra have been computed, one including couplings in the model Hamiltonian and the other uniquely happening on the $S_2$ potential energy surface. The spectra that best fit the experimental one are those obtained from a static perspective and from the simulation without including couplings in the model Hamiltonian. The broadening of the peaks in the latter are too wide because of the short damping factor used, but this was used to be consistent with the other spectrum with quantum dynamics where larger damping factors are not possible. These results clearly indicate that the potential energy surface for $S_2$ is well-represented

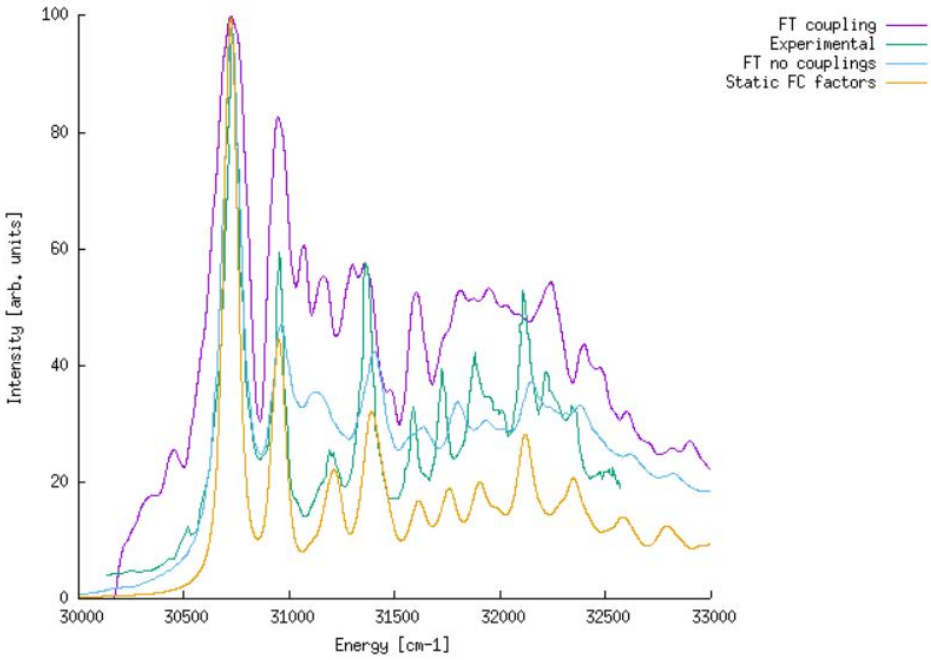


**Figure 5.8.** $S_2$ vibrationally resolved spectrum for xanthone. Intensities are scaled and the energies are shifted to coincide the computed lower energy peak with the experimental $0_0^0$ peak. The experimental spectrum in green, the computed spectrum using the sum of Franck-Condon factors in orange, the Fourier transform without couplings in blue and considering couplings with other states in purple.

but, probably, the couplings in our model Hamiltonian do not fit exactly with the experimental ones. A more precise description of the vertical energies might reduce the discrepancy.

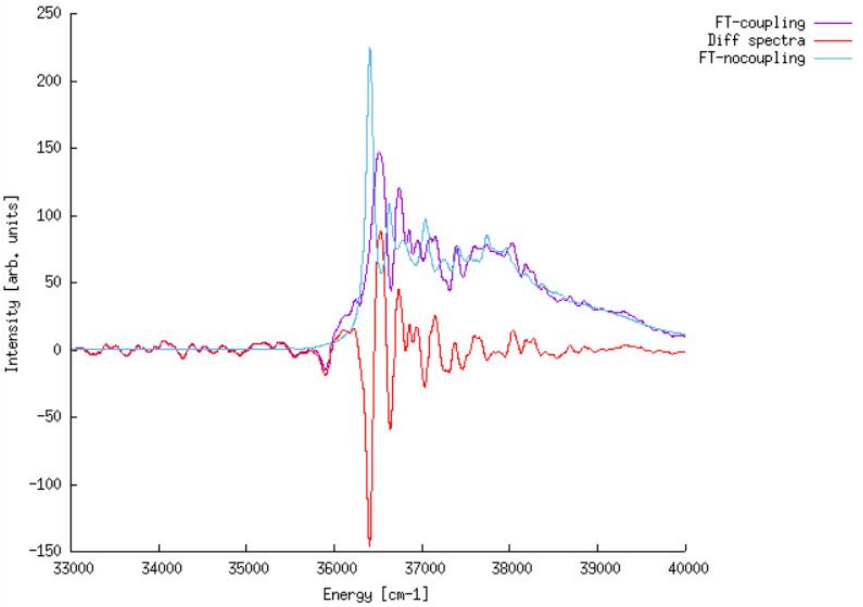


**Figure 5.9.** Unshifted vibrationally resolved spectra for xanthone. In purple the spectrum including couplings in the model Hamiltonian, in blue the one without considering couplings and in red the difference between them.

Figure 5.9 exhibits with more detail the difference between the spectra with and without couplings between electronic states. The population from the bright $S_2$ state is partially transferred to $S_1$ and remains between these states during the first 100 fs, which is the damping factor used. Then, the discussion for the spectrum where the couplings are activated is limited to the $S_1$ state. The figure shows that the inclusion of the couplings in the model Hamiltonian significantly decreases the intensity which can be easily explained by the lower oscillator strength for the interaction between the $S_1$ state and the ground state. Moreover, a slight blue-shift of approximately 100 $cm^{-1}$ is also observed, which could be explained by the largest zero point vibrational energy of $S_1$ state when compared with the one of $S_2$.

## 5.4. Conclusions

The Duschinsky rotation allows to build an elegant and efficient model Hamiltonian to be used in MCTDH. This model needs the Hessians at the optimised geometries of excited states and let us express the diabatic potentials of all the states within the harmonic approximation without the need of a fitting procedure. The effect of the normal modes mixing can also be studied by means of switching the real J matrix by the identity matrix, making use of the somewhat crude approximation of assuming the same normal modes for all the states. Unfortunately, it turned out to be unavoidable to fall back on fitting procedures to obtain accurate estimates for the non-adiabatic couplings between the electronic states, partially invalidating the original attempt to parametrize the Hamiltonian without fitting the potential energy surfaces.

This model has allowed us to study the xanthone photodeactivation mechanism. The results of the fully quantum mechanical time evolution clearly suggest a sequential El-Sayed allowed deactivation mechanism. The overall mechanism is $S_2$ ($^1\pi\pi^*$)$\rightarrow$ $S_1$ ($^1$n$\pi^*$) $\rightarrow$ $T_2$ ($^3\pi\pi^*$) $\rightarrow$ $T_1$ ($^3$n$\pi^*$) with two internal conversions and one intersystem-crossing. The calculations also indicate an almost negligible influence of the vibronic spin-orbit interactions. However, the vibronic effect for the non-adiabatic couplings is crucial because the $S_1$-$S_2$ coupling is almost zero in the ground state geometry (strictly zero when symmetry is imposed) and a fast deactivation requires the displacement along the out-of-plane normal modes to be sizable.

The proposed model Hamiltonian gives a correct perspective of the photophysical problem. However, the large amount of population still remaining in the initial state at the end of the simulation seems to indicate that the model is not completely representing what happens in the real system. The relatively large discrepancies in the vertical excitation energies among the different electronic structure methods suggest that this could be a shortcoming in our model. To increase the quality of the calculated excitation energies, the active space has to be extended beyond the CAS(15,15) limit of the ordinary CASSCF algorithm. Therefore, we are currently exploring the possibility of DMRG, which allows the treatment of much larger active spaces. MCTDH calculations using energies

obtained with the DMRG-CASSCF/NEVPT2 methodology are planned in the near future.

Xanthone molecule shows similar couplings and vertical energies as other carbonyl aromatic compounds such as acetophenone. However, xanthone exhibits intersystem crossing rates significantly faster than the others. The question why immediately comes to the mind, and we conclude that this is mainly for three different reasons based on our calculations and the results obtained for similar systems. The first is that the rigidity of xanthone, on the contrary to other less rigid carbonyl aromatic compounds, largely prevents dissipation of energy along non-efficient normal modes and a larger part of the kinetic energy is employed to reach singular points to transfer population to other electronic states. The second is that the lower symmetry and smaller rigidity characteristic for other compounds of this family allow to directly excite to the $S_1$ state, whereas in xanthone, this state is clearly dark and the $S_2$ is the only state that is initially populated. The population of $S_2$ is rapidly transferred to $S_1$ which implicitly acts as a direct population to this latter but adding some impulse to the wave package arriving in the $S_1$ state via $S_2$ instead of directly from the ground state. The extra impulse leads to a faster continuation of the deactivation process. The last factor that influences the intersystem crossing rate is that the high symmetry of xanthone increases the probability to reach singular points on the potential energy surface, i.e. more accessible conical intersections are available for this molecule than for low symmetry ones.

Finally, we have shown that wave packet quantum dynamics can also be used to compute the vibrationally resolved photoabsorption spectrum by means of Fourier transform of the autocorrelation function of the time dependent wave function. This is not only restricted to pairs of states, but one can also include the influence of couplings with other states on the vibrational spectrum. This seems unnecessary in xanthone, but could become an important ingredient in the study of other systems where the coupling strongly affects the vibrationally resolution of the spectrum.

## 5.5. References

[1] X. Asvos, M. G. Siskos, A. K. Zarkadis, R. Hermann, and O. Brede, *The 2-benzoyl xanthone/triethylamine system as a type II photoinitiator: A laser flash photolysis and computational study*, J. Photochem. Photobiol. A **219**, 255–264 (2013).

[2] T. Shan, Q. Ma, K. Guo, J. Liu, W. Li, F. Wang, and E. Wu, *Xanthones from mangosteen extracts as natural chemopreventive agents: potential anticancer drugs.*, Curr Mol Med. **11**, 666 (2013).

[3] G. Chen, Y. Li, W. Wang, and L. Deng, *Bioactivity and pharmacological properties of α-mangostin from the mangosteen fruit: a review*, Expert Opin. Ther. Pat. **28**, 415–427 (2018).

[4] Y. Ohshima, T. Fujii, T. Fujita, D. Inaba, and M. Baba, *$S_1$ $^1A_2(n\pi^*)$ and $S_2$ $^1A_1$ $(\pi\pi^*)$ states of jet-cooled xanthone*, J. Phys. Chem. A **107**, 8851–8855 (2003).

[5] T. Itoh, *$S_1$, $^1A_2$ fluorescence and $T_1(n,\pi^*)$,$^3A_2$ phosphorescence spectra of xanthone vapor*, Chem. Phys. Lett. **599**, 12–14 (2014).

[6] V. Rai-Constapel, M. Etinski, and C. M. Marian, *Photophysics of xanthone: A quantum chemical perusal*, J. Phys. Chem. A **117**, 3935–3944 (2013).

[7] M. Huix-Rotllant, I. Burghardt, and N. Ferré, *Population of triplet states in acetophenone: A quantum dynamics perspective*, C. R. Chimie **19**, 50–56 (2016).

[8] S. T. Park, J. S. Feenstra, and A. H. Zewail, *Ultrafast electron diffraction: Excited state structures and chemistries of aromatic carbonyls*, J. Chem. Phys. **124**, 174 707 (2006).

[9] F. Duschinsky, Acta Physicochim. URSS **7**, 441 (1937).

[10] M. J. Frisch, G. W. Trucks, H. B. Schlegel, G. E. Scuseria, M. A. Robb, J. R. Cheeseman, G. Scalmani, V. Barone, G. A. Petersson, H. Nakatsuji, X. Li, M. Caricato, A. V. Marenich, J. Bloino, B. G. Janesko, R. Gomperts, B. Mennucci, H. P. Hratchian, J. V. Ortiz, A. F. Izmaylov, J. L. Sonnenberg, D. Williams-Young, F. Ding,

F. Lipparini, F. Egidi, J. Goings, B. Peng, A. Petrone, T. Henderson, D. Ranasinghe, V. G. Zakrzewski, J. Gao, N. Rega, G. Zheng, W. Liang, M. Hada, M. Ehara, K. Toyota, R. Fukuda, J. Hasegawa, M. Ishida, T. Nakajima, Y. Honda, O. Kitao, H. Nakai, T. Vreven, K. Throssell, J. A. Montgomery, Jr., J. E. Peralta, F. Ogliaro, M. J. Bearpark, J. J. Heyd, E. N. Brothers, K. N. Kudin, V. N. Staroverov, T. A. Keith, R. Kobayashi, J. Normand, K. Raghavachari, A. P. Rendell, J. C. Burant, S. S. Iyengar, J. Tomasi, M. Cossi, J. M. Millam, M. Klene, C. Adamo, R. Cammi, J. W. Ochterski, R. L. Martin, K. Morokuma, O. Farkas, J. B. Foresman, and D. J. Fox, *Gaussian˜16 Revision A.03* (2016), gaussian Inc. Wallingford CT.

[11] I. Fdez. Galván, M. Vacher, A. Alavi, C. Angeli, F. Aquilante, J. Autschbach, J. J. Bao, S. I. Bokarev, N. A. Bogdanov, R. K. Carlson, L. F. Chibotaru, J. Creutzberg, N. Dattani, M. G. Delcey, S. S. Dong, A. Dreuw, L. Freitag, L. M. Frutos, L. Gagliardi, F. Gendron, A. Giussani, L. González, G. Grell, M. Guo, C. E. Hoyer, M. Johansson, S. Keller, S. Knecht, G. Kovačević, E. Källman, G. Li Manni, M. Lundberg, Y. Ma, S. Mai, J. P. Malhado, P. A. Malmqvist, P. Marquetand, S. A. Mewes, J. Norell, M. Olivucci, M. Oppel, Q. M. Phung, K. Pierloot, F. Plasser, M. Reiher, A. M. Sand, I. Schapiro, P. Sharma, C. J. Stein, L. K. Sørensen, D. G. Truhlar, M. Ugandi, L. Ungur, A. Valentini, S. Vancoillie, V. Veryazov, O. Weser, T. A. Wesołowski, P.-O. Widmark, S. Wouters, A. Zech, J. P. Zobel, and R. Lindh, *OpenMolcas: From Source Code to Insight*, J. Chem. Theory Comput. **15**, 5925–5964 (2019).

[12] H. D. Meyer, and O. Vendrell, *The MCTDH package*, http://mctdh.uni-hd.de/ (2013).

[13] F. Gatti, and C. Iung, *Exact and constrained kinetic energy operators for polyatomic molecules: The polyspherical approach*, Physics Reports **484**, 1 – 69 (2009).

[14] J. W. Ochterski, *Vibrational analysis in Gaussian* (1999), help@gaussian.com.

[15] M. Etinski, *The role of Duschinsky rotation in intersystem crossing: A case study of uracil*, J. Serb. Chem. **76**, 1649–1660 (2011).

[16] G. A. Worth, H.-D. Meyer, H. Köppel, L. S. Cederbaum, and I. Burghardt, *Using the MCTDH wavepacket propagation method to describe multimode non-adiabatic dynamics*, Int. Rev. Phy. Chem. **27**, 569–606 (2008).

[17] T. P. Straatsma, R. Broer, S. Faraji, R. W. A. Havenith, L. E. Aguilar Suarez, R. K. Kathir, M. Wibowo, and C. de Graaf, *GronOR: Massively Parallel and GPU-Accelerated Non-Orthogonal Configuration Interaction for Large Molecular Systems*, J. Chem. Phys. **152**, 064 111 (2020).

[18] A. Raab, G. Worth, H.-D. Meyer, and L. S. Ceberdaum, *Molecular dynamics of pyrazine after excitation to the $S_2$ electronic state using a realistic 24-mode model Hamiltonian*, J. Chem. Phys. **110**, 936 (1999).

[19] U. Manthe, H.-D. Meyer, and L. S. Cederbaum, *Multiconfigurational time-dependent Hartree study of complex dynamics: Photodissociation of $NO_2$*, J. Chem. Phys. **97**, 9062 (1992).

[20] V. Barone, J. Bloino, and M. Biczysko, *Vibrationally-resolved electronic spectra in GAUSSIAN 09* (2009), help@gaussian.com.

# 6.

# Azobenzene trans-cis isomerization studied with trajectory surface hopping molecular dynamics

## 6.1. Introduction

Jean-Pierre Sauvage, J. Fraser Stoddart and Bernard L. Feringa were awarded with the Nobel prize for the design and synthesis of molecular machines in 2016. These molecular machines are subunits joined by a mechanical bond and are mainly grouped in two different families, the catenanes which are compounds formed by interlocked rings and the rotaxanes that are rings threaded by a molecular axis. The most important application of these compounds is that they can act as a motor by the interchange between their two-different forms which are known as the extended and the contracted, mimicking the muscle behaviour. Reversible motions proceed through hydrophobic forces, size constraints, changes in the polarity of solvents or the photoisomerization of azobenzene or stilbene derivatives. [1]

The application of azobenzene photoisomerization in molecular machines has been probably the most relevant in the last years. However, there are other important applications such as light energy harvesting or energy storage because of their strong electronic absorption. The ring substitution allows also the tuning of this family of compounds to create appropriate molecules to work as solar fuels, pigments or dyes. [2] Another interesting property of azobenzene derivatives is their capacity to induce spin-crossover by the trans-cis forward and backward reaction. Venkataramani et al. published a working example of reversible SCO induced by coordination changes in a porphirine $Ni^{2+}$ complex. [3] In their work, the azobenzene derivative (3-phenyl-azopyridine) was joined to the porphyrine ring and after light irradiation the initial square planar structure with low-spin electron configuration system was converted to a penta-coordinated square-pyramidal coordination sphere with a triplet electron configuration. The change in the Ni coordination is because the N of the pyridine ring is located much closer to the Ni ion in the cis- than in the trans isomer and henceforth leading to an increase of the Ni coordination.

These diverse possibilities of azobenzene and its derivatives have put them on the focus of many researchers for quite some years. The forward and backward isomerization reaction of azobenzene (Fig. 6.1) can be induced by several mechanisms such as mechanical stress, electrostatic stimulation or light irradiation. The latter has been extensively studied from both

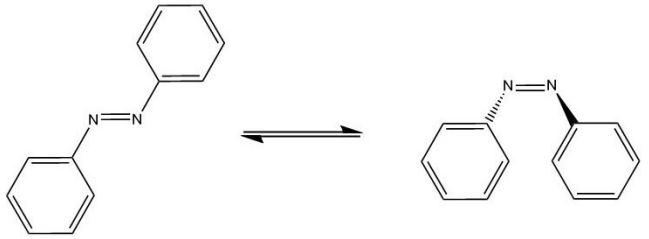

**Figure 6.1.** Schematic representation of the trans-(left) to cis-(right) azobenzene isomerization.

experimental and theoretical perspectives. Most of the peculiarities have been rationalised but some of them still remain unclear. The backward reaction (formation of the trans-) can be carried out without necessity of an external stimulus because of the larger stability of the trans isomer.

The main singlet excited states involved in the process are $S_1$ with $n\pi^*$ character, the $S_2$ state with $\pi\pi^*$ character and a higher-lying state with $n^2\pi^{*2}$ character, following the ordering at the Franck-Condon geometry. The trans-azobenzene shows a $C_{2h}$ symmetry which explains the weak $S_0 \rightarrow S_1$ transition, in principle forbidden by symmetry, and the strong $S_0 \rightarrow S_2$ symmetry-allowed transition. This has been observed from the first spectroscopic experiment in the 1950s,[4] and allows to classify the $S_2$ as a bright and the $S_1$ as a mostly dark state. The role of the triplet states in the deactivation process has also been extensively studied. Despite the controversies during the decade of the 1960s,[5,6] Bortolus determined at the end of 1970s a very low quantum yield for the lowest triplet state, proving that they do not participate in the photochemical isomerization process, which hence, uniquely happens in the singlet manifold.[7]

The first experiments on azobenzene and its derivatives showed wave length dependent quantum yields which varied depending on the irradiated initial excited state.[8,9] The yield for the trans $\rightarrow$ cis isomerization was approximately 0.2 from the $^1n\pi^*$ state and 0.1 from the $^1\pi\pi^*$.[9] This was explained because the different excited states induced different isomerization mechanisms. Two main mechanisms for the process were proposed: the rotation along the CNNC dihedral angle and the inversion along one

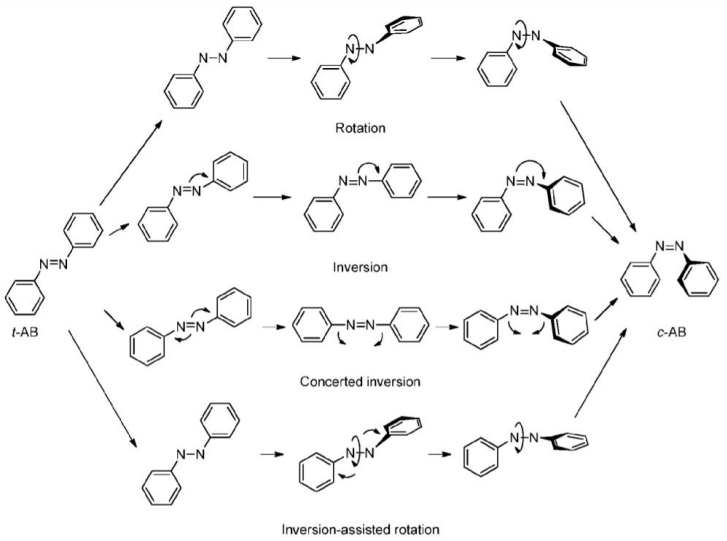


**Figure 6.2.** Main photoisomerization mechanisms for azobenzene. The two classic mechanisms at the top and the more recently proposed at the bottom. Figure extracted from Ref. 10.

of the NNC angles. Figure 6.2 shows the proposed isomerization mechanisms in azobenzene, the classical rotation and inversion are at the top of the figure.

Nerbonne was one of the first studying the thermal isomerization of azobenzene. The conclusions of this study were that the rotation mechanism were favoured above the inversion after determining the variation of enthalpy and entropy in different solvents and a cholesteric liquid crystal solvent.[11] Rau et al. studied the rotation-blocked azobenzene-2-phane derivative and they observed that its quantum yield was 0.24 for the excitation to the $^1n\pi^*$ and 0.21 for the excitation to the $^1\pi\pi^*$ state, showing almost wave length independent yields when the rotation was blocked.[8] Later, Bortolus et al. determined the quantum yields using cyclodextrins, cyclic oligosaccharides compounds, of different hollow sizes.[12] The experiments again confirmed that the quantum yields were wave length independent when the rotation was blocked. Moreover, they suggested that the isomerization along the $^1\pi\pi^*$ state was mainly through a rota-

tion mechanism and along the $^1n\pi^*$ through an inversion mechanism. In addition, a conical intersection between these states should be accessible close to a planar geometry.

More recent experimental studies determined the variation of spectroscopic data during the isomerization process. Lednev et al. performed femtosecond time-resolved UV-visible absorption spectroscopy in trans-azobenzene.[13] They observed a first transition of about 1 ps and a longer-lived component of 13 ps, the first was assigned to a relaxation from the $\pi\pi^*$ to the $n\pi^*$ state and the latter to a transition from the $S_1$ to the ground state. However, the low time resolution of the instruments at that time and the signal to noise ratio on the bleaching did not allow to clearly determine the quantum yield neither the overall mechanism. At the end of 1990s, Fujino et al. performed a time-resolved Raman spectroscopy in trans-azobenzene which also suggested a very rapid internal conversion to the $S_1$ state and later a much slower decay time to the ground state which was highly solvent dependent. They concluded in this study that the inversion mechanism was dominant because they found similar frequencies in the N=N stretching for the first excited and the ground state and larger N-N distances would be necessary for a rotation mechanism.

From the theoretical perspective, Diau performed calculations of the $S_1$-$S_0$ potential energy surfaces topology at CASSCF level.[14] In the methodology, he included 6 electrons distributed over 6 molecular orbitals and performed scans with restricted optimizations along one CNN angle (inversion mechanism), CNNC dihedral angle (rotation) and both CNN angles (concerted inversion). He found a conical intersection for the rotation path which is a reactive channel (formation of the cis isomer) and a sloped conical intersection for the new concerted inversion mechanism (third row Fig. 6.2) where a non-reactive channel is described (formation again of the trans isomer in the ground state). Gagliardi et al found in their static calculations at MS-CASPT2 level, whose active space is formed by 14 electrons over 12 molecular orbitals, that the $S_3$ at Franck-Condon geometry (the $n^2\pi^{*2}$ state) has a deep minimum at the 90° value of the CNNC dihedral angle.[15] Moreover, their results showed that this state crosses with the $\pi\pi^*$ state near the equilibrium geometry through the potential energy surfaces they rationalised the short lifetime of the $S_2$ state and the lower quantum yield from this.

Around the same time, the study of the azobenzene photoisomerism was extended to non-adiabatic dynamic simulations. Persico and coworkers performed, to the best of our knowledge, the first simulations, combining Tully's algorithm with an on-the-fly semiempirical calculation of the potential energy surfaces. They started the simulations from a large number of independent geometries close to the cis and trans Franck-Condon geometries and excited both the $S_1$ and the $S_2$ states. Their results showed that the rotation mixed with an opening of the CNN angles, i.e. inversion assisted-rotation (fourth row in Fig. 6.2) was the preferred mechanism. They also observed larger quantum yields from the cis isomer and when the process started from the $^1n\pi^*$ state.[16,17] Yuan et al. performed simulations using a semiclassical method where the electronic states were calculated at each time step solving the time-dependent Schrödinger equation at TD-DFTB level and the laser pulse was explicitly included in the Hamiltonian.[18] Their dynamics suggested that dominant mechanism starting the process from both the $^1n\pi^*$ and the $^1\pi\pi^*$ states was the rotation. They suggested that the quantum yield from the $S_2$ state was lower because the decay could occur at partially twisted geometry (CNNC dihedral 135°) in contrary to the twisted geometry (CNNC dihedral 90°) reached from the lower excited state. Ootani et al. performed a dynamic simulation from the $S_1$ state using trajectory surface hopping with Tully's algorithm using CASSCF potential energy surfaces computed with a minimal basis set and an active space including six electrons distributed over four molecular orbitals.[19] Their simulations also suggested that the main mechanism was a rotation and they distinguished between clockwise and counterclockwise torsions depending on the positive or negative value of the CNNC dihedral angle, respectively. Weingart et al. carried out dynamic simulations using trajectory surface hopping and OM2/MRCI methodology for the electronic structure. They started the processes from the cis isomer irradiating the $S_1$ state.[20] They observed that the deactivation mechanism was a rotation and the quantum yields were high, as expected for the cis-isomer. Moreover, they studied the chiral character of the cis-isomer because of its helicity and they concluded that the deactivation follows mostly a P-channel because this channel has larger gradients to the $S_1/S_0$ conical intersection than the M-channel. Their results found a ratio 77:23 favouring the P- over the M-helicity.

The deactivation of the $^1n\pi^*$ state is generally accepted to take place through inversion and rotation, i.e. the inversion assisted rotation, but the deactivation mechanism from the $\pi\pi^*$ state for trans-azobenzene still shows some controversies. A recent study combining highly accurate methodologies from both experimental and theoretical perspectives by means of sub-20 fs transient and non-linear absorption spectroscopy and CASPT2 MD simulations were proposed with the aim of clarifying some details about the $S_2$ deactivation.[21] Three different mechanisms to explain the apparent violation of Kasha's rule in trans-azobenzene has been proposed. These three non-reactive (or at least low-reactive) channels are: a) the inversion-assisted rotation shared in the deactivation from both excited states, b) the "hot" channel which considers that there is a conical intersection at higher energy than the vertical $S_1$ energy and c) the "phantom" state which suggests that dark states participate in the deactivation of the process. Their 0 K dynamics indicates that the internal conversion to the $n\pi^*$ state from the $\pi\pi^*$ state is produced in a planar geometry with a distortion along the CNN bending, then the system could reach a conical intersection with the ground state along the torsion mode or a non-reactive conical intersection along the CNN bending which is not accessible from a direct excitation to the $n\pi^*$ state. Then, their results strongly suggest that there is no violation of Kasha's rule and the deactivation is produced from the "hot" channel because they also indicated that no more states were necessary in their calculations.

This chapter is based on a previous static study in our group based on a MS-CASPT2 description of the potential energy surfaces and critical points.[22] Casellas et al. observed an intersection between the $\pi\pi^*$ and the $n^2\pi^{*2}$ states near the Franck-Condon geometry with a small CNNC dihedral distortion. This state has larger gradients than the $n\pi^*$ state to reach a minimum at the twisted geometry which has a value of 90° for the CNNC dihedral. They also found at this level of theory a conical intersection between the $\pi\pi^*$ and the $n\pi^*$ states in a pedal-like conformation. They found for the $n\pi^*$ state a conical intersection with the ground state at the twisted conformation and another conical intersection in a planar conformation at a higher energy. They also studied the potential energy surfaces at CASSCF level and did not found the pedal-like conical intersection neither a twisted minimum for the $S_1$ state.

The main goal of this chapter is to explore the deactivation paths from an explicit dynamic treatment. A large number of independent trajectories calculating the potential energy surfaces at MS-CASPT2 is (almost) impossible. Alternatively, we exclude the dynamic electron correlation on the electronic structure calculation by means of CASSCF method. We have used trajectory surface hopping simulations at room temperature with the potential energy surfaces computed at state-averaged CASSCF level starting the simulations from the states with largest oscillator strengths with the ground state and from the $n\pi^*$ state. In addition, we have performed a vibrationally cold simulation including the dynamic electron correlation in the calculation of the potential energy surfaces by means of MS-CASPT2. This simulation is started at the pedal-like geometry.

## 6.2. Computational details

We have performed the non-adiabatic simulations with trajectory surface hopping using Tully's algorithm as implemented in *Molcas*.[23] The potential energy surfaces are computed using the state-average complete active space self consistent field (SA-CASSCF) including six states in the average. The active space is formed by 10 electrons distributed over 8 molecular orbitals (Fig. 6.3) and the basis set is 6-31G*. The simulations are started at different initial conditions (geometries and momenta). The geometries are taken from a CPMD ground state dynamics and the momenta are randomly established with the condition that the initial velocities are scaled for a 298 K dynamics and the time step used is 1 fs. The gradients of the potential energy surfaces are computed analytically, therefore Cholesky decomposition is not used (it has only been implemented in very recent versions). The default set-up for the surface hopping part is kept, the decay factor is established at 0.1 $E_h$ to enable the decoherence correction in the population density matrix and 200 integration steps are used to interpolate/extrapolate between two consecutive Newton steps.

The different initial geometries are taken from a ground state CPMD dynamics. This is obtained performing one simulation on the ground state in gas phase during 60.5 ps with a time step of 0.12 fs through the CPMD 3.15 package[24] using periodic-boundary-conditions (PBC). The

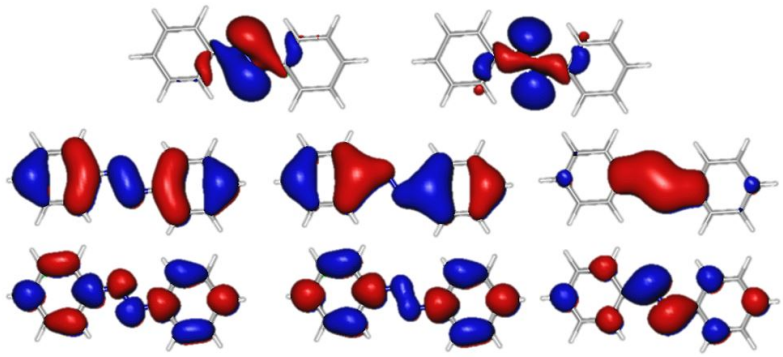

**Figure 6.3.** Active space natural orbitals in azobenzene for a CAS(10,8). The two N non-bonding orbitals in the top row, the three $\pi$ bonding orbitals in the middle and the three $\pi^*$ orbitals at the bottom row.

system cell is a cubic box of 12 Å of side length where the core electrons are described using Troullier-Martins non-conserving pseudopotentials and valence electrons are treated using a plane waves basis set using a cut-off of 70 Ry.

The simulation at MS-CASPT2 level for the potential energy surfaces included 10 states in the state-average and used the same active space previously mentioned. At this level of theory, the gradients have to be determined numerically which dramatically increases the computational cost of the simulation. However, the default $10^{-4}$ Cholesky decomposition can be employed to partially reduce it. The simulation is a 0 K MD simulation, the system does not have initial velocity, with 1 fs as time step and is started at the pedal-like conformation in the n$\pi^*$ state. This calculation is performed using version 2 of COBRAMM package [25] which computes the non-adiabatic transitions by means of Tully's algorithm and is coupled with OpenMolcas which determines the potential energy surfaces. Tully's algorithm with the Persico decoherence are included in the trajectory surface hopping.

## 6.3. Results and discussion

Most ab initio non-adiabatic molecular dynamics are performed using (TD-)DFT to determine the potential energy surfaces.[26–29] This electronic structure based method includes dynamic electron correlation at very low computational cost. In the standard linear response TD-DFT the excited states are calculated using the ground state reference wave function which is only formed by one Slater determinant. This is problematic in strongly correlated materials or in situations where the electronic structure shows strong biradicalar character such as the twisted conformation in the rotation mechanism for azobenzene. However, the introduction of the spin-flip algorithm in TD-DFT enhances the performance of the method in most of these situations.[30] The inability of the standard method to represent this conformation was the reason to discard it and we decided to perform the trajectory surface hopping simulations with a multi configurational electronic structure based method such as SA-CASSCF or MS-CASPT2.

The results are divided in two sections, in the first we show the static calculations at the level of theory that we used in the simulations and in the second we present the results of the simulations with different initial states and electronic structure methods.

### 6.3.1. Static calculations

There are in the literature four isomerization mechanisms in azobenzene (Fig. 6.2). We have studied their plausibility by means of monodimensional scans with restricted optimizations along the internal coordinates that define each mechanism. In the inversion-assisted rotation mechanism, the CNNC dihedral is kept fixed at each point of the scan and all the other internal coordinates are optimised. In the rotation mechanism, a scan of the CNNC value is performed with the CNN angles fixed at 120°. In the inversion mechanism, one CNN angle is gradually increased while the other coordinates are freely optimised and in the concerted inversion not just one but the CNN angles on both sides of the N=N bond are simultaneously scanned, taking the same value for them at each point of the

scan. All the geometries are obtained by a restricted optimizations for the ground state at CASSCF level.

The mechanisms for the inversion and the concerted inversion do not show a favourable gradient for the cis-formation from any of the excited states. The results for the inversion-assisted rotation and the rotation are similar and both indicate a strong tendency for the excited states to reach the twisted geometry. Figure 6.4 shows the scan along the CNNC dihedral angle in the inversion-assisted rotation mechanism.

The observation of the adiabatic energy of the states shows that at the trans geometry (CNNC=180°) the $S_2$ and $S_3$ are nearly degenerate at CASSCF level. The former has a mixed $n\pi^*$ and $\pi\pi^*$ character and its dominant electronic configuration arises from a double excitation from the n and $\pi$ orbitals to the $\pi^*$. The $S_3$ state is clearly a $\pi\pi^*$ state. At MS-CASPT2 level, the $S_2$ is the $\pi\pi^*$ state largely separate to the $S_3$. The $n^2\pi^{*2}$ state is not found at this geometry among the 6 lowest roots. The analysis in a partially twisted geometry (CNNC=120°) shows that the $S_0$ has closed shell character, the $S_1$ is the $n\pi^*$, the $S_2$ is the $n^2\pi^{*2}$ and the higher states are mixtures of $n\pi^*$ and $\pi\pi*$ states. The comparison of the CI-coefficients at this geometry and at the Franck-Condon geometry exhibits that the coefficient in the former for its main configuration is smaller, which indicates that the adiabatic states are more mixed in this twisted conformation. This is even more pronounced in the twisted geometry where the ground and the second excited states are the in-phase and out-of-phase linear combinations of the closed shell and the $n^2\pi^{*2}$ configurations. The strong mixture of configurations suggests a strong non-adiabatic coupling between these diabatic states, arising from each configuration, which should be nearly degenerate at this conformation.

Figure 6.4 also allows to identify the root flipping in the adiabatic basis. At the trans conformation the $n^2\pi^*$ state does not appear within the six roots and in the twisted conformation is the third root at both levels of theory. One can distinguish the $n^2\pi^{*2}$ state as the fourth adiabatic root ($S_3$) at MS-CASPT2 level in the range of 150-170° and as the third adiabatic root ($S_2$) at smaller dihedral values, with a careful attention on the gradients in each adiabatic surface. The root flipping is also responsible for the strange

shapes of the adiabatic surfaces on the borders of the graph because states with different character are represented at each geometry.

The most important differences between CASSCF and MS-CASPT2 for the dynamic simulations are found in the gradients of the $S_2$ state, where they are significantly larger in the former. The ground state is similarly represented at both levels of theory and the curves for the first excited state along this mode are nearly parallel but with an overestimation of 8 kcal/mol approximately for CASSCF with respect to the, in principle,

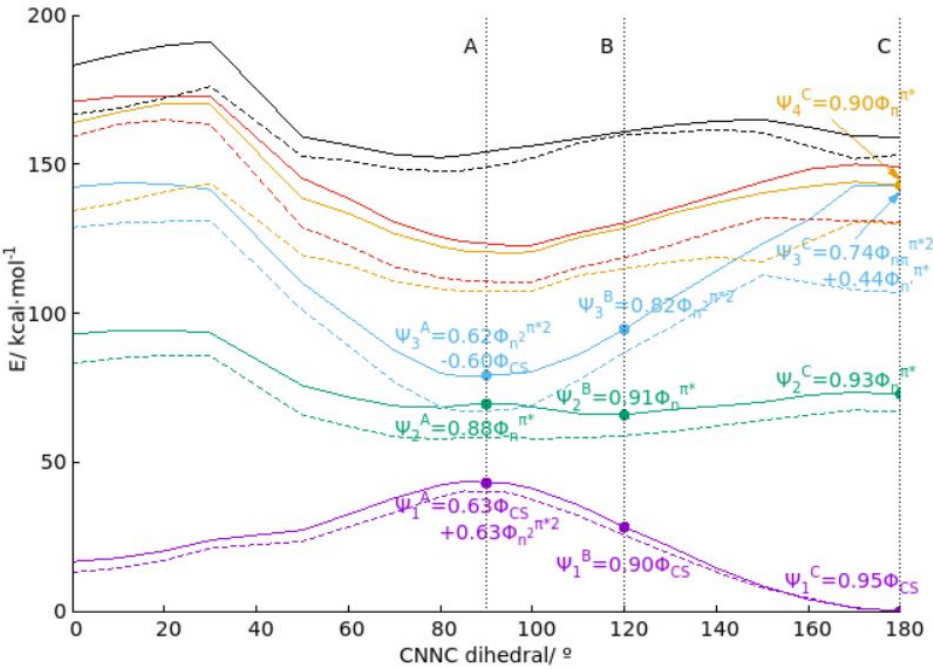


**Figure 6.4.** Adiabatic potential energy surfaces along the CNNC dihedral angle for the inversion-assisted rotation mechanism. The ground state is represented in purple, $S_1$ state in green, the $S_2$ in blue, the $S_3$ in orange, the $S_4$ in red and the $S_5$ in black. The solid lines represent the SA(6)-CASSCF energies and the dashed lines the MS(6)-CASPT2 ones. The wave function for the low-lying states in two different geometries is expressed in the basis of their main CSFs. The reference CSF is the closed-shell ($\phi_{CS}$) and all the others are expressed as singly or doubly configurations respect this one.

more accurate MS-CASPT2 curves. In addition, the energy of the $\pi\pi^*$ state is also overestimated in the Franck-Condon conformation at CASSCF level, in this case by not less than 35 kcal/mol.

### 6.3.2. Dynamic simulations

The results of the simulations mainly consist in the determination of quantum yields, the lifetimes of the excited states and the confirmation of the proposed mechanism from the static calculations. We distinguish between the two enantiomers of cis-azobenzene that are formed when reaction occurs and classify the inversion-assisted rotation mechanism depending on the direction of rotation of the molecules. These concepts are probably not so standard and are briefly explained in the next lines.

The chirality is not only limited to molecules possessing a stereogenic center. Axial chirality is referred to stereo-isomerism resulting from a chirality axis when the molecule is not superposable to its mirror image. This property can also be called helicity, since the axis has a helical or propeller geometry which is observed in cis-azobenzene (Fig. 6.5). It shows the P- and M- enantiomers which the plus or minus rotation of the helix axis, respectively.

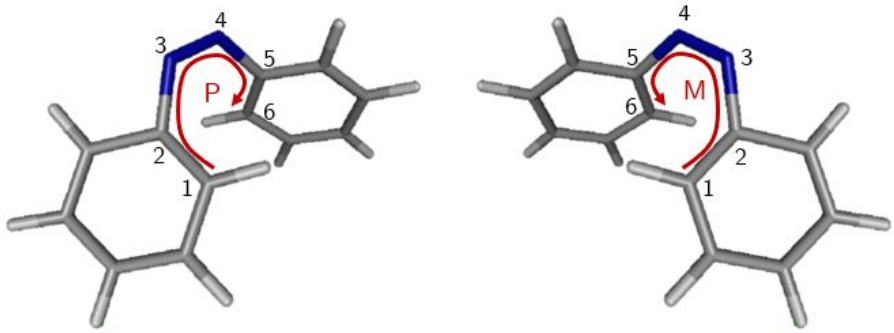


**Figure 6.5.** Chirality in the cis-azobenzene due to helicity. P- enantiomer in the left and M- in the right.

The generation of the cis from the trans isomer following a rotational mechanism can be produced by a clock- or counter-clockwise rotation depending on the sense of this rotation from the trans region to reach the twisted conformation (Fig. 6.6). The clockwise rotation generates the P-enantiomer and the counter-clockwise the M- when the cis isomer is reached. However, this also is used to give name to the channels and the path along twisted conformations with positive CNNC dihedral is known as P-channel and the M-channel goes across twisted conformations with negative dihedral values. The positive or negative value of the dihedral in the hopping to the ground state conformations has been the criterion that we have followed to discern between the cis enantiomer formed and the P or M channel gone through. The dihedral angle 100 fs after the hopping to the ground state has been used to determine whether the produced isomer was the cis when values were close to 0 or the trans when values oscillate around 180°.

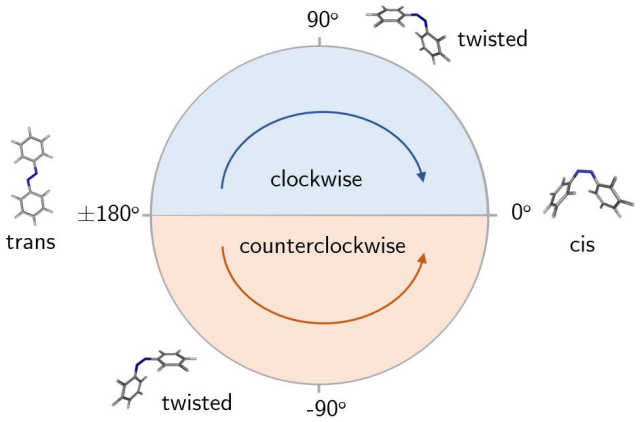


**Figure 6.6.** Clockwise and counter-clockwise torsion from trans to cis-azobenzene.

The results are presented in three different sections. The first and the second section describe the simulations using CASSCF to determine the potential energy surfaces and in the third section, we present the simulation at the MS-CASPT2 level. The results from the high-lying and bright $\pi\pi^*$ states are shown in the first section and those obtained from the simulations at the $n\pi^*$ state are shown in the second. In these simulations,

we have employed different initial conditions, whereas we have only calculated one trajectory for MS-CASPT2 because of the large amount of CPU time required in these calculations.

### CASSCF MD starting at $^1\pi\pi^*$ state

The dynamics from the bright states are started from 190 different random conformations generated by a CPMD ground state dynamics simulation. The directions of the initial momenta are randomly generated and adjusted to the kinetic energy corresponding to 298 K. The simulations are started in those states with large oscillator strengths (>0.1). We analyse the results of 296 independent simulations each of them using a time step of 0.97 fs and run along 970 fs. Two of these trajectories have been discarded because during the simulations, the bond between one C-H pair has been broken artificially.

Figure 6.7 shows the time evolution average population of the adiabatic states. The initial populated states are the $S_2$, $S_3$, $S_4$ and $S_5$ adiabatic states with larger populations for the first two. The analysis of the character of adiabatic multiconfigurational electronic states is intrinsically complicated as both CI expansion and orbitals have to be looked at simultaneously. Therefore, an accurate analysis of the character of each state along the trajectory requires an important amount of human intervention or an efficient program which has not been developed. At the CASSCF ground state optimised geometry, $S_2$ and $S_3$ are nearly degenerate at this level of theory, small geometrical distortions can induce a change in the order of the character of these states. The $\pi\pi^*$ state has larger oscillator strengths than the $S_2$ state at Franck-Condon which is a linear combination of different configurations containing n$\pi^*$ excitations. This suggests that character of the initial state is mainly $^1\pi\pi^*$, for both $S_2$ and $S_3$ adiabatic states. The evolution of the adiabatic states population in time also indicates that the $S_3$-$S_5$ states rapidly transfer their population to the $S_2$ state which reaches a maximum of population at 55 fs. The $S_1$ state maximum population is found at 90 fs and after that starts a relatively slow population decay. The ground state population increases rapidly and achieves a 50% of the population at 274 fs.

The analysis of the adiabatic state populations in time induces a general idea about the rates of the overall process, but it is not enough to determine the character of the states playing a role neither the exact details of the possible relaxation paths gone across. In this case, the simultaneous rise of the $S_0$ population and the decrease of the $S_1$ and $S_2$ populations cannot distinguish between the deactivation paths in which the second excited singlet state directly transfers population to the ground state or via the intermediate first excited state. To have a clearer picture about the mechanism, we have performed a more exhaustive analysis about whether the hopping to the ground state is produced from the second or the first excited state. Table 6.1 shows the amount of trajectories that relax for each of these channels and their quantum yields. The sum of the trajectories for each of these paths does not coincide with the total number of analysed trajectories because some of them are still found in excited states at the end of the simulation, the so-called resonant or non-reactive trajectories. This is also observed in the population of the adiabatic states that the ground state does not reach the 100% of population at the end

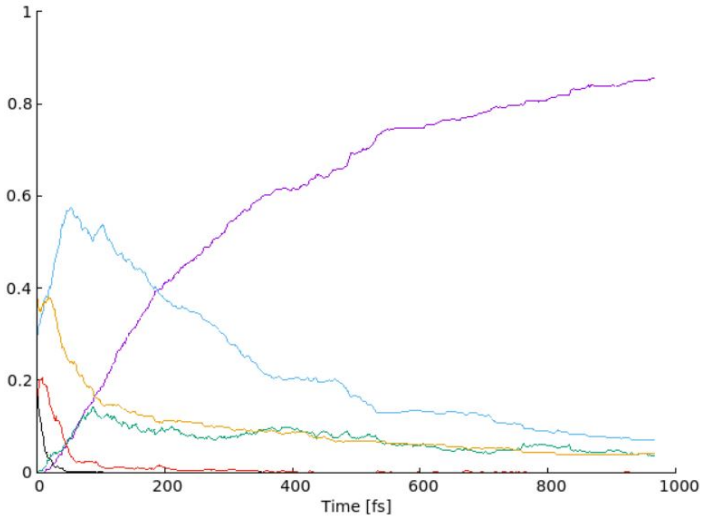


**Figure 6.7.** Time evolution of the adiabatic state population for the dynamics starting from the bright states. The ground state is represented in purple, $S_1$ state in green, the $S_2$ in blue, the $S_3$ in orange, the $S_4$ in red and the $S_5$ in black.

**Table 6.1.** Number of trajectories with the percentage from the total of reactive trajectories and quantum yield along each path.

| Paths | Trajectories (Percentage) | $\Phi_{cis}^{(a)}$ |
|---|---|---|
| $S_2 \rightarrow S_1 \rightarrow S_0$ | 158 (68%) | 0.25 |
| $S_2 \rightarrow S_0$ | 75 (32%) | 0.25 |

$^{(a)}\Phi_{cis}$is the quantum yield defined as $\frac{\#cis}{\#reactive} = \frac{\#cis}{\#cis+\#trans}$

of the simulation time (Fig. 6.7).

Furthermore, we have analysed in the reactive trajectories (those that finish in the ground state) the most relevant geometrical parameters (CNNC dihedral angle, CNN angles and both C-N and N-N distances) at the hopping points to the ground state.

Figure 6.8 shows that the geometries where the hopping from the excited to the ground state is produced have a CNNC dihedral value typically oscillating around the twisted geometry (90°) and a CNN average angle in the range between 120-135°. This confirms that the main isomerization mechanism in azobenzene is the inversion-assisted rotation, because the rotation along the dihedral is accompanied by a slight increment of the CNN angle which in the ground state has a value of 114° in the trans isomer for the CASSCF optimised geometry. In addition, the results show that the surface hoppings produced in geometries with smaller CNNC dihedrals, in absolute value, than the 90° form the cis photoproduct and those geometries of larger dihedral values form the trans isomer. There is no apparent relation between the value of the CNN angle in the hopping geometry and the final isomer. The C-N and the N-N distances have also been studied in these geometries but again no relation is observed between these values and the photoproduct.

In addition, Figure 6.8 does not indicate any preference for any of the enantiomeric channels. Almost the same number of trajectories decay through the P- and M- channels. The results also show nearly identical results from the direct deactivation from the $S_2$ and the deactivations via $S_1$ state. The only observed difference is that those trajectories relaxing to the ground state without a large modification of the dihedral angle (those

points closer to the borders in Fig. 6.8) mainly belong to a relaxation via the $S_1$ state, this could be explained because the larger gradients from the Franck-Condon to the twisted geometry for the $S_2$ state compared with $S_1$.

Figure 6.9 exhibits the variation of the adiabatic states energy and the main geometrical parameters for two representative trajectories. One of them is a reactive trajectory which produced a cis photoproduct where the ground state is populated from the second excited state and the second is a non-reactive trajectory trapped in $S_2$ at the end of the simulation. There are more different types of independent trajectories such as reactive ones forming the trans photoproduct, non-reactive trajectories trapped in $S_1$... For the sake of simplicity, we perform a careful analysis of these

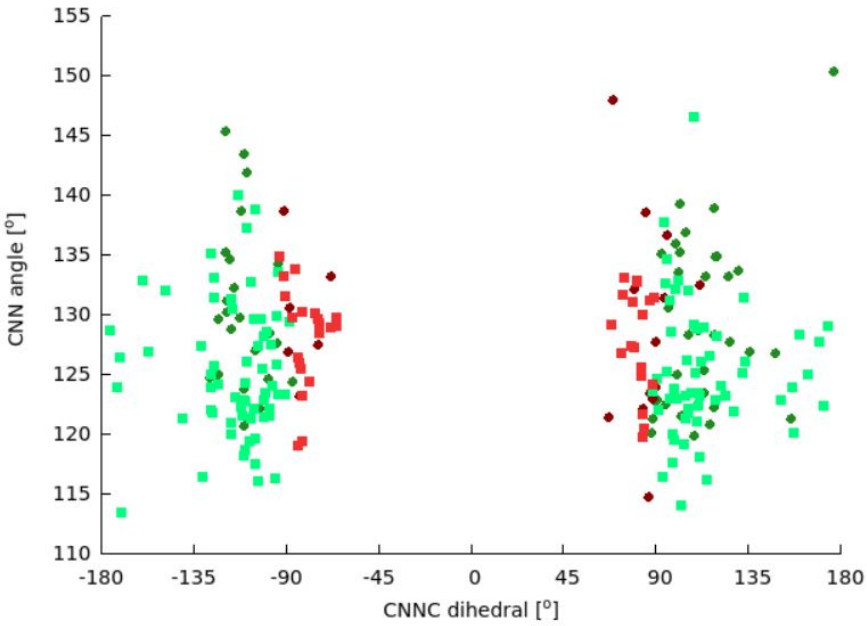


**Figure 6.8.** CNNC dihedral angle and average CNN angle at the ground state hopping geometry. The colors indicate the resulting photoproduct: green, trans-azobenzene and red, cis-azobenzene. The circles with darker colors indicate the direct hopping from $S_2$ and the squares with light colors the hopping from the $S_1$ state.

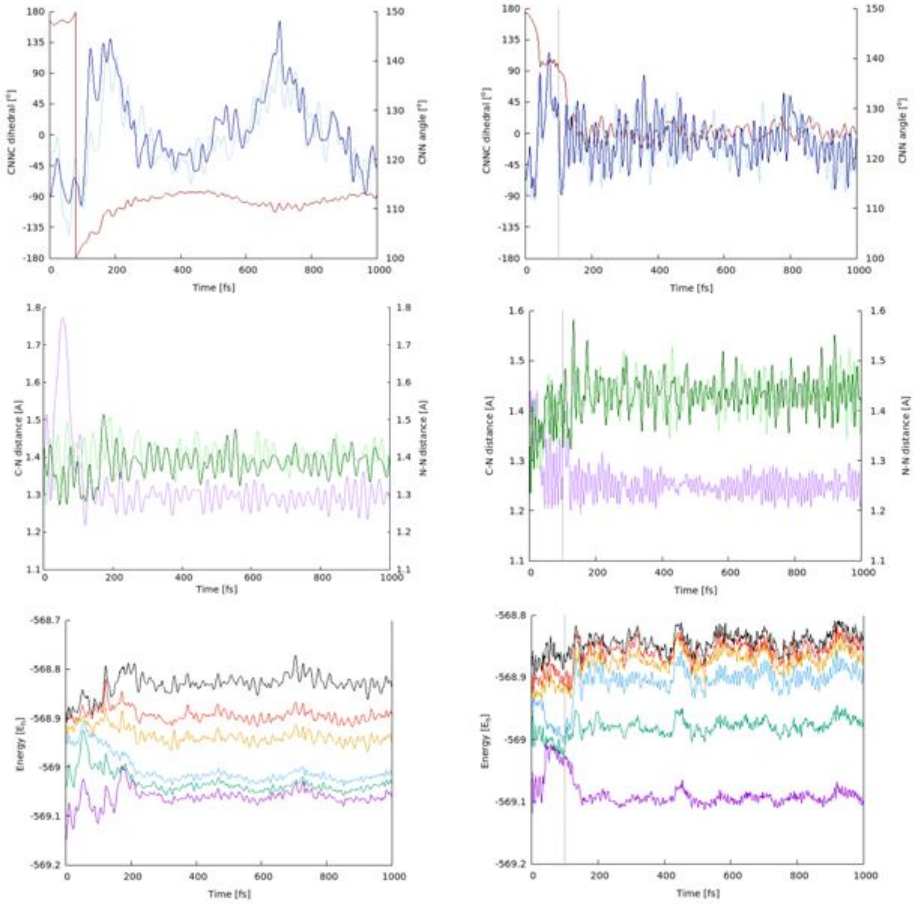


**Figure 6.9.** Plots of the main geometrical parameters and the adiabatic energies as function of time in two trajectories: a non-reactive trajectory trapped in $S_2$ (left) and a reactive trajectory forming the cis photoproduct (right). In the top row the evolution of the CNNC dihedral angle (dark red) with the values range in the primary (left) y-axis and the CNN angles (light and dark blue) with the values range in the secondary (right) y-axis. In the middle row, the evolution of the N-N distance (purple) and the C-N distances (light and dark green). In the bottom row, the time dependence of the adiabatic energies, the $S_0$ is represented in purple, the $S_1$ in green, the $S_2$ in blue, the $S_3$ in orange, the $S_4$ in red and the $S_5$ in black. The time at which the switch from the $S_2$ to the ground state is produced in the reactive trajectory (right), 102 fs, is represented with a vertical dashed line.

two trajectories. The time evolution of the different parameters have a one to one correspondence with the events that take place during the simulation.

The time-evolution of the geometrical parameters of Figure 6.9 can be used to rationalize the diabatic states populated at each moment. The non-reactive trajectory is initially populated at the adiabatic state $S_3$ and a hop to the energy surface of the $S_2$ adiabatic state is produced at 85 fs. The C-N distances at the beginning of the simulation oscillate around 1.35 Å together with the 115° value for the CNN angle and the value close to 180° CNNC for the dihedral angle seems to indicate that the character of the state is $^1\pi\pi^*$. The CASSCF optimised geometry for this state shows two C-N distances of 1.351 and 1.361 Å two CNN angles of 113.6° and a CNNC dihedral value of 180°. The gradients of the energies and the CNNC dihedral angle seems to indicate that the character of the state has changed to $n^2\pi^{*2}$ before the adiabatic hop, approximately at 65 fs. Then, the trajectory remains in the adiabatic $S_2$ state during the rest of the simulation, maintaining its $n^2\pi^{*2}$ character. The C-N distances oscillate around 1.37 Å, the N-N distance around 1.29 Å, the CNNC angle around 129° with large oscillations and the CNNC dihedral angle around the 95°, values close to those of the $n^2\pi^{*2}$ CASSCF optimised geometry which are 1.378 Å, 1.266 Å, 126.9° and 94.1°, respectively. The energies of the three lowest adiabatic states (Fig. 6.9 top-row left panel) are similar and they evolve parallel in time, but the couplings among them are not large enough to produce the hop to the ground state.

The reactive trajectory starts at $S_3$ adiabatic state and rapidly undergoes a surface hop to the $S_2$ adiabatic state in 35 fs. Then, the hop from this latter adiabatic state to the ground state is produced at 102 fs. The nearly identical C-N and N-N distances around 1.35 Å at the start of the simulation indicates that the character of the $S_3$ state is of $\pi\pi^*$ character. Then, the $S_2$ state has $n^2\pi^{*2}$ character and reaches a twisted conformation with a CNNC dihedral angle around 95° similar to the minimum found for this state. After that, the ground state is reached and the dihedral angle oscillates around 0° characteristic of the cis-photoproduct. In addition, the N-N distance oscillates around 1.25Å and the C-N distance around 1.44 Å, in close agreement with the geometrical parameters obtained for the optimised geometry of the cis-ground state which are 1.269 Å and

1.436Å, respectively. The analysis of the direct hopping from the $S_2$ to the $S_0$ is particularly interesting because there is no report of a conical intersection between these states to our knowledge. However, this is not a limitation for having a direct transition among them provided there is a strong coupling among them and the diabatic energy difference is small enough. This is exactly what we would expect in a twisted conformation, the closed shell, the $n\pi^*$ and the $n^2\pi^{*2}$ should become nearly degenerate at this geometry and the coupling should be relatively important between the latter and the closed shell states. This would explain the static picture described in the twisted conformation (Fig. 6.4) for three diabatic states nearly degenerate and strong couplings with the first and the last. Then, our results suggest that an open path for the deactivation from the $n^2\pi^{*2}$ state is possible, and in fact very probable, despite this channel will be very hard to be observed from static descriptions of the system.

### CASSCF MD starting at $^1n\pi^*$ state

The dynamics from the dark $^1n\pi^*$ state are started from the first excited state in random conformations, the same as used for the bright states simulations. The initial momenta are also randomly selected and scaled to a kinetic energy corresponding to 298 K. Here, we analyse the results obtained for 148 independent trajectories employing a larger time step of 1.95 fs run along 1930 fs. Nine of these trajectories have been discarded because of the artificially C-H bond breaking, which suggests that this time step is probably above the advisable limit.

The time-evolution of the adiabatic states population (Fig. 6.10) for the simulation from the $n\pi^*$ states shows that the decay to the ground state is slower than in the simulations from the bright states. The ground state reaches the 50% of population at 720 fs. The smaller number of trajectories in this analysis makes the curves of the time-evolution population slightly step-wise, contrary to the smooth curves obtained for the other simulations where more independent trajectories have been analysed.

The main geometrical parameters at the hopping points are represented in Figure 6.11. The results show that the hops are mainly produced close to the CASSCF $n\pi^*$ minimum, 128.9° and 180.0° for the CNN angle and the

CNNC dihedral angle respectively. This is associated with the almost zero gradients for this state to reach the twisted conformation along the dihedral angle evolution, contrary to the minimum observed at MS-CASPT2 level for this state at the twisted conformation (CNNC=90.1°). These small gradients indicates a very low probability to reach the twisted conformation for this state at CASSCF level of theory and is probably the reason for the small quantum yield determined ($\Phi_{cis}$=0.05) significantly smaller than the 0.2 value experimentally observed. In addition, our results do not suggest any preference for the P or M channels, but a small fraction of reactive trajectories reached the twisted conformation.

CASSCF is probably not the most accurate method to describe the relative energies of the electronic states in azobenzene, as in many other systems. There are at least three points where this method has shown a discrepancy with MS-CASPT2, which is in principle more accurate because it introduces dynamic electron correlation. These three discrepancies are i) the much larger gradients in CASSCF to reach the minimum for the $n^2\pi^{*2}$

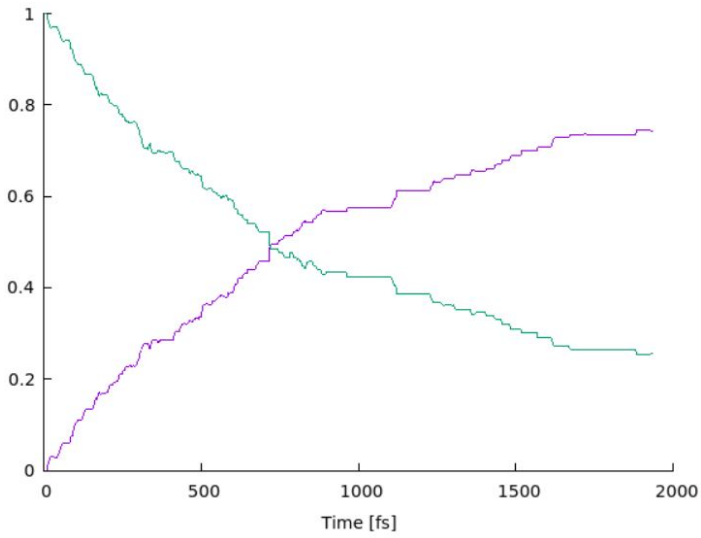


**Figure 6.10.** Time evolution of the adiabatic states population for the simulations starting in the $n\pi^*$ state. The ground state is represented in purple and the first excited state in green.

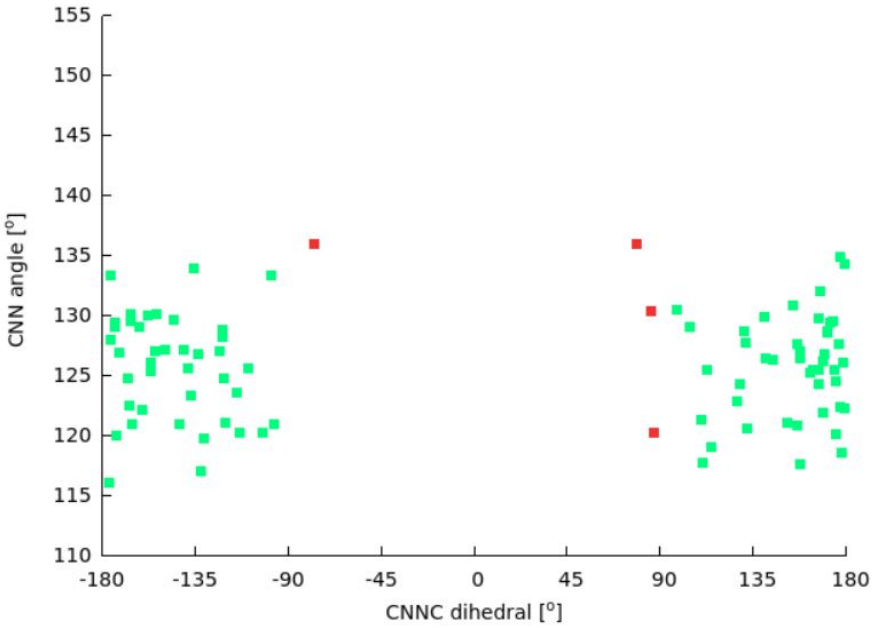


**Figure 6.11.** CNNC dihedral angle and average CNN angle at the ground state hopping geometry. The colors indicate the resulting photoproduct: green, trans-azobenzene and red, cis-azobenzene.

state in the twisted conformation, ii) the planar minimum for the n$\pi^*$ state at CASSCF level, contrary to the MS-CASPT2 minimum for this state which has a twisted conformation and iii) the absence of a CASSCF to describe the $\pi\pi^*$/n$\pi^*$ conical intersection in the pedal-like conformation. Despite these facts, the results above presented are not without meaning, but they need to be carefully interpreted keeping in mind these shortcomings. Obviously, the studies presented in this chapter are completely prohibitive at MS-CASPT2, not only for the larger computational time required for one single energy calculation, but also for the lack of analytical gradients. As an alternative, we present a single 0 K trajectory at MS-CASPT2 level to extend the interpretation of our results.

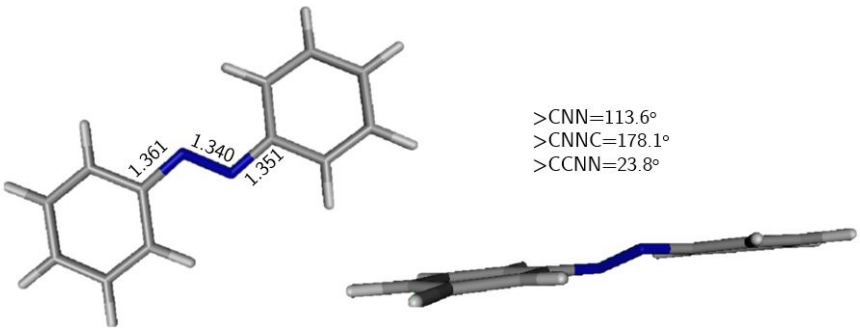


**Figure 6.12.** The pedal-like conformation which is taken from Ref. 22.

### MS-CASPT2 simulation

We have performed our 0 K simulation starting in the first excited state at the pedal-like geometry, shown in Figure 6.12. This simulates to some extent a situation in which the excited state has reached the $^1\pi\pi^*/^1\mathrm{n}\pi^*$ conical intersection after the absorption in the Franck-Condon geometry and that the population has been transferred from $^1\pi\pi^*$ to $^1\mathrm{n}\pi^*$. We have performed a simulation at MS-CASPT2 level using a time step of 1 fs.

Table 6.2 shows the SA-CASSCF and MS-CASPT2 energies at this conformation, using 6 and 10 states in the calculations. The results almost do not present differences between both SA-CASSCF results, but large

**Table 6.2.** SA-CASSCF and MS-CASPT2 energies [kcal/mol] at the pedal-like conformation using 6 or 10 states in the state-average (and the multi-state).

| | 6 states | | 10 states | |
|---|---|---|---|---|
| | SA-CASSCF | MS-CASPT2 | SA-CASSCF | MS-CASPT2 |
| $S_1$ | 66.5 | 61.6 | 66.5 | 63.3 |
| $S_2$ | 108.0 | 77.9 | 108.8 | 66.7 |
| $S_3$ | 115.1 | 103.7 | 115.2 | 107.3 |
| $S_4$ | 127.9 | 117.4 | 128.5 | 118.3 |

differences are found between the MS-CASPT2 results. Particularly, the adiabatic energy of $S_2$ is reduced more than 10 kcal/mol when including more states in the calculation. The energy of $S_2$ at SS-CASPT2 level using 10 roots in the pedal-like conformation is 91.1 kcal/mol, compared with the 108.8 and 66.7 values for the SA-CASSCF and MS-CASPT2, with almost the same value when including 6 states in the average. All these facts suggest that the discrepancies come from the multi-state mixing and not from the average description of the reference wave function. This is reflected in the so-called perturbation-modified wave functions, linear combinations of CASSCF roots arising from the diagonalization of the effective MS-CASPT2 Hamiltonian. There are rather large coefficients of the higher-lying CASSCF roots in the description of the lower energy MS-CASPT2 wave functions. Therefore, to properly describe this region one needs to change the SA(6)-CASSCF description for the MS(10)-CASPT2 methodology, which shows at this conformation the conical intersection found by Casellas et al. [22]

We have also performed a short cold simulation at this level of theory starting in the $^1\pi\pi^*$, i.e. the adiabatic $S_2$ state. This simulation undergoes a surface hop to the the lower-lying $^1n\pi^*$ state in less than 10 fs showing that this conformation is a very efficient region for the population transfer between these states.

The simulation starting in the $S_1$ state where it remains for the next 300 fs. Figure 6.13 shows the evolution of the energies for the adiabatic states along the simulation. These results show that the energy of the $S_1$ state is almost constant during the whole simulation and the energy gap to the ground state is too large to hop to the ground state. The geometry of the conformation at 340 fs, is analysed. This is very similar than the pedal-like conformation and shows a CNNC dihedral angle of 146° which indicates a small tendency to reach the twisted conformation from the pedal-like geometry.

More dynamics with random initial momenta and starting in the bright states at this level of theory would be necessary to obtain a more detailed picture about the mechanism. There are a lot of decay paths to the ground state and an electronic structure method taking into account all of them at an equal footing is necessary to obtain reliable information about the

probability of each path. Unfortunately, the MS(10)-CASPT2 electronic structure based method is not a real option to generate a large number of independent trajectories. As alternative, it would be useful to find a method generating the same potential energy surfaces at much lower computational cost. A multi configurational method accounting for dynamic electron correlation would be a good candidate, such as OM2/MRCI[20,31] which has proved its efficiency in this system for the relaxations from the $n\pi^*$ state.

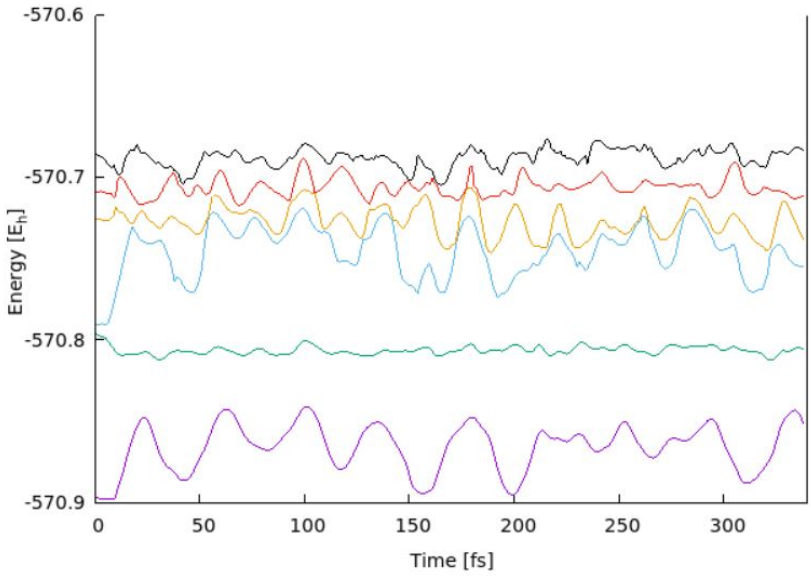


**Figure 6.13.** Time-evolution of the adiabatic states energies along the MS(10)-CASPT2 simulation. The ground state in purple, $S_1$ in green, $S_2$ in blue, $S_3$ in yellow, $S_4$ in orange and $S_5$ in black.

## 6.4. Conclusions

Trajectory surface hopping (TSH) has been proven to be an accurate method to determine the relative importance of the different deactivation paths from the excited states when an important amount of independent trajectories is analysed. This method computes the gradients along all the directions, and does not force the deactivation process to occur along a particular mode. However, the results, as in any other dynamic simulation, are strongly dependent on the electronic structure method employed. A poor description of the adiabatic potential energy surfaces in an important region will cause unphysical simulations when exploring these parts of the conformational space. In addition, we have found that a time step of 1 fs is probably on the limit of the methodology and larger values start to be dangerous for the simulations.

The selection of the electronic structure based method is a key step in the process, because the simulations would explore those regions accessible from the surfaces generated with the method. The standard TD-DFT methodology shows a good relation between accuracy and computational cost. Unfortunately, the pronounced biradical character observed in the twisted conformation makes the DFT ground state single determinant wave function a bad reference to account for the singlet excited states in geometries close to this region. The spin-flip TD-DFT (SF-TD-DFT) uses as reference the lowest triplet state and the response states are generated by the spin-flip of an electron from $\alpha$ to $\beta$. This generates accurate wave functions for the singlet ground state, the doubly excited singlet and the spin-adapted singlet and triplet open-shells but does not describe properly other excited states arising from electron replacements involving other orbitals than the singly occupied ones in the triplet reference state. Such states are likely to suffer of spin-contamination by the lack of corresponding configurations with inverted spins of the unpaired electrons. The state-average CASSCF (SA-CASSCF) gives a proper qualitative description of the states involved in the photoprocess along all the interesting regions of the conformational space. However, this method shows large gradients towards the twisted conformation for the $^1n^2\pi^{*2}$ state, when compared with MS(10)-CASPT2. In addition, this method neither presents the minimum for the $^1n\pi^*$ state at the twisted conformation nor the ($^1\pi\pi^*/^1n\pi^*$) mini-

mum energy conical intersection at the pedal-like conformation, contrary to what was observed at MS(10)-CASPT2 level. Unfortunately, the MS-CASPT2 method is not a realistic alternative to determine the potential energy surfaces nowadays. The above-described MS-CASPT2 simulation 340 fs has been running on 32 cores during more than 2 months, while each of the 1000 fs trajectories at SA-CASSCF level could be completed in 11 days running on one single core. This, roughly speaking, means that simulations at MS-CASPT2 level are 2000 times more demanding than at SA-CASSCF level. That is the reason why –limited by the computational power available nowadays– we selected SA-CASSCF as the electronic structure method to determine the potential energy surfaces.

The main isomerization mechanism was shown to be the inversion-assisted rotation, i.e. the hoppings to the ground state are produced in the vicinity of the twisted conformation and with larger CNN angles than those found in the trans and cis ground state minima. Our results suggest that whether the formed photoproduct is cis or trans is controlled by the CNNC dihedral angle at the hopping geometry, the former is formed with values smaller than 90° and the latter with larger values. The quantum yield for the cis formation in simulations from the bright states is 0.25 and for the simulations starting from the first excited state is 0.05, contrary to what was observed experimentally where the quantum yield for the latter was twice the observed for the former. The rate for the ground state recovery from the bright states is 274 fs and from the dark $^1n\pi^*$ state is 720 fs. Both the quantum yields and rates can be rationalised by the overly large SA-CASSCF gradients to reach the twisted conformation in the $^1n^2\pi^{*2}$ state. In addition, the $^1n\pi^*$ state shows an almost flat potential energy surface along the dihedral angle, generating only a small driving-force to reach the twisted conformation and hop to the ground state producing the cis photoproduct. Moreover, our studies have not shown any preference for the P-channel over the M-channel, with almost the same amount of hoppings from each of them. The calculations with MS-CASPT2 seem to indicate that the $S_1$ state presents relatively flat surfaces in the vicinity of the pedal-like conformation, although the system is most probably artificially trapped there because no initial velocities are defined and the system is only evolving along the calculated gradients. In the real system, the simulation in the $^1n\pi^*$ state at the pedal-like conformation is started

with some velocities which are obtained after the system reaches the conical intersection in the $S_2$ state, these velocities are almost impossible to predict a priori and an option could be to start some simulations at this conformation using different random initial momenta.

The use of nuclear dynamics simulation has allowed to observe a channel which was not expected from the static calculations in which only special points on the potential energy surfaces are calculated. This is the direct relaxation from the $^1n^2\pi^{*2}$ state to the closed shell ground state, which is in fact an important path with more than 30% of the trajectories decaying through it. This channel cannot be found from static calculations because there is not a conical intersection between these states. However, the three diabatic states corresponding to the 'closed shell', $n\pi^*$ and $n^2\pi^{*2}$ are in principle nearly degenerate, with strong non-adiabatic coupling between the latter and the first. Then, this ends up in a very efficient population transfer region between these states without the appearance of a conical intersection.

## 6.5. References

[1] J.-P. Sauvage, *From chemical topology to molecular machines*, Nobel Lecture (2016), Sweden.

[2] Z. Mahimwalla, K. G. Yager, J. ichi Mamiya, A. Shishido, A. Priimagi, and C. J. Barrett, *Azobenzene photomechanics: prospects and potential applications*, Polym. Bull. **69**, 967–1006 (2012).

[3] S. Venkataramani, U. Jana, M. Dommaschk, F. D. Sönischsen, F. Tuczeck, and R. Herges, *Magnetic Bistability of Molecules in Homogeneous Solution at Room Temperature*, Science **331**, 445–448 (2011).

[4] P. P. Birnbaum, J. H. Linford, and D. W. G. Style, *The absorption spectra of azobenzene and some derivatives*, Trans. Faraday Soc. **49**, 735–744 (1953).

[5] L. B. Jones, and G. S. Hammond, *Mechanisms of Photochemical Reactions in Solution. XXX.*[1] *Photosensitized Isomerization of Azobenzene*, J. Am. Chem. Soc. **87**, 4219–4220 (1965).

[6] E. Fischer, *Photosensitized isomerization of azobenzene*, J. Am. Chem. Soc. **90**, 796–797 (1968).

[7] P. Bortolus, and S. Monti, *Cis-trans photoisomerization of azobenzene. Solvent and triplet donors effects*, J. Phys. Chem. **83**, 648–652 (1979).

[8] H. Rau, and E. Lueddecke, *On the rotation-inversion controversy on photoisomerization of azobenzenes. Experimental proof of inversion*, J. Am. Chem. Soc. **104**, 1616–1620 (1982).

[9] J. Griffiths, *II. Photochemistry of azobenzene and its derivatives*, J. Chem. Soc. Rev. **1**, 481–493 (1972).

[10] H. M. D. Bandara, and S. C. Burdette, *Photoisomerization in different classes of azobenzene*, Chem. Soc. Rev. **41**, 1809–1825 (2012).

[11] J. M. Nerbonne, and R. G. Weiss, *Elucidation of the Thermal Isomerization Mechanism for Azobenzene in a Cholesteric Liquid Crystal Solvent*, J. Am. Chem. Soc. **100**, 5953–5954 (1978).

[12] P. Bortolus, and S. Monti, *Cis* $\rightleftarrows$ *Trans Photoisomerization of Azobenzene-Cyclodextrin Inclusion Complexes*, J. Phys. Chem. **91**, 5046–5050 (1987).

[13] I. K. Lednev, T.-Q. Ye, R. E. Hester, and J. N. Moore, *Femtosecond Time-Resolved UV-Visible Absorption Spectroscopy of trans-Azobenzene in Solution*, J. Phys. Chem. **100**, 13 338–13 341 (1996).

[14] E. W.-G. Dau, *A New Trans-to-Cis Photoisomerization Mechanism of Azobenzene on the* $S_1(n,\pi^*)$ *Surface*, J. Phys. Chem. A **108**, 950–956 (2004).

[15] L. Gagliardi, G. Orlandi, F. Bernardi, A. Cembran, and M. Garavelli, *A theoretical study of the lowest electronic states of azobenzene: the role of torsion coordinate in the cis–trans photoisomerization*, Theor. Chem. Acc. **111**, 363–372 (2004).

[16] C. Ciminelli, G. Granucci, and M. Persico, *The Photoisomerization Mechanism of Azobenzene: A Semiclassical Simulation of Nonadiabatic Dynamics*, Chem. Eur. J. **10**, 2327–2341 (2004).

[17] G. Granucci, and M. Persico, *Excited state dynamics with the direct trajectory surface hopping method: azobenzene and its derivatives as a case study*, Theor. Chem. Acc. **117**, 1131–1143 (2007).

[18] S. Yuan, Y. Dou, W. Wu, Y. Hu, and J. Zhao, *Why Does trans-Azobenzene Have a Smaller Isomerization Yield for $\pi\pi^*$ Excitation Than for $n\pi^*$ Excitation?*, J. Phys. Chem. A **112**, 13 326–13 334 (2008).

[19] Y. Ootani, K. Satoh, A. Nakayama, T. Noro, and T. Taketsugu, *Ab initio molecular dynamics simulation of photoisomerization in azobenzene in the $n\pi^*$ state*, J. Phys. Chem. **131**, 194 306 (2009).

[20] O. Weingart, Z. Lan, A. Koslowski, and W. Thiel, *Chiral Pathways and Periodic Decay in cis-Azobenzene Photodynamics*, J. Phys. Chem. Lett. **2**, 1506–1509 (2011).

[21] A. Nenov, R. Borrego-Varillas, A. Oriana, L. Ganzer, F. Segatta, I. Conti, J. Segarra-Marti, J. Omachi, M. Dapor, S. Taioli, C. Manzoni, S. Mukamel, G. Cerullo, and M. Garavell, *UV-Light-Induced Vibrational Coherences: The Key to Understand Kasha Rule Violation in trans-Azobenzene*, J. Phys. Chem. Lett. **9**, 1534–1541 (2018).

[22] J. Casellas, M. J. Bearpark, and M. Reguero, *Excited-State Decay in the Photoisomerisation of Azobenzene: A New Balance between Mechanisms*, Chem. Phys. Chem. **17**, 3068–3079 (2016).

[23] I. Fdez. Galván, M. Vacher, A. Alavi, C. Angeli, F. Aquilante, J. Autschbach, J. J. Bao, S. I. Bokarev, N. A. Bogdanov, R. K. Carlson, L. F. Chibotaru, J. Creutzberg, N. Dattani, M. G. Delcey, S. S. Dong, A. Dreuw, L. Freitag, L. M. Frutos, L. Gagliardi, F. Gendron, A. Giussani, L. González, G. Grell, M. Guo, C. E. Hoyer, M. Johansson, S. Keller, S. Knecht, G. Kovačević, E. Källman, G. Li Manni, M. Lundberg, Y. Ma, S. Mai, J. P. Malhado, P. A. Malmqvist, P. Marquetand, S. A. Mewes, J. Norell, M. Olivucci,

M. Oppel, Q. M. Phung, K. Pierloot, F. Plasser, M. Reiher, A. M. Sand, I. Schapiro, P. Sharma, C. J. Stein, L. K. Sørensen, D. G. Truhlar, M. Ugandi, L. Ungur, A. Valentini, S. Vancoillie, V. Veryazov, O. Weser, T. A. Wesołowski, P.-O. Widmark, S. Wouters, A. Zech, J. P. Zobel, and R. Lindh, *OpenMolcas: From Source Code to Insight*, J. Chem. Theory Comput. **15**, 5925–5964 (2019).

[24] *CPMD V3.15 2012, CPMD, http://www.cpmd.org/ Copyright IBM Corp 1990-2008, Copyright MPI für Festkörperforschung Stuttgart 1997-2001.*

[25] P. Altoé, M. Stenta, A. Bottoni, and M. Garavelli, *A tunable QM/MM approach to chemical reactivity, structure and physico-chemical properties prediction*, Theor. Chem. Acc. **118**, 219–240 (2007).

[26] M. Barbati, *Nonadiabatic dynamics with trajectory surface hopping method*, Comput. Mol. Sci. **1**, 620–633 (2011).

[27] N. L. Doltsinis, and D. Marx, *Nonadiabatic Car-Parrinello Molecular Dynamics*, Phys. Rev. Lett. **88**, 166 402 (2002).

[28] I. Frank, and K. Damianos, *Restricted open-shell Kohn-Sham theory: Simulation of the pyrrole photodissociation*, J. Chem. Phys. **126**, 125 105 (2007).

[29] I. Tavernelli, E. Tapavicza, and U. Rothlisberger, *Non-adiabatic dynamics using time-dependent density functional theory: Assessing the coupling strengths*, J. Mol. Struc. THEOCHEM **914**, 22–29 (2009).

[30] L. Yue, Y. Liu, and C. Zhu, *Performance of TDDFT with and without spin-flip in trajectory surface hopping dynamics: cis–trans azobenzene photoisomerization*, Phys. Chem. Chem. Phys. **20**, 24 123 (2018).

[31] X. Pang, C. Jiang, Y. Qi, L. Yuan, D. Hu, X. Zhang, D. Zhao, D. Wang, Z. Lan, and F. Li, *Ultrafast unidirectional chiral rotation in the Z–E photoisomerization of two azoheteroarene photoswitches*, Phys. Chem. Chem. Phys. **20**, 25 910 (2018).

# 7.
# General conclusions

The main objective at the beginning of this road was to go beyond the static electronic structure description of excited states for different organic compounds and transition metal complexes. To contextualize the problem, one needs first to take a look at the experience of our group in the resolution of problems involving excited states using accurate electronic structure methods of these aforementioned systems. The experience in dynamic studies was limited to the ground state molecular dynamics to sample the conformational space and the use of Fermi's golden rule, which can be considered a quasi-dynamic method, for the study of intersystem crossing rates in transition metal complexes. This methodology has also been used in Chapters 3 and 4 of this doctoral thesis for the study of transition metal complexes, however, we demonstrate in this text the limitation of the methodology for the study of ultrafast processes. As an alternative, we propose the use of wave packet quantum dynamics in the so-called Multi-Configuration Time-Dependent Hartree (MCTDH) approach. This method is based on the propagation of a nuclear wave function, therefore the nuclei are also treated at a quantum level, using a previously defined model Hamiltonian. This has been the methodology used in calculations of Chapters 4 and 5 in transition metal complexes and xanthone. Trajectory surface hopping (TSH) is another methodology to explicitly compute excited state dynamic simulations but with a classical treatment for the nuclei. This methodology is based on the simulation starting in an initial excited state, which is used to compute the gradients on-the-fly to describe the nuclear motion, that can transfer population to other states by means of an algorithm studying the hopping probability. This last have been employed in Chapter 6 for the study of azobenzene photoisomerization process.

The other general objective proposed at the earlier steps of this project was to achieve the capacity of discerning the appropriate method for each particular problem. Fermi's golden rule is an appropriate tool to describe the rates and lifetimes of relatively slow processes in which intermediate electronic states can relax to their equilibrium geometry, as demonstrated in chapter 3 of this work. However, this is not the best method for determining rates of ultrafast non-equilibrium transitions. The accurate results obtained with this methodology in previous studies in the group are not general and probably achieved because of similar equilibrium geometries

among the ground and the initially populated states. One needs to go beyond this quasi-dynamic treatment to study ultrafast processes such as the photodeactivation paths in the LIESST (or reverse-LIESST) of transition metal complexes. The use of the static description to describe the physics of the process by the search of critical points on the potential energy surfaces is not enough to accurately describe all the possible deactivation paths because the limited number of dimensions that one can explore. In addition, without an explicit introduction of time, it is not possible to determine lifetimes of the states only considering the critical points.

The wave packet dynamic simulations has the great advantage of a quantum treatment for both the nuclei and electrons, therefore processes such as tunneling are directly included in the description in an ab initio manner. Another advantage of the methodology is the flexibility to create the model Hamiltonian which allows to add and remove parameters (by means of their inclusion) in the model Hamiltonian. This is of great importance if one wants to study the effect of a mode, coupling or state in the overall mechanism and allow to easily identify their influence. Moreover, once the model Hamiltonian is defined, the calculations are fast because the wave function is propagated numerically using a predefined grid. The main shortcomings of the methodology are: i) the creation of an appropriate model Hamiltonian, ii) the complicated expressions of the nuclear kinetic operators when the nuclear displacements are not expressed in normal modes coordinates, but in another more appropriate set of coordinates for the particular problem under study and iii) the extension of the simulations for more than 2 ps has little physical sense without the inclusion of bath modes able to dissipate energy from the irradiated molecule to its surroundings, this obviously complicates even more the construction of the model Hamiltonian.

The creation of the model Hamiltonian used in MCTDH is far from trivial. Except for the smallest model systems, the number of parameters is immense and one has to abandon the pretension of being complete. Assumptions are to be made to restrict the parameter set to the most relevant ones and typically those terms involving more than two modes at the same time are neglected and often from a practical point of view, it is only possible to consider interactions along a single mode. Concern-

ing the use of other than normal mode coordinates, the expression of the nuclear kinetic energy operators in curvilinear coordinates is necessary to describe regions far from the small amplitude motions around the equilibrium geometry where the rectilinear normal coordinates behave well. The ordinary normal mode coordinates usually involve delocalized vibrational motions and one would need the combination of several modes to describe the variation of one or two internal coordinates far from the equilibrium geometry as illustrated in the introduction of this thesis.

The trajectory surface hopping methodology has the great advantage that it does not require a large amount of human intervention. It explicitly computes the gradients on-the-fly, avoiding tedious procedures on the construction of model Hamiltonians. In addition, the gradients are calculated (analytically or numerically) using Cartesian coordinates, therefore there is not any inconvenience in the study of processes involving displacements not directly described by a limited set of normal modes. The limitations of this method mostly come from the classical treatment of the nuclei which cause coherence/decoherence problems in these dynamics or the need of empirical parameters such as the fewest switching algorithms and the necessity of a large number of independent trajectories to sample the different competitive paths. Other limitations of this methodology are associated to the electronic structure method used to compute the gradients. The calculations at an accurate level of all the electronic states and their gradients is really expensive, and this becomes almost prohibitive when analytical gradients are not available and have to be determined numerically. The inherent instability of second order perturbation theory causes the surfaces not to be completely free of numerical noise and small instabilities on them from the electronic structure could derive in inaccurate gradients.

The use of dynamic calculations is really important in some cases and in others becomes totally a must to have an exhaustive picture of the overall process. However, the results obtained from the dynamic simulations directly depends on the electronic structure method employed. Then, it is obvious that the quality of the dynamics will depend on the accuracy of the electronic method applied to determine couplings and relative energies. The best option would be the use of the most accurate electronic structure determination combined with the most appropriate excited state

dynamics method, but evidently, this is hardly ever possible. Then, one should keep in mind not only the limitations of the dynamics method used but also those arising from the electronic structure method and the accuracy in the potential energy surface description.

More detailed conclusions for each particular problem together with a brief description of why each method has been chosen for them is given in the next lines.

Fermi's golden rule has been employed to determine the lifetime of the high-spin state in these two iron (II) prototype complexes. One of these complexes, $[Fe(bpy)_3]^{2+}$, shows a relatively fast relaxation of the quintet state and the other complex, $[Fe(mtz)_6]^{2+}$, exhibits a very slow relaxation process. The time-dependent expression of the Fermi's golden rule has been successfully applied to determine the lifetimes of these quintet states and can be considered as a very appropriate methodology to study processes happening at this time scale where the minimum of the initial state is reached.

Fermi's golden rule has badly failed to determine the intersystem crossing rates between pairs of states, the calculated rates were several orders of magnitude off from the experimentally determined rates. As an alternative, we have created a model Hamiltonian and used it to determine the overall deactivation mechanism. The latter has been successfully applied to determine sequential rates and propose a general deactivation mechanism. The first intersystem crossing is from the initial $^5E_g$ state to the intermediate $^3T_{2g}$ in 350 fs which slowly starts to lose population towards the high-spin and the low-spin state with a predicted lifetime of around 24 ps. The simulations also suggest a preference toward the high-spin over the low-spin state, therefore indicating a small quantum yield for the reverse-LIESST process. Our results also show that the overall process is qualitatively well-defined with a small nuclear wave function but does not give enough flexibility to accurately describe it along all the process. This causes an important overestimation of the population in the initial state because the small amount of SPFs is not able to account a proper wave function for more than one electronic state at the same time and an important part of the population that should be transferred remains trapped in the $^5E_g$ state.

The unphysical rates obtained with Fermi's golden rule together with the calculations performed to construct the model Hamiltonian has allowed us to rationalize the reason why the former was successfully applied in many other situations and failed so badly here. This is mainly caused because Fermi's golden rule is expected to give accurate results when the intersystem crossing happens from the equilibrium geometry of the initial state. There are two situations for which this can occur: first, by an excitation directly to the excited state minimum when the equilibrium geometries of ground and excited state are similar, and second when the process is sufficiently slow allowing the initial state in the intersystem crossing to reach its minimum geometry. The former is the case in the LIESST process in $[Fe(bpy)_3]^{2+}$, as we have observed with the projection of the optimised geometries into the ground state normal modes basis. This is our explanation why previous calculations in the group succeeded and not the ones for the reverse-LIESST. In addition, we have observed the complications to deal with a CASPT2 fitted model Hamiltonian including MLCT states because of the intrinsic limitations of the electronic structure methodology such as the active space conservation along the normal modes or the different couplings at CASSCF and CASPT2 level. As an alternative, we have presented TPSSh as a valid electronic structure method to generate the model Hamiltonian based on previous results in this complex and similar systems.

The construction of the model Hamiltonian using the Duschinsky rotation matrix has been applied in wave packet quantum dynamic simulations with promising results. This is an elegant and efficient, manner of expressing the diabatic states potential energies. Unfortunately, there are no analytical expressions to determine the couplings from the equilibrium geometry and the corresponding Hessian of each excited state. Then, to complete the model Hamiltonian with the couplings, we had to fall back on the less elegant fitting procedures and interpolations/extrapolations from calculations at displaced geometries. The results with the model Hamiltonian created for xanthone indicate a sequential deactivation from the bright $S_2$ state to the $T_1$. There is a first internal conversion involving $S_2$ and $S_1$, this latter is the singlet state that transfers population to the triplets, specifically to the $T_2$ which acts as a Japanese rocking fountain accumulating population before transferring it to the $T_1$. Our simula-

tions also suggest an insignificant amount of population transferred via vibronic spin-orbit couplings through El-Sayed forbidden channels. In a wider context, these results also explain why xanthone shows ultrafast intersystem crossing rates contrary to other carbonyl aromatic compounds: i) populating the $S_2$ instead of $S_1$ gives an impulse to the deactivation process, ii) the rigidity of xanthone does not allow to distribute an important amount of energy along non-efficient normal modes and iii) the symmetry of the molecule gives to this molecule more probabilities to reach critical points.

Trajectory surface hopping (TSH) has been proved to be a really efficient method to perform dynamic simulations which need to explore regions far away from the equilibrium ground state geometry. This gives reliable results of the rates and average paths after analysing an important amount of independent trajectories. The results with this methodology are obviously inherently related with the potential energy surfaces described for the employed electronic structure based method. In addition, we have observed in situ that the time step of 1 fs is probably on the limit of what can be considered a safe value, the larger value of 2 fs seems to be too large and should be discarded. The results in azobenzene show clearly that the isomerization mechanism is an inversion-assisted rotation. The rates and quantum yields for the dynamics starting in the bright states are probably overestimated for the large gradients toward the twisted conformation in the SA-CASSCF potential energy surfaces for this state. The opposite story happens for the simulations starting from the first excited state. However, the use of dynamic simulations has allowed to open the possibility of a direct deactivation from the $n^2\pi^{*2}$ state which is not considered from static calculations because of the lack of a conical intersection between these states. In addition, our results has not shown any preference for the P- or M- channel and do not suggest any enantiomeric excess towards any of the cis enantiomers.

UNIVERSITAT ROVIRA I VIRGILI
BEYOND THE STATIC DESCRIPTION OF THE ELECTRONIC STRUCTURE:EXCITED STATE DYNAMICS IN TRANSITION METAL COMPLEXES AND ORGANIC COMPOUNDS
Marc Alías Rodríguez

# Appendix A.
## Multi-layer trees

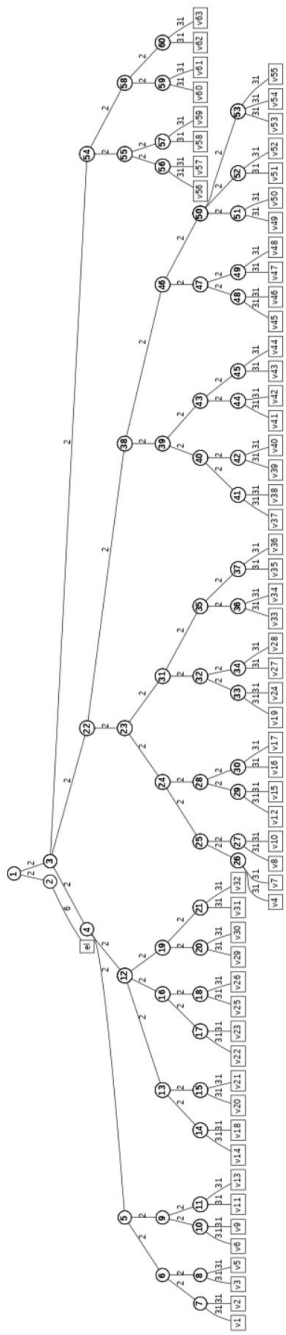

**Figure A.1.** Multi-layer representation of vibrational normal modes in xanthone. The circles represents the nodes and the squares the modes. The number above the squares coincides with the primitive functions or DVRs for each mode and the other numbers are the SPFs for each node or branch.

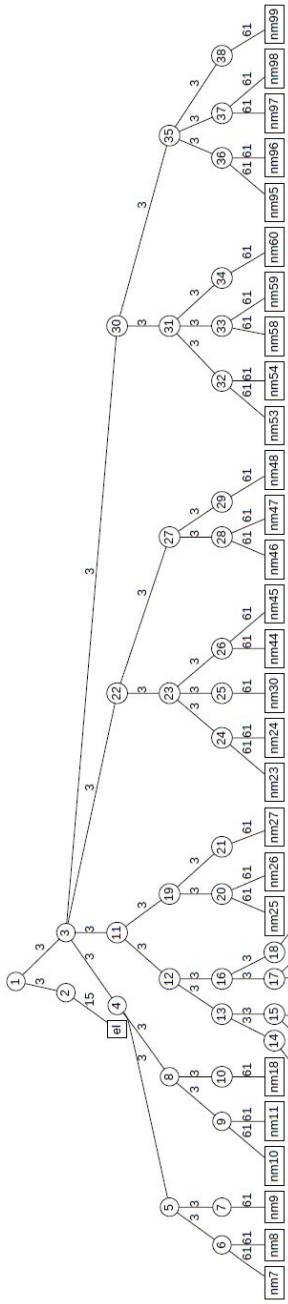


**Figure A.2.** Multi-layer representation of vibrational normal modes in $[Fe(bpy)_3]^{2+}$. The circles represents the nodes and the squares the modes. The number above the squares coincides with the primitive functions or DVRs for each mode and the other numbers are the SPFs for each node or branch.

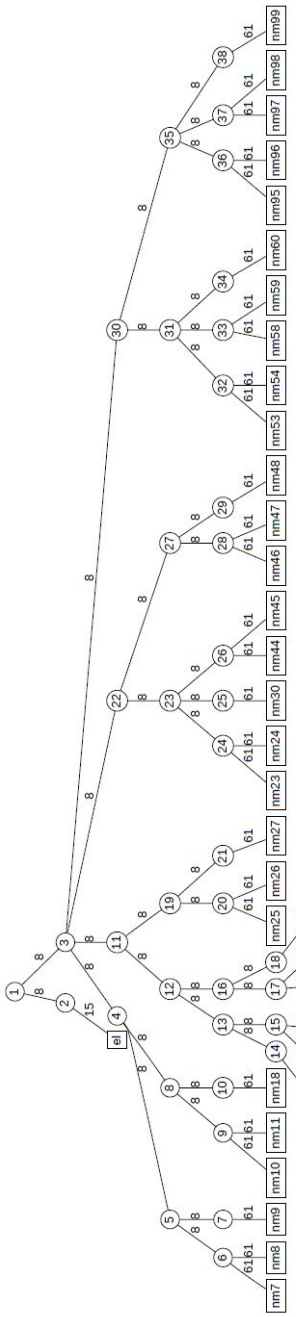


**Figure A.3.** Multi-layer representation of vibrational normal modes in $[Fe(bpy)_3]^{2+}$with larger amount of SPFs. The circles represents the nodes and the squares the modes. The number above the squares coincides with the primitive functions or DVRs for each mode and the other numbers are the SPFs for each node or branch.

UNIVERSITAT ROVIRA I VIRGILI
BEYOND THE STATIC DESCRIPTION OF THE ELECTRONIC STRUCTURE:EXCITED STATE DYNAMICS IN TRANSITION METAL COMPLEXES AND ORGANIC COMPOUNDS
Marc Alías Rodríguez

UNIVERSITAT ROVIRA I VIRGILI
BEYOND THE STATIC DESCRIPTION OF THE ELECTRONIC STRUCTURE:EXCITED STATE DYNAMICS IN TRANSITION METAL COMPLEXES AND ORGANIC COMPOUNDS
Marc Alías Rodríguez

UNIVERSITAT ROVIRA I VIRGILI
BEYOND THE STATIC DESCRIPTION OF THE ELECTRONIC STRUCTURE:EXCITED STATE DYNAMICS IN TRANSITION METAL COMPLEXES AND ORGANIC COMPOUNDS
Marc Alías Rodríguez

UNIVERSITAT ROVIRA I VIRGILI
BEYOND THE STATIC DESCRIPTION OF THE ELECTRONIC STRUCTURE:EXCITED STATE DYNAMICS IN TRANSITION METAL COMPLEXES AND ORGANIC COMPOUNDS
Marc Alías Rodríguez

UNIVERSITAT
ROVIRA i VIRGILI